UTS UNIVERSITY OF TECHNOLOGY SYDNEY

Powertrain Electrification for Jerk Reduction and Continuous Torque Delivery

by Peter Shaker Tawadros

Thesis submitted in fulfilment of the requirements for the degree of

Doctor of Philosophy

under the supervision of Professor Nong Zhang

University of Technology Sydney
Faculty of Engineering and Information Technology

June 2019

UTS School of Mechanical and Mechatronic Engineering (MME)
Faculty of Engineering & Information Technology (FEIT)

Powertrain Electrification for Jerk Reduction and Continuous Torque Delivery

Research Centre: The UTS Centre for Green Energy and Vehicle Innovations (GEVI)

Completed by: Peter Shaker Tawadros

Supervisor: Prof. Nong Zhang

Co-supervisors: Dr. Paul Walker

Course code: C02018
Subject Number: 49986 Doctor of Philosophy (PhD)
Date: 01/01/2009 to 30/06/2019

University of Technology Sydney (UTS)
P.O. Box 123, Broadway, Ultimo, N.S.W. 2007
Australia

Certificate of Original Authorship

I, Peter Shaker Tawadros declare that this thesis, is submitted in fulfilment of the requirements for the award of Doctor of Philosophy, in the Faculty of Engineering and IT at the University of Technology Sydney.

This thesis is wholly my own work unless otherwise reference or acknowledged. In addition, I certify that all information sources and literature used are indicated in the thesis.

This document has not been submitted for qualifications at any other academic institution.

This research is supported by the Australian Government Research Training Program.

Signature:

Production Note:
Signature removed prior to publication.

28 June 2019

Statement of Contribution

This research project was a collaboration between the Author (Peter Shaker Tawadros) and Mohamed Mahmoud Zakaria Awadallah. Both the Author and Dr Awadallah studied under Prof. Nong Zhang and Dr Paul Walker in the preparation of this project. The project in its entireity required the design, modelling, simulation, verification, construction of a prototype, and experimental validation of a novel P3 mild hybrid vehicle with torque hole elimination.

Mohamed's thesis "A Mild Hybrid Vehicle Control Unit Capable of Torque Hole Elimination in Manual Transmissions", is focused on the development of the control system for the mild hybrid vehicle. It presents the modelling, simulation and hardware-in-the-loop verification of the powertrain and elements of its functionality.

My thesis "Powertrain Electrification for Jerk Reduction and Continuous Torque Delivery", is focused on the development and validation of the physical prototype powertrain. It presents the initial design process, construction of the prototype, experiment design, laboratory testing, and analysis of the data obtained from testing of the physical powertrain prototype.

At all stages of this project both Mohamed and I worked together as a team, collaborating and assisting each other to ensure the project goals were met. For the tasks listed above, where that task is presented in one candidate's thesis, that candidate made the majority contribution to the completion of that task whilst the other provided support as needed.

Signature:

Production Note:
Signature removed
prior to publication.

Peter Shaker Tawadros

28 June 2019

Signature:

Production Note:
Signature removed
prior to publication.

Mohamed Mahmoud Zakaria Awadallah

28 June 2019

Acknowledgements

Without a doubt I first need to thank God for guiding me along the ten-year long path to completion of this research. To have finally reached this point can really only be described as a miracle.

I also need to thank my parents, Laurice and Lotfi for instilling a sense of never being quite satisfied in my brother Paul and I. Between Paul and I we now have amassed some 62 years of institutional education – almost a literal lifetime. I think now's a good time to be satisfied. I wish Dad were here to see it all finished but seeing things from above probably looks better anyway.

My supervisors, Prof. Nong Zhang and Dr. Paul Walker, who have been tirelessly supportive and endlessly patient. The car works. You get a workshop manual to go with it, too. I hope it was worth the wait.

My research colleague Dr Mohamed Awadallah, for motivating me to carry on no matter the setbacks. If everyone had a work ethic like yours the rest of us could go on holiday forever.

Team KERMIT – Jack Liang, James Tawadros, Enoch Zhao, Mohamed Awadallah, Fatma Al-Widyan. Thank you for putting in an amazing effort to help get the car assembled in record time.

Finally, my wonderful wife Dina. Thank you for your love, support, distractions, and cheekiness. You make everything fun.

Financial support for this project is provided jointly by the Australian Research Council

(Linkage ID number LP0775445), and The UTS Centre for Green Energy and Vehicle Innovations (GEVI).

Abstract

A mild-hybrid electric powertrain is proposed for the principal purpose of providing continuous drive torque using a single, dry-plate clutched transmission. The powertrain is optimised to deliver several benefits, in relation to cost, complexity, vibration (jerk), as well as dynamic and emissions performance.

The powertrain proposed is a post-transmission type, with the motor being placed inline with the transmission output shaft, prior to the differential. This allows the powertrain to be controlled for providing continuous drive torque to the wheels during gear shifting and take-off, eliminating the “torque hole” due to disengagement of the clutch plate, and providing a degree of damping during clutch re-engagement. A pressure-based clutch model is used to modulate the electric drive torque to minimise torsional vibration during the gear shifting process, whilst engine speed is controlled proportionally to road speed to minimise discontinuity of rotational velocity during the re-engagement process. The system is designed as a driver assistance function, but can optionally be implemented with automatic clutch and gear actuation units.

A rule-based energy management strategy (EMS) allows the powertrain to be additionally controlled for drive torque supplementation, battery recharging, brake energy recuperation, and electric vehicle (EV) crawl.

System optimization is conducted on several levels. The system architecture is optimized to minimize modification cost from a typical conventional vehicle (CV) by careful consideration of powertrain topology. The selection of the post-transmission (P3) architecture was made to eliminate the cost and complexity of a dual-motor configuration whilst maximising the utility of a single electric motor (EM) using a sophisticated EMS. The

electric power components, primarily the electric motor and battery are optimized for component size and cost based on benchmarking criteria and power needs analysis.

A V-cycle development process using model-based design was followed. A hardware-in-the-loop (HIL) vehicle model was built in a virtual environment, allowing testing of performance and comparison with the CV by running the software model through standard drive cycles in Advanced Vehicle Simulator (ADVISOR). Certain model parameters were tested on a HIL bench and refined, and then the model was downloaded onto a real-time controller (dSPACE MicroAutoBox II) for implementation in the prototype validation stage.

The powertrain is designed to meet the requirements of a typical light vehicle. The prototype powertrain was built into a 1990 Mazda MX-5 (Miata) body, which was modified to fit the additional powertrain components selected through the optimization process. These components include a 1.2 KWh, 96 V $LiFePO_4$ battery pack, a 10 KW cont./30 KW pk. permanent magnet motor, four quadrant 600 A motor controller, battery management system, electronic throttle system, and supervisory controller. The vehicle was instrumented for clutch pedal position, clutch line pressure, gear lever position, brake pedal position, brake line pressure, throttle pedal and butterfly position, engine manifold vacuum, transmission output torque, transmission output speed, and electric motor torque. The battery is also instrumented through the battery management system (BMS) and is capable of logging individual cell voltages and temperatures, as well as pack statistics including state of charge, depth of discharge, current and voltage.

As implemented, the system is designed to suit low-end vehicles typically sold in developing nations, and serves as a way to reduce fossil-fuel dependency, introduce fleet electrification (particularly in areas where access to electricity is unreliable), and improve urban air pollution whilst also improving vehicle driveability through powertrain refinement. In developing the vehicle for such purpose, a tight manufacturing cost control of no more than

105% of the manufacturing cost of the base vehicle is imposed. With changes to the benchmarking criteria and control, the powertrain architecture could also be used for dynamic performance enhancement.

Results of experimental testing of the prototype against the CV are presented and discussed. The experimental testing encompasses acceleration, jerk, torque continuity, and emissions. Results validate the modelled system to a high degree, showing that the powertrain meets its design objectives, effectively providing continuous drive torque, substantially reducing torsional drivetrain vibrations manifested as longitudinal jerk.

Based on the test results of the prototype, a number of refinements, optimizations, and further works are suggested. Principally, the major system improvements include the implementation of an auto-clutch system (ACS), computerized gear selection, or the combination of both in the form of an automated manual transmission (AMT). These improvements eliminate the need for predictive algorithms required to fill the torque hole, as the target speed and torque are known at all stages during the gear selection process. Further refinements include optimization of the traction battery, new approaches to motor control, and further cost reductions in the transmission componentry through the use of electronic synchronization control.

Contents

List of figures

List of tables

Acronyms and abbreviations

4WD	Four-Wheel-Drive
5MT	5-speed Manual Transmission
A/D	Analog-to-Digital
ABB	ASEA Brown Boveri (company name)
AC	Alternating Current
ACG	Automatic Code Generation
ACIM	Alternating Current Induction Motor
ADC	Analog-to-Digital Converter
ADVISOR	ADvanced VehIcle SimulatOR
AER	All-Electric Range
AMT	Automated Manual Transmission
AT	Automatic Transmission
BEV	Battery Electric Vehicle
BLDC	BrushLess Direct Current
BMEP	Brake Mean Effective Pressure
BMS	Battery Management System
BOL	Beginning Of Life
BSFC	Brake-Specific Fuel Consumption
CAN	Controller Area Network
CARB	California Air Resources Board
CD	Coast Down
CRAC	Computer Room Air Conditioning
CSHVR	City-Suburban Heavy Vehicle Route
CTM	Cost To Manufacture
CV	Conventional Vehicle
D/A	Digital-to-Analog
DAC	Digital-to-Analog Converter
DAQ	Data AcQuistion
DC	Direct Current
DCT	Dual-Clutch Transmission
DHT	Dedicated Hybrid Transmission
DOF	Degrees Of Freedom
ECE/UNECE	United Nations Economic Commission for Europe
ECU	Electronic Control Unit
EM	Electric Motor
EMF	ElectroMotive Force
EOL	End Of Life
EPA/US EPA	United States Environmental Protection Authority
EPS	Electric Propulsion System
ESM	Engine Simulation Motor
EV	Electric Vehicle
FE	Fuel Economy
FF	Front-engine/Front-wheel-drive
FOC	Field Orientation Control
FR	Front-engine/Rear-wheel-drive
HAMT	Hybridized Automated Manual Transmission

HAP	Hazardous Air Pollutants
HC	Hydrocarbons
HEV	Hybrid Electric Vehicle
HIL	Hardware-In-the-Loop
HPEVS	Hi-Performance Electric Vehicles
HSD	Hybrid Synergy Drive
HWFET	HighWay Fuel Economy Test
I/O	Input/Output
I2V	Infrastructure-to-Vehicle
I4	Inline 4-cylinder
ICE	Internal Combustion Engine
IGBT	Integrated Gate Bipolar Transistor
IoT	Internet of Things
ISC	Idle Speed Control
KERMIT IV	Kinetic Energy Recovery and Motor Infill Torque Investigation Vehicle
LiFePO4	Lithium Iron Polymer
Li-ion	Lithium-Ion
LSB	Load Simulation Brake
MAHA	MAHA Maschinenbau Haldenwang Gmbh & Co. KG (company name)
MBD	Model-Based Design
MHEV	Mild Hybrid Electric Vehicle
MR	Mid-engine/Rear-wheel-drive
MT	Manual Transmission
N/C	Normally Closed
N/O	Normally Open
n-D	n-Dimensional
NEDC	New European Driving Cycle
NEMA	National Electrical Manufacturers' Association
NI	National Instruments (company name)
NiMH	Nickel Metal Hydride
NOVC	Non Off-Vehicle Charging
NOx	Nitric Oxide
NVH	Noise, Vibration and Harshness
NYCC/NYCDDS	New York City Cycle/New York City Dynamometer Drive Schedule
OBD/OBDI/OBDII	On-Board Diagnostics (version I/II)
OEM	Original Equipment Manufacturer
OTA	Over-the-Air
OVC	Off-Vehicle Charging
PC	Personal Computer
PCB	Printed Circuit Board
PEMS	Portable Emissions Measurement System
PESTEL	Political, Economic, Social, Technological, Environmental, Legal
PHEV	Plug-in Hybrid Electric Vehicle
PID	Proportional Integral Differential
PIL	Processor-In-the-Loop
PM2.5	Particle Matter <2.5um
PMSM	Permanent Magnet Synchronous Motor

PMSRM	Permanent Magnet Switched Reluctance Motor
PPF	PowerPlant Frame
PSI	Pounds per Square Inch
PTO	Power Take-Off
RCP	Rapid Control Prototyping
REEV/BEVx	Range-Extended Electric Vehicle/Battery Electric Vehicle - Extended Range
RHS	Rectangular Hollow Section
RLD	Road Load Determination
RON	Research Octane Number
RPM	Revolutions Per Second
RR	Rear-engine/Rear-wheel-drive
RTI	Real Time Interface
SAE	Society of Automotive Engineers
SIL	Software-In-the-Loop
SOC	State-Of-Charge
SPDT	Single-Pole Double-Throw
SRM	Switched Reluctance Motor
TCO	Total Cost of Ownership
TCO	Total Cost of Ownership
THS/THS-II/THS-III	Toyota Hybrid System (I/II/III)
TTR	Through-the-Road
UDDS	Urban Dynamometer Drive Cycle
UN	United Nations
UTS	University of Technology Sydney
UUT	Unit Under Test
V&V	Verification and Validation
V2I	Vehicle-to-Infrastructure
VDV	Vibration Dose Value
VFD	Variable Frequency Drive
VI	Virtual Instrument
VOC	Volatile Organic Compounds
WHO	World Health Organization
WLTP	World-harmonized Light-duty Test Procedure
ZEV	Zero Emissions Vehicle

Chapter 1: Introduction

Electrification of automotive powertrains has been one of the most dominant themes of vehicle development over the last three decades. It offers significant advantages, including favourable power characteristics, improved thermal efficiency, reliability, and favourable packaging. Other advantages flow well beyond the end-user, including reduced or eliminated tailpipe emissions, reduced noise emissions, the ability to interface with a smart electricity grid to provide grid-connected storage, and favourable characteristics upon which to develop autonomous automotive capabilities. Though vehicle electrification is as old as the automobile itself, it is only in recent years that technologies such as high-power switching, energy-dense battery chemistries, and high-fidelity motor control techniques have allowed electric powertrains to mature to the stage where they are a credible alternative to the internal combustion engine. They are now relatively commonplace in many developed regions throughout the world, and indeed the benefits of their presence in significant numbers have begun to be realised. Despite this, throughout the majority of the world's population, vehicle fleet electrification rates are still low or negligible, despite increasing rates of transport motorization. Many reasons exist for this disparity, but they can largely be classified as:

- Prohibitive capital purchase cost of electrified or electric vehicles
- Electrified vehicles not being offered for sale by OEMs
- A lack of legislative or regulatory impetus
- Vehicle markets being largely based on older, grey-market import vehicles
- Bowser price of petrol and/or retail price of electricity making the case for electrified vehicles uneconomic
- Misinformation or lack of trained service personnel discouraging consumer purchases
- Unreliable electricity supply making electric vehicles impractical

The exact mix of reasoning for the lack of fleet electrification varies for each region studied, but the majority of these reasons are based largely in economics. Others, such as unreliable electricity infrastructure, apply only to grid-connected vehicles such as plug-in hybrids (PHEVs) and pure electric vehicles (EVs). The majority of electrified vehicles on the road today are hybrid electric vehicles (HEVs), which still rely on combustion of hydrocarbon fuels as their only energy input, and it would seem that development of an economically-attractive HEV specifically for such regions would achieve greater fleet electrification, availing the population in those regions of the benefits of fleet electrification whilst supporting the regional needs in regards to transport motorization.

The paradox of HEV powertrains is that they are intrinsically complex, having the need for the packaging of a complete internal combustion powertrain and another, interconnected electric powertrain, as well as the means for controlling the interaction of the two sides to ensure a smooth delivery of tractive effort. This is resource intensive and expensive to manufacture. Further; since (generally) neither side of the powertrain is designed to provide the total demanded tractive effort, each power source is typically significantly undersized from the componentry that would be installed in a battery electric vehicle (BEV) or internal combustion engine (ICE) vehicle. This has led to HEV powertrains sometimes being described as “the worst of both worlds”. Despite this impression however, HEVs far outperform equivalent ICE vehicles for fuel consumption and emissions performance. They also sidestep the drawbacks of BEVs, being significantly cheaper, offering significantly improved travel range, and being independent of a reliable charging network. They can also be developed to offer better dynamic performance than an equivalent ICE vehicle, through novel control methods, topologies, or the combination of both.

Research conducted in this study complements the work of Dr Mohamed Awadallah, in which simulation, modelling, and control methods for a low-cost parallel hybrid vehicle

featuring gearshift torque-filling are developed. The main features of this study and its primary goals are the development process of the physical prototype vehicle and its control methodology, performance testing, with particular focus on continuous torque gearshift performance, and contextual analysis with regard to the viability of the prototype to meet design and economic targets. To date, most research in the field of HEV powertrain development has focused on novel control methods, design and development of novel powertrain components, powertrain topologies, and interconnection with infrastructure (V2I/I2V). In contrast, this research focuses on the simplification, downsizing, and cost reduction of the physical powertrain componentry, coupled with novel control methods to deliver enhanced functionality. The focus on simplification, downsizing and cost-reduction is chosen in part to highlight the poor fleet electrification rates outside western countries. Research in the field of economic, regulatory, and social impact of fleet electrification has been focused on use cases in regions where electrification is advanced – typically Europe and North America, with some limited investigation in other countries. Throughout the research, development of low-cost technologies for developing markets is largely neglected, as is investigation of the problems associated with low fleet electrification in the same. With fleet electrification being largely a western phenomenon, the understanding, and where possible, removal of technological or market barriers for the majority of the world's population is important in achieving a stable worldwide energy mix for the automotive sector, as well as achieving globally-improved environmental, economic, and health outcomes. Therefore, the research conducted herein, as well as the complementary research of Dr Mohamed Awadallah, has as its secondary goal an aim to explore the large variance in regional fleet electrification rates through investigation of a novel, low-cost hybrid electric powertrain, as well as add to the body of knowledge regarding electrification in developing regions.

This thesis contributes significant knowledge to the automotive engineering community through the proposal and engineering development of a novel powertrain electrification solution providing continuous torque gear changes through the use of low-cost hardware, the complex, multidisciplinary investigation of the proposed solution, and the exploration of the social, environmental, and economic impact of such a solution.

The significant and novel aspects of this research are the development of a P3 low-cost parallel hybrid powertrain using model-based design, the physical construction of the prototype vehicle, the use of the model-based design process to achieve simulated data, bench-test data, and full-scale prototype testing data, comparison of that data, and the novel torque control and sensing methodology used for the continuous torque delivery during gear shifting.

1.1 Research Statement

The model-based development and experimental validation of a post-transmission mild-hybrid electric powertrain, including a novel torque-filling function during gearshift; analysis of its performance characteristics including torque delivery, and dynamic benchmarking against an internal combustion (base vehicle) benchmark for control values such as acceleration, emissions, fuel consumption, and induced vibration.

1.2 Objectives

This thesis presents the theoretical development, construction, and experimental validation of an electrified powertrain utilising a manual transmission and single dry-plate clutch, and including a post-transmission traction motor. The main objectives of the project are:

1. Construction of a prototype vehicle based on the P3 HEV topology for the purpose of experimental validation of simulation results previously published by Dr Mohamed Awadallah;

2. Testing, calibration, and validation of gear changes using the electric traction motor as a torque fill-in device under both acceleration and coasting conditions;
3. Testing, calibration and validation of a rule-based control methodology for the operation of a P3 HEV topology;
4. Contextual analysis of the P3 HEV prototype in regards to its suitability for the aim of improved fleet electrification
5. Experimentally validate the emissions and dynamic modelling previously conducted by Dr Mohamed Awadallah, using dynamometer drive schedules and cycles as well as targeted testing aiming to characterize particular features.

1.3 Scope

The scope of the project includes the following:

1. Engineering design study and complete vehicle design definition
2. Construction of the prototype hybrid electric vehicle including implementation of control algorithms for gear-shift infill torque.
3. Dynamic testing of vehicle jerk during gear shift events as well as dynamic benchmarking comparison with non-hybrid powertrain.
4. Definition of the need for a market-based, low-cost fleet electrification solution based on global data sources
5. Emissions drive cycle testing for validation of emissions model, using engine-out emissions

Scope exclusions are:

1. Modelling based on the vehicle design definition, which was completed by (Awadallah 2018)

2. Investigation of the effect of emissions after-treatment devices such as additives; investigation of emissions reduction control strategies that do not relate to the hybrid powertrain
3. Tailpipe-out emissions study; due to the nature of the powertrain development work, this study refers to engine-out emissions, inclusive of the use of a 3-way catalytic converter.
4. Investigation of environmental effects on the emissions performance of the hybrid powertrain

1.4 Thesis Presentation

The development of a hybrid powertrain is a complex task combining mechanical design and analysis, simulation and modelling, control methods, and physical testing, control calibration, and validation. In describing the work undertaken, this thesis is generally organized according to these broad task definitions. Fundamental methodology required for each task is introduced at the beginning of each section or chapter. In addition, contextual information is provided in the background and literature review. The contextual information provides some insight into the social, economic, and legislative environment out of which the concept for this powertrain was conceived, and canvasses the broad range of automotive powertrain technology and topologies currently available. This provides the reader with a level of insight into the reasoning for the research team's pursuit of this particular technology in the chosen topology. The structure and content of each chapter is described in the following sections.

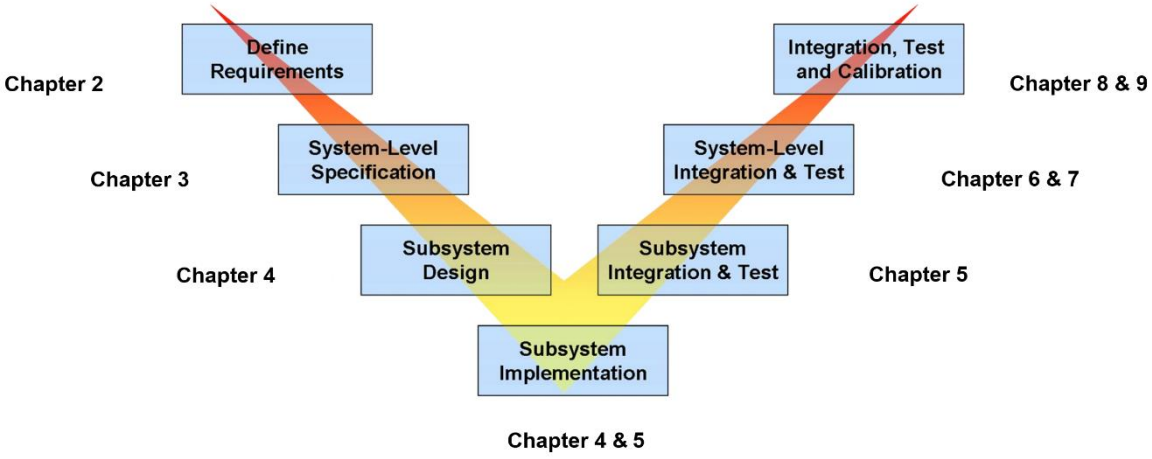

Figure 1.1 The structure of this thesis generally follows the V-cycle for model-based design

Chapter 2

This chapter provides the framework for the research of this thesis. Initially, it introduces the problem by way of background information, including historical context, environmental impacts and regulatory measures. Technical background information including vehicle powertrain architectures, such as ICE powered vehicles, electric vehicles (EVs), HEVs and hybrid development trends are also discussed. This is followed by a detailed technical review examining information on relevant aspects of automotive powertrain development in the literature, focusing on similar architectures and projects the focus of which has been on low-cost developments and construction methods, parallel MHEVs and experimental validation.

Chapter 3

This chapter introduces the context of the project, continuing the detailed analysis presented in Chapter 2 with a description of the market trajectory for light duty vehicles, internal combustion engines, hybrid powertrains, and electric vehicles over the decades to 2050. A PESTEL analysis is also conducted with specific reference to the goal of improving fleet electrification in growing markets and addressing the need for increasing motorization. This

contextual analysis provides the framework for the solution proposal, namely the development of a low-cost mild hybrid electric vehicle. The top-level design constraints are documented and design benchmarks and constraints are formulated, including general topology and basic architecture.

Chapter 4

The initial design analysis is presented, describing the backward-looking vehicle model that was used to determine overall vehicle and component characteristics including power requirements, energy storage needs, system voltages, and so on. After determining these quantities, design studies and market research is presented, the objective of which is to make appropriate selections of off-the-shelf componentry that can be used to assemble the prototype powertrain. Selections are presented for the base vehicle, electric motor, motor controller, traction battery, BMS, and supervisory controller. Other items required for the build, such as the electronic throttle body, pedal, and controller, as well as ancillary items, (relays, contactor, battery charger) are not discussed as they are relatively generic and have little to no influence on vehicle performance.

Chapter 5

A discussion of the forward-looking simulation is presented from first principles. The simulation model is discussed, along with the heuristic rule-based control methodology. Model verification using both virtual simulations and hardware-in-the-loop testing is also presented. The model verification utilises benchmarking tests, some of which will later be replicated at the prototype validation stage. The verification also uses a variety of drive cycles for comparison of fuel economy and emissions between the base vehicle and the MHEV.

Chapter 6

The assembly process for the prototype vehicle is shown. The assembly process is divided into mechanical assembly processes and electrical assembly processes. The considerations for each are described, and where improvements can be made they are described. Electrical wiring diagrams for selected subsystems are also presented to aid discussion.

Chapter 7

The novel torque control methodology used for continuous torque delivery during gear changes is disclosed in this chapter. The control methodology is described referring to the controller hardware and software, the control algorithm, software topology, and a description of the state machine is provided. Additionally, the torque sensors which form the basis of validation testing for this project are described. The torque sensors are designed and built at UTS, and are used for the validation of continuous torque delivery performance and jerk estimation. Their development and validation process is described.

Chapter 8

The test programme and methodology under which the prototype vehicle is to be validated is presented in this chapter. The test programme covers performance in regards to torque hole reduction, dynamic performance testing with regard to vehicle acceleration, jerk performance, and fuel consumption. The test apparatus is described, including the environmental controls, system control parameters, setup procedures such as temperature soaking and road load determination, and data preparation procedures.

Chapter 9

This chapter covers the experimental validation of the prototype vehicle. Experimental data is analysed, presented and discussed. Results cover the acceleration, torque hole reduction, jerk, fuel consumption and emissions of the prototype vehicle.

Chapter 10

The concluding chapter reviews and summarizes this thesis with a general summary of the contributions each of the previous chapters, presenting significant and novel results of this thesis as well as identifying the important areas for further research.

1.5 List of Publications

1.5.1 First Author Publications

Conference Submission

Tawadros, P., Zhang, N., 2012, *Quantitative Experimental Study of HEV Regenerative Braking Systems*, EB2012-TM-06, FISITA Eurobrake Conference, Dresden, Germany

Book Chapter

Tawadros, P., Zhang, N., Boretti, A., 2014, *Integration and Performance of Regenerative Braking and Energy Recovery Technology in Vehicles* in Folkson, R. (ed.), *Alternative Fuels and Advanced Vehicle Technologies for Improved Environmental Performance: Towards Zero Carbon Transportation*, Woodhead Publishing, Cambridge, United Kingdom, pp.541-563

Journal Article

Tawadros, P., Awadallah, M., Walker, P. & Zhang, N. 2019, *Using a Low-Cost Bluetooth Torque Sensor for Vehicle Jerk and Transient Torque Measurement*, Proceedings of the Institution of Mechanical Engineers, Part D: Journal of Automotive Engineering.

1.5.2 Second Author Publications

Conference Submissions

Awadallah, M., Tawadros, P., Zhang, N., 2015, *Rapid Prototyping and Validation of MARS 0913 Brushless Motor to Develop Mild HEV*, Proceedings of the 2015 China Automotive Engineering Society Annual Conference, pp. 92-98, Shanghai, China

Awadallah, M., Tawadros, P., Walker, P., Zhang, N., 2016, *Comparative System Dynamic Modeling of a Conventional and Hybrid Electric Powertrain*, Proceedings of the International Conference on Power Transmissions, pp. 231-238, Chongqing, China

Awadallah, M., Tawadros, P., Walker, P., Zhang, N., 2016, *Eliminating the Torque Hole: Using a Mild Hybrid EV Architecture to Deliver Better Driveability*, Proceedings of the 2016 IEEE Transportation and Electrification Conference and Expo, pp. 173-179, Dearborn, Michigan

Awadallah, M., Tawadros, P., Walker, P., Zhang, N., 2016, *Selection and Characterisation of PMSM Motor for Mild HEV Applications*, Proceedings of the 29th International Electric Vehicle Symposium (EVS), Montreal, Canada

Awadallah, M., Tawadros, P., Walker, P., Zhang, N., 2017, *A Low-cost and Novel Approach in Gearshift Control for a Mild-Hybrid Powertrain*, Proceedings of the 2017 IEEE Transportation Electrification Conference and Expo, pp.754-760, Chicago, Illinois

Awadallah, M., Tawadros, P., Walker, P., Zhang, N., Tawadros, J., 2017, *A Comparative Fuel Analysis of a Novel HEV with Conventional Vehicle*, Proceedings of the 2017 IEEE Vehicular Technology Conference, Sydney, Australia

Awadallah, M., Tawadros, P., Walker, P., Zhang, N., Tawadros, J., 2017, *A System Analysis and Modeling of a HEV based on Ultracapacitor Battery*, Proceedings of the 2017 IEEE Transportation and Electrification Conference and Expo, pp.792-798, Chicago, Illinois

Awadallah, M., Tawadros, P., Walker, P., Zhang, N., 2018, *Hardware-in-the-Loop Simulation for the Design and Testing of Motor in Advanced Powertrain Applications*, Proceedings of the IEEE International Symposium on Industrial Electronics, pp. 817-824, Cairns, Australia

Journal Articles

Awadallah, M., Tawadros, P., Walker, P., Zhang, N., 2017, *Dynamic Modelling and Simulation of a Manual Transmission Based Mild Hybrid Vehicle*, Mechanism and Machine Theory (112), pp. 218-239

Awadallah, M., Tawadros, P., Walker, P., Zhang, N., 2017, *Impact of Low and High Congestion Traffic Patterns on a Mild-HEV Performance*, SAE Technical Paper Series, 2017-01-2458

Awadallah, M., Tawadros, P., Walker, P., Zhang, N., 2018, *Comparative Fuel Economy, Cost and Emissions Analysis of a Novel Mild Hybrid and Conventional Vehicles*, Proceedings of the Institute of Mechanical Engineers, Part D: J Automobile Engineering, 232(13) pp. 1846-1862

Chapter 2: Literature review

A wide range of studies of hybrid vehicle development have been published in the literature. Studies range from single-subsystem development (Sung Bang et al. 2018; Williamson et al. 2005) through to the development of an entire vehicle or powertrain (Park et al. 2017; Wu & Zhang 2015; Zulkifli et al. 2017). Studies that focus on the development of low-cost hybrid platforms are less common – the focus is generally geared toward better emissions (Karaoğlan, Kuralay & Colpan 2019) or fuel economy (Bao, Avila & Baxter 2017). A review of some of the more comparable studies to that presented herein will be undertaken.

Similarly, there is much information on vehicle fleet profiles, standards, and compliance in the western world (André et al. 2006; Chen & Borken-Kleefeld 2014; Sharma et al. 2012; Silva, Farias & Ross 2010). Indeed the vast bulk of the modern research is based on compliance with current European (UNECE) or north American (US EPA) standards. Less common is the information on emissions, particularly tailpipe emissions, in developing countries, although some studies have been completed (Kamble, Mathew & Sharma 2009; Manish & Banerjee 2006; Mansour, Haddad & Zgheib 2018; Mutenyo et al. 2015). Much of this information is available from sources other than the academic literature, such as various sub-organizations of the United Nations (Akumu 2017), World Health Organization (World Health Organization 2018), and the World Bank. A review of the available information and literature will be presented.

The measurement of torque during gear shifting as well as jerk measurement and human perception is another important field that will be investigated. The measurement of torque during gear changes is a relatively common activity in the literature, although the studies tend towards AMT, DCT, or other automated technologies rather than studies on a fully manual

transmission. Because AMTs are essentially MTs with robotized inputs, these studies are helpful for this research and can provide further understanding.

2.1 The Emissions Problem

Beginning in the 18th Century, the industrial age brought huge technological advancement, driven at a fundamental level by the development of transformational technologies such as combustion engines and power transmission systems. The first combustion engines used external combustion principles to generate steam as a working fluid, which was used to mechanise factories and drive transportation. Internal combustion engines followed in the mid- to late-18th century, and were developed further in the 19th century. The development of internal combustion greatly increased the power density of engines, allowing them to become small enough to drive personal implements, including automobiles, motorcycles, and even tools and toys. However, the very first commercially successful automobiles were not powered by internal combustion, but rather, were electric vehicles. This makes vehicle electrification a concept as old as the car itself. Electric motor cars were favoured because they were quiet, smooth, and did not need to be crank-started or refilled with volatile liquid fuels. Despite a smaller range and reliance on electricity supply, several models, such as the Baker Electric, reached sales in the tens of thousands well before the challenges of internal combustion engines were solved (Narins 2017). With the advent of the electric starter for internal combustion engines, as well as development of infrastructure for the transportation and delivery of fuel, the convenience of internal combustion-powered motoring soon halted any further development of electric vehicles.

Internal combustion proliferated worldwide throughout the 20th century, democratizing and personalising transport through the invention of the automobile. However, this together with the concurrent development of large-scale electrical power generation using coal-fired power plants caused exponential increases in air pollution. The power plants of the time were often

required to be located close to urban centres due to high transmission losses. This, combined with the concentrated proliferation of automobiles in the same locations, resulted in combustion byproducts entering the urban environment almost unchecked. Regulation and scientific understanding of these byproducts was still in its infancy, and therefore early attempts to regulate the problem were ineffectual. In the 1930's through the 1950's, a series of deadly air pollution events caused thousands of deaths worldwide. These events include the 1930 Meuse Valley fog, 1939 St. Louis smog, 1948 Donora smog, and the Great Smog of London in 1952. Undoubtedly, high overall levels of air pollution contributed to rates of mortality and illness outside these major recorded events. Growing public concern led to concerted efforts to understand the problem scientifically and regulate it legislatively by the late 1940's and 50's (Dockery, Schwartz & Spengler 1992).

Various efforts have been made, both scientific and legislative, to reduce the problem, and the road transport sector in particular, has made significant progress, although not without setbacks. The first legislative measures to control road transport emissions arrived in the late 1960s, following a little over a decade of research into the sources of air pollution and effective control methods (Smith & Davies 1996). These first measures limited tailpipe emissions for hydrocarbons and carbon monoxide from 1966 onwards, and were the result of significant public health concerns in California, leading to the creation of the world's first state-level air pollution regulator – the California Air Resources Board (CARB 2018). Later, the US Federal Clean Air Act Extension of 1970 gave the regulator the power to adopt, implement, and enforce controls, many of which were adopted on a federal, and eventually, international level. The United States EPA was established in the same year, marking the first time environmental protection was consolidated under a single federal body. By the mid-1970s, most industrialised nations had regulated emissions standards for road-going vehicles. These standards were typically based on US Federal standards (which in turn were based on

CARB standards), or standards set by the United Nations Economic Commission for Europe (specifically, ECE 15). Throughout this period, development work on electric vehicles was almost non-existent. A small number of electric vehicles were built for production, such as the Henney Kilowatt and GM Electrovair. However, production runs were limited to units numbering in the hundreds at best. The reasons for the lack of development are many-fold, but can broadly attributed to the global success of internal combustion vehicles and the spread of supporting infrastructure, coupled with gradual introduction of emissions regulations resulting in a high level of compliance.

Today, airborne pollution is cited by the World Health Organization as the biggest environmental risk to health, accounting for three million deaths annually (World Health Organization 2018). Airborne pollution is categorized into three different groups (Australian Government Department of the Environment and Energy 2015). These are:

- Criteria pollutants, which are regulated internationally and used as indicators of air quality,
- Air toxics (or Hazardous Air Pollutants, "HAPs"), which are pollutants known to be hazardous to life, and
- Biological pollutants, which are products of microbiological contamination, such as mould, insect droppings, or human skin cells.

Of these, the transportation sector contributes to both criteria pollutants and air toxics. Transportation accounts for over 50% of all NO_x emissions and is a significant contributor to other pollutants (Carslaw et al. 2011). Road transport is of particularly significant concern as it is not only a significant contributor in terms of magnitude of pollutants, but also because of its proximity to urban centres and high population concentrations (European Environment Agency 2017). Road transportation produces air pollutants through a number of pathways. These pollutants mostly arise from the exhaust byproducts of fuel combustion, although non-

exhaust sources of pollution also exist. These include particulate matter from tyre and brake wear (steel, rubber, and ceramic particles created by the rubbing of friction surfaces), road abrasion, and volatile organic compound (VOC) emissions from materials and textiles used in the construction of the automobile (e.g., painted panels, vinyl and plastic interior trim).

Unfortunately, despite increasingly stringent emissions targets, the magnitude of the issue continues to grow. Whilst many, particularly western, countries observed reductions in air pollutants, global $PM_{2.5}$ levels rose by 11% on average between 1990 and 2015 (IHME 2018). This trend is especially marked in East and Southeast Asia, North Africa and the Middle East, and many eastern European countries, where more developed regions of the world have observed falling levels of pollution overall.

There are many reasons for this trend. Certainly, increasing industrialisation in these regions plays no small part. This, along with decreasing capital cost of automobiles is encouraging populations to aspire to vehicle ownership, increasing national fleet size, and therefore emissions quanta. Demand for affordable personal transportation creates a grey (or black) market for used vehicles, often imported from more developed countries where such vehicles may have previously been deemed unroadworthy (Baskin 2018; Coffin et al. 2016). These vehicles necessarily exhibit poorer emissions performance compared to newer models. Unenforceable or non-existent in-service vehicle emissions standards allow the issue to proliferate . Finally, new vehicle emissions standards are often years or decades behind the most recent worldwide standards, and apply only to vehicles sold new through official distribution channels, which in some cases represent a small percentage of new vehicle registrations.

The solution to these issues is not straightforward. Legislative solutions are in place throughout many countries, but have limited effect if there are no practical instruments of enforcement. Economic penalties such as tariffs or taxes are likely to be politically unpopular

or structurally unworkable in countries of limited resources, and limiting importation to just newer vehicles can artificially drive up the value of the existing fleet, keeping older vehicles in service longer and reducing economic activity by putting motorization out of reach. Regulatory solutions such as mandating the adoption of more up-to-date emissions standards have cost implications, which may drive unintended consequences. An effective solution needs to be technologically robust and market-driven.

In the west, tightening emissions standards drove increasingly technologically-advanced automotive solutions. The first technological solution was the positive crankcase ventilation valve, introduced in California in the 1961 model year (CARB 2018). In the following two decades, carburetted vehicles were progressively equipped with (at the time, newly-developed) emissions control equipment such as secondary air injection, exhaust gas recirculation, evaporative emissions control systems, and two-way catalytic converters. This first generation of emissions-controlled vehicles became known as the “emissions-era”. The second generation of technologies introduced three-way catalytic converters, electronic engine management, engine downsizing and forced induction. The third generation saw the introduction of lean-burn engines, flex-fuel vehicles, hybrid electric vehicles (HEVs), and lightweighting through advanced materials. The current generation includes plug-in hybrid vehicles (PHEVs), hydrogen fuel-cell vehicles (FCVs) and battery electric vehicles (BEVs). In the rush to meet tightening legislation, whilst there has generally been compliance, sometimes the legislation has outpaced the rate of technological progress, which has led to repeal (Matthews & Roback 1998) and graft (Skeete 2017).

2.2 Modern Vehicle Electrification

Modern vehicle electrification developments began following the 1990 Zero-Emission Vehicle (ZEV) mandate implemented by the California Air Resources Board (CARB) (Collantes 2008). This spurred vehicle manufacturers to investigate alternative energy

sources for vehicles, with electrification featuring strongly. Notably, the GM EV1, which can be considered a harbinger of modern electric vehicles, was produced for the 1996 production year, featuring a fully electric powertrain. The first mass-produced electrified vehicle followed a year later, in the first-generation Toyota Prius. The Prius was the world's first mass-produced hybrid vehicle, featuring a 43-kilowatt, 1.5 litre four-cylinder engine, coupled with a 30 kilowatt electric motor through a novel power-split device in place of a regular transmission. The power split device is, in essence, a planetary gearset in which the traction motor and engine are connected to the ring and planetary gears, respectively, and a reaction motor is connected to the sun gear. By varying the speed and direction of the reaction motor, it is possible to control the power split between the two power sources.

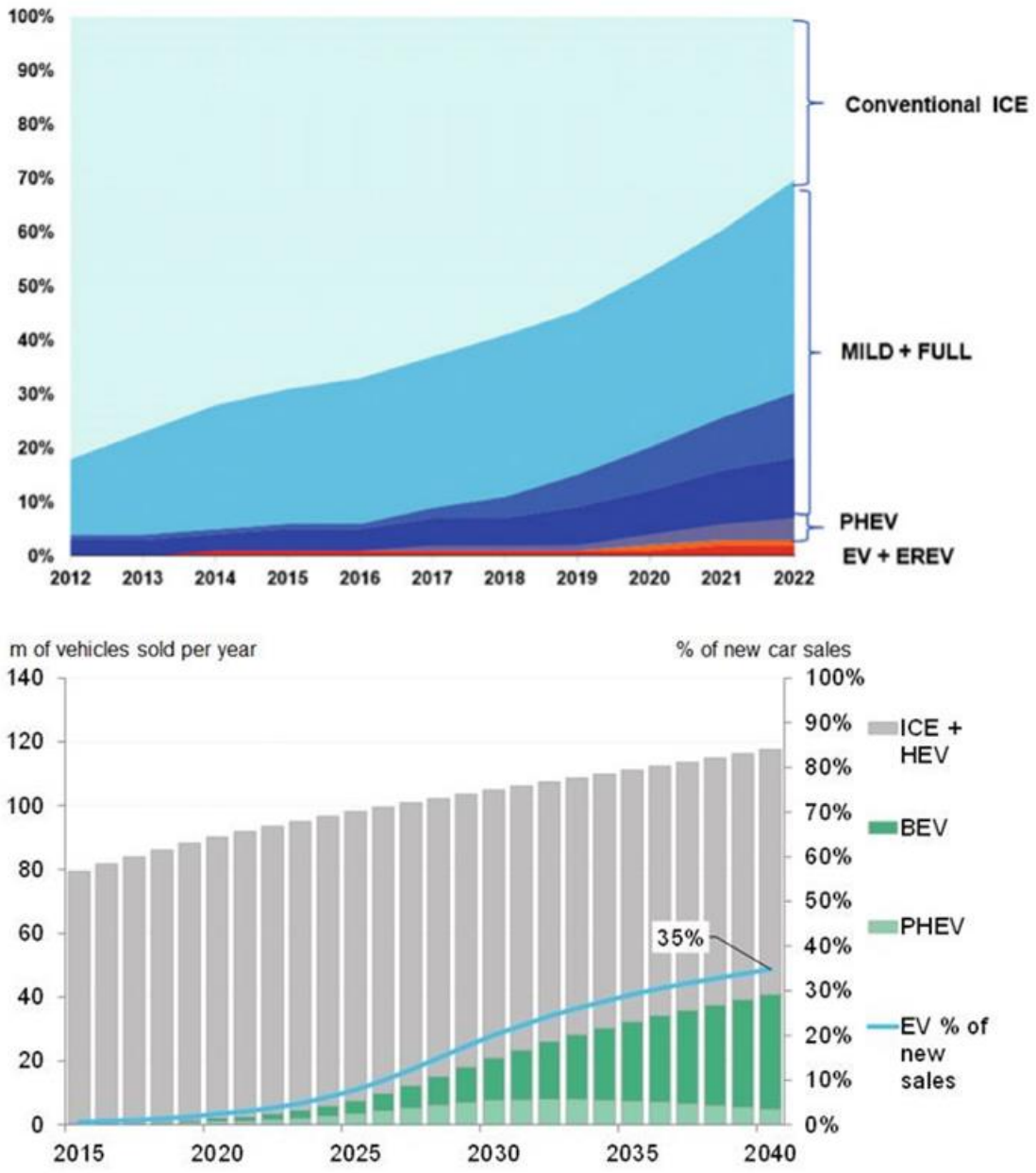

Figure 2.1 Sales forecasts from Valeo (Nikowitz 2016) (top) and Bloomberg (McDonald 2016) (bottom). Dominance of ICE vehicles (including HEV) is likely to continue for another 20-30 years.

Whilst pure electric vehicles remained largely a niche product in the following years, hybridization reached significant market penetration and became a common path towards electrification (McKerracher et al. 2019). Some two decades later, there are now dozens of hybrid vehicle models, ranging from A-segment mini-cars such as Honda Jazz through to S-segment limited production sports vehicles including Porsche 918 and BMW i8. The primary

reason for this success is the flexibility and scalability of hybrid powertrains, and their ability to meet a wide range of design targets from economy, to power, to emissions.

The beauty of hybridization is that the permutations and combinations of electric motor (EM) and ICE topology, combined with targeted control strategy allow various systems to be developed to achieve a diverse range of design goals, whether they be aimed at improving dynamic performance, economy, or emissions. This is achieved by balancing the compromise between maximising each power source's advantages and using each to compensate for the other's disadvantages. HEVs (regardless of their specific configuration) are more efficient in optimising engine operation with the added benefit of regenerative braking. This efficiency comes at the expense of needing a secondary power source like a battery, which may be heavy and inefficient. The implications of their usage include spatial complications in fitting the system within the body of the vehicle, a decrease in loading capacity and the loss of energy from the loaded tyres. Another variable available to the designer is the degree of hybridization, which gauges the proportion of power sourced from the secondary power source against the power sourced from the ICE. Hybrid vehicles (disregarding for the moment plug-in hybrids and extended range electric vehicles) are denoted as micro-, mild-, and full-hybrids depending broadly upon the degree of hybridization.

The same topology with the same control strategy can deliver different benefits simply by varying the component sizes. The exercise therefore becomes a multivariate optimization problem. In our case, the problem is being optimized for fulfilment of the dual goals of having a remarkably low manufacturing cost, but also providng enhanced drivability through continuous torque delivery, and reasonable emissions performance.

2.3 Technological State-of-the-art

There are a number of authors who have spent significant effort performing and publishing reviews of the state-of-the-art. These valuable literatures are useful for quickly understanding

the landscape in hybrid vehicle technology and determining the position of the current research in that literature. Three publications will be discussed in this section. They are (Hutchinson, Burgess & Herrmann 2014), who surveyed the state-of-the-art in current hybrid-electric powertrain architectures; (Tammi, Minav & Kortelainen 2018), who presented a discussion of the last thirty years' developments in hybrid vehicle powertrain simulation, and (Xu et al. 2018), who published on the totality of current and future directions for automotive transmission technology, including not only hybrid and electric vehicle transmissions, but also those used in standard internal combustion engines.

(Hutchinson, Burgess & Herrmann 2014) collected design and sales data on 44 hybrid vehicles available for sale in the United States. The purpose of the data analysis was a lifecycle assessment of greenhouse gas emissions and cost analysis. The data is valuable for a number of reasons. Firstly, it provides a summary of the design topologies or architectures of almost the entire hybrid vehicle market at the time of publication. This allows the designer to quickly understand all the permutations and combinations of hybrid vehicle technology and determine design trends in the market, as well as how the topology being considered in this project fits within the broader market. Secondly, the lifecycle cost analysis provides valuable information based on currently-available vehicles in terms of their actual total cost of ownership (TCO). The cost analysis is also presented in the frame of reference of different topologies. Six distinct topologies are presented. These are: the mild hybrid; Toyota hybrid synergy drive; GM two-mode; P2 Hybrid (described as inline full-hybrid); plug-in hybrid synergy drive; and plug-in series hybrids. The authors make significant findings, including that the mild hybrid powertrain offers the most economical TCO, and due to the cost of batteries, plug-in series hybrids are wholly uneconomical. This information is highly relevant as it confirms the analysis presented in 3.5. The authors also make further conclusions based on their cost analysis, including that:

- hybrid vehicles have the capacity to dominate the automotive industry,
- hybrids with smaller batteries offer more consistent, and lower greenhouse gas emissions,
- hybrids with plug-in capability can vary between 25% and almost 100% of the emissions of a conventional vehicle depending on the source of grid power,
- the biggest obstacle to the success of hybrid vehicles is the upfront cost premium, and
- battery longevity does not match vehicle lifetime, therefore vehicles with larger batteries suffer from substantially higher cost of ownership due to the forecast need to replace the traction battery at least once

These results match well with the background research presented in chapter 3.

(Tammi, Minav & Kortelainen 2018) present a modern history of hybrid and electric vehicle development, and a parallel history of the development platforms used to simulate vehicle powertrains. Future trends are identified, such as the development of Internet of Things (IoT) capability into vehicles so that real data and simulation models are connected, increasing use of over-the-air (OTA) updates for vehicles based on data collected and analysed from in-service vehicles, and improvements in the efficiency of modelling through design automation and artificial intelligence (AI). The value of this publication for the present project lies in the variety of simulation tools that are discussed and presented. An in-depth discussion of tools based on MATLAB, Simulink, Simscape, and Modelica is presented. This allows familiarity with some of the operating principles of standard packages such as ADVISOR, PSAT, Autonomie, Dymola, SimulationX and others. Further, the verification tools currently used are also discussed, including software-in-the-loop, model-in-the-loop, and hardware-in-the-loop development. Finally, fundamental tools are also presented, including power balance models, kinematic models, and average torque engine models. The wide scope of the paper

provides some guidance on the appropriate combination of tools that can be implemented for the current project.

Finally, (Xu et al. 2018) reviews progress in automotive transmission technology for internal combustion engine vehicles, hybrid vehicles, and electric vehicles. There is discussion of efficiency, NVH, shift strategies, hybrid mode control, energy management, and transmissions for EVs. An initial treatment of synthesis methods is provided as grounding. The line chart, component analysis, lever, graph theory, and coding methods are all presented. Of particular interest is the discussion of dedicated hybrid transmissions and transmissions with electrification built in. A comparison of the various hybrid topologies that have been demonstrated to date using existing standard transmission technologies (AT, AMT, DCT) and dedicated hybrid transmissions (DHTs) is presented. The comparison outlines the benefits of each transmission type in terms of cost and complexity, as well as realised driving outcomes such as shift time, jerk, acceleration, energy dissipation and overall efficiency. A detailed overview of control strategies is also conducted. This overview is valuable because it refers to overall energy management strategies for hybrid vehicles, rather than just those concerning transmissions. The hybrid system control literature is reviewed and presented in short-form in a tree-diagram reproduced in Figure 2.2.

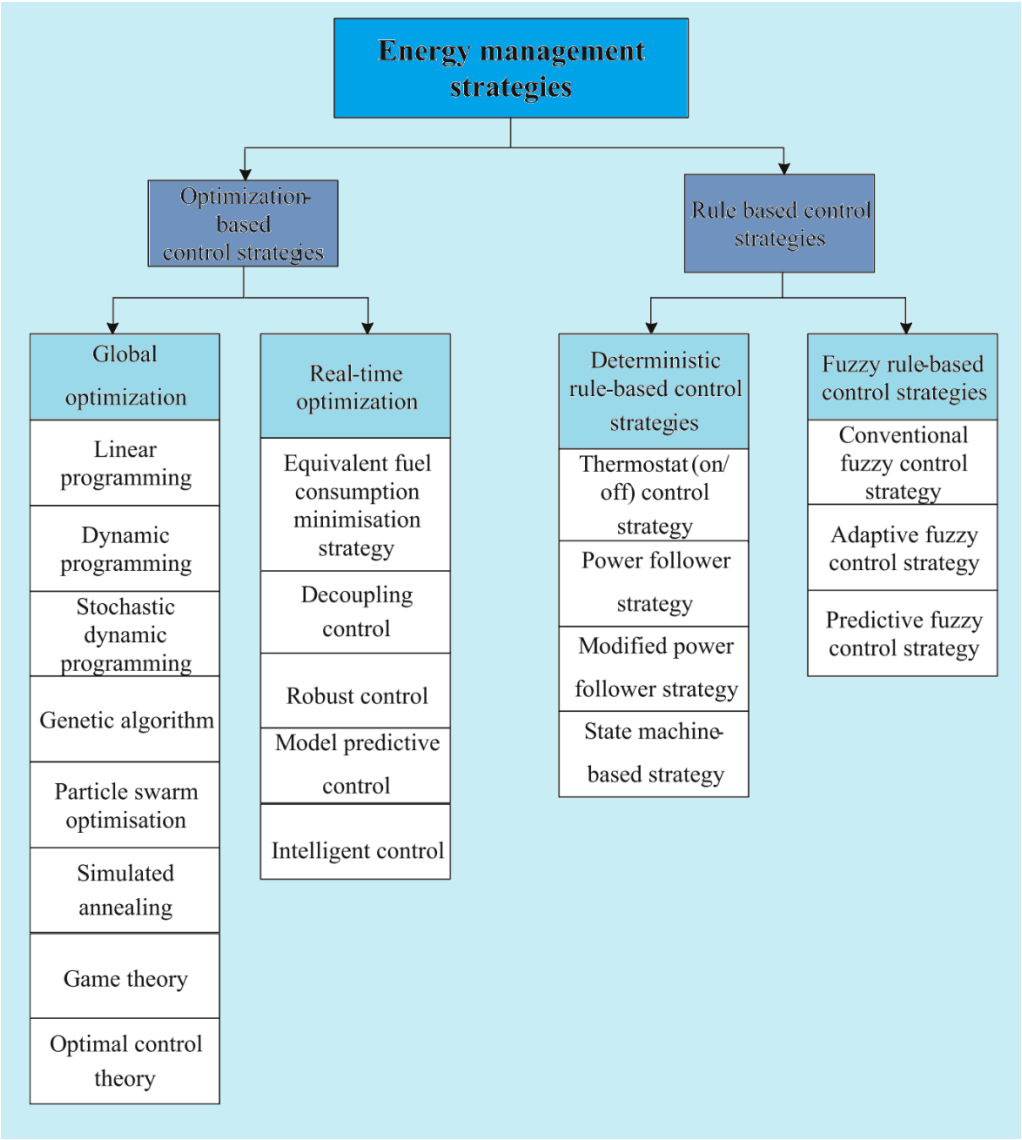

Figure 2.2 Tree-diagram of all energy management strategies described in the literature to date (Xu et al. 2018)

Interestingly, the authors do not discuss manual transmissions (as opposed to AMT or DCT) in a hybrid application at all. This is strange as the MT-hybrid is not without precedent. The Honda Insight and CR-Z both feature P2-hybrid topology paired with a 5MT. Although the CR-Z was discontinued in 2016 with no immediate replacement, in 2017, Schaeffler group developed a system known variously as e-clutch or “P2 module”, which combines an electronic clutch with a 12kW electric motor to provide a simple path to hybridization (Lakshminarayanan et al. 2017). The impetus behind the development of the module was

particularly to cater for markets in which the manual transmission plays a dominant role. India is mentioned in particular in the paper but other developing markets share much in common with the Indian market.

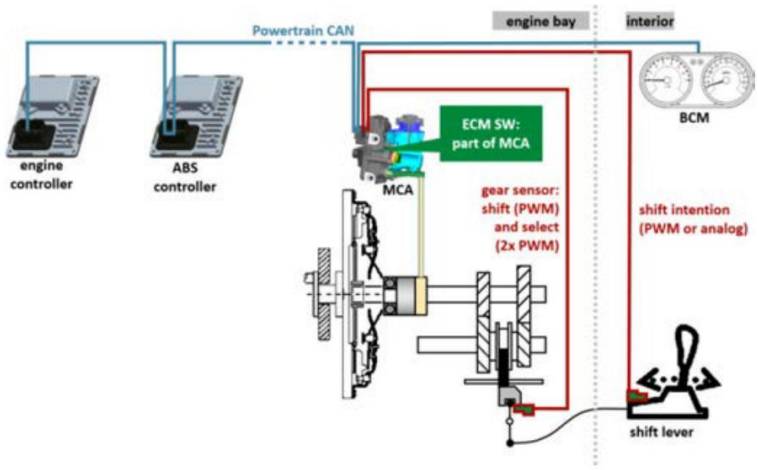

Figure 2.3 Electronic clutch module "e-clutch" architecture developed by Schaeffler Group (Lakshminarayanan et al. 2017)

The benefits of the P2 module are claimed to be numerous, including a reduction in fuel consumption between 3.2% amd 7.9% for a prototype vehicle, improved NVH through better clutch control at the low-speed resonance zones under idle-speed, engine stall prevention, traffic congestion assistance, engine start-stop, and compatibility with gear actuation. The P2 module developed by Schaeffler has much in common with the P3 topology proposed in this thesis, but lacks the continuous torque delivery mode during gear changes. This is purely as a result of the trade-off between cost of manufacturing a P2 module such as that described and the extra expense incurred in providing a P3 module which would, in a manufacturing setting, require integration of an electric module into the manual transmission or differential assembly. In contrast, the P2 module simply replaces the clutch/pressure plate/flywheel assembly within the existing transmission bell housing.

2.4 Hybrid Powertrain Development

The literature in the field of hybrid powertrain is extensive. It can broadly be defined into three subgroups. The first of these is literature that proposes a novel powertrain concept and describes a level of initial design and analysis. The second subgroup, by far the largest, is concerned with the verification of a system or subsystem within a hybrid powertrain. These publications generally use some combination of simulation, modelling, and testing (usually HIL) to verify system operation. The final subgroup is concerned with validation. This subgroup describes the physical testing of a complete powertrain to ascertain its real functionality. This testing may be to validate the real operating parameters of a homologated and commercially available vehicle model, or provide validation of a prototype such as is described in the following sections of this thesis.

(Baraszu & Cikanek 2002) presented one of the earliest torque fill-in hybrid powertrains in the literature. The powertrain is a post-transmission P3/P4 type, employing a 4x4 differential to drive a single axle, using the propshaft output of the differential as an input which is connected via a clutch to the electric motor.

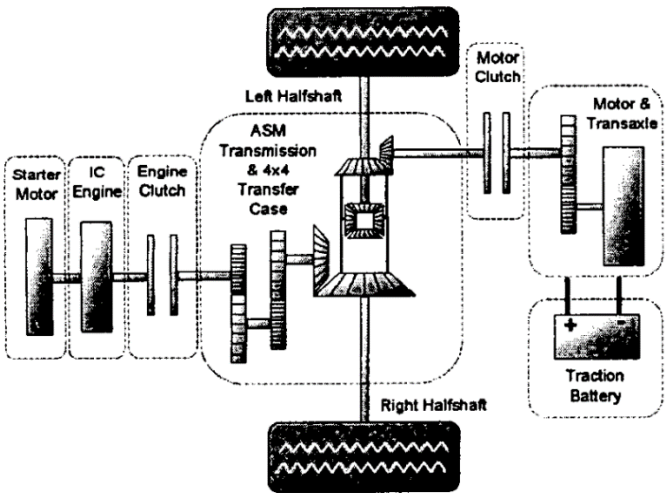

Figure 2.4 Torque fill-in drivetrain proposed by (Baraszu & Cikanek 2002)

The powertrain is robust and offers several advantages. The motor is clutched to reduce losses, and is on a separate shaft from the engine which allows the independent gearing of the motor to achieve optimal efficiency. Because it is clutched there is a high level of controllability from the perspective of driveline vibration, which is the focus of this work. An automated manual transmission (AMT) is implemented. A high-power (55kW, 190N.m) electric motor is used, but the type of motor is not specified, nor is any information about the traction battery. The high output power of the motor allows the vehicle to operate in EV mode only, IC mode only, or hybrid mode. The hybrid mode operation provides the motor torque application during shifting (torque fill-in), motor assist during power boost, and regenerative braking modes.

Interestingly, the gear shift is also used to fire the IC engine when transitioning from IC mode to any other. This prevents undesirable vibrations being transmitted down the driveline.

The paper also introduces the concept of vibration dose value (VDV) as an objective measure of shift quality. Whilst VDV is commonly calculated based on accelerometer readings at the human-machine interface (generally, the seat squab for drivers), raw halfshaft torque measurements are used in this case. This validates the process undertaken in this thesis.

The principal drawback of this powertrain design is its cost. A 55kW electric motor would require a substantial, high voltage traction battery to provide appropriate power discharge. The addition of a 4x4 differential and clutch is an elegant solution to minimize driveline losses but a similar outcome can be achieved using a power take-off and a two-wheel drive differential.

(Gavgani et al. 2015, 2016; Vacca et al. 2017) presents a high-performance parallel hybrid driveline using a hybridized automated manual transmission (HAMT) in a rear-drive transaxle configuration. The driveline is unique, in that it integrates the electric motor with

the transaxle through a dedicated two-speed planetary gearset. The gearset is meshed to the 3rd gear in the six-speed transmission and closed loop speed control for the motor allows any other gear to be simultaneously engaged for hybrid propulsion. Both the 3rd gear and the two-speed planetary gears are controlled engaged by dog clutches and do not require synchronizers.

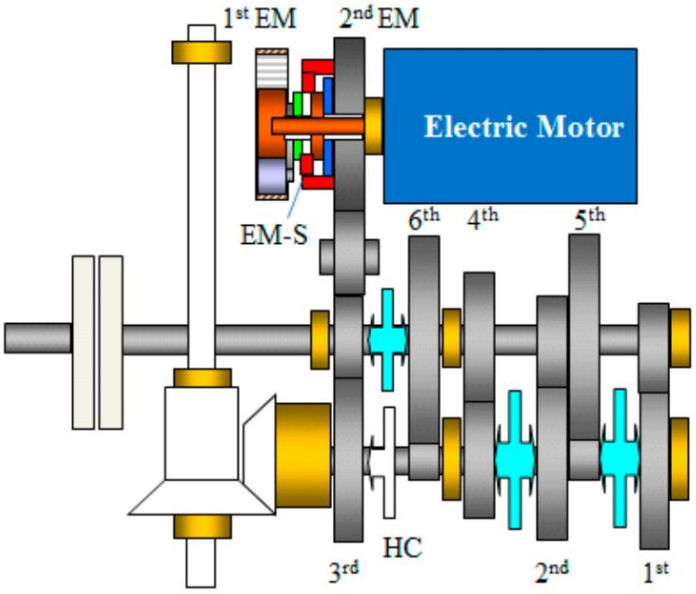

Figure 2.5 The Oerlikon 6-speed Hybrid AMT (Gavgani et al. 2015, 2016; Vacca et al. 2017)

The results presented are unique and exciting. In the first instance, the closed loop control of the electric motor is shown to negate the requirement for synchronizer cones, which are effectively replaced with dog clutches in the electric power path. It could be surmised that with effective engine speed control the remaining synchronizers could also be removed.

The transmission is also compared to an identical ICE-driven vehicle equipped with a seven-speed DCT. Due to the significant power dissipation in the wet-clutch packs of the DCT during power-on shifts, the HAMT delivered fuel economy savings of better than 9% in comparison. This result was obtained under the NEDC driving cycle which is relatively low powered. It would be expected that these fuel economy savings are proportional to the drive

power (and, more specifically, the energy dissipation associated with clutch actuation) so whilst this result is dramatic, in a low-powered vehicle designed for economy rather than outright dynamic performance the savings would be proportionally smaller. Nevertheless, the results demonstrate the potential of hybridization using a manual transmission.

In (Tribioli 2017), a post-transmission series-parallel hybrid topology is proposed using two electric machines and two clutches. The purpose of the topology is not so much to demonstrate the physical possibility, but rather to provide the largest number of possible energy paths to an optimization algorithm (the Dijkstra algorithm), which then determines the vehicle configuration that provides the lowest fuel consumption.

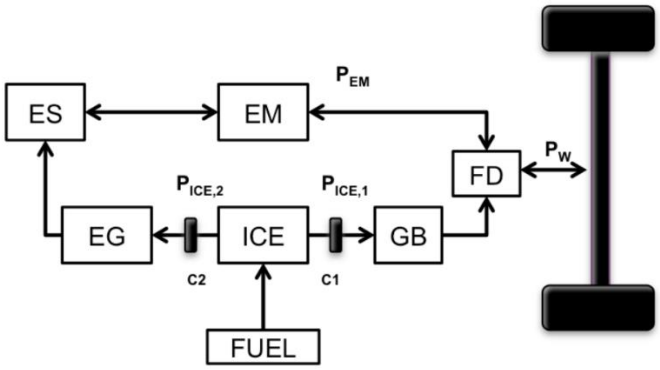

Figure 2.6 A theoretical series-parallel topology used for optimization study (Tribioli 2017)

The optimization results are constrained by the energy paths and the component parameters in the topology, so that for instance, multiple studies must be run to determine the optimum engine size, gear ratios, or shift schedule. The findings are broadly somewhat intuitive, although the size optimization and the process to achieve those results can not be achieved without a form of computational optimization. The limitations of the optimization process are also the strengths of heuristic and backward-looking modelling, in that the heuristic approach allows the exploration of concepts outside the limitations of the modelled environment. No

matter the development approach, there is necessarily an element of heuristics required to begin.

(Karaoğlan, Kuralay & Colpan 2019) proposes a parallel hybrid topology based on a pre-transmission torque coupling device. The powertrain is used as a gear ratio study to determine the effects of gear ratio selection on hybridized vehicles. A backward-looking vehicle model is implemented in Simulink to determine power demands and load states based on a drive cycle input. The gear ratios of both the torque coupling device and the transmission are varied according to a set of five options to determine the best option in terms of fuel economy and emissions. Both the operation modes and the gear ratios are selected heuristically. The operation mode is not altered, but the backward-looking simulation is used to determine the optimal gear ratio combination.

(Skoog 2017) presents a study of the outer limits of hybrid topologies in terms of their potential for fuel consumption reductions. The study is interesting in that it is designed to examine the best possible fuel consumption improvements in a pre-transmission hybrid topology assuming there are no constraints on the amount of energy that can be stored (i.e., a perfect battery) and the amount of power that can be handled by the system instantaneously, within the limits of the ability of the electric machine to convert that power into motion or vice versa. This scenario is analogous to a hybrid vehicle test cell where the electrical power is supplied from and sent back to a grid-connection, rather than a battery. Various reasonable assumptions are made regarding system efficiencies and sizing of tractive devices. The results are naturally wildly optimistic with regard to real systems and the author acknowledges this. However there are other conclusions drawn which are questionable. Because the author observes up to 41% fuel consumption reduction using one configuration the inference is drawn that even mild-hybrid topologies benefit in terms of fuel consumption by being designed with the average power being supplied by the electric device and the peak

power being supplied by the ICE, rather than the other way around. Whilst this may be true it is simply not practical, and the size of a P0 or P2 device with high power capability is unlikely to be simple to package.

(Opila et al. 2012) describes the testing of a prototype controller for the gear selection and engine control (load state and start-stop) of a through-the-road (TTR) hybrid vehicle. The development process is described and follows the V-cycle methodology, wherein the simulation model is verified first, then model-in-loop testing is conducted, followed by hardware-in-loop testing and finally vehicle testing. This particular publication focuses on the last part – the vehicle testing. The test setup is based on the dSpace MicroAutoBox 1401, which is the same rapid control prototyping platform used for the project presented in this thesis. The control algorithm is computationally intensive, with solved optimizations taking approximately one second, and therefore for realtime implementation several simplifications are made by making calculations offline and uploading the results to the controller as relatively coarse lookup tables to reduce computational requirements without sacrificing significant numerical precision. Another step taken to reduce computational demand is the implementation of multirate updates which split computational outputs into fast, medium and slow updates. The electric machine is updated at 60Hz to ensure fast pedal response, whereas engine torque is updated at 2.5Hz. Finally, gear transitions and the engine start-stop are both updated at around 1Hz.

There are a number of other studies in the literature for which the dSpace MicroAutoBox has been used. (Golchoubian & Azad 2017) implement the rapid control prototyping platform for the development of a non-linear predictive control method for the energy storage system in a Toyota Rav4EV; (Guo et al. 2018), for an energy management strategy using state-of-charge trajectory planning, and (Vacca et al. 2017) for the control of the HAMT described previously.

There is also a significant body of work around the Toyota Hybrid Synergy Drive (HSD), otherwise known as the Toyota Hybrid System (THS). This type of powertrain is known as a power-split powertrain, because it is not quite a series nor a parallel topology, instead relying on a planetary gear transmission and multiple electric machines to control the ratio of engine and motor torque being used to drive the wheels.

(Burress et al. 2011; Olszewski et al. 2005), as part of the work of the Oak Ridge National Laboratory, developed detailed reports into the THS-II and THS-III system. These reports were made possible by disassembling and testing every component of the electric powertrain, in order to understand the operation and report on construction methods, power handling capability, and other component characteristics. The reports are highly detailed and are an artefact of the immense success of Toyota's hybrid technology, which represents the world's most popular electrified vehicle technology by sales volume. They were commissioned with the aim of bringing the public domain understanding of the intellectual property in line with the state-of-the-art, improving understanding of propulsion technology and benchmarking non-US-domestic alternative vehicle technologies. (Borhan et al. 2012; Guo et al. 2018; Liu & Peng 2008; Vinot, Reinbold & Trigui 2016) all use the basis of the THS, the power-split device as a means to propose and investigate novel technologies. (Guo et al. 2018) supplements the basic THS system with a grid-connection (converting to PHEV) and adding ultracapacitors. (Vinot, Reinbold & Trigui 2016) proposes an equivalent system to the THS using only two electric motors and no power-split device. The electrical variable transmission (EVT) is claimed to be functionally equivalent. It works using a double-rotor electric machine (analogous to two concentric motors). The internal rotor is connected to the engine, the central rotor/armature to the wheels, and the external armature to the battery only. (Borhan et al. 2012) and (Liu & Peng 2008) both use the power-split architecture to propose different control methodologies. (Liu & Peng 2008) proposes an equivalent consumption

minimization strategy (ECMS) using stochastic dynamic programming, somewhat similar to (Opila et al. 2012), whereas (Borhan et al. 2012) pursues a predictive model.

2.5 Torque and Jerk

Many studies in the literature describe novel transmissions, electrification strategies, or control schemes aimed at providing continuous torque delivery during gear changes. This field of inquiry began to gain momentum in the 1960s when automatic transmissions became commonplace (Anderson & Bierley 1965), requiring an increasing focus on their transient torque and jerk performance in shifting, whereas previously the prevalence of manual transmissions placed the responsibility for shifting quality on driver action. Automated manual transmissions (AMTs) became somewhat more commonplace in the 1990s. including the Alfa Romeo Selespeed, BMW SMG, and Mercedes Funshift. With the increasing focus on emissions standards coupled with the increasing capability of electronic control, AMTs were seen as a way to improve efficiency, capitalising on the efficiency and cost advantage of the MT hardware whilst also providing the driving simplicity of an AT. The operating principle was largely the same regardless of the trade name – the fundamental transmission was a standard manual with single dry-plate clutch. The clutch actuation was automated, and in most cases also the gear selection. The automation of a manual transmission presented new challenges in terms of jerk. The experienced driver is able to modulate the clutch input according to sensory feedback from the vehicle to obtain desired gear shifting characteristics. Automating a manual transmission presents challenges in terms of driver satisfaction. Clutch feed-in can be controlled for smooth shifting at the expense of shift time and acceleration performance, or can be controlled for minimum time at the expense of occupant comfort. Maximising both attributes is the desired goal, but the nature of the single dry-plate clutch, which necessitates a torque hole, means this is difficult to achieve.

Studies on the shift quality of AMT necessarily focus on clutch control. (Horn et al. 2002) derives a system function that linearizes the feedback control with respect to the clutch position output. Prior control methods typically modelled a simplified non-linear system. The system is tested on a Mercedes-Benz Sprinter and CLK, and benchmarked against the prior control methodology. The benchmarking is positive although the authors note that results are limited by computing resources onboard the transmission control unit, particularly low sampling rate.

The measurement and control of transient vibrations is particularly difficult in a system such as a transmission in terms of computing resources. It is necessary to be prudent with computing resources because for the majority of operation the input and output are linear, therefore there is little control or measurement required. However, during gear changes or clutch actuation, the control and measurement requires high computing power to ensure transients are faithfully captured. The excitation frequencies of the system during transients may often be an order of magnitude higher than other frequency-based quantities of interest, and therefore a balance is required in terms of data acquisition to ensure sufficient fidelity for transient analysis against dataset size.

(Dolcini, De Wit & Béchart 2008) approaches the same task as (Horn et al. 2002) using a different approach, taking into account the drivers intention. The standard approach to clutch control described in this work is via a stacked lookup table whereby the clutch feed-in is controlled by a lookup table according to the driver's throttle input. The entire control is open loop but considers driver intention to define the clutch feed in rate. The disadvantage of the open loop control is that it is necessarily longer than optimal to ensure no vehicle lurch or stall is induced. The authors postulate that the open loop control is sufficiently responsive for the first part of the shift but use a clutch torque controller to prevent lurch in the second part of the shift. The transition is governed by an "observer" that measures clutch slip and engine

torque, and when clutch slip reaches a predetermined trigger, begins optimal control to minimise the oscillation caused by inertia matching after engagement.

The approach is attractive as it minimises the control time and computing hardware required and focuses on the most uncomfortable part of the gear shift, which is the lurching after full engagement. The sensitivity of the control to time delays is also noteworthy, with even the time delay introduced from the CAN broadcast of the engine speed causing challenges in implementation. In the project presented in this thesis, the clutch controller is the human in the loop. This takes advantage of the driver's sensory perception (or lack thereof) to provide some reasonable control of the clutch, but uses the motor, downstream of the clutch as the jerk controller. There are challenges associated with this, as the motor control must either counteract torque fluctuations as they arrive in real time, which is a challenging control task, or must act as a passive damper, which is a more limited form of jerk control.

By the turn of the 21st century, hybridization was becoming a significant research focus in the automotive community. Because of the second prime mover, the transmission technology paired with hybrid powertrains can make a significant difference to the functionality. Electrified transmissions (Xu et al. 2018) began to be developed. These transmissions differ from typical transmission technology in that they often collocate the secondary tractive device and are designed to switch between, or blend outputs from both prime movers. Despite this, particularly with parallel hybrid topologies, traditional transmission technology continued to be used. The benefits of hybridization could also be leveraged to improve system functionality.

(Baraszu & Cikanek 2002), mentioned previously, presented torque results very similar to those demonstrated in this thesis in Chapter 9, albeit using a somewhat more complex powertrain utilising an AMT and a 4x4 differential. Whilst the torque hole was successfully filled, it was not eliminated and acceleration fluctuations (therefore, likely jerk as well, which

was not presented) during gear shifts were similar in nature to those observed here. This gives a good level of confidence in the validity of the results obtained herein.

In (Gavgani et al. 2015, 2016; Vacca et al. 2017), experimental torque results from the HAMT are presented. Partial results from there are reproduced in Figure 2.7. The results from the HAMT are shown to give better torque-fill performance than a DCT at part throttle, but due to the limitation of the torque capability of the electric motor, as engine load increases, the performance of the DCT eclipses that of the HAMT. However, the authors make several observations. Firstly, the main driver for the development of the HAMT is the energy efficiency benefit, and not the performance benefit. This parallels the reasoning for the development of our hybrid powertrain. Secondly, it is not practical to increase the size of the motor for the sole purpose of providing complete torque in-fill. This is a limitation that was experienced in the development of our current project, as the motor size must be considered along with the battery discharge capacity. The third observation is that despite the partial torque fill-in achieved, subjective testing showed that occupants considered short torque gaps more comfortable than large torque gaps of the same peak-to-peak value. This raises the very pertinent issue of occupant perception of vibration and harshness.

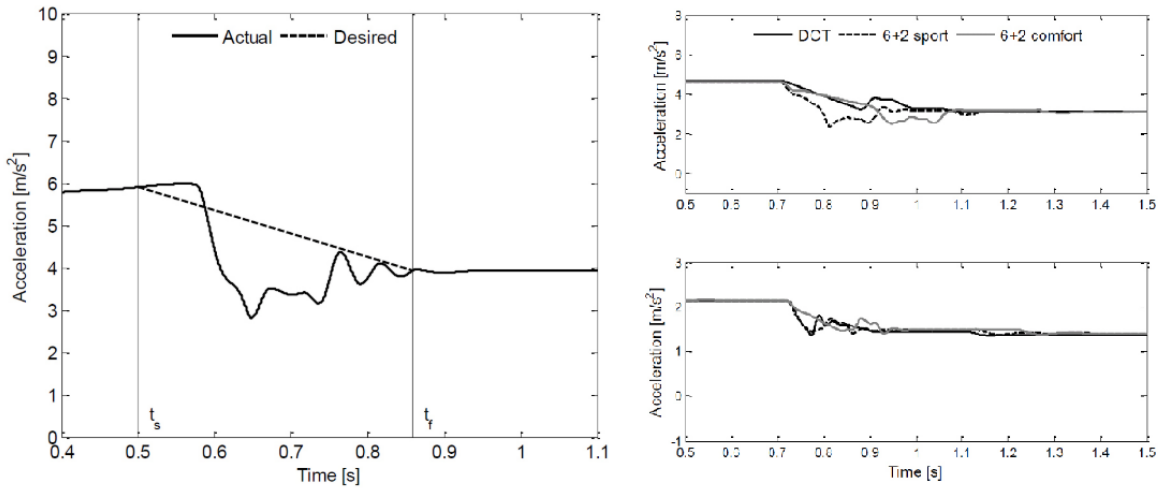

Figure 2.7 HAMT torque output results during shifting – from (Gavgani et al. 2015)

The perception of shift harshness is an important consideration when considering gear shifting, as it is generally not possible to tune out all transient vibration. Therefore, it is necessary to understand what is considered comfortable and what is uncomfortable to vehicle occupants, so that vibration can be tuned appropriately. One of the measures appropriate to this perception is jerk, the first derivative of acceleration. Two studies relating to driveline jerk from shifting will be discussed.

The first of these, (Zhang et al. 2010) considers the driveability of a P0+P2 hybrid with an AMT. The longitudinal jerk is selected as a measure for the quantification of driveability because of its correlation with the human perception of vibration. A series of experiments are designed to test different vehicle functions such as starting, accelerating, mode-switching, gear-shifting, and a combined cycle. The data on jerk is acquired using a MEMS accelerometer, the output of which is differentiated to obtain jerk.

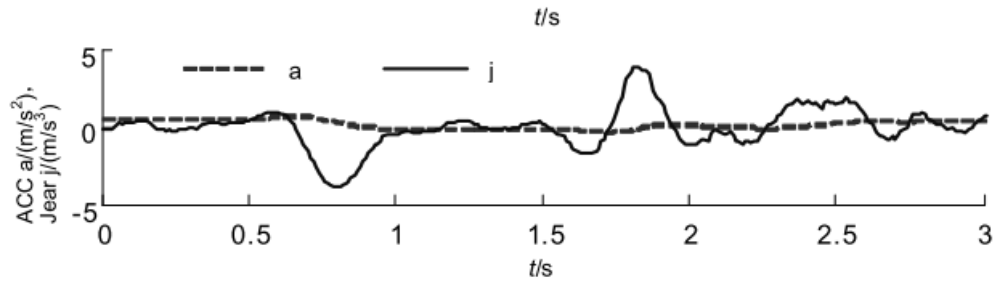

Figure 2.8 Jerk during a shift in (Zhang et al. 2010). The negative and positive jerks from clutch actuation as well as lurch are similar to those observed here

The researchers present jerk data on the various experiments and find that jerk during shifting (Figure 2.8) is characterized by two peaks of approximately ±4.2g/s. The jerk due to shifting is much smaller, generally, than that due to starting, changing vehicle mode, or braking. But it is more than the jerk during acceleration.

The second reference, (Huang & Wang 2010) attempts to characterize the physiological experience of jerk and objectively quantify levels of jerk that are comfortable and uncomfortable to passenger vehicle occupants. The research places occupants in a vehicle which is accelerated, shifting through all the gears and then brought back to standstill. The intensity of gear shifting is varied, and the number of acceleration repetitions are also varied. Occupants are given a feedback device consisting of buttons that correlate to the perceived level of discomfort. The authors find a complex correlation between jerk magnitude, jerk frequency, and jerk duration, all of which appear to affect the human perception. The results are interesting to know as the use of a stationary test facility for measuring jerk does not afford the luxury of the researcher's perception of performance during the test. These results provide some idea of the perception of jerk that is calculated on a dynamometer using rotational velocity measurements alone.

Chapter 3: Problem Definition and Solution Proposal

Despite almost three decades of intense research and development in vehicle electrification, the humble internal combustion vehicle still reigns supreme around the world. The winning combination of excellent energy density of petroleum-based fuels and highly efficient, power-dense internal combustion engines benefiting from over a century of development is proving a difficult beast to kill. Despite increased EV market penetration in western countries, on a global level, the conventional internal combustion vehicle still holds an unassailable global market position largely due to its performance, range, and consumer familiarity, although the gap is narrowing (see 2.2). This position persists despite immense progress in the development of higher power inverters, more efficient motors, and energy-dense batteries, making possible the technological spectacles of Formula-E, electric dragsters, and Tesla Model S vehicles in “Ludicrous Mode” (Figure 3.1).

Figure 3.1 Advances in electric traction drive technologies have made electric racers, such as this one built by students at UTS, possible

The performance advantages of the internal combustion vehicle also come with significant disadvantages. The most thermally efficient engine in the world claims a peak efficiency of 41% (Toyota 2018). In contrast, any modern electric powertrain can easily eclipse 90% peak efficiency, and average efficiency in the 80-90% range (De Santis et al. 2018). The news gets

worse for the piston party. Global emissions legislation at the moment is focused on the very real problem of tailpipe emissions from internal combustion engines. Euro 6 emissions limits are driving increasing energy diversification of vehicle fleets, mostly through petrol-electric hybridization, which appears likely to be the dominant form of energy diversification of road-going vehicles until at least 2030 (McKerracher et al. 2019). This energy diversification stems from unavoidable fundamental byproducts of combustion that are being slowly, and rightly, legislated out of existence. In contrast, detrimental tailpipe emissions are non-existent in electric powertrains. A wheel-to-well approach to emissions raises the obvious concern of spent battery byproducts, but this problem is far enough in the future that current legislation is mostly unconcerned with it, although it too has the potential to become a global issue if electrification, rather than diversification, becomes the ultimate legislative aim (Gaines 2014). However, full electrification is still some way off mass-market penetration. Battery-electric vehicle (BEV) sales make up less than 2% of total vehicle sales worldwide, and there still technological and economic disadvantages that need to be overcome (Bohnsack, Pinkse & Kolk 2014) namely energy density, charging infrastructure, indirect emissions, and mass manufacturing economy of scale.

3.1 Future of Internal Combustion

The internal combustion engine isn't going anywhere anytime soon. Even the most bullish forecasts modelled on the strictest scenario of legislative framework predict ICE dominance in the new vehicle market until at least 2025 (Harendt et al. 2016). These forecasts seem improbable given (at the time of writing) Euro 6 standards are yet to be fully implemented, and the next stage of emissions restrictions have not yet been discussed. More moderate forecasts (Harendt et al. 2016; McKerracher et al. 2019) suggest that ICE dominance in new vehicle sales will continue until around 2040, while the global fleet will have only achieved 33% electrification by that stage. What is clear from these forecasts is that the emissions

regulatory and legislative framework will be the primary driver of this change, rather than market demand, which follows technological or price advantages. This raises some interesting questions. What will happen in countries where emissions standards do not exist, or are poorly enforced? What will happen in countries where electricity is uneconomical compared to oil? Precious little has been published on these questions. Likewise, the literature is almost entirely silent on the effect of international trade in used vehicles on global emissions. However, if these factors are not carefully considered, the effect of emissions regulation may be adverse in particularly vulnerable regions. We present a possible scenario below.

The typical fleet-averaged vehicle age in high-income countries is between 8 and 11 years (ACEA 2017). Fleet turnover in much of the western world is largely driven by strict roadworthiness regulations, ensuring vehicles must meet certain emissions, maintenance and safety standards. As vehicles age, and notwithstanding those that are taken out of the fleet by crash damage, the expense of meeting roadworthiness standards increases in proportion to the vehicle value, prompting vehicle owners to make an economic decision to dispose of the vehicle at some point in its life. From there, vehicles may follow any of three different paths. The first is recycling for raw materials. In this case the vehicle is destroyed – often shredded, and raw materials are recycled into other goods. The second path is re-use for parts. Valuable parts are stripped from the vehicle and on-sold either domestically or internationally for use maintaining and repairing other in-service units. The third path is the used vehicle export market. This path results in the transfer of vehicles from markets where they are deemed unroadworthy and uneconomic to repair, to markets where they can be economically put back into service.

In contrast, fleet averaged vehicle age in low-income countries can be as high as 25 years or more (Elias 2010; Krambeck 2010). Many low-income countries do not legislate, or do not enforce strict roadworthiness standards (Tran et al. 2018). This combines with low wage rates, lowering operation costs and making older vehicles more desirable, creating a trade flow of used vehicle and spare part exports from high-income countries to low-income countries where older vehicles retain value and serviceable life substantially longer.

This trade flow causes vehicles built to older, inferior emissions standards to concentrate in low-income countries (Baskin 2018; Coffin et al. 2016 *inter alia*). Worse, as these countries may not test in-service emissions, vehicles may operate with defective and unchecked emissions equipment. However, the global trade in used vehicles is only one of a quadrumvirate of aggregating factors suggesting the focus of emissions reduction efforts will need to shift to low-income countries. The lagging adoption of emissions regulations (Akumu 2017) in comparison to the leading countries worldwide (as well as, in many cases, similar lags in safety regulation adoption) serves to reinforce global used vehicle trade, geographically concentrating vehicles with poorer tailpipe emissions to those countries that provide the path of least export resistance . The trend of increasing motorization rates in the same countries drives market demand for affordable transportation, which is met almost entirely through the used-vehicle market (Trouve, Lesteven & Leurent 2018). By increasing the size of the vehicle fleet, increasing motorization rate compounds the emissions problem even if vehicle tailpipe emissions are relatively cleaner. Finally, adoption of electric vehicles is hampered not just by initial purchase cost (Rahmani & Loureiro 2018), but also the cost, availability, and reliability of electricity in lower income countries (Arlet 2017), which can compound typical consumer concerns regarding range anxiety, or nullify the typical running cost advantage enjoyed by many EV owners.

3.2 Hybrid Vehicle Market Gap

Unfortunately, the answer to this dilemma cannot be found through regulation alone. The cost of achieving compliance with emissions regulations is significant (Bresnahan & Yao 1985; Skeete 2017; Subramanian, Gupta & Talbot 2007, *inter alia*). The cost is made up of two components: the development work required to achieve type approval, and the component costs for exhaust aftertreatment built into every compliant vehicle. These costs are ultimately recouped through the vehicle purchase price. In price-sensitive markets it is not practical to ban used-vehicle imports; many countries are reliant on used vehicle imports for motorization. Neither is it practical to enforce expensive emissions regulations; this forces the cost of new vehicles up, or forces the importation of only newer, more expensive used vehicles. However, a market-based solution delivering an appealing product to those markets may have a good chance of commercial and environmental success. Such a market-based solution exists in the low-cost new vehicle market dominated by lower-cost regional competitors, which could be motivated to develop a rugged, low-cost vehicle demonstrating superior, although not cutting-edge, emissions performance. These regional players have significant experience catering directly for the highly-competitive developing markets. In China, where government targets for fleet electrification have been aggressively pursued (Wu et al. 2017; Zhao et al. 2019), they have also shown they have the ability to rapidly innovate and develop new products. They are ideally placed to develop a market-based solution. Outside China however, in the developing world there is no legislative incentive to pursue a pure EV electrification strategy. Nor is there a market incentive – compounding the consumer concerns and potentially poor economic return is also the fact that consumers and automotive professionals alike are not familiar with the technology.

If EVs are impractical and emissions-compliant ICEVs are too expensive, perhaps a suitably-adapted hybrid-electric vehicle could deliver an appropriate market-based solution. A HEV is no doubt costlier to build than an ICEV, but has the potential to deliver better running costs, making more economic sense. By carefully controlling the degree of hybridization, the increased bill-of-materials (BOM) costs can be minimised, which in turn minimizes the purchasing cost premium. A HEV is also more likely to deliver better emissions performance later in its life as its electric powertrain is unlikely to be simply 'deleted' if defective, whereas the removal of in-service emissions hardware is commonplace. Kept simple, a HEV will also remain familiar to consumers and repairers, aiding with market adoption. Finally, a HEV powertrain can be optimized to provide unique features not possible in an ICE powertrain, which can be used to enhance market appeal.

In the following sections, the HEV solution is investigated and described, and the design goals for the solution are developed. The solution is framed in the context of a political, economic, social, technological, environmental, and legislative (PESTEL) analysis.

3.3 Political, Legislative and Economic Considerations

Some significant political considerations relate to tax structures around vehicle importation in developing countries. Vehicles are subject to a wide range of taxes. These are commonly grouped into import taxes which are paid once, registration or road taxes which are paid annually, and transfer taxes paid upon the transfer of the vehicle title. Additionally, many developing countries are highly reliant on used vehicle imports for supply of their national fleet. For instance, Kenya relies on used vehicle imports for 99% of new registrations (de Jong 2017). This effectively exports pollution from developed countries to developing ones (Edwards 2017), because many cars being transported no longer meet safety and emissions criteria in their country of origin. Import taxes on these vehicles are an effective way of

discriminating between desirable and undesirable vehicles. A preferential duty system generally skews toward newer, lower-emissions vehicles. Many countries implement preferential duty systems on both new- and used-vehicle imports. Duties may be tied to engine capacity, emissions, vehicle weight, and/or prescribed value. In all cases where preferential duties are implemented, lighter, lower-emissions vehicles with lower swept engine volume are encouraged. This can be seen in countries such as Mauritius, Sri Lanka, and Egypt. In Mauritius, a carbon dioxide-based fee rebate and fifty percent discount on excise duty for hybrid vehicles has resulted in road vehicle emissions reductions of about twenty percent between 2009 and 2018 (Molin Valdés 2018), with a corresponding reduction in fleet average economy from 7L/100km to 5.8L/100km (de Jong 2017). A similar scheme in Sri Lanka saw partial or fully electric vehicle registrations in the country climb to 82,400 in 2015 (Sugathapala 2015), with a commensurate reduction in fleet average economy from 6.4L/100km to 5.3L/100km. By contrast, in Uganda, fleet average economy deteriorated from 12.5L/100km to 13.7L/100km between 2005 and 2014. During this time, no limits were placed on vehicle imports and an environmental tax of 20% was levied on vehicles over 8 years old (Mutenyo et al. 2015).

It is clear that there is a demand for affordable, clean transportation. However, the current model of delivering this objective relies mostly on “trickle-down economics”, where older, devalued vehicles no longer meeting exacting western standards are “trickled” into poorer countries through the used car trade. Many new hybrid and almost all new electric vehicles are simply unaffordable in developing nations, even with discounts on government duties for new vehicles (Mansour, Haddad & Zgheib 2018). The major import path for these vehicles is via used trade, where there is a smaller volume of trade due to their relative rarity and continuing acceptable emissions performance. A low-cost hybrid vehicle catering specifically

to this market would take advantage of preferential taxation and provide an option in the new vehicle market for a significant customer base.

Another significant consideration is the cost of petrol in developing nations. Whilst in the west, many are used to fuel excise being levied by governments, the volatile price of petrol on the global market is often state-subsidised in developing nations, at great expense to the public purse. This subsidy can be considered a form of state welfare, where often a large portion of households would be unable to factor the full cost of fuel into their budget (Boughanmi & Khan 2019; Davis 2014). However, when viewed in this manner, fuel subsidies are highly inefficient and quite expensive. Analysis of fuel subsidies in developing countries has found that the richest 20% of households capture on average six times more in fuel subsidies than the poorest 20% (Arze del Granado, Coady & Gillingham 2012). Despite this, many governments find subsidy reform politically difficult, due to concerns for the adverse impact on poverty. Reducing the national fleet average fuel economy has many positive effects on this cycle. It reduces the financial burden on consumer budgets by way of a reduction in the rate of fuel consumption. By reducing consumption, the government subsidy expenditure is also reduced. In turn, subsidy reform becomes more politically palatable as its impact is reduced. The impacts allow government spending to be redirected toward more efficient measures, improving national resilience against volatile fuel markets and improving airborne pollutant concentrations, with all the flow-on benefits that this brings. The development of a low-cost hybrid vehicle specifically designed for developing markets would likely be welcomed and encouraged by regional governments.

Legislative considerations must also be made with regard to emissions standards. Increasing motorization rates in developing nations are leading to increased airborne pollutant concentrations in urban areas. Even if vehicle fleets are modern, and produce low tailpipe emissions, the environmental emissions do not decrease in proportion to the tailpipe

emissions improvement because of the increasing numbers of vehicles on the road. Currently, a majority of the developing countries have either no, or very minimal policies regarding the emissions standards of vehicles, either when first imported or in-service. Legislated emissions standards typically dictate both tailpipe-out emissions and fuel quality, which must be strictly governed to ensure emissions compliance.

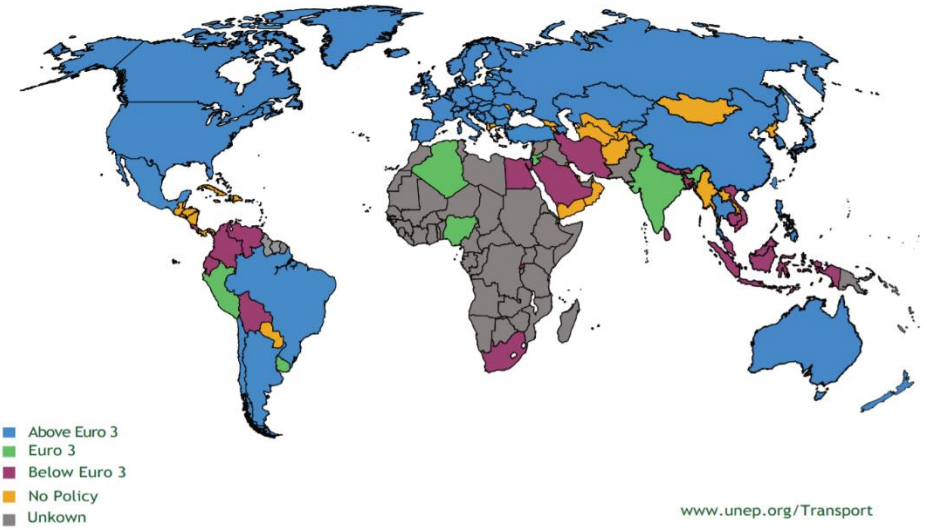

Figure 3.2 United Nations Environment Programme - World map of emissions standards (Akumu 2017)

Where a country is seeking to implement some level of emissions standards, it is simply impractical to leap-frog from a state of no, or lax emissions standards to meeting modern emissions standards. It is therefore necessary to invoke some level of transitional emissions standards and ensure the standards can be sustainably met by the market conditions. With the world's leading countries beginning to adopt Euro 6d emissions standards for light duty vehicles, the risk for countries that are yet to adopt emissions standards (Figure 3.2), or do not follow a practical, but accelerated plan for the introduction of emissions standards, is that they become the de facto dumping ground for undesirable vehicles. Whilst the benefits of emissions standards are well-understood, governments can often face opposition to such legislation, borne out of a notion that emissions reductions are costly to end users. These

notions are present even in many western nations. The development of a low-cost vehicle that meets modern, if not the latest, emissions standards, and qualifies for preferential taxation would support government initiatives in emissions legislation, as well as providing social benefit to the general population.

3.4 Technological, Environmental and Social Considerations

There are a range of considerations, interlinking the technological, environmental, and social aspects of low-cost hybridization of light-duty vehicles. The technology being used directly affects environmental outcomes, and environmental conditions are a direct social burden. Considerations flow from broad infrastructure issues such as access to electricity charging infrastructure, issues that manifest as barriers to market entry for fully electrified vehicles, through to social equity issues such as the human cost of emissions, which is manifested in higher mortality rates and increased burden on healthcare systems.

It is worth noting that many western governments have announced plans to ban internal combustion vehicles from 2025 through to 2050 (Coren 2018). Similarly, one of the world's largest automakers and manufacturer of over 40% of current electrified vehicles globally, Toyota has announced that it plans to phase out internal combustion powered vehicle in 2050 (Lord 2017). The time lag between adopting new vehicle regulations and achieving 50% national in-service fleet compliance with the regulations can be up to 18 years (Lutsey 2015; Mazur et al. 2018) in the developed world, a figure which only increases as the quality and longevity of light duty vehicles improves. If countries that are reliant on used vehicle trade for motorization continue on current trends, it may well be 2080 before national fleets are majority electrified in these developing nations. There is a clear opportunity to make accelerated progress in the intervening decades.

One of the key barriers to vehicle electrification in developing nations is access to electricity. Electric power distribution grids can be unreliable or non-existent, forcing a disproportionate

reliance on combustible fuels. Due to inadequate grid infrastructure, this issue affects not only low-income households for whom vehicle ownership of any kind is too expensive, but rather can be a daily issue for a large part of the population (Arlet 2017). Whilst the benefits of distributed energy storage using off-vehicle charging (grid-connected) electrified vehicles are well-known, the benefits cannot be realized if base distribution infrastructure is not fundamentally reliable or is not accessible (Sadri, Ardehali & Amirnekooei 2014; Sovacool et al. 2018). Another key barrier is the relative cost of petrol and electricity. In many countries, petrol and other combustible fuels are relatively more affordable than electricity. Often, this can be due to fuel subsidies that apply to fuels such as petrol, diesel, and kerosene, but are not applied to electricity (Boughanmi & Khan 2019). In other cases, it is because the generation of electricity is primarily accomplished through the combustion of liquid fuels. A comparative heat map of the cost of electricity and the cost of petrol is shown in Figure 3.3 and Figure 3.4, using 2017 data obtained from the World Bank database (World Bank 2017, 2018). Of particular note is the unfavourable relationship between the cost of both forms of energy throughout much of Africa, the Middle East, Asia, and parts of South America, which discourages the use of grid electricity as a source of energy for mobility. Coupled with the high purchase cost of BEVs, this limits the market potential of a fully electric solution.

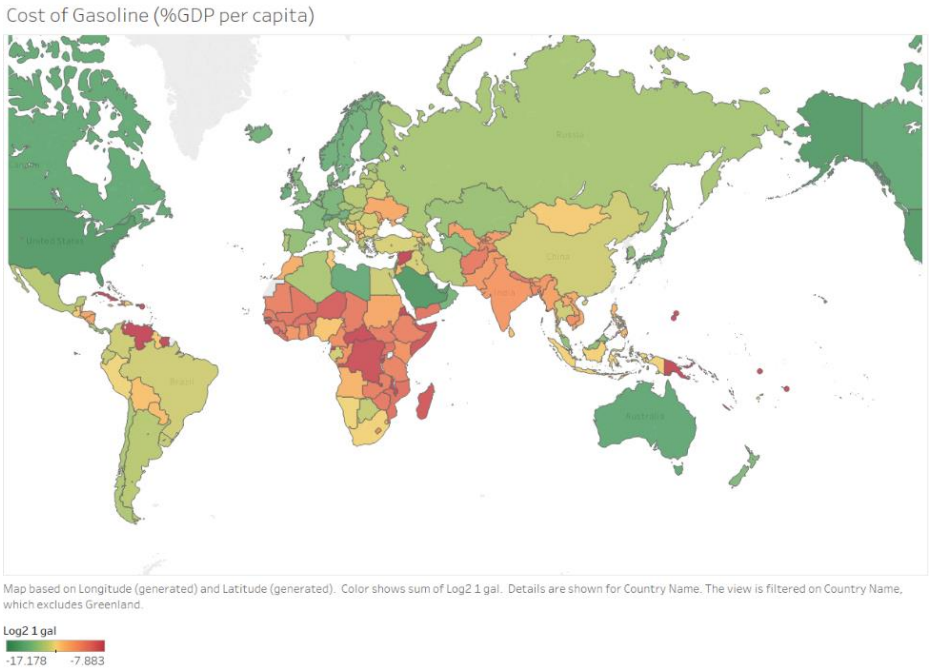

Figure 3.3 Heat map - relative cost of gasoline as a function of GDP per capita. Original map using data from the World Bank (World Bank 2017)

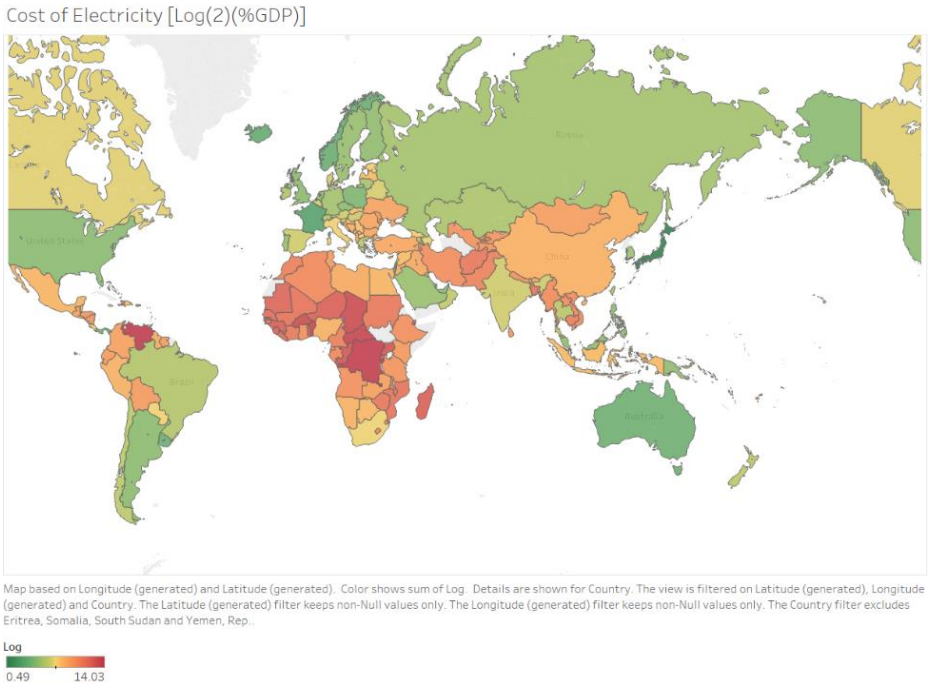

Figure 3.4 Heat map - relative cost of electricity (average consumer tariffs) as a function of GDP per capita. Original map using data from the World Bank (World Bank 2018)

In contrast, partial electric vehicles begin to make a more compelling financial case. Whether charging is accomplished using on-vehicle (engine load levelling and brake energy

regeneration) or off-vehicle (grid-connected) methods, the independence from unreliable electrical infrastructure and potentially costly electricity tariffs can translate into lower total cost of ownership (TCO) (Sharma et al. 2012, 2013). In addition, plug-in hybrid vehicles, whilst being generally costlier initially, will not cause an owner concern should the electricity supply be unexpectedly interrupted, and can, with appropriate infrastructure, be leveraged as grid-connected storage to improve network reliability. The technological benefit of increased vehicle electrification through a low-cost, partial electrification approach is that it functions synergistically with existing infrastructure, allowing greater change in the energy mix being exploited for mobility than could be achieved by a shift to BEVs when the infrastructure has yet to develop sufficiently to support significant growth in electric mobility. Another advantage of partial electric vehicles is simply that, where electricity is generated by burning fuels such as coal, diesel, kerosene, and natural gas, they can deliver better or similar emissions performance than a vehicle that relies on grid power for charging (Sandy Thomas 2012). In the best-case scenario, the emissions generated from charging a vehicle using non-renewable power generation is roughly equal to the emissions that would be generated had the vehicle been fueled directly. This, in effect, moves emissions from one location to another. In the worst-case, such as where diesel or heavy oil is used to generate electricity, the use of a hybrid electric vehicle results in a net emissions reduction (McLaren et al. 2016; Requia et al. 2018).

The environmental and social considerations of low-cost hybridization are also highly dependent upon each other. Global mortality as a result of airborne pollutants is estimated to cost 5.5 million lives annually, with some 246,000 in Africa alone costing the continental economy some US$215bn (Roy 2016). Whilst this figure cannot be attributed to tailpipe emissions alone, a significant attribution on the order of 30-40% of this figure can be made given the concentration of tailpipe emissions in densely populated areas and the contribution

to overall pollution from the transport sector. Air pollution also drives ecological change in land quality and water quality. Acid rain is one particularly well-known symptom of air pollution, being a byproduct of sulfur dioxide and nitrogen oxide deposits in water (Montero 1999). Acidification affects the quality of arable land which increases reliance on food importation and reduces plant cover. Loss of vegetative mass reduces the natural absorption of air pollutants, which can also increase eutrophication in water bodies. This causes algal blooms and de-oxygenation of the water which directly affects aquatic life (United Nations Economic Commission for Europe 2019). The environmental and human cost is high.

To compound the issue, increasing affluence drives motorization rates, fueling a demand for personal transport. This demand is underpinned not just by economic ability, nor by psychological factors such as social status, but also by fundamental policy decisions gearing metropolises toward automobile-orientation (Vasconcellos 1997). It is difficult to diffuse the desire for personal transportation without fundamentally changing the physical layout of cities. To do so takes, often, generations, and therefore it is necessary to consider motorization solutions that satisfy competing needs.

3.5 **Design Constraints**

In order to develop a low-cost hybrid vehicle for price-sensitive developing markets, a relentless focus on cost is required. A vehicle must be reliable and rugged, eschewing needless complexity which is likely to require maintenance or be a point of failure. It must also deliver low operating costs. For our hybrid powertrain, this also presented further requirements. The electric side of the powertrain must be kept as simple as possible. This minimises component costs, reduces potential points of failure, and minimises the training needs for service technicians to be able to provide maintenance and repair. The powertrain also needs to maximise emissions benefit within its design criteria, in order to achieve its stated aim of providing a market-based solution to regional emissions problems. Other

requirements were fairly obvious. A light/small car platform was selected for its popularity, affordability to the consumer, and for its manufacturing cost advantage compared to larger body styles. A small-capacity four-cylinder gasoline engine was selected for the ICE side of the powertrain, for refinement and the ability to generate acceptable drive power without advanced aspiration or fuelling technologies such as forced induction or direct fuel injection. A manual transmission was mandated by the key goal of this research, which is the investigation of jerk reduction and continuous torque delivery using a hybrid electric powertrain. The manual transmission also fits in with the remainder of the design constraints in that it offers the best efficiency for its cost. A series of design constraints were derived based on this initial brief, and are summarized in Table I.

A series of design benchmarks, shown in Table II were set for the purpose of guiding the design decisions. The benchmarks cover financial considerations, performance considerations, and technical considerations.

Design Constraints	
Purchase Cost Target	No more than 10% cost premium over ICE benchmark
Operating Cost Target	Break-even in 36 months compared to ICE costs No service items for electric powertrain
Emissions	Measurable and significant reduction in NOx, HC
Fuel Consumption	5% or better improvement over ICE benchmark
Acceleration	Identical or better than ICE benchmark
Cornering dynamics	No set benchmarks due to powertrain only study

Table I Initial Design Constraints

Design Benchmarks	
Body	
Body Style	light/small car
Kerb weight	1200kg
Layout	Front engine/Rear wheel drive
Engine	
Layout	I4
Swept volume	1300cc min., 1800cc max.
Peak power	70KW min, 90KW max
Peak Torque	110N.m min, 140N.m max
Fuel	Petrol, unleaded 91 RON
Fuel Injection	Sequential port injection
Ignition	Coil on plug
Aspiration	Naturally aspirated
Emissions compliance	Euro 3 or equivalent (prior to hybridization)
Transmission	Fully synchronized manual, five forward gears

Table II Initial Design Benchmarks

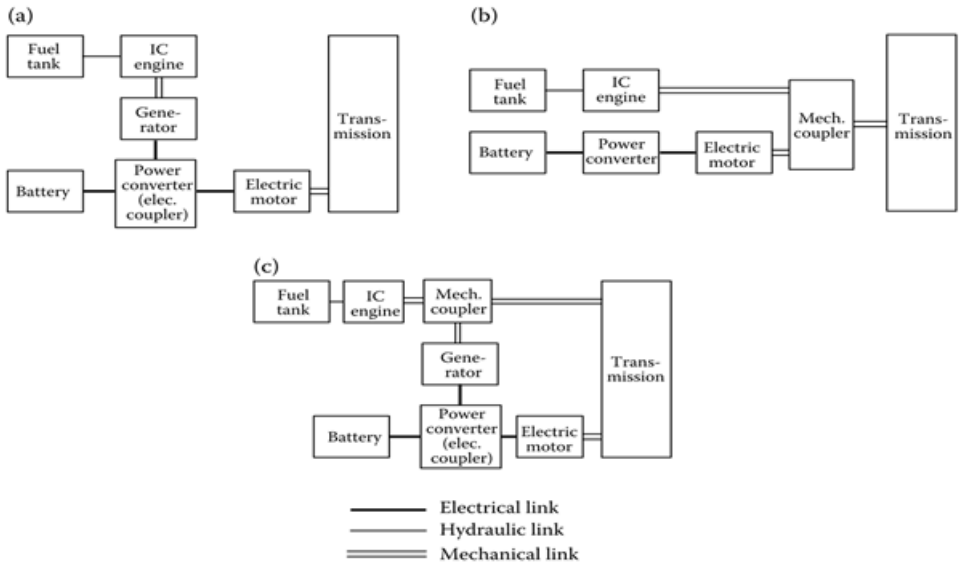

Figure 3.5 Hybrid vehicle topologies - (a) Series, (b) Parallel, (c) Series-Parallel

The hybrid powertrain topology was carefully considered within the guiding design principles previously described. The topology is required to deliver an excellent feature set, be robust, and cheap to produce. Hybrid powertrains are broadly classified into three main topologies. These are the series, parallel, and series-parallel topology (Ehsani et al. 2018). A range of other topologies are generally classed as “complex” hybrids. These topologies do not fall into a clear series or parallel pattern, often due to the use of two or more motors/generators or multiple power paths (Alamoudi et al. 2019). Vehicle charging methods are classed into “off-vehicle charging” (OVC), which represents a grid-connected vehicle, and “non-off-vehicle charging” (NOVC), which represents a vehicle that can only be charged using on-board power sources (the engine or electric braking). OVC hybrid vehicles are known as “plug-in hybrids” (PHEVs). Battery electric vehicles (BEVs) are the only other type of vehicle falling into the OVC classification (Engeljehringer 2016).

3.5.1 Series Hybrid Topology

The series hybrid topology describes a hybrid system in which power flows sequentially from one component to the next without a secondary power path. In this case, the internal combustion engine is used to drive a generator, which supplies power to charge a battery and drive an electric traction motor. The engine is sized to provide the average tractive power requirement, whilst the motor is sized to provide the peak requirement. The battery can be selected to provide the difference between the average and peak power needs, or may be designed to be larger than this, which allows the hybrid vehicle to operate in charge-depleting mode as well as charge-sustaining mode. The advantage of a series hybrid is that the engine can be designed to operate consistently at a fixed load point, or series of fixed load points. Because of this highly defined operating range, the efficiency of the engine can be better optimized. Consequently, the battery series hybrid can deliver the lowest tailpipe emissions (but not necessarily well-to-wheel emissions) of any internal combustion configuration.

However, two electric machines are required – a generator coupled to the engine, and a motor coupled to the road wheels. No mechanical connection exists between the engine and the rotating assembly. A series hybrid with grid-connected charging is classified as a range-extended electric vehicle.

3.5.2 Parallel Hybrid Topology

The parallel hybrid topology utilises two power paths that may operate independently or simultaneously. To achieve this, a mechanical coupling is used, usually in the form of a clutch or multiple clutches, attached to a transmission capable of accepting multiple inputs, usually through concentric shafts, or co-locating multiple power machines combined on a single shaft (on-axis). By including multiple power paths, neither the engine nor the traction motor need be sized to provide the peak power need of the vehicle, as the power can be summed through the mechanical coupling to provide peak capacity. If peak capacity is not required, either one or both of the power machines can be used to provide motive power, as dictated by operating environment and system efficiency. Whilst engine operating efficiency optimization can be limited in a parallel hybrid, load-levelling can be accomplished by using the electric machine to provide assistive motive power or generate charge current. In the parallel topology, usually the motor is sized to provide the average power requirement and the engine provides peak needs. The principal benefit of the parallel hybrid topology is its scalability and flexibility. Parallel topologies may be as simple as a belt-driven starter-generator (BSG) which employs a belt-coupled starter motor applied to the engine crankshaft to provide engine assistance and stop-start functionality, or can also be as complex as a multi-motor solution independently driving a separate axle. Because of this scalability and flexibility, parallel hybrid powertrains vary widely in cost and complexity. Parallel hybrid configurations are classified using the nomenclature P0-P4, according to the location of the electric machine. The nomenclature is described below.

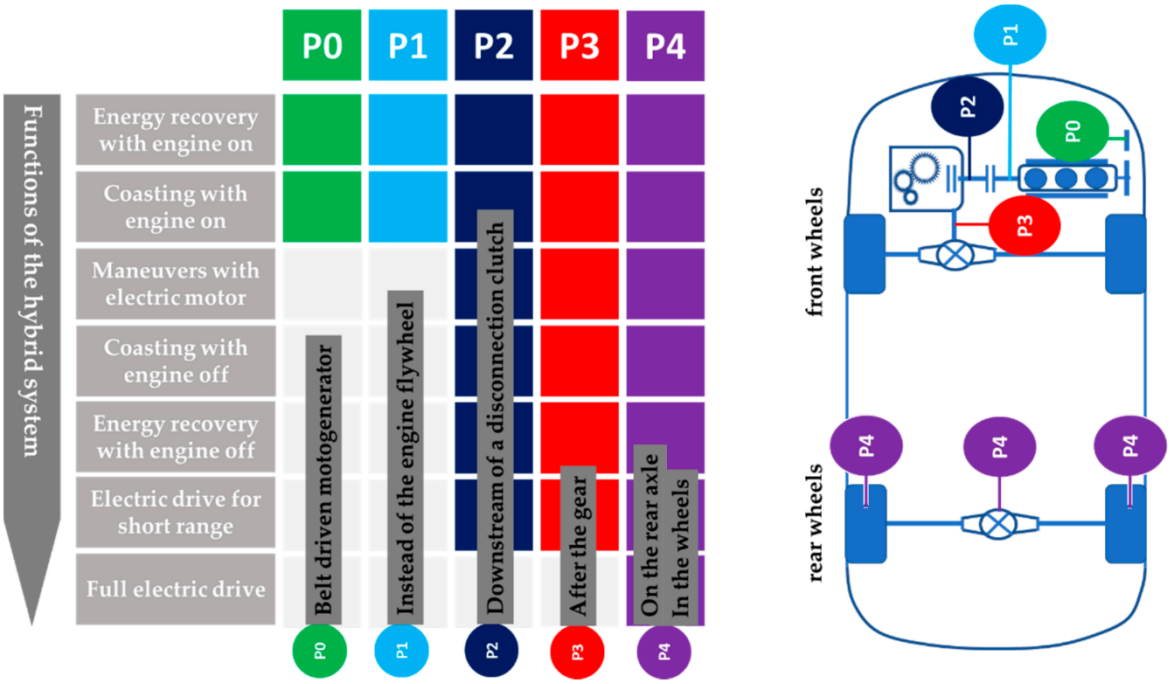

Figure 3.6 Parallel hybrid topology nomenclature, adapted from (De Santis et al. 2018)

P0

The P0 configuration entails a BSG placed on the front-end accessory drive (FEAD) of the engine. This machine is used to drive vehicle accessories independently of the engine as well as assisting the engine to propel the vehicle. The configuration can also be used for regenerative braking. However, the efficiency in this mode is quite low, as parasitic losses occur along the entire driveline, through the final drive, transmission, engine, and belt. Because of space constraints, high power density is required, and therefore the electric machine must rotate at high velocity (typically, 15-18,000 RPM) with a large gear reduction in order to develop appropriate torque and power. However, the design provides a high degree of cost-effectiveness.

These systems are also sometimes described as belt starter-alternator (BSA).

P1

This configuration sees the electric machine located on the output of the engine crankshaft, ahead of the drivetrain. The electric machine is often integrated with the flywheel to improve transient torque response. This configuration can be harder to package and requires motor characteristics exhibiting relatively high power-density. The benefits include better regenerative braking performance than is possible with P0, and relatively simple design.

P2

Whereas the P0 and P1 configurations are dependent on the ICE, the P2 configuration decouples the electric motor from the engine by placing it behind the clutch plate. This configuration allows the independent operation of both the ICE and the electric machine, providing greater opportunity for optimization as well as possibilities such as a pure electric drive mode. This also reduces drive losses by placing the electric motor downstream of engine pumping losses and inertia. The motor is still constrained by size due to its location at the transmission bell-housing. P2 is commonly referred to as an integrated starter-generator (ISG).

P3

This configuration sees the electric motor moved one step further downstream, placing it at the driven shaft of the transmission. This configuration is markedly different to the previous ones as it decouples the electric motor from both the engine and the transmission, meaning the motor is coupled to the driven wheels via only the differential. Regenerative braking efficiency is further improved, as is drive efficiency, through elimination of transmission losses. The placement also opens the possibility of continuous independent electric drive, as tractive effort is not driven through the transmission. Conversely, because the motor loses the

benefit of the first gear reduction, the motor operates at relatively lower speeds and is therefore required to be a higher-torque design than previous configurations.

P4

The P4 configuration decouples the electric machine from the mechanical powertrain entirely, using hub-motors (a.k.a in-wheel motors) to directly drive the wheels, or by using the electric powertrain to drive a separate axle to the ICE powertrain (Figure 3.6) The latter configuration is popularly known as a through-the-road (TTR) hybrid, because it uses the road surface as the mechanical coupling. The benefit of the P4 configuration is that it eliminates the need for complex powertrain componentry by directly coupling the motors to the wheels. It also allows complete flexibility, using the motors for features such as all-wheel drive (AWD) or torque-vectoring (yaw control). Its primary disadvantages are it requires the highest-torque motor design of any parallel-hybrid configuration, or installation of a second differential and associated half-shafts. It also the need for careful control under split-μ conditions. Finally, the P4 configuration works best in a series-parallel setup with the addition of a second electric machine functioning as a generator. This is because, unlike in previous configurations, it is not possible to use the electric machine as a generator without inducing a retarding torque at the wheels.

3.5.3 Series-Parallel Topology

A series-parallel hybrid provides twin mechanical power paths as well as an electric power path, to allow the engine to provide both motive power and electrical generation by driving an electric machine simultaneously. The electric power path allows both electrical generation and electric drive to be conducted simultaneously as can be achieved using a series hybrid. This takes advantage of the benefits of both topologies, by keeping the engine load site independent of the vehicle power demand, which provides engine optimization similar to a

series hybrid, and taking advantage of twin mechanical power paths to allow downsizing of both power machines and batteries.

3.5.4 Degree of Hybridization

Hybrid vehicles are classed according to the degree of hybridization, as well as the topology and their ability to be grid-connected (Basavaradder, Dayananda & Chethan 2018). The degree of hybridization is typically defined as a ratio of maximum electric power to total maximum power, where a ratio of 10% or less is known as a micro-hybrid, 10% up to 20% is called a mild-hybrid, and above 20% is called a full-hybrid. The degree of hybridization dictates the sizing (and therefore, cost) of components insofar as the topology applies practical limits. For instance, a series hybrid must also have a very high degree of hybridization by nature of its requirement for all motive power to be provided by the electric traction motor. A series-parallel hybrid is also most effective if there is a significant degree of hybridization to allow effective power delivery in series mode, parallel mode, and at all power split paths between the two. However, whilst a series hybrid requires degrees of hybridization typically in excess of 60% (based on the need to provide full motive power from an electric machine), a series-parallel hybrid can be optimized at degrees of hybridization in the range of 30-50%, because of the ability to use both power machines to simultaneously provide tractive effort. Below this lower limit the benefits of the series-parallel topology begin to approximate those of a pure parallel topology as circumstances in which series operation can be used become restricted. A parallel hybrid offers benefits even at very low degrees of hybridization, as it does not have any series power path and therefore never needs to provide sole motive power using the electrified powertrain. A summary of the key characteristics of the varying degrees of hybridization is provided in Table III

Hybrid System type	Engine Start/Stop	Regenerative Braking	Motor Assist	Electric Drive	Motor Main Power	System Voltage	Best Topology
Micro HEV	YES	No	No	No	No	~12V	ICE only (accessory loads)
Mild HEV	YES	YES	Modest	No	No	~42V	Parallel
Full HEV	YES	YES	YES	Modest	No	~200V	Series-parallel
Plug-in HEV	YES	YES	YES	YES	YES	>200V	Series/Series-parallel

Table III Key characteristics of varying degrees of hybridization

3.5.5 Topology Selection

The increased cost and size associated with the relatively larger, higher-voltage electric components required for a series hybrid makes the selection of a series hybrid topology impractical for use in light duty vehicles. Pure series hybrid topologies are commonly reserved for heavy duty vehicles where the mass of the vehicle is not a significant concern, or where the laden mass varies substantially due to attached loads. For this reason, a series hybrid topology was rejected. Grid-connected series hybrids (REEVs) are becoming relatively common in western markets, however this topology still cannot be achieved economically due to the significant battery capacity required and mandated by CARB BEVx definition (CARB 2012)

The series-parallel topology is the most common topology used for hybrid vehicles currently available, and is the most dominant from a sales perspective. The benefits are numerous – by using smaller electric components and smaller engines it allows significant manufacturing cost savings compared to a series hybrid whilst also delivering outstanding fuel economy and emissions performance. It can be paired with OVC to deliver partial zero-emissions capability (Lukic et al. 2005). However, the cost of a series-parallel hybrid powertrain is still relatively significant due to the high complexity of the topology, which requires at least two electric machines and often employs complex multi-mode transmissions to manage the

various drive modes, as well as the relatively high voltages used (commonly 200-300V battery paired with 650V motors). Another consideration is its significant mechanical divergence from typical ICE powertrains, which can cause issues for service technicians who are unfamiliar with the functionality of the powertrain.

In contrast, the parallel topology is highly scalable, and can be deployed flexibly in many configurations, allowing for a wide range of solutions that can be designed to meet both technical requirements and budgetary needs (Table IV).

Functionality	P0	P1	P2	P3	P4
ICE-independent operation	Only for powering engine accessories	No	Yes	Yes	Yes
Transmission-independent operation	Yes	No	No	Yes	Yes
Regeneration level	Minimal - after engine pumping losses	Low – after transmission losses	Low – after transmission losses	Higher – after diff losses	Highest
Motor as generator?	Yes – replaces alternator	Yes	Yes – only when in motion	Yes – only when in motion	Not optimized
Motor location and accommodation	Engine front-end modification (replaces alternator)	Transmission bell-housing and flywheel (replaces flywheel)	Transmission bell-housing and flywheel (drives input shaft)	Transmission output (transmission casing or output shaft)	Wheel hubs or front/rear subframe
Direct Engine Accessory Drive	Yes	No	No	No	No
Engine idle-off	Yes	Yes	Must retain starter	Must retain starter	Must retain starter
Engine Load Management	Not significant	Yes	Yes	Yes	Yes
EV Mode	No	No	Limited	Yes	Yes
Torque-fill during gearshift	No	No	No	Yes	Yes
Torque-vectoring (yaw control)	No	No	No	No	Yes
Relative cost	1 (cheapest)	3	3	2 (RWD/4WD) 3 (FWD)	5 (most expensive)

Table IV Functionality of the various parallel hybrid topologies P0-P4

The P3 configuration was selected after a careful design study with respect to the design benchmarks. The low-cost requirement discounted the possibility of a P4 hybrid. The P0 was discounted because its main benefit, namely, the ability to drive engine accessories independently of engine operation, could also be realised using electric accessories in conjunction with any other hybrid configuration. The generator operation is also dependent

upon engine rotation, limiting potential energy-saving benefits, which is the same reasoning for which a P1 configuration was dismissed. This left the P2 and P3 configurations, which are relatively similar. However, whilst the P2 configuration works best with an automatic transmission, the P3 configuration, being independent of the transmission, frees the design to adopt any kind of transmission, and provides the opportunity to optimize shifting quality by regulating torque during the gearshift event. This is an important consideration for cost, because it opens up the potential to use a manual, or AMT transmission in place of more costly transmission types.

3.6 **Summary**

Whilst electric vehicle technology has advanced considerably in the last three decades, there is a significant divide between the penetration of vehicle electrification in western countries, who have largely been technology leaders in this industry, and developing countries that are lagging behind, in many cases by over a decade in terms of fleet average statistics. In many developing countries, the cost of a new vehicle is prohibitive to much of the population, making new technology such as EVs inaccessible. Many OEMs have responded to this cost issue by developing low-cost vehicles based on licensed designs that may be decades old. This brings new cars to the market at cost effective prices but does not bring any emissions or electrification benefit. Compounding the problem is the relatively high cost and low reliability of electrical grid infrastructure, which is prerequisite to market penetration of grid-connected EVs. The global trade in used cars supports the demand for low-cost motorization in these countries, and is a key driver of increasing rates of motorization. However, the used car trade relies on a steady flow of older vehicles, many of which are no longer emissions compliant, or in some cases have had valuable emissions components such as catalytic converters removed prior to export. This effectively exports the emissions problem of developed nations to developing ones. The dilemma for developing countries is that they are

reliant on the used vehicle trade and older national fleets for motorization, which enhances economic output, but cannot then adopt strict emissions regulations due to compliant vehicles being inaccessible to a large portion of the population.

A market-based approach is proposed as one way of addressing this dilemma. A low-cost hybrid electric vehicle using the P3, post-transmission parallel hybrid topology is proposed. The P3 topology was considered against a range of other topological configurations, including series, series-parallel, and other parallel configurations. It was selected because it offers a relatively low-cost method of partial electrification. It is not dependent upon off-vehicle charging which can be inaccessible in many developing countries, and it offers the possibility of configuring the vehicle with a strong feature set, including positive and negative engine load levelling, low speed EV mode, and continuous torque gear changes using a low-cost manual transmission.

Chapter 4: Initial Design and Requirement Benchmarking

The design process for the MHEV prototype vehicle is the third step in the V-cycle development and verification model. At this stage of the development process, the project requirements are analysed to develop a design brief, which is the tool against which component selection is justified. The project requirements are described in Chapter 3, and are broadly defined in three categories. These are:

Fixed component definitions: The project requirements dictate a manual gearbox with single, dry clutch for motor in-fill torque investigation. The MHEV topology dictates an electric motor at the transmission output shaft or further downstream in the drivetrain, and a storage device for the energy used to drive the electric traction motor

Broad component definitions: The requirement to control the electric motor and supply a traction battery dictates a number of supporting devices, such as a motor controller and battery management system.

Design quantities: System dimensions such as motor power, battery energy storage, speed or temperature limits are either known, calculated from project requirements or prescribed based on component selections.

In the following sections the project requirements will be discussed and from these, the fixed component definitions will be justified. The design quantities for those fixed components will be articulated, and broad component definitions will be used to justify the remaining component selections.

4.1 Project Requirements

The project requirements call for the development of a MHEV powertrain for torque-filling during gear changes, and testing and development of other functions including engine load-

levelling, engine assistance, regenerative braking, and engine start-stop. The primary goals of the project are to develop a high-feature, low-cost, simplified hybrid powertrain, to increase fleet electrification in developing markets. The impetus behind the desire to increase fleet electrification is to improve local emissions performance and reduce reliance on petroleum oil. Therefore, the identified needs required to be met by the project became:

1. Cost minimisation (purchase and operation)
2. Rugged, reliable, simple
3. Favourable emissions performance
4. Adequate dynamic performance
5. Feature-rich

4.2 Base Vehicle Specification

To meet these needs, it was determined that a B- or C- segment vehicle (small/medium car) would present the most cost-effective platform for building the MHEV prototype. Therefore a kerb weight of no greater than 1200kg was set as a preliminary design constraint. An acceptable 0-100km/h acceleration time of between 8.5 and 9.5 seconds was also determined as satisfying dynamic performance criteria. This determination was made by surveying vehicles in the B segment and adopting similar performance to that published in the literature.

From these basic fixed definitions of kerb weight and acceleration, it was possible to make a rough estimation of the engine power and torque design quantities. This was accomplished by modelling a generic powertrain, using a generic engine peak power curve and typical drive ratios. The generic characteristics are provided in Figure 4.1 to Figure 4.3.

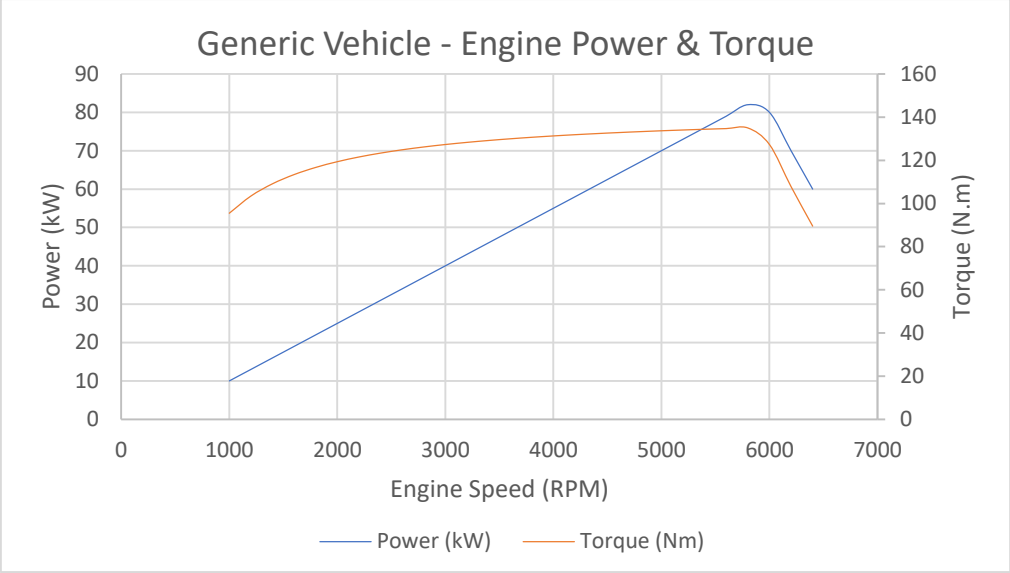

Figure 4.1 Generic engine characteristic (peak values)

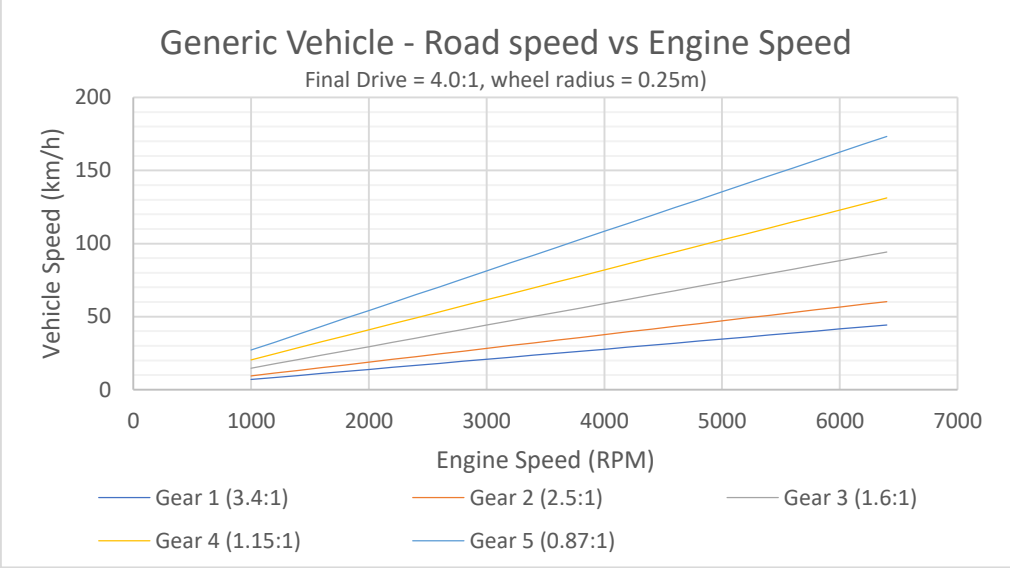

Figure 4.2 Generic vehicle characteristic (in-gear velocities)

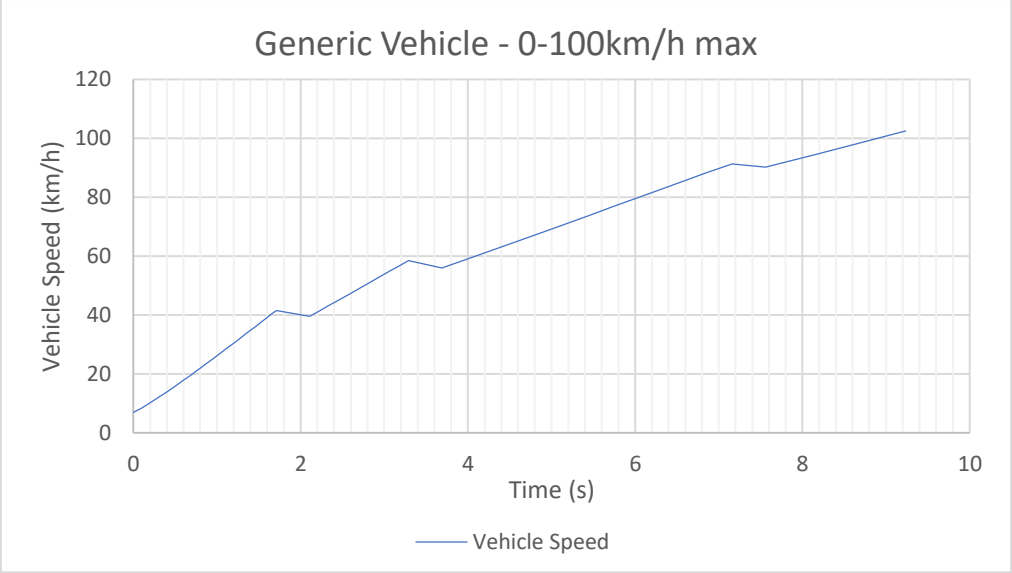

Figure 4.3 Generic vehicle characteristic (simulated peak acceleration)

By varying the model inputs (engine characteristic curves and drive ratios), acceleration performance may be estimated reasonably simply. From the modelling, the generic vehicle achieved a 0-100km/h time of 8.9s, with a peak engine power of 82kW and torque of 134N.m. These figures satisfy the dynamic performance criteria and were therefore adopted as the engine design quantities. These design quantities suggest a small capacity (sub-2.0 litre) four-cylinder naturally aspirated petrol engine. These quantities are achievable using downsized or diesel engines, however the cost of manufacturing these increases the base price of the vehicle, due to requirements for forced induction or high-pressure direct injection systems (Ebbesen, Elbert & Guzzella 2013; Simmons et al. 2015). In contrast, a four-cylinder engine can achieve the desired output without the need for forced induction, using low-pressure port fuel injection, whilst maintaining acceptable emissions performance without the need for specialised after-treatment (Isenstadt et al. 2016). Typically, this also means that fuel quality requirement is not especially high, which is particularly useful in regions where high quality fuel is not easily available.

Following this modelling exercise, the base vehicle design quantities could be set. These are shown in Table V

Base Vehicle Specifications	
Category	**Design Quantity**
Kerb Weight	1200kg
Engine Layout	I4
Peak Power	82kW
Peak Torque	134N.m
Fuel	Petrol, Unleaded 91 RON
Fuel Delivery	Port injected
Ignition	Coil on plug
Transmission	5MT
Drive type	Front-engine/RWD
Onboard Diagnostics	OBDI/Early OBDII

Table V Base vehicle specifications

Other vehicle specifications were set based on practical limitations. The requirement for providing continuous torque delivery during gear changes can only be satisfied by providing a prime mover at, or downstream of the transmission output shaft. In a Front-engine, Front-wheel drive (denoted 'FF') vehicle (or Mid-engine/Rear-engine, Rear-drive vehicle 'MR/RR'), the gear ratios and final drive are combined into a single unit (transaxle). The differential is usually directly meshed with the transmission output shaft, with the entire transaxle output embodied in two articulated half-shafts directly driving the front wheels. Because of this, there is no practical means of inserting an electric motor into a pre-existing transaxle housing, and therefore no practical way to build the prototype vehicle as an FF, MR or RR vehicle. Notwithstanding this, it is recognised that in a manufacturing scenario, a transaxle unit housing an electric motor at the transmission output would be significantly more cost-effective and compact than the prototype FR version.

The selection of an early OBDII or OBDI vehicle was made to circumvent the need to decode proprietary CAN messages, a difficult and time-consuming process which involves using a CAN bus sniffer to correlate CAN IDs to physical events. Complex OBDII vehicles may have monitoring that may flag faults if the vehicle is modified. If a fault code is triggered, this can often cause the vehicle to behave unexpectedly under testing.

4.3 Electric Propulsion System Specification

The design of the electric propulsion system requires the optimization of many more variables than the base vehicle design. As previously discussed in 3.5, hybridization is not just an exercise in component sizing, but also in vehicle topology, and control methodology. The beauty of hybridization is that the permutations and combinations of electric motor (EM) and ICE topology, combined with targeted control strategy allow various systems to be developed to achieve a diverse range of design goals, whether they be aimed at improving dynamic performance, economy, or emissions. This is achieved by balancing the compromise between maximising each power source's advantages and using each to compensate for the other's disadvantages. HEVs (regardless of their specific configuration) are more efficient in optimising engine operation with the added benefit of regenerative braking. This efficiency comes at the expense of needing a secondary power source like a battery, which may be heavy and inefficient. The implications of their usage include spatial complications in fitting the system within the body of the vehicle, a decrease in loading capacity and the loss of energy from the loaded tyres. Another variable available to the designer is the degree of hybridization, which gauges the proportion of power sourced from the secondary power source against the power sourced from the ICE. Hybrid vehicles (disregarding for the moment plug-in hybrids and extended range electric vehicles) are denoted as micro-, mild-, and full-hybrids depending broadly upon the degree of hybridization. The same topology with the same control strategy can deliver different benefits simply by varying the component

sizes. The exercise therefore becomes a multivariate optimization problem. To develop a hybrid powertrain that is cost-effective in manufacturing, feature-rich, offers high dynamic performance, efficiency, and smooth driving characteristics, it is necessary to strike a functional balance against all the desired criteria.

4.3.1 Hybrid Topology

Broadly speaking, there are three main hybrid powertrain topologies available for us to consider. These are; series, parallel, and series-parallel (Emadi, Lee & Rajashekara 2008; Lukic et al. 2005) The series hybrid was rejected due to the increased cost associated with providing an electric motor, inverter drive, and battery capable of providing the peak power for the vehicle. The series-parallel hybrid was rejected because it would either require a second electric machine or a split power path. This increases system complexity and component cost, leaving the parallel hybrid topology as the best choice in terms of both maximising simplicity and minimising cost. Within the parallel topology, based on the location of the electric machine there are still several configurations that require consideration (Bao, Avila & Baxter 2017; Masrur & Mi 2011). However, the choice of which topological configuration to use is simplified by way of the project requirement of providing continuous drive torque during gear changes. This criterion limits the topology of the electric propulsion system is limited to the P3 or P4 parallel hybrid topology.

The P3 topology uses a single electric motor placed at the transmission output shaft, prior to the final drive. The benefit of the P3 topology is that it is simple to implement, requiring only one electric machine. In production, the electric machine can be integrated into a transaxle in the case of FF/RR/MR vehicles, or in the case of FR vehicles, it can be a separate assembly directly flanged to either the transmission housing (replacing the typical rear extension housing), or the rear differential. Its primary drawback is that the electric machine must

operate efficiently within the speed range of the transmission output shaft, which does not exceed 4000 RPM in typical usage. One way to overcome this drawback is to mesh the motor to the transmission output shaft using a reduction drive (Figure 4.4), rather than directly driving through the motor, although this in itself has other drawbacks in terms of efficiency, noise, and cost.

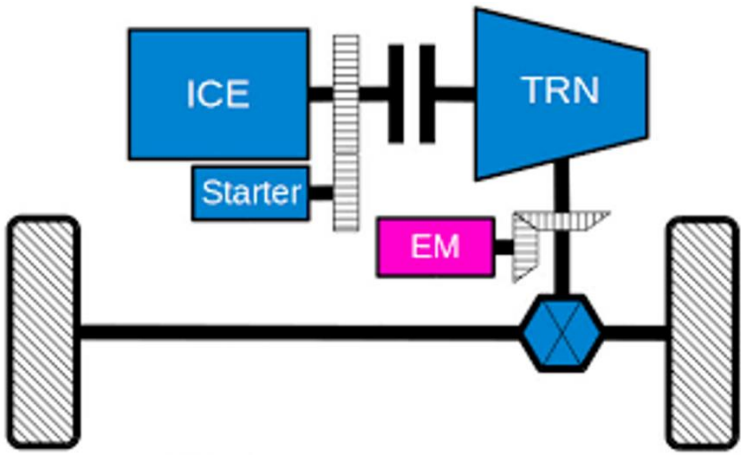

Figure 4.4 P3 topology can incorporate gear reductions for the electric motor to improve efficiency (x-engineer.org 2019)

The P4 topology requires either two hub motors placed on an axle, or a single motor driving the non-driven axle (a so-called through-the-road, or TTR hybrid). In the case of twin hub motors, the designer is free to select whether to place the motors on the driven or non-driven axle. However, typically for packaging reasons, hub motors are placed on the rear axle as it is not steered, and the installed brake hardware is generally smaller than that installed on the front axle. This provides greater clearance for the hub motor.

The use of hub motors is disadvantageous in many ways. Such a topology has significant vehicle kinematics disadvantages (unsprung weight), electrical disadvantages (motor must have atypically low base speed), and cost disadvantages (cost of twin motors and two-channel motor controller). For these reasons, the P4-hub motor topology was rejected.

The second embodiment of the P4 topology is the deployment of a single electric machine on the non-driven axle to provide a TTR hybrid. This embodiment has significant advantages. It provides the opportunity to deliver a compact, efficient, four-wheel drive (4WD) powertrain. This can be used to provide increased low-μ or split-μ traction. It also offers improved acceleration performance compared to a two-wheel drive powertrain. The disadvantage of the single motor P4 topology is that a second differential or side-by-side electric machine is required, through which the electric motor drives its axle. This also adds associated hardware, including a rear subframe, second pair of half-shafts, constant velocity joints, and driven hubs, all of which represent a further increase in cost (Murata 2012). Care must also be taken when calibrating the operation of the P4 hybrid, as changes in the applied torque can cause undesirable vehicle dynamics (Crolla & Cao 2012; Kaiser et al. 2011). The final benefit of this increase in hardware is that the motor is independent of the transmission output speed, and therefore the differential drive ratio can be chosen to be particularly suited to the characteristics of the motor, rather than constraining motor choice as is required in a P3 topology.

Comparing the P3 and single-motor P4 topology, the primary choice was a trade-off between the favourable manufacturing cost associated with P3 vs the 4WD functionality of the single-motor P4 (Table VI).

Feature set	P3	P4-single motor
Power path	Mechanical link	Through the road
Continuous torque delivery	Yes	Yes
Engine load levelling	Yes	Yes
Regenerative braking	Yes	Yes
Drivetrain torque oscillation damping	Yes	No
Engine Start-stop	Yes	Yes
Four-wheel drive	No	Yes
Manufacturing Cost	Low	High

Table VI P3 and P4 hybrid topology featureset

Another notable difference in functionality is the inability of P4 to provide active drivetrain torque oscillation damping. Such torque oscillations are commonly observed on clutch engagement due to the relatively small damping elements present in the driveline. Because the P4 electric machine is not in the primary power path, it is therefore unable to exert a direct torque in that path. There is also a high level of damping present in the TTR power path. This damping is in the form of tyre flex, suspension and subframe mount compliance, and body flex, and prevents the active control of drivetrain torque oscillations in the same way that is possible using P3.

Ultimately, the P3 topology was selected as it represents the most cost-effective method of hybridization possible and maintains a strong feature set in comparison to the single motor P4. Therefore, it became possible to add a single electric motor, battery, BMS and motor controller to the fixed component list for further design work in terms of component sizing and selection.

4.4 Component Sizing and Selection

There are many methods to calculate the desired design quantities for hybrid vehicle components. Methods that have been discussed in the literature are based on heuristic

optimization (Passalacqua et al. 2019), numerically simulated using forward-modelling (Guo et al. 2018), backward-modelling (Mamikoglu & Dahlander 2019), computationally derived using a variety of algorithms such as variations on search technique (Kim, Kim & Park 2018), variable minimization (Ebbesen, Elbert & Guzzella 2013), single-objective or mutli-objective (Wu et al. 2011). There are likely as many ways to arrive at an optimization as there are optimizations themselves. (Huang et al. 2018) presented a comprehensive review of optimization methods and each method's positive and negative characteristics, as well as case studies from the literature describing published outcomes.

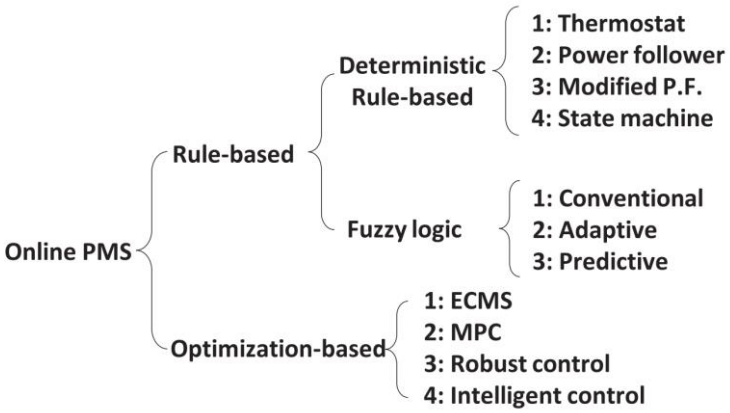

Figure 4.5 A tree-diagram of all "online" (i.e., not using static component relationships) component sizing methods (Huang et al. 2018)

Regardless of the method used, the process of optimization requires at least one reference criterion to which the component being designed is to be optimized, and one design quantity, the dimension(s) of which is the characteristic being optimized to meet the reference criterion. Further criteria may be added, which has the effect of further restricting the set of design quantity dimensions that constitute a valid solution. Additionally, further design quantities may be added, which has the effect of increasing the set of possible (but not necessarily valid) solutions. It is possible to restrict the valid solution set such that no optimized solution can exist, particularly if mutually exclusive criteria are added to the design

problem. It is also possible to add design quantities to the problem such that it is difficult or impossible to reach a valid optimized solution with a meaningful level of confidence. It is for precisely this reason that optimization can become computationally intensive. Therefore, it is always preferable to limit both the inputs and outputs of an optimization problem sufficiently to ensure a solution exists and can be clearly identified.

For the build of the prototype P3 hybrid vehicle, there are several design quantities that must be optimized, and components must be designed or selected to meet the optimized quantities. In the first instance, a base vehicle that lends itself to the modifications required to build the prototype must be selected. Based on its characteristics as well as the stated design objectives, it is then necessary to define the electric motor characteristics. This is achieved by modelling the MHEV system operation in representative drive cycles for the purpose of obtaining motor operating points. The distribution of the operating points will be used to specify motor operation speed range, torque curve and power demand. The same methodology can also be used to understand electrical power demand, which allows battery characteristics such as pack voltage, maximum stored energy, maximum discharge and charge rates to be determined. These are determined by integrating the power demands and supplies over the drive cycle, as well as investigating the motor operation events exhibiting peak characteristics.

Once battery pack characteristics and electric motor characteristics are understood, the selection of motor controller and BMS hardware is made ensuring compatibility with the desired hardware characteristics and control methodology. For the prototype vehicle, considerations of packaging, weight, or volume of hardware are secondary and may be disregarded due to their minimal effect on overall vehicle characteristics. The selection of the supervisory controller was not considered as it was limited to the dSPACE MicroAutoBox II, due to its availability in the laboratory. Further, the MicroAutoBox II is an ECU development

platform, rather than a hard-programmed ECU, and therefore is not representative of the hardware that would be used on a final version of the prototype vehicle.

The optimization and selection process for the primary hardware items (base vehicle, electric motor, motor controller, battery, BMS) is discussed in detail in the following sections.

4.4.1 Base Vehicle

As discussed in 4.2, the base vehicle was required to have a base powertrain in the rear-wheel drive, front-engine configuration with an inline four-cylinder engine and manual gearbox providing traction drive (FR/I4/5MT). The rated peak power and torque of the engine was to be approximately 82kW/134N.m and the total weight of the vehicle was specified at approximately 1200kg.

To locate appropriate base vehicles, a search of the market was conducted, inputting the various requirements into the search engine. The search covered the Australian new and used vehicle market using the largest vehicle classifieds website (by number of advertisements) in Australia (www.carsales.com.au). The search returned ten vehicle models as potential candidates for the base vehicle. These models along with key details are listed in Table VII.

Make	Model	Series	Engine Size (L)	Power (kW)	Torque (N.m)	Kerb Weight (kg)	Min. Advert. Cost	Suitability Index
BMW	116i	E87	1.6	85	150	1215	$8,000	83.15%
BMW	118i	E87	2.0	95	180	1220	$8,000	48.15%
BMW	318i	E36	1.8	85	168	1275	$3,000	64.72%
BMW	318i	E46	1.9	87	180	1330	$4,500	48.74%
Mazda	MX-5	NA	1.6	85	130	995	$3,000	76.27%
Mazda	MX-5	NB	1.8	106	195	1026	$4,000	10.71%
Mitsubishi	Express	SJ	2.0	83	165	1280	$3,000	68.98%
Suzuki	APV		1.6	68	128	1165	$5,000	75.53%
Toyota	Hilux	RZN147	2.0	86	166	1294	$3,500	63.41%
Toyota	Townace	KR42R	1.8	56	142	1196	$3,000	61.99%

Table VII The results of a market search for potential base vehicles for the MHEV assembly process

The models consisted of four light commercial vehicles and six light duty passenger vehicles. To evaluate their suitability as a base vehicle, a suitability index was calculated, by calculating the deviation from design quantities as a percentage. The formula used for the suitability index was (Eq. 4.1):

$$Suitability(\%) = 1 - \left(\frac{|Power - 82|}{82} + \frac{|Torque - 134|}{134} + \frac{|Weight - 1200|}{1200}\right) \quad (4.1)$$

This showed the BMW 116i E87 to have the lowest deviation from design quantities by a considerable margin. However, due to large price differential between it and the next most suitable vehicle, ultimately the Mazda MX-5 NA was selected. This choice was made not just for budgetary considerations, but also because the powertrain parameters of the MX-5 had smaller deviation from design quantities than those of the 116i, meaning much of the deviation came from the lighter weight of the MX-5 (see Figure 4.7 and Table VIII). This light weight, rather than being detrimental to the development process, allowed two main advantages:

- The prototype vehicle can be simply loaded with ballast for any road testing to increase its weight as required.
- For dynamometer testing, vehicle inertia is simulated by dynamically altering roller brake load according to input values of sprung mass (force of inertia) and unsprung mass (moment of inertia). Because the sprung mass is stationary during dynamometer testing, its only effect is to vary the tyre-roller interface friction. Therefore, the kerb weight of the vehicle is largely insignificant for such testing.

As it turned out, there were also some unexpected advantages of the selection of the MX-5. The lack of a fixed roof made installation of the electric powertrain components a much easier physical task than would have been possible with any other selection, as much of the installation could be done standing in or beside the car, rather than crouching in the confined cabin space. There was also a large, convenient space available for the installation of components once the retractable cloth roof was disassembled and removed from the vehicle (Figure 4.6). This greatly simplified the physical assembly and wiring process.

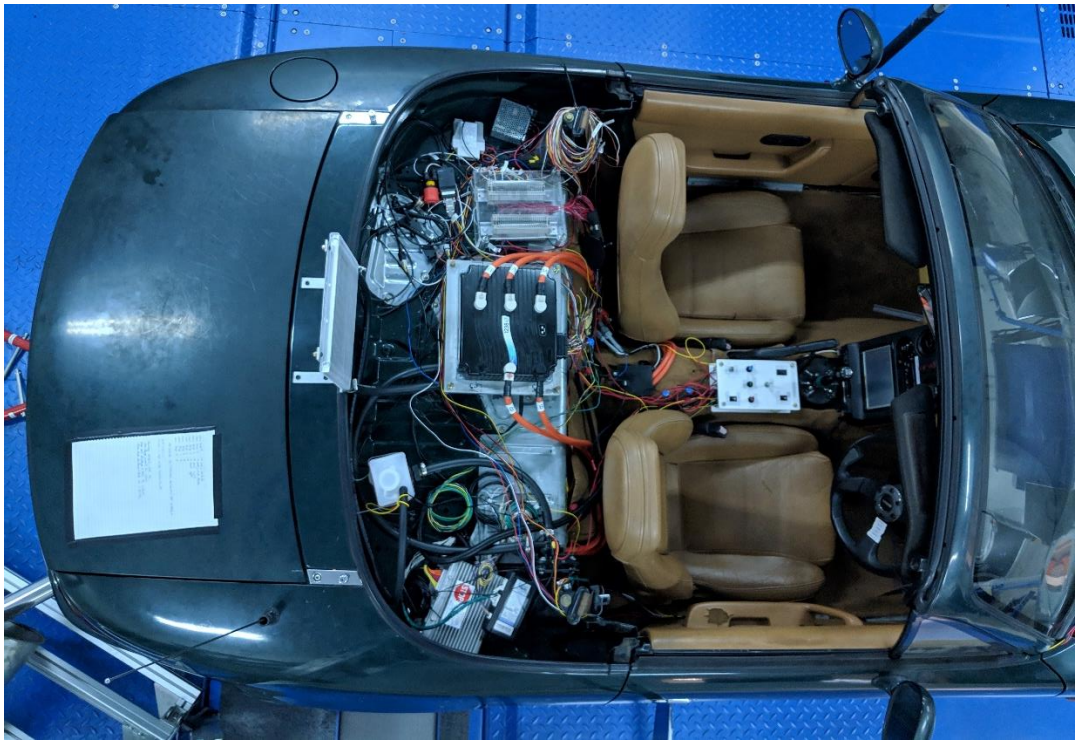

Figure 4.6 Top-down view of the prototype vehicle with the roof removed

As a final step in confirming the base vehicle selection, the generic design quantities derived in 4.2 were compared against measured quantities taken from an example of the selected base vehicle model, showing good correlation.

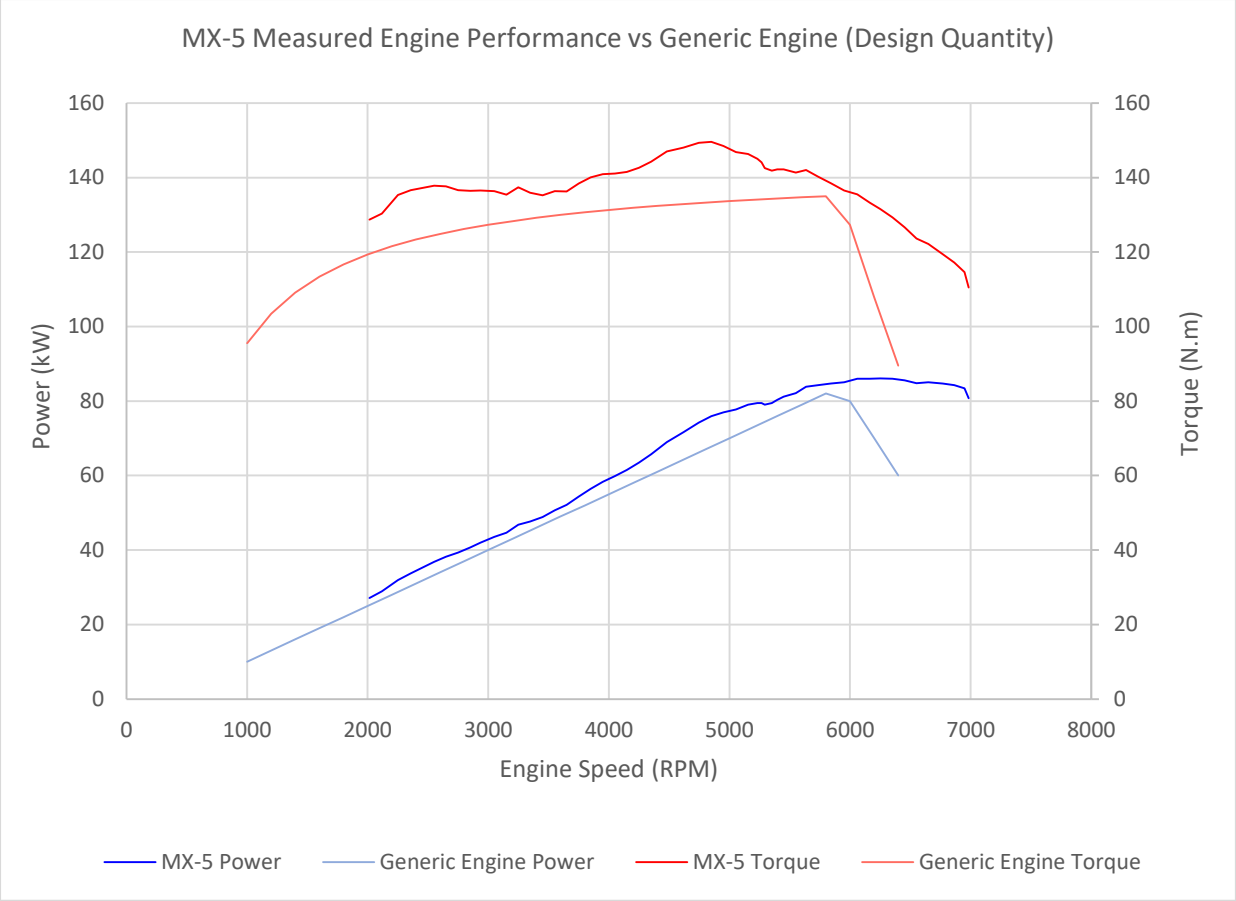

Figure 4.7 Comparison of generic engine and prototype vehicle engine peak power and torque

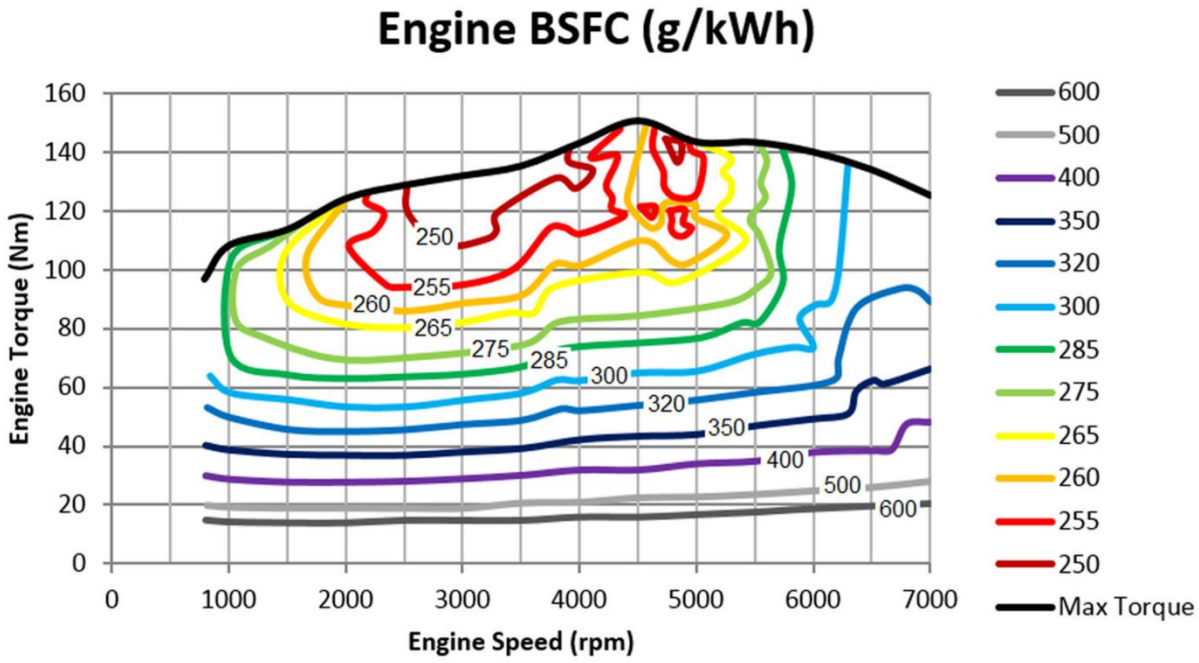

Figure 4.8 Engine BSFC Map (Oglieve, Mohammadpour & Rahnejat 2017)

Ratio	Generic	Actual (MX-5)	Effective (generic)	Effective (MX-5)
1st	3.4	3.136	13.6	12.189
2nd	2.5	1.888	10	7.333
3rd	1.6	1.330	6.4	5.169
4th	1.15	1.000	4.6	3.887
5th	0.87	0.814	3.48	3.164
Final Drive	4.0	4.1		
Wheel Radius	0.25m	0.237m (0.948)		

Table VIII Gear ratio comparison - generic vehicle and prototype MX-5 (Mazda Motor Corporation 1989)

4.4.2 Electric Motor Charaterization

The electric motor in the P3 prototype hybrid vehicle was required to be inserted into the powertrain at the transmission output shaft (in the case of the prototype vehicle, at the prop shaft). In this position, the electric motor is required to provide, at various times:

- in-fill torque during gear changes,
- battery charging through regenerative braking,
- battery charging through engine load levelling,
- Acceleration assistance through engine load levelling, and
- Electric-only crawling (EV start-stop)

The execution of these functions represents the reference criteria for which optimization was required. The design quantities required to be optimized include the electric motor mechanical power and torque demands, and the speed range at which these demands must be met. There were also other limitations set. For instance, the maximum diameter of the motor with its housing could not exceed 310mm, which represented the width of the transmission tunnel in the base vehicle at its widest. The operating voltage of the motor was also required

to be minimized as far as practical, in order to reduce the total manufacturing cost, by limiting the need for a high voltage battery pack, buck/boost converter hardware, and high-voltage IGBTs used for motor control. Practical limitations to the voltage limit include the motor diameter, which is required to be physically larger to generate the same torque, comparatively speaking, as a higher voltage motor. Current draw and parasitic loss is also a practical limitation, as the battery pack may not be physically capable of discharging safely at high current draws. Therefore, it becomes necessary to optimize the motor operating voltage in terms of cost, motor size, and battery discharge characteristics.

To ascertain electric motor mechanical power and torque demands, the MHEV vehicle characteristics were used to compute instantaneous power demand for a given drive cycle. Because drive cycles are defined by one-second time intervals with an associated speed indicator, the instantaneous power demand was computed by assuming constant acceleration for each one-second interval and calculating the power required to achieve the desired acceleration between each interval and the next. There were several drive cycles available but the New York City cycle (NYCC, Figure 4.9) was selected for its high dynamic variation, low average speed, and frequent stops. This cycle is highly representative of a chaotic urban road network, which is the environment for which this MHEV is being designed.

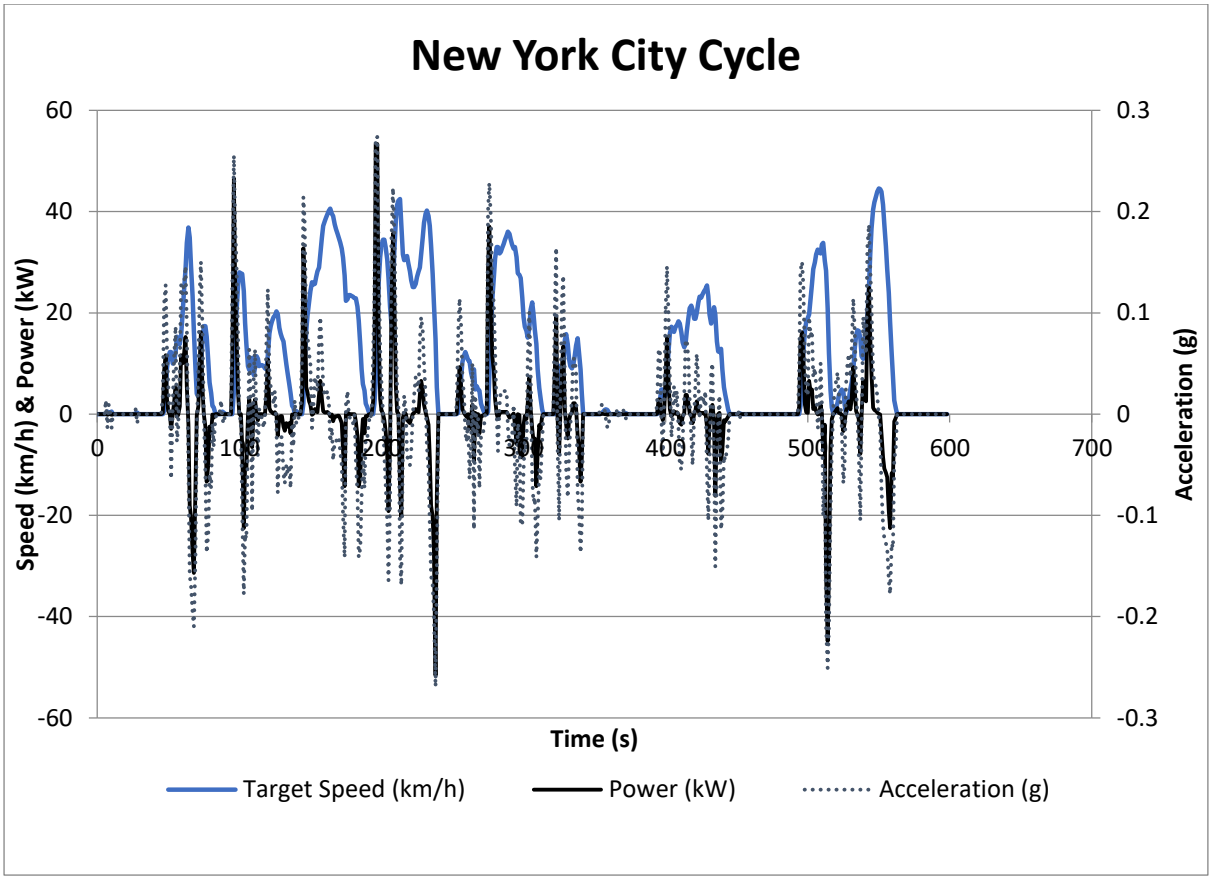

Figure 4.9 New York City Cycle (NYCC) speed and acceleration trace, as well as power requirements using base vehicle specifications

Once the power required by the base vehicle was determined, it was possible to characterize motor power demands in a piece-wise manner, by applying each operation mode individually to the cycle. The engine load-levelling does not alter the final outcome for motor selection as the instantaneous (peak) power demand from both engine assistance or battery charging does not exceed the peak demand from the modes in which the vehicle is solely relying on electric motive power. These two modes do, however, have a large influence on battery sizing, which is discussed in later sections. Because of the on-axis coupling of the electric motor to the petrol engine in the P3 hybrid, the load-levelling strategy follows a linear optimization process whereby both BSFC and emissions are optimized by targeting the optimum engine manifold pressure (or more precisely, BMEP) for a given engine RPM.

The power demand for the in-fill torque mode was characterized by overlaying a gear change pattern to the NYCC (Figure 4.10). The gear change pattern was developed by applying a speed trigger to the cycle to determine gear shift points. The speed trigger was modified using a time delay, so that rapid gear shifts in quick succession cannot occur if the cycle speed fluctuates around the trigger speed. Forty-two gear change events were identified across the cycle length of 598 seconds (Figure 4.11 and Figure 4.12). When the gear change events were identified, it was possible to determine the motor speed, torque, and power required to provide 100% in-fill torque at each gear change event.

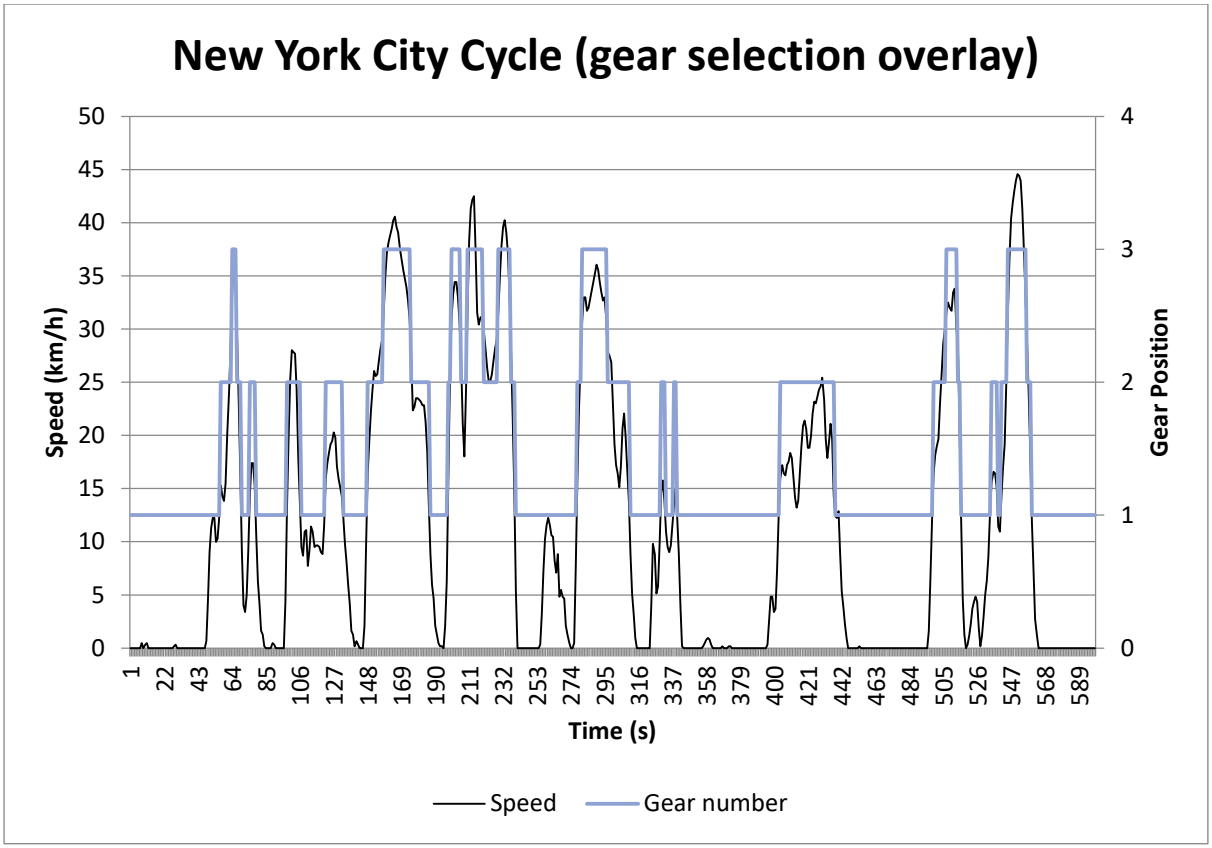

Figure 4.10 NYCC shift points based on the prototype vehicle specifications

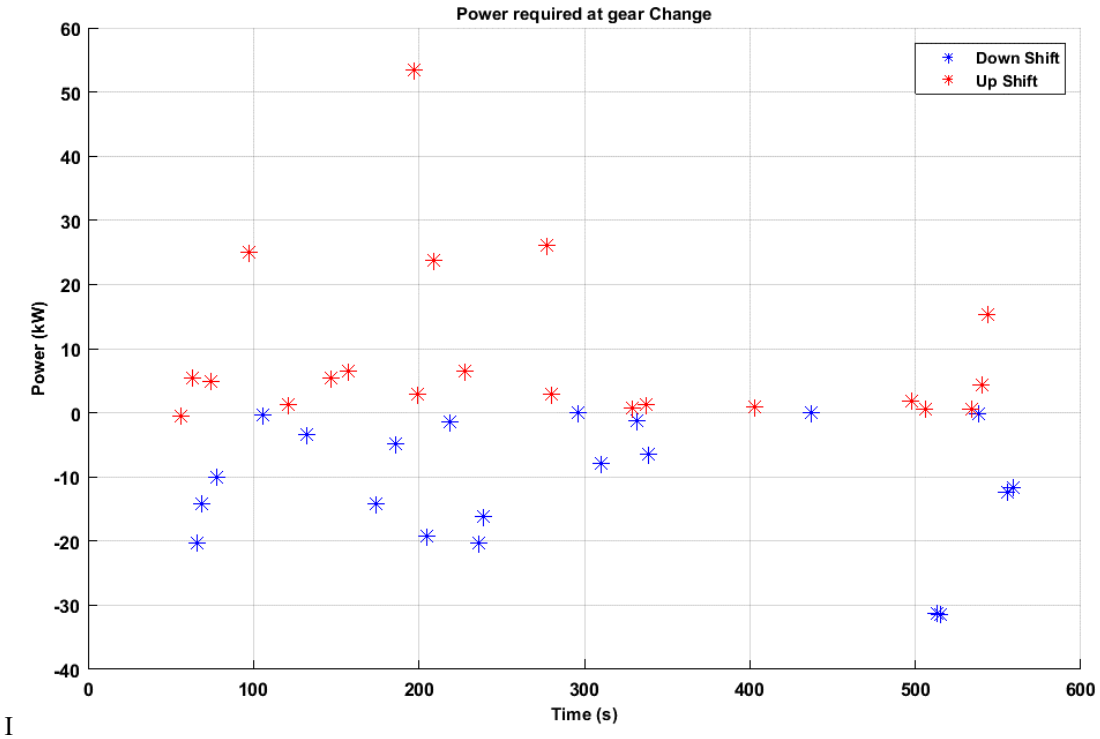

I

Figure 4.11 Power required for gear change using NYCC

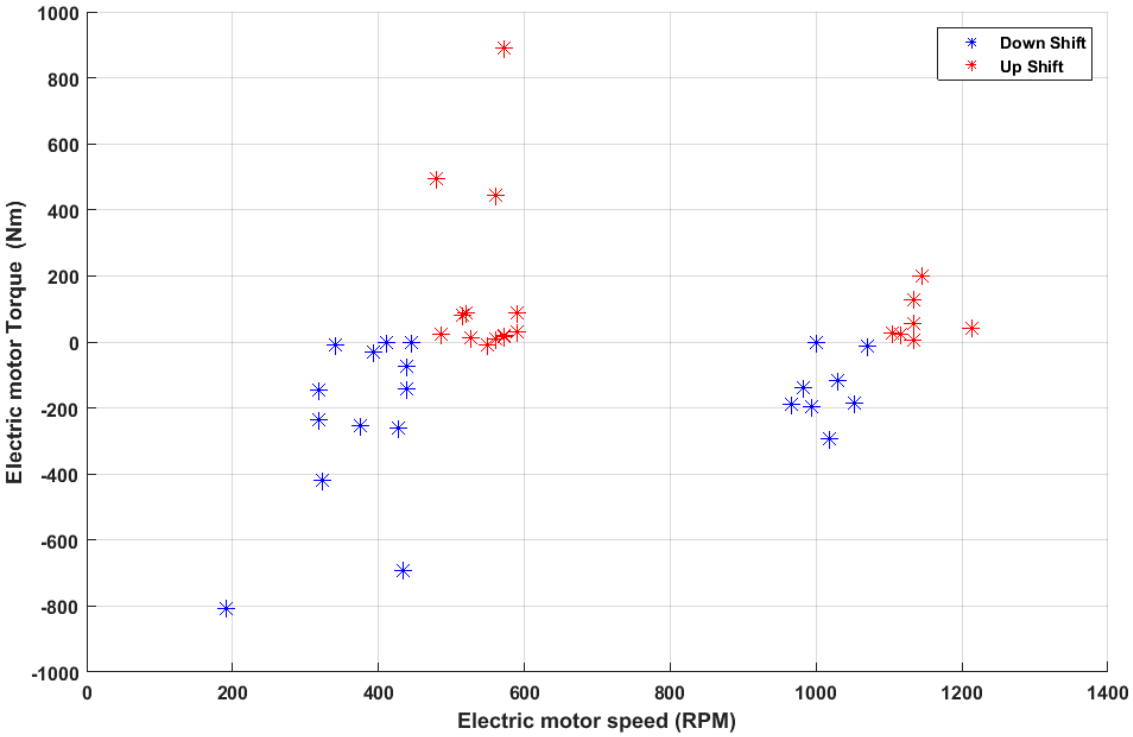

Figure 4.12 Electric motor torque and speed required at gear change.

Because the motor in the P3 hybrid configuration is placed after the transmission output shaft, it is not necessary to account for the first reduction ratio. Motor speed is a function of road speed only and motor torque is calculated based on the required tractive torque and the final drive ratio. The average up-shift power required during gear changes was 9.46kW, and all but one gear shift event recorded required less than 30kW for full torque in-fill. The down-shift (regen) in-fill power was similar, recording an average of -10.33kW. Therefore, a motor power rating of 10kW continuous and 30kW peak was adopted as a design quantity. It should be noted that because the NYC cycle is a low-speed cycle with a maximum velocity of only 44.5km/h, there are no 3-4 or 4-3 gear shift events recorded in the cycle. The gear shift events in Figure 4.12 are clustered into 1-2/2-1 events in the left-most cluster, and 2-3/3-2 events in the right-most cluster. Power demands in higher gears (3-4, 4-5) are unlikely to differ significantly, as the 4^{th} and 5^{th} gear ratios are lower, therefore prop shaft torque is also lower, and power remains similar despite increased motor speed.

The motor rated speed was calculated based on prop shaft speed at the design maximum velocity v_{max}. The design maximum velocity is achieved at maximum engine power in top gear, which for the chosen base vehicle was approximately 6200 RPM with the overdrive gear ratio of 0.814. This gives a rated maximum motor speed of 7616 RPM.

The same design exercise was repeated for the EV crawl mode (Figure 4.13). In this mode, an overlay was applied to the cycle data by limiting crawl speed to 20km/h and crawl acceleration to $0.8 m/s^2$. It was assumed that at speed or acceleration above these limits the EV crawl mode would be cancelled and the vehicle would revert to hybrid operation. These limits were selected as being representative of a typical 1-2 up-shift speed for the base vehicle (keeping engine revolutions under 3000 RPM in each gear) and a gentle acceleration as would be required in congested stop-start city traffic.

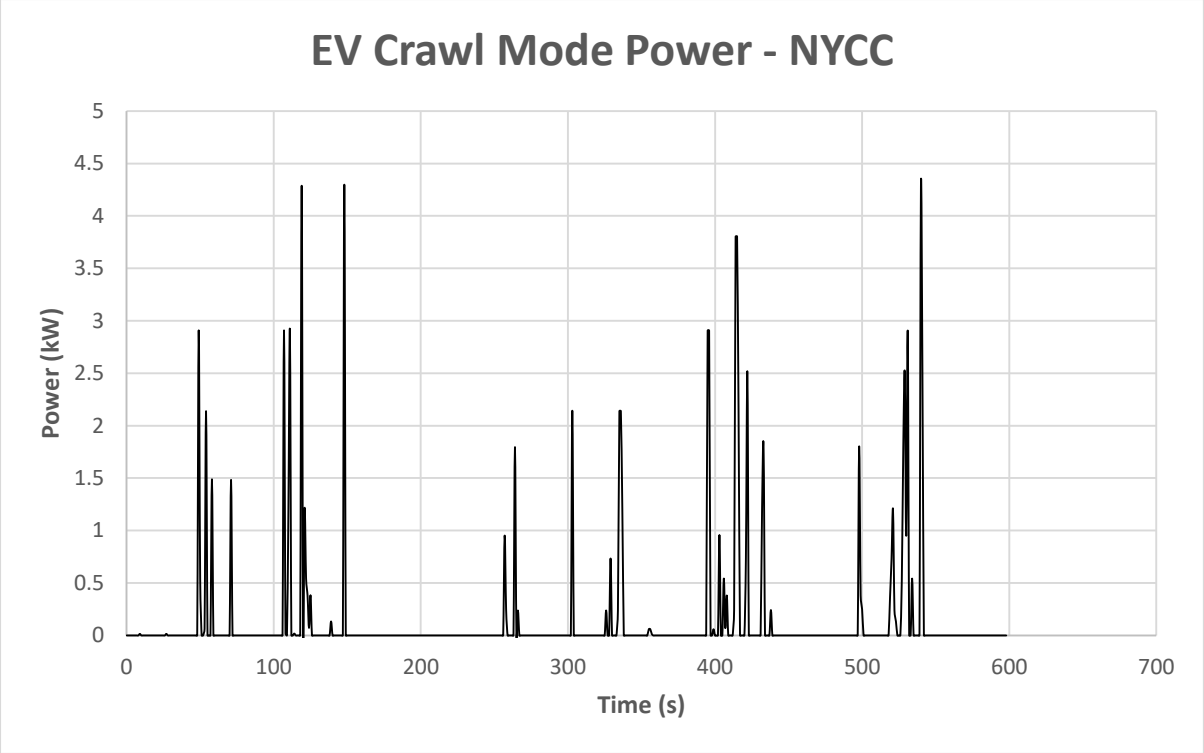

Figure 4.13 EV crawl mode power demand

The peak motive power required was 4.4kW, and over the entire 598 second cycle, total mechanical energy consumption was recorded as 0.024kWh. Incorporating the energy consumption for the motor in-fill function, the total energy consumption rose to 0.027kWh, if downshifts (where negative power flow is demanded) are ignored. Incorporating the negative power flow, energy consumption is reduced to 0.012kWh (Figure 4.14).

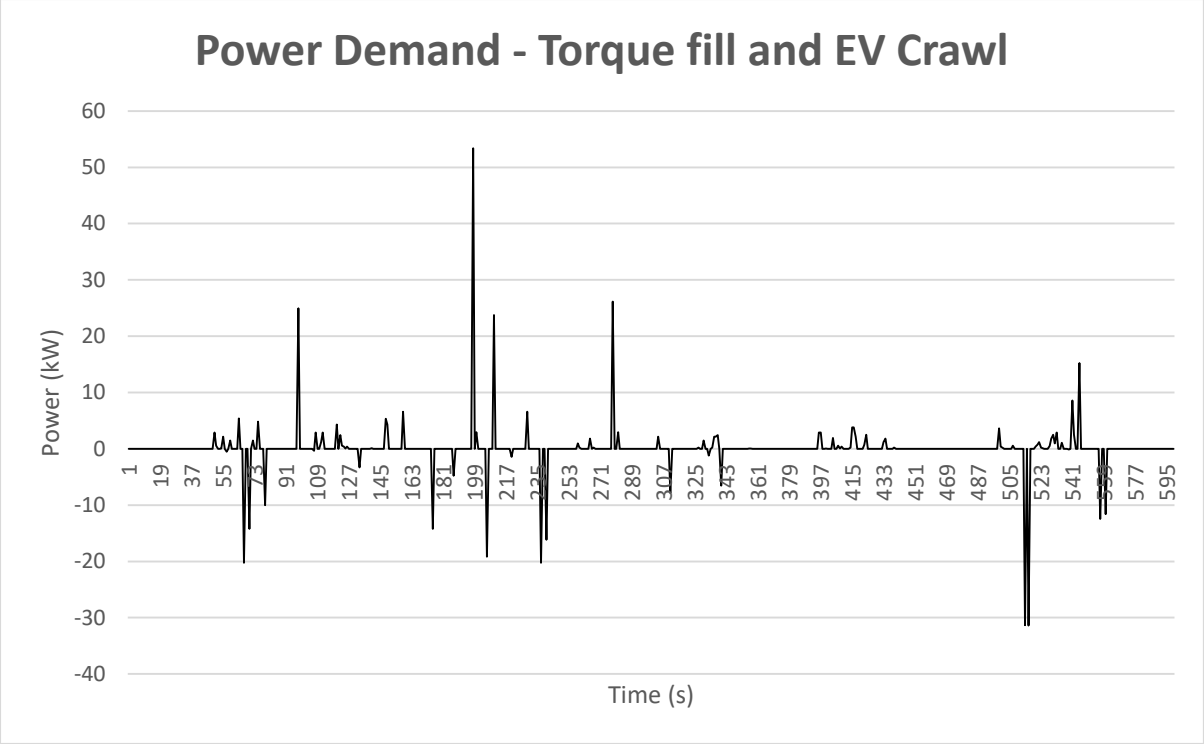

Figure 4.14 EV crawl mode and torque fill (summed) power demand

To characterize the regenerative braking energy recuperation possible throughout the cycle, a braking event overlay was applied to the cycle. Where the braking event power exceeded 30kW, the power was limited to this value using the overlay. This occurred for five seconds out of the 598 second cycle, or less than 1% of the cycle time, and therefore its effect was negligible in the overall analysis. This also reflects the operation of a blended braking system, in which regenerative braking power must be regulated according to the maximum capability of the battery to pulse charge, the maximum power generation capability of the motor at its operation speed, and the dynamic vehicle load shift under braking, to ensure vehicle stability under braking and prevent wheel lock-up. As vehicle deceleration increases, the axle load becomes increasingly biased toward the front axle. The relationship between the front-to-rear axle load ratio and the vehicle deceleration is shown in a generalised form in Figure 4.15. This dynamic variation is particularly important to note in the design of a P3 hybrid powertrain, as the safe energy recuperation limit for otherwise identically-specified systems

will vary depending on if the powertrain configured as FF or FR. The blended brake torque for a braking event from 100km/h to complete stop is shown in Figure 4.16. The blending strategy is not affected by axle load, but the torque magnitude varies as a function of axle load and the friction co-efficient between the tyre and the road.

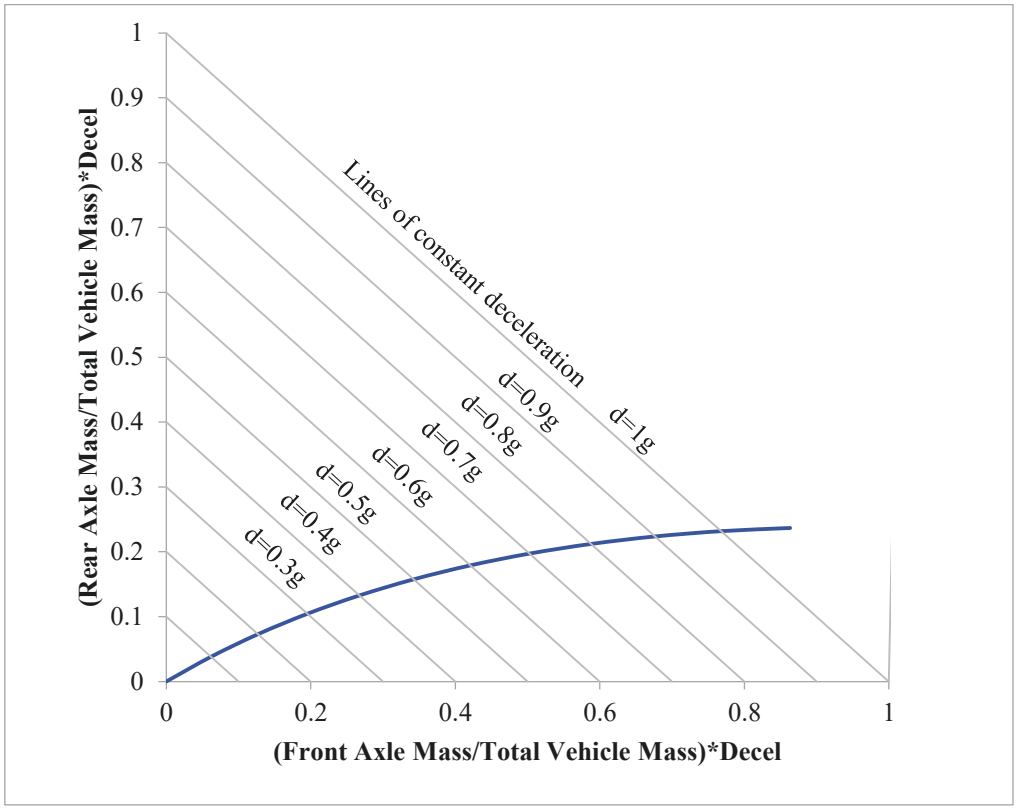

Figure 4.15 Generalized front/rear brake bias (Tawadros, Zhang & Boretti 2014)

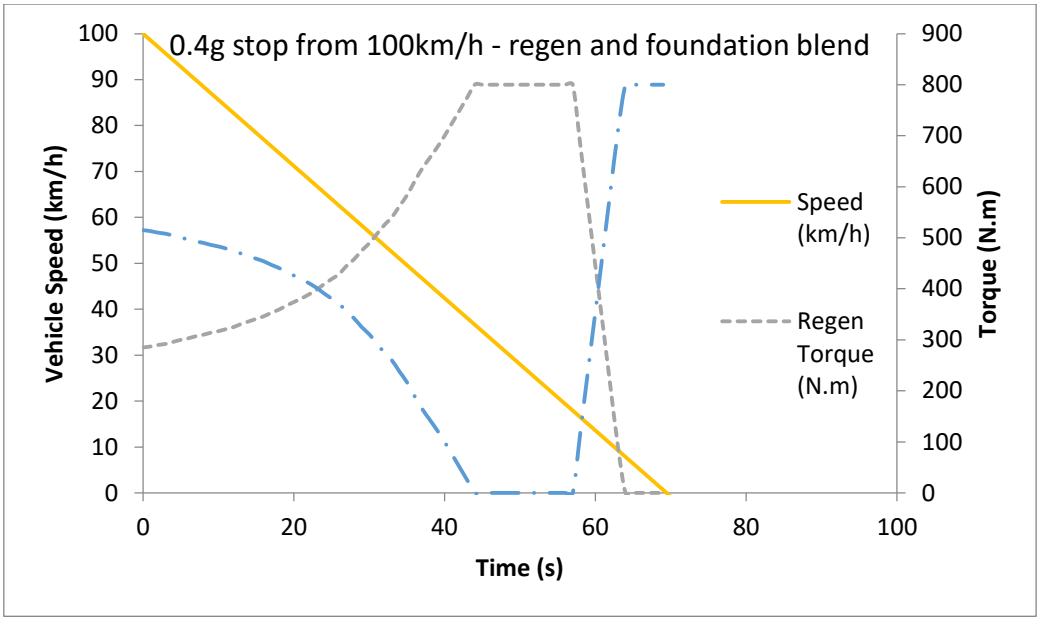

Figure 4.16 Brake blending strategy for hybrid vehicles, taking into account envelopes of motor operation (Tawadros, Zhang & Boretti 2014)

The regenerative braking energy recuperation for the entire cycle was calculated to be 0.26kWh. Regenerative braking was active for 194 seconds, and of this time, the braking power was less than 10kW for 160 seconds (Figure 4.17 & Figure 4.18).

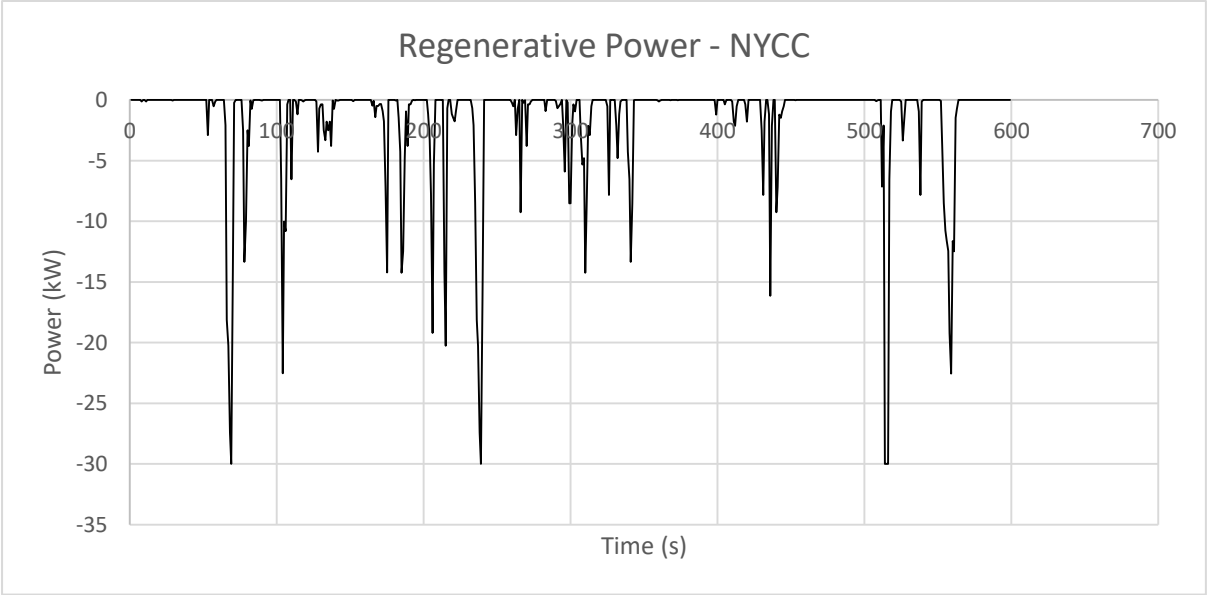

Figure 4.17 Regenerative braking profile on the NYCC

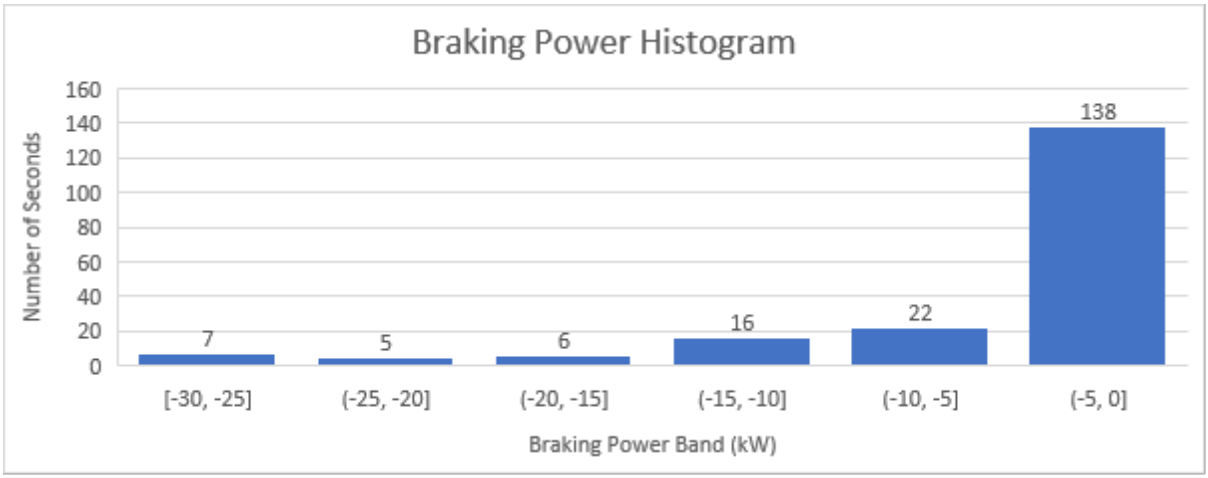

Figure 4.18 Brake power histogram using the NYCC (averaged over 1sec time unit)

Finally, total motor torque was computed by aggregating the power demands in all three modes evaluated operating modes and dividing by the prop shaft speed at each cycle time.

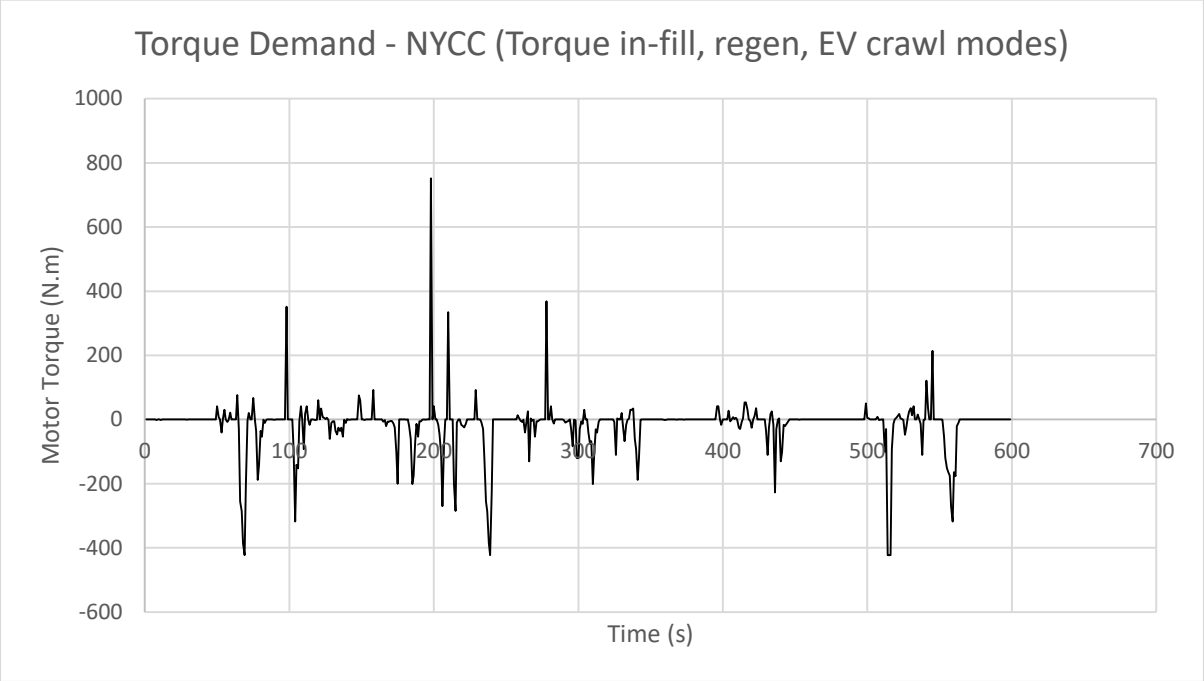

Figure 4.19 Total electric motor torque demand profile on the NYCC

The analysis of torque requirements suggests that 200N.m motor torque is sufficient to provide the majority of electric tractive force demand for the vehicle, and a peak figure of

300-400N.m would be sufficient for the torque in-fill demands. The outlier of 752N.m at 198s cycle time was disregarded for this purpose Figure 4.19.

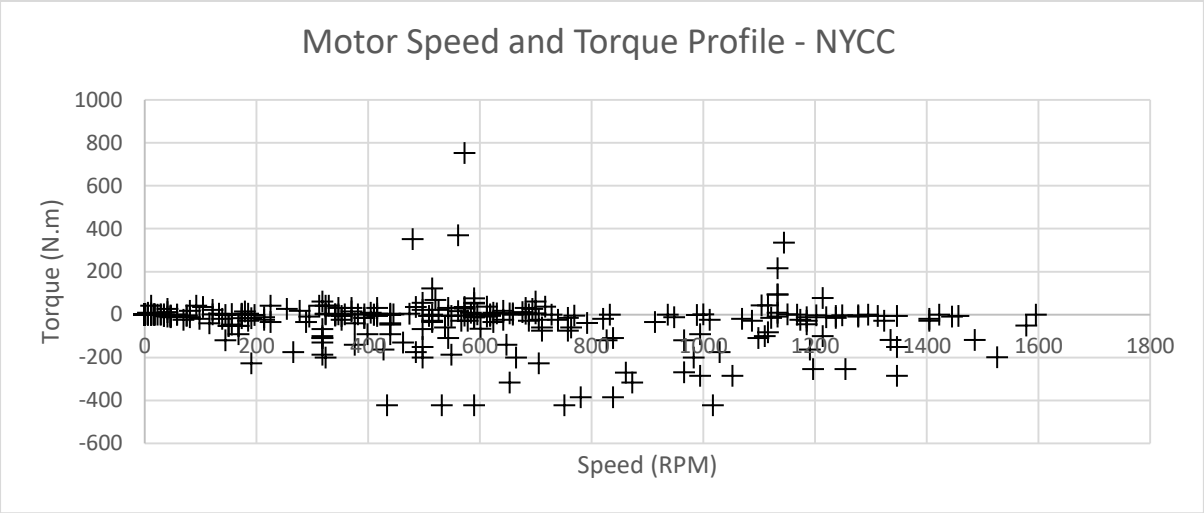

Figure 4.20 Electric motor load points on the NYCC

By plotting motor speed and torque (Figure 4.20) it can be seen that the motor's constant torque region should extend to approximately 1000-1100 RPM, therefore the base speed was set to the higher value.

Based on the piece-wise characterization of the motor, it was determined that the motor should meet the specifications listed in Table IX. These design quantities correlate well with other electric machine design requirements in automotive applications, which typically call for similar ratios of continuous to peak ratings, as well as high maximum speed to base speed ratio.

Motor Design Quantities	
Power – Continuous	10kW
Power – Peak	30kW
Torque - Continuous	200N.m
Torque – Peak	400N.m
Maximum Speed	7616 RPM
Base speed	~1100 RPM
Diameter - maximum	310mm

Table IX Motor design parameters

4.4.3 Electric Motor Selection

Selection of the electric motor relies on much more than just the design quantities listed above. There are many different types of electric motor construction, and the design quantities listed above may be met by a large subset of them. It is important to consider the type of motor and the advantages and disadvantages offered when making a selection. The most commonly used motors in an EV traction application are the permanent magnet synchronous motor (PMSM, also commonly called the BLDC, or brushless direct current), AC Induction motor (ACIM), and the switched reluctance motor (SRM) (Xue, Cheng & Cheung 2008). Older EVs employ a brushed DC motor, however these motors are no longer commonly used due to high electrical noise caused by the continuous movement of the commutator ring against the brushes, as well as increased maintenance needs caused by friction and arcing across the sliding surfaces.

The PMSM drive type is a high-efficiency, high power-density construction due to its permanent magnet construction, which eliminates the need to separately energise the magnetic field. This leads to higher efficiency than either a brushed DC or an ACIM unit. They also have an extended speed range compared to a brushed DC unit, because they do not require mechanical switching by brushes and commutator rings, and can operate in regen down to zero speed owing to the presence of the permanent magnets. The disadvantage of a

PMSM drive is that it is typically more expensive than an AC induction motor owing to the high cost of magnets required for the design. It is also difficult to build high-torque PMSM devices due to the brittle nature of magnetic material, which can, under cyclic stress, fatigue and crack. Another drawback is the limited ability to sustain field-weakening, due to the permanent magnetic field which can only be weakened by creating an opposed stator magnetic field. PMSM drives, as with all permanent magnet devices, are characterized by a non-zero cogging torque and exhibit mild torque ripple, which can be problematic in automotive applications, particularly at low speeds where it is felt as a pulsation in tractive force by vehicle occupants (Momen, Rahman & Son 2019).

Switched reluctance motors, by comparison to the PMSM, are simpler and more robust in operation. The power is delivered to the stator windings rather than the rotor and because of this they are considerably easier to cool, as it is the stator that requires cooling. This can be accomplished through case-mounted cooling hardware such as fins or a cooling jacket. The SRM is also a much more robust machine than PMSM, because its rotor is quite simple, being a non-wound multi-pole ferrous shaft, with positional encoding for control. Its operational characteristics (wide constant power region, low base speed, fault-tolerant controllability) make it ideal for deployment in automotive powertrains. The principal drawbacks of the SRM design are high inherent cogging torque and acoustic noise emissions. Research into eliminating these drawbacks is still ongoing. (Zhang et al. 2011) has proposed the inclusion of permanent magnetic material within the stator as a method of minimising ripple. Other methods (Ding, Liu & Li 2019; Gengaraj et al. 2018; Sadat, Ahmadian & Vosoughi 2018, *inter alia*) utilise various distortions of the control signal to smooth the ripple. It has been reported that the recently released Tesla Model 3 utilises a permanent magnet SRM (PMSRM) as its rear traction drive. Whilst the SRM motor is well-suited to implementation in the powertrain, it was not possible to find an SRM motor or controller to

meet the design requirements as an off-the shelf item. Custom solutions based on SRM technology were significantly outside the project budget.

The AC Induction motor, whilst not as efficient as the PMSM or the SRM, and not as simple as the SRM, offers many advantages. It is relatively simple in construction, requiring a series of windings around the stator, and utilising a solid rotor consisting of an electrical path (usually aluminium) and a magnetic path (a ferrous squirrel cage). It also exhibits low torque ripple and no cogging torque due to the absence of permanent magnets in its construction. The control of AC induction motors is somewhat more complex than that of DC or SRM motors. The well-established control method of Field orientation control (FOC), otherwise known as vector control is used to accomplish torque control, and speed control is via variable frequency drive (VFD). FOC relies on a high-resolution position signal for control of the motor. The position signal is used to compute motor slip frequency and is an input to the transformation of the 3 phase currents from the stator frame of reference to the rotor frame of reference. This allows the reduction of the three-phase input to two orthogonal components, which control the magnetic flux and the torque. This same method is also used for the control of PMSM machines.

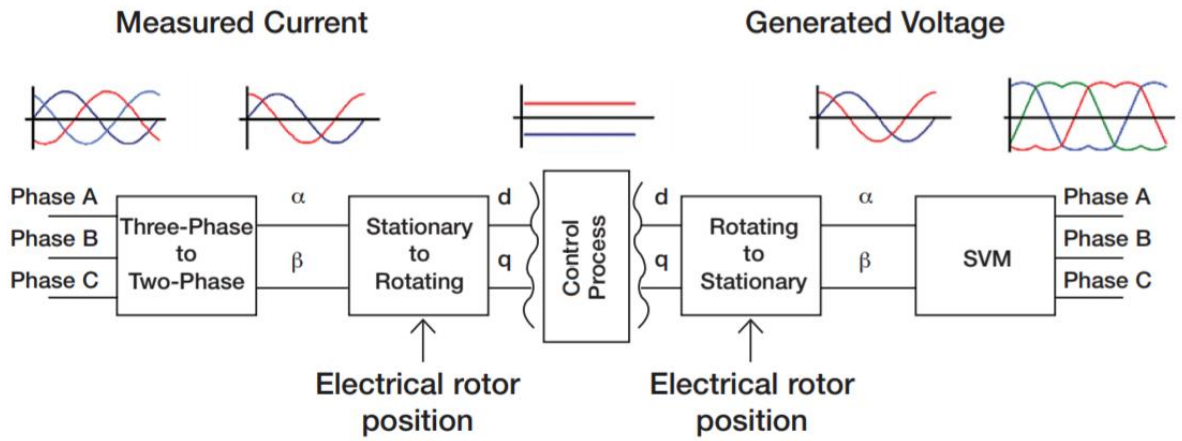

Figure 4.21 The operating principle of Field-oriented control (Freescale Semiconductor 2014)

Due to the PMSM's always-on (permanent) magnetic field, control of a PMSM for an on-axis P3 hybrid powertrain where the motor is permanently coupled is inherently less efficient than that of an ACIM. This is because of the need to actively control the magnetic field rotation speed with the rotor rotation speed at all times. Failure to do this causes the rotor to experience rapidly alternating positive and negative torque due to permanent magnet construction. This results in excessive mechanical vibration, noise, and wear. Conversely, even if the PMSM in an on-axis permanently coupled application is not required to produce torque, such as if the vehicle is cruising at an efficient operating point, the magnetic field must always still be controlled, requiring energy input to control the machine at zero torque. This disadvantage is not present in ACIM drives. For this reason, the only practical solution for the prototype vehicle was the selection of an AC induction motor.

Motor Design Quantities	
Power – Continuous	10kW
Power – Peak	30kW
Torque - Continuous	200N.m
Torque – Peak	400N.m
Maximum Speed	7616 RPM
Base speed	~1100 RPM
Diameter - maximum	310mm
Construction	AC Induction
Shaft	Double-ended

Table X Updated motor parameters

It should be noted that were the motor to be mechanically engaged and disengaged as required by way of a clutch, the PMSM drive would have likely represented a better choice. The efficiency of the PMSM drive is preferable, and in a clutched arrangement the cogging torque is insignificant unless starting from zero speed. In the clutchless topology as proposed, the SRM drive would also be preferable to the ACIM were there suitable commercial solutions available.

A review of the literature found several HEV and EV research activities using AC induction motors from a US-based company, Hi Performance Electric Vehicle Systems (HPEVS) (Akritidis 2015; López et al. 2018; Wu & Zhang 2015; Wu, Partridge & Bucknall 2018) . A range of other motor manufacturers were contacted, including Siemens, ABB & others, however no suitable solution could be offered within specification and budget. HPEVS has a wide range of ACIM drives available and specialises in motors for use in electric vehicles. When provided with the design quantities, the company proposed a HPEVS AC-9 drive. The motor meets many of the design quantities specified. Its specifications are listed in Table XI and the efficiency curve is provided in Figure 4.22.

HPEVS AC-9	
Power – Continuous	16.5kW
Power – Peak	44.58kW
Torque - Continuous	17N.m
Torque – Peak	94.6N.m
Maximum Speed	9000 RPM
Base speed	4600 RPM
Diameter	182mm (+42mm terminal block)
Construction	AC Induction
Shaft	Double-ended

Table XI Motor parameters - HPEVS AC-9

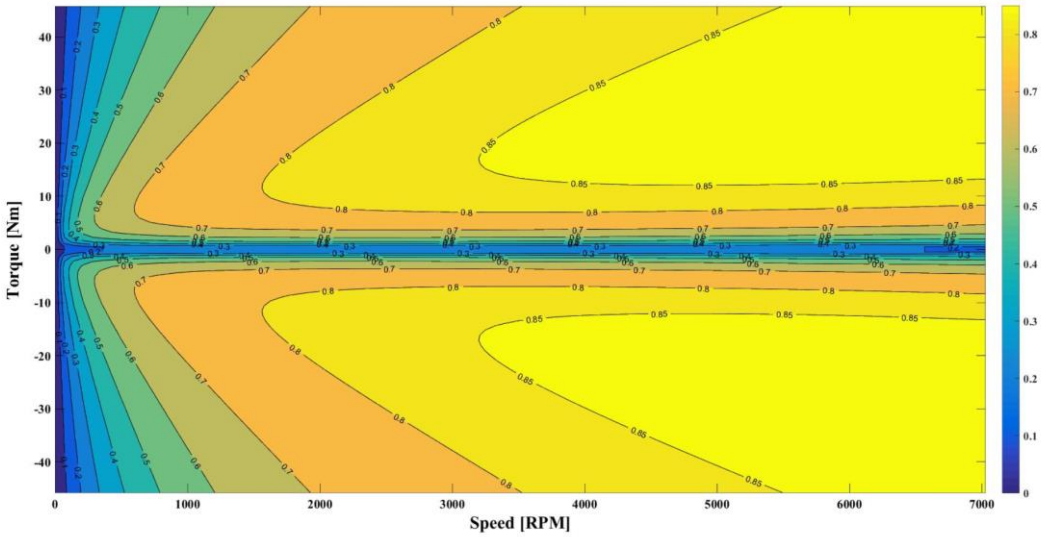

Figure 4.22 HPEVS AC-9 motor efficiency map (Akritidis 2015)

The motor continuous torque rating was noted to be substantially lower than design quantity, however the test method for obtaining the continuous rating required the continuous operation of the motor at the rated load for five minutes. This was considered to be substantially higher than required in the MHEV powertrain application, and therefore the peak rating was considered to be of higher importance. Whilst the peak rating was also substantially lower than desired, it was nevertheless sufficient to meet the torque requirement for 220 out of the 275 total seconds for which the electric motor is active in the NYCC cycle. The remainder of the time the motor could be used to meet the needs partially. An analysis of the AC-9's expected performance on the NYCC cycle is shown in Figure 4.23.

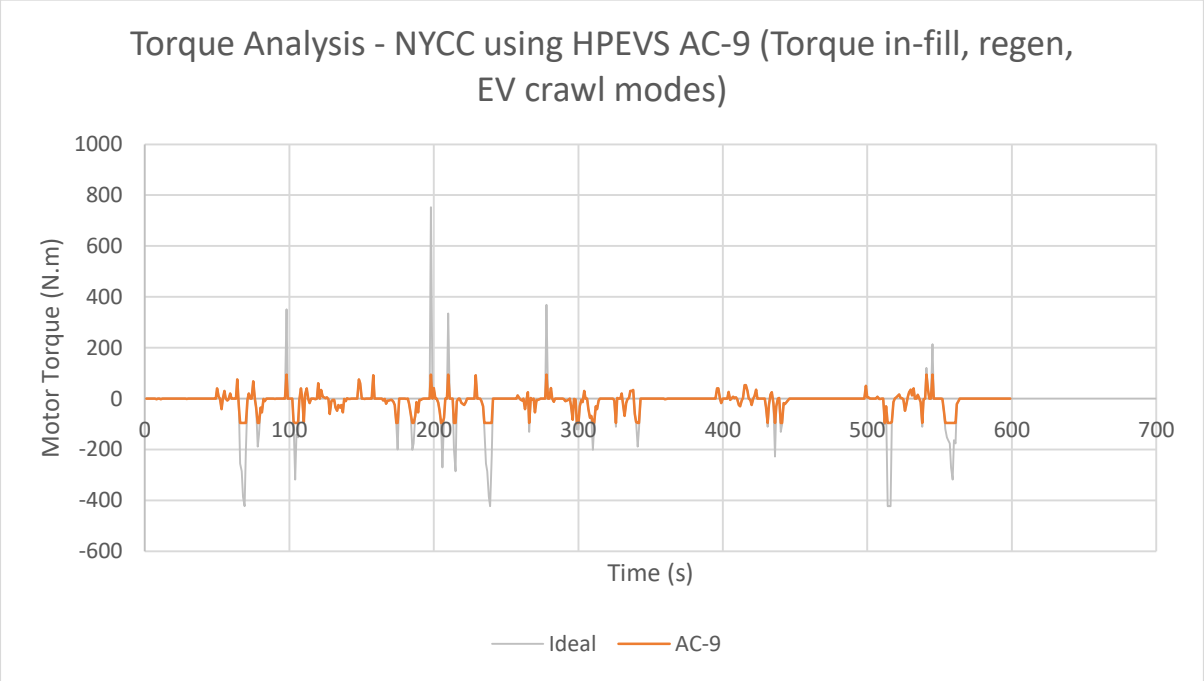

Figure 4.23 Torque performance analysis of the HPEVS AC-9 in the NYCC cycle using MX-5 parameters

There are five drive events and nineteen regen events for which the AC-9 cannot supply sufficient torque to satisfy total vehicle demand. However, because the motor is largely able to satisfy the drive torque requirements of the vehicle, the vehicle will exhibit acceptable performance. The torque analysis in Figure 4.23 reflects the total drive (or braking) torque

required by the vehicle, rather than just the torque on the driven axle. It also does not account for brake bias required to maintain vehicle stability. The rear-axle coupling of the motor restricts the practical regeneration that can be achieved, due to the need to bias braking toward the front axle. Therefore, the motor will satisfy the needs of the prototype vehicle.

4.4.4 Motor Controller

A market survey found three models of AC induction motor controller that would be compatible with the AC-9 induction motor. These controllers are:

- Kelly KAC96601-8080i
- Curtis Instruments 1238e-7621
- Tritium WaveSculptor200

The Curtis controller was recommended for purchase with the AC-9 induction motor, and can be supplied pre-configured to operate the AC-9 motor as a “drive kit”. The other two models are standalone controllers and would need to be configured on delivery. A comparison of the three controllers was conducted, which is presented in summary in Table XII.

Motor Controller Comparison							
Model	Operating Voltage (DC)	Continuous Current (A)	Peak Current (A)	Maximum Switching Frequency (Hz)	Cooling	Cost	Communication
KAC96601-8080i	72-144	240	600 (1 min)	250	Air	AUD$1200	CAN bus/RS232
1238e-7621	24-96	200	650 (2 min)	300	Air/Liquid	AUD$3100	CAN bus & Analog I/O
WaveSculptor200	0-400	N/S	300	N/S	Liquid	AUD$6600	CAN bus only

Table XII Comparison of the commercially available motor controllers

The Wavesculptor200 is clearly designed for higher DC voltage applications than are required herein, evidenced by the high operating voltage but relatively low peak current of only half that of the other two options. This is also reflected in the high cost of the Wavesculptor200, which is over double that of the next most expensive choice. The Kelly controller cannot reach the full 650A peak current at which the AC-9 reaches its peak ratings. This is not necessarily problematic given the ability of the traction battery to safely discharge is also unlikely to match the maximum motor current draw. However, the lack of a liquid cooling option suggests that the controller is not designed sustained high current switching. The documentation available for the Kelly controller (Kelly Controls 2017) was also less comprehensive than that available for the Curtis, and the interconnections available on the Curtis were far superior, with a single 35-pin AMPSEAL bulkhead connector providing all I/O. The connector is environmentally sealed and designed for automotive and off-road use. In contrast, the Kelly controller is provided with four molex connectors serving all I/O functions on wiring harnesses protruding from the case. The Kelly controller is not IP-rated, whereas the Curtis is rated IP65. This, along with the lack of a liquid cooling capability, suggested that the Kelly controller was not as robust in construction as the Curtis. For these reasons, the Curtis 1238e-7621 was selected as the most appropriate motor controller.

4.4.5 Traction Battery Sizing

Traction battery sizing is determined by both energy demands, that is, the total electrical energy requirement of the vehicle over a given timeframe, as well as power demands, which are the instantaneous charge or discharge needs for a given event. There are a range of design objectives that must be optimised. Power capacity and energy storage capacity are the primary objectives, but consideration must also be made for pack weight and volume, pack voltage, which determines the number of individual cells in series, the pack charge/discharge

rate, which determines the number of parallel strings within the pack, thermal considerations, and energy conversion efficiency.

Because the primary objective of this work is the experimental exploration of the use of powertrain electrification for enhancing torque delivery and operational characteristics of the vehicle, a complete traction battery optimization process has not been completed. Rather, some basic analysis is conducted and described in this section, following a variation on the methodology described by (Sharer et al. 2006). The methodology is modified due to the removal of the need to estimate an all-electric range (AER) for KERMIT IV, as the design intent is a mild hybrid vehicle with no significant AER. Additionally, thermal effects are not considered. Coulombic efficiency and motor efficiency are simplified to an average value derived from the respective maps, rather than being taken at each instantaneous operating point. Further optimization of the battery size would yield a lower cost-to-manufacture (CTM).

The battery charge, discharge, and energy storage requirements are derived by continuing the analysis of the MHEV on the NYCC. The inclusion of engine load levelling events in the analysis allows the accurate estimation of energy storage requirements, which can then be added to the charge and discharge power as design quantities.

To begin the analysis of the engine load levelling needs, it is first necessary to define a simple load-levelling strategy. Because of the on-axis coupling of the electric motor to the petrol engine in the P3 hybrid, the load-levelling strategy is reduced to a simple two-variable (4-DOF) model, based on engine brake mean effective pressure (BMEP) and electric motor torque (Figure 4.24). The fixed inputs to the model are driver requested torque and battery SOC. Battery SOC is used as a state input; if the SOC is within the acceptable range then engine load levelling will function, and if not, then there will be no load-levelling available.

However, for the purpose of the initial design study, the battery SOC is considered to be acceptable all the time.

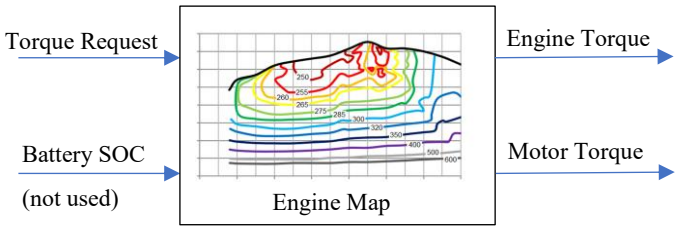

Figure 4.24 Load levelling strategy

Engine load-levelling for the on-axis hybrid configuration is accomplished using a vertical lookup which is based on the current torque request, and a horizontal lookup which is based on the measured change in engine speed Figure 4.25. The vertical lookup determines if an optimized load-site is available at the current engine speed. If no optimized site is available, the horizontal lookup determines if an optimized load site will be available if the engine load vector is altered within the parameter determined by the current torque request.

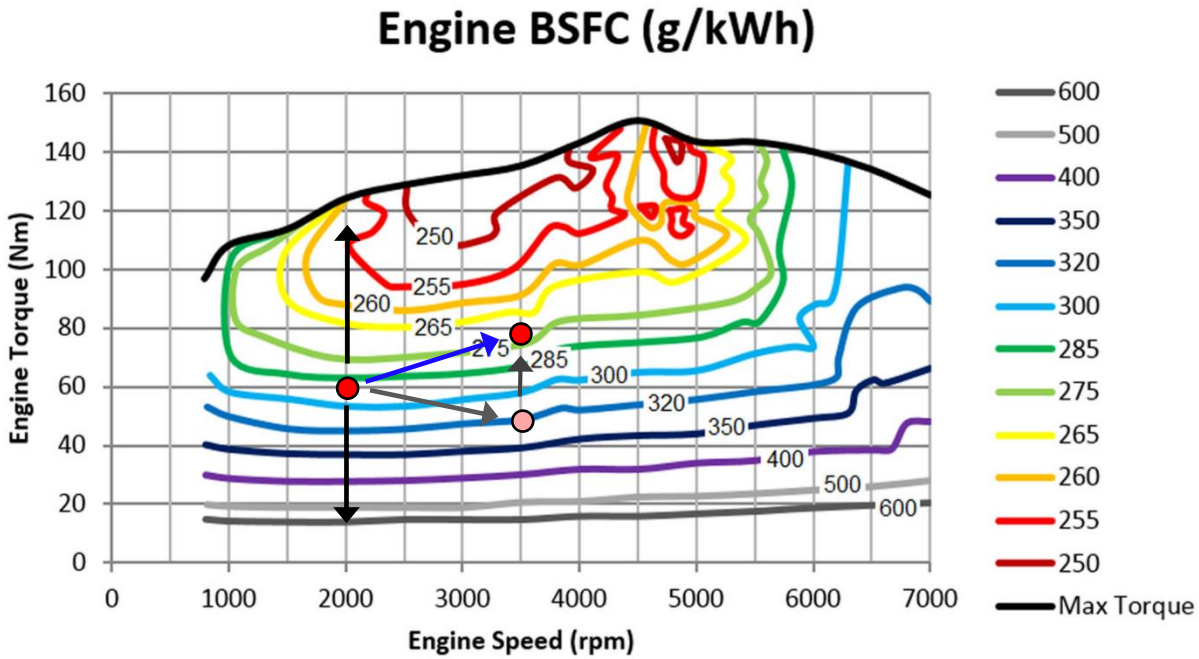

Figure 4.25 Engine load levelling with on-axis permanently coupled motor is constrained by the road speed, which constrains engine speed when a gear is selected. The vertical and horizontal lookup strategy is shown

The load-levelling electrical energy demands are added to the loads determined from the EV crawl, torque in-fill, and regenerative braking analysis conducted in 0, allowing accurate estimation of the battery requirements.

1. Energy and Power

The instantaneous power demand from the electric powertrain is calculated and shown in Figure 4.26. By integrating the power demand, the total energy storage need for the vehicle can be calculated.

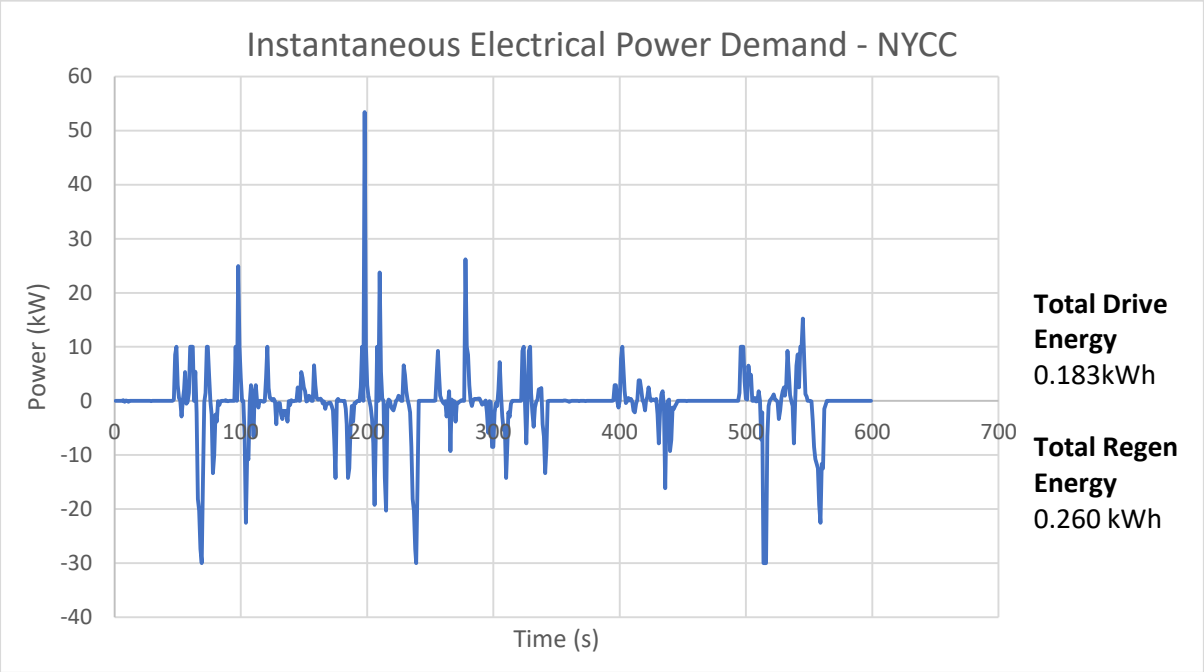

Figure 4.26 Instantaneous electrical power required by the prototype in the NYCC

The electrical drive energy used by the vehicle over the entire cycle is 0.183 kWh, and the vehicle regenerates up to 0.260 kWh. The difference between the charge input energy and discharge output energy is related to the change in state of charge (ΔSOC) of the battery. For battery cell life, the SOC minimum is set to 30% and the maximum is set to 80% (Nitta et al. 2015; Pesaran 2001). This gives a useable capacity of 50% of the total energy stored in the battery for electric propulsion. Because of the short duration of the NYCC cycle (only 598 s),

for battery capacity calculations it is prudent to consider a longer cycle duration. Therefore, trebling the cycle allows the consideration of the equivalent of 30 minutes of driving. By trebling the cycle, the difference between battery input and output energy is also trebled. The equations 4.4 to 4.4 describe the calculation of total battery energy storage capacity:

$$E_{max} - E_{min} = \Delta SOC(E_{total}) \quad (4.2)$$

$$3(0.260 - 0.183) = 0.5(E_{total}) \quad (4.3)$$

$$E_{total} = 0.462 \text{ kWh} \quad (4.4)$$

Based on the analysis, the battery energy storage capacity should be at least 0.462kWh.

2. Current and Voltage

The battery current demand, shown in Figure 4.27was calculated using a 96V battery. The motor and controller combination that was previously selected necessitates a 96V battery as a practical minimum. The maximum DC voltage that can be supplied to the controller is 144V, which would reduce battery discharge current, improving cycle life but also increasing cost-to-manufacture.

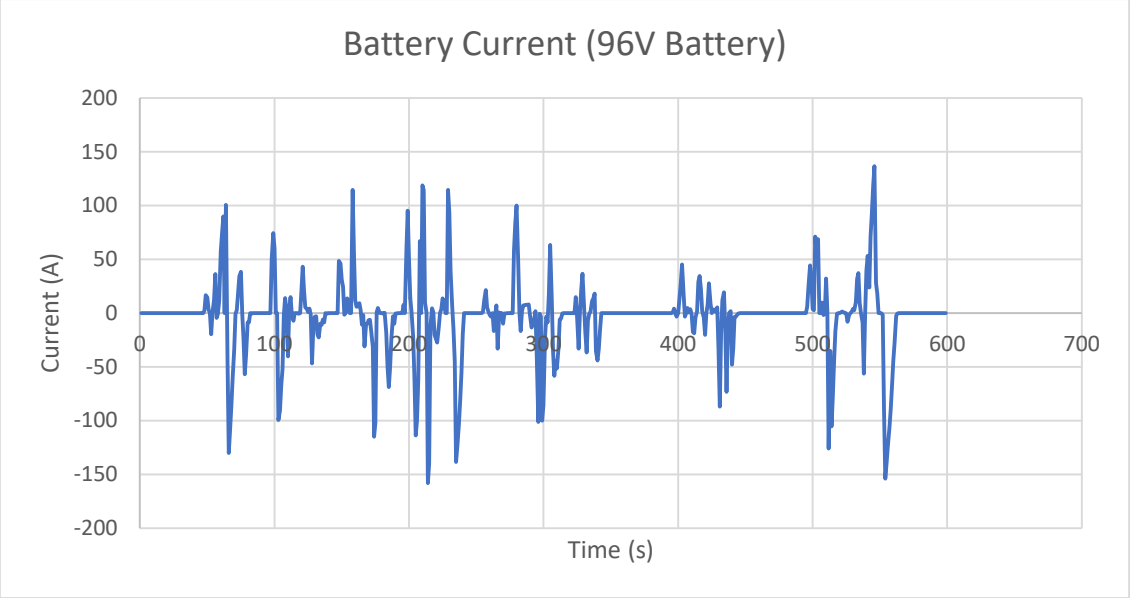

Figure 4.27 Simulated battery current on the NYCC

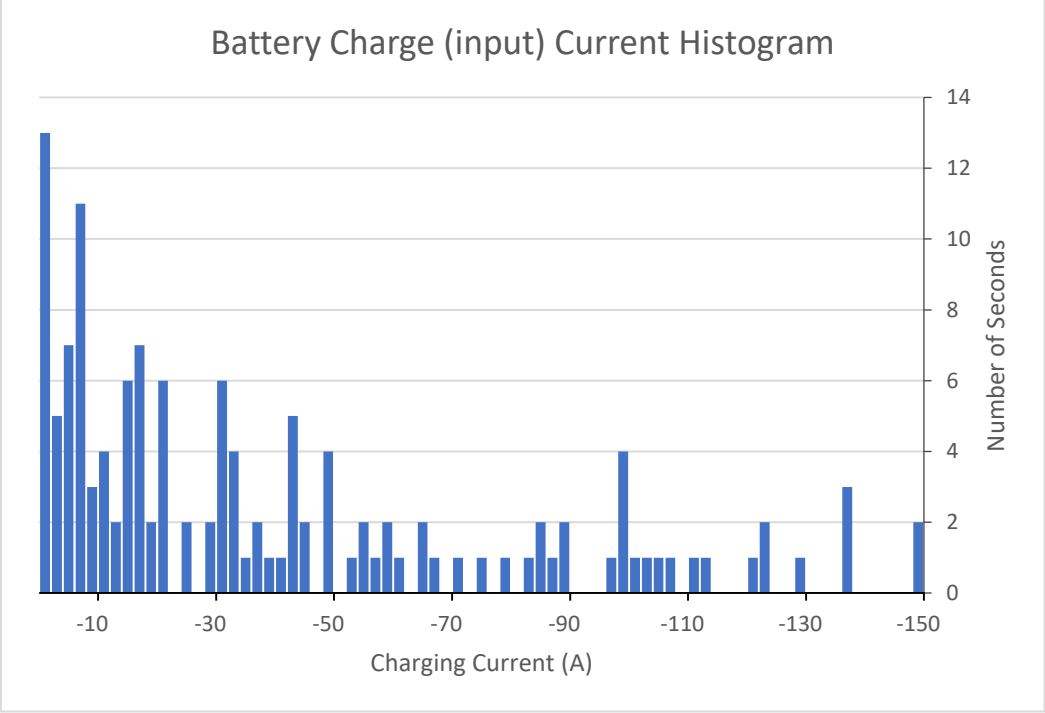

Figure 4.28 Charge current histogram on the NYCC

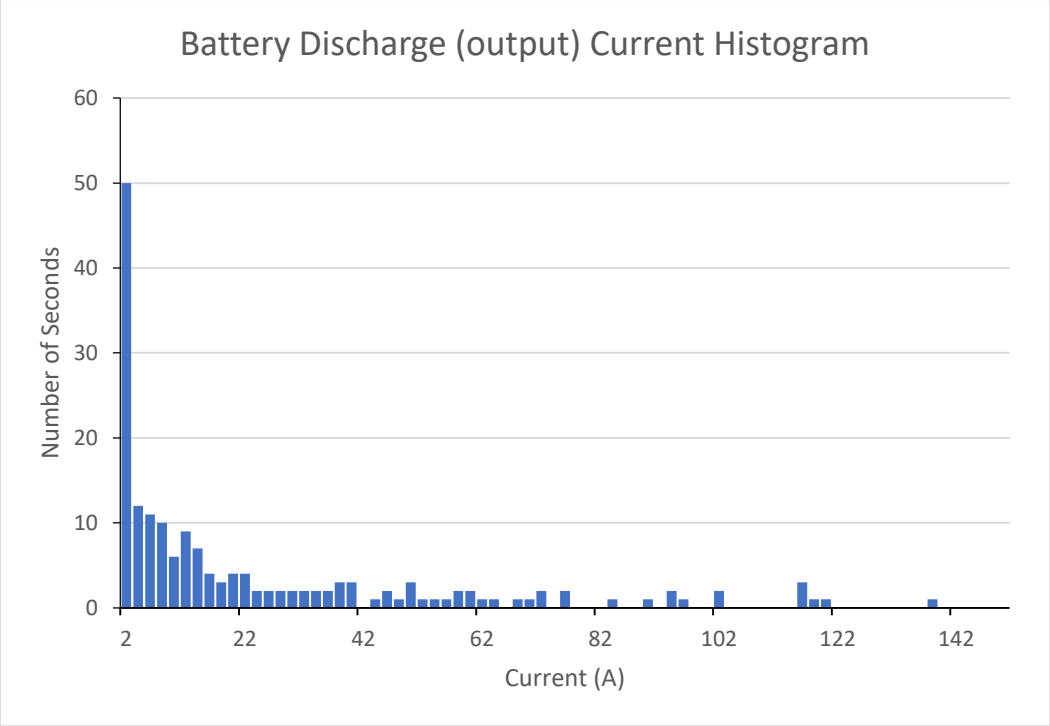

Figure 4.29 Discharge current histogram on the NYCC

The charge current histogram (Figure 4.28) shows that most of the charging events occur at less than 100 A, with a maximum of 158 A being held for two events of one second each. The discharge current histogram (Figure 4.29) shows most of the discharge events occur at less than 42 A, with the maximum discharge current of 138 A being held for one second throughout the entire cycle. These values are not unreasonable, and it must be noted again that the brake biasing of the vehicle will constrain regenerative braking current further than is calculated using the analysis conducted herein, due to the rear-drive powertrain layout.

For a 96 V, 0.462 kWh battery, the typical discharge current of 42 A represents a discharge rate of 8.72C. The maximum discharge rate of 138 A represents 28.68C. Conversely, the typical and maximum charge currents equate to charge rates of 20.78C and 32.83C, respectively. These rates are too high for safe operation, and necessitate the use of a larger traction battery pack. The pack must therefore be sized based on the maximum terminal power required, rather than the cycle energy storage requirement.

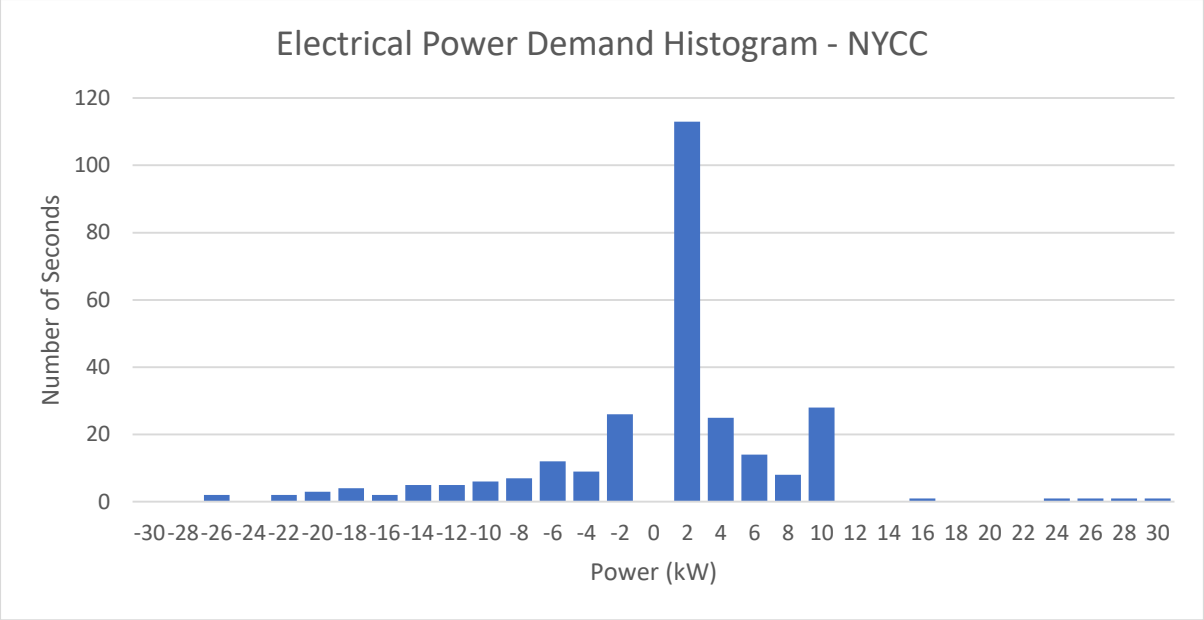

Figure 4.30 Electrical power histogram on the NYCC

The electrical power demand (Figure 4.30) for the cycle shows the majority of discharge events occur at less than 10kW, and most charge events occur at less than 14kW, with maximum pulses of 30kW in discharge and 26kW in charge.

Traction Battery Characteristics	
Energy Storage Capacity	Larger than 0.462kWh
Voltage	96V or higher (max 144V)
Discharge (continuous/pulse)	10kW/30kW
Charge (continuous/pulse)	14kW/26kW

Table XIII Calculated traction battery requirements

To appropriately size the traction battery pack, a particular cell must first be selected, and the pack must be sized to ensure the cell charge and discharge ratings (C ratio) are not exceeded based on the analysis conducted thus far.

4.4.6 Battery Component Selection

The traction battery serves as the secondary energy accumulator for the vehicle. A hybrid vehicle requires a primary and a secondary energy accumulator, and in hybrid electric

vehicles the second accumulator is usually the battery pack (although some are built with supercapacitors). Other forms of secondary accumulator include hydraulic accumulators, or high-speed flywheels. To be effective, the accumulator must be energy dense, so that it does not occupy significant volume and weight. It must also be power dense, so that it meets the energy flow needs of the connected apparatus. It is required to withstand repeated charge-discharge cycles without significant degradation, and it must be safe and intrinsically efficient.

Commonly, EV and HEV battery packs are composed of nickel metal hydride (NiMH) battery cells or a variant of lithium-ion (Li-ion) battery technology. Most modern HEVs, with the exception of Toyota Prius, utilise Li-ion batteries owing to their higher energy and power density (Figure 4.31). There are a wide range of lithium-ion batteries available, each offering unique specific energy, specific power, and charge/discharge characteristics (Figure 4.32). Lithium chemistry was chosen for this application due to the large variations in current draw required by the vehicle, the power density of lithium cells, as well as their relatively common availability and reasonable cost.

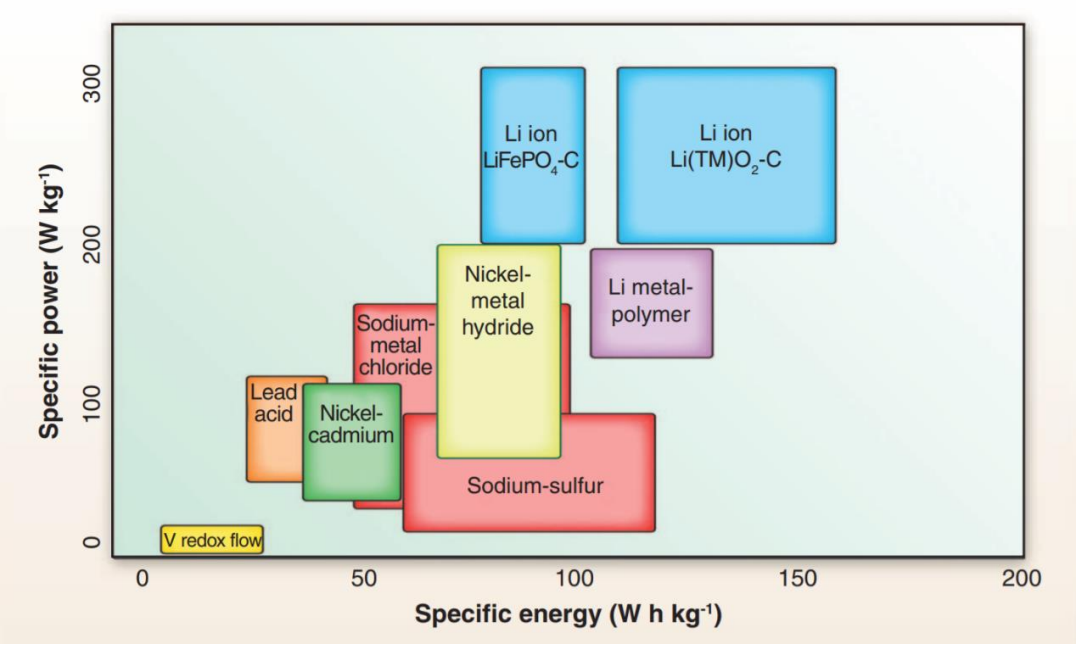

Figure 4.31 Energy and power density of various battery chemistries (Dunn, Kamath & Tarascon 2011)

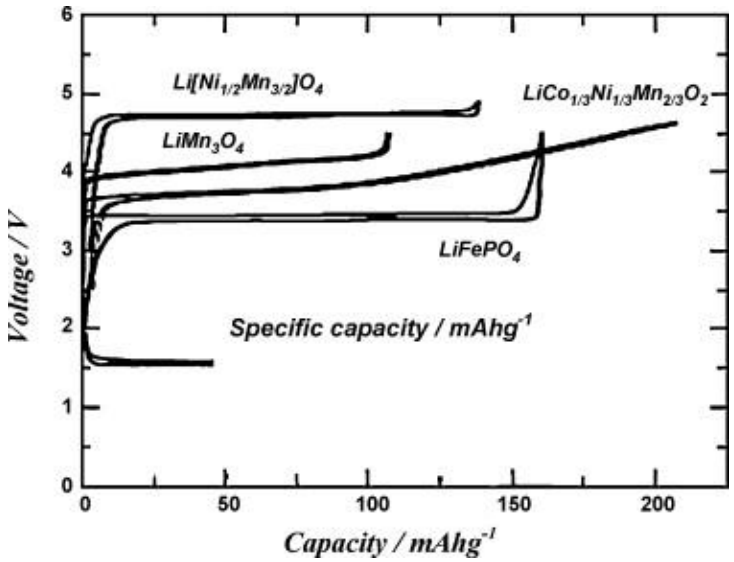

Figure 4.32 Lithium Ion chemistries - charge/discharge curves (Scrosati & Garche 2010)

To fulfil the power needs of the prototype vehicle, it is necessary to achieve an acceptable balance between pack capacity and discharge rate. By increasing the pack storage capacity the total current draw (expressed in terms of the C-ratio) can be reduced to acceptable limits. This minimises thermal effects and maximises cycle life. Conversely, increasing pack storage

increases the manufacturing cost and vehicle weight. Additional energy storage above the determined system requirement can also be detrimental to efficiency, as the energy required to accelerate and decelerate the increased mass is not offset by any further improvement in the fuel efficiency of the vehicle.

Based on the power needs specified above, a range of commercially available cells were considered for use. All commercially available cells considered were lithium iron phosphate cells, varying in geometry (prismatic, pouch, and cylindrical), and capacity (from 8 to 40 Ah). The specifications of the cells (Table XIV) were used to arrive at a range of resultant pack configurations that could be considered for implementation in the vehicle.

Model Designation	Cell Volts (V)	Cell Amp-hours (Ah)	Chemistry	Charge cont./peak (C) Charge Power (kW)	Discharge cont./peak (C) Discharge Power (kW)	Pack Configuration	Pack Capacity (kWh)	Pack weight (kg)
Winston WB-LP12V40AH	12 (4S1P case)	40	LiFePO4	0.5C/3C 1.9/11.5kW	3C/10C 11.5/38.4kW	8S1P	3.84	66.4
				1C/6C 3.8/23kW	6C/20C 23/76.8kW	8S2P	7.68	132.8
A123 48V 8Ah Ultraphosphate	48 (14S1P case)	8	LiFePO4	23C/41C 17.6/31.5kW	19C/40C 14.6/30.7kW	2S1P	0.768	15.8
Headway 40152s	3.2	15	LiFePO4	1C/3C 1.4/4.3kW	5C/10C 7.2/14.4kW	30S1P	1.44	14.4
				3C/9C 4.2/12.9kW	15C/30C 21.6/43.2kW	30S3P	4.32	43.2
GWL ZG-LFP020AH	3.2	20	LiFePO4	0.5C/1C .96/1.92kW	3C/10C 5.7/19.2kW	30S1P	1.92	19.5
				1.5C/3C 2.88/5.76kW	9C/30C 17.1/57.6kW	30S3P	5.76	58.5

Table XIV Battery characteristics - commercially available cells

Of note is a large difference in charge and discharge power between the A123 cells and all others. This is, in large part, due to the method of calculation of the cell power. Whilst all other manufacturers quote continuous power as a true continuous figure (with no time limit imposed), the A123 continuous figure is based on a 60 second current draw at the beginning of life (BOL) of the cell (i.e., when the cell has never previously been cycled). Likewise, the

peak cell power values for the A123 cells are quoted for 10 second current draw at BOL (A123 Systems 2016). All other cells are quoted based on a 30 second peak pulse. The reason for this deviation is that the A123 cell is specifically designed and tested for automotive hybridization applications. The Winston cell, by comparison, is designed as a sealed lead-acid battery replacement (hence the 12V configuration), whereas the Headway and GWL cells are both general purpose cells. Notwithstanding the differences in measurement technique, the A123 cells appeared to be the most compatible with the design quantity. Unfortunately, when contacted the company would not supply the battery module as it is only supplied to OEMs. This limited the choice of battery cells to the Winston, Headway, and GWL units. Out of these three options, the Headway cells were chosen due to superior charge characteristics compared to the GWL cells and superior energy density compared to the Winston cells. It was also anticipated that the cells could also be safely "over-driven" beyond their specified power characteristics for short periods without significant degradation.

4.4.7 Battery Management System

The Battery Management System (BMS) is a battery controller which is required for lithium battery packs of more than two cells. The BMS actively monitors individual cell voltage, resistance, and temperature, as well as these same characteristics at the pack level, in addition to pack current. It can be used to create battery profiles which use the monitored values as inputs to determine the safe charge or discharge limits for the pack. It also ensures individual cells are balanced with each other to limit parasitic draw resulting from weak cells and provides notification if weak cells are identified. The Ewert Systems Orion2 BMS was selected due to its high level of native interoperability with the Curtis 1238E motor controller. The two units are pre-configured to operate on the same CANOpen protocol, allowing the simple setup of a two-wire CAN bus between the two components to provide

complete system controllability through the included software utilities, without the need for text-based programming.

4.4.8 Supervisory Controller

The supervisory controller selected was the dSpace MicroAutoBoxII 1401. This controller is a complete rapid control prototyping platform and was available at UTS at no cost to the project. The MicroAutoBox II supports the complete model-based design process through integration with Matlab/Simulink, allowing the development of a plant model and control algorithms in software, and then using automatic code generation to upload the model to the controller. The controller can then be simply deployed for bench testing using HIL, or as a complete system controller in the prototype vehicle for system verification. Whilst the controller can work as a standalone unit, it requires a host PC connection to enable multiple functions, such as real-time data collection, software switching of operation functions (that are not wired to physical inputs), simulation start and stop, and data post-processing.

4.5 Summary

The initial design and benchmarking of the hybrid vehicle required the initial selection of a base vehicle, used as the platform for the assembly of the hybrid powertrain, the characteristics of which were well-understood. In order to make an appropriate base vehicle selection, the primary design constraints were used to define a set of base vehicle specifications. The specifications were then input into a vehicle search to select a range of vehicles that met the design criteria. By evaluating the vehicles against the design criteria, a base vehicle model, the NA Mazda MX-5 cabriolet, was selected. This selection allowed detailed specifications to be input into a backward-looking mathematical model of the vehicle. The major electric powertrain components (namely, the battery and motor), were added to the model in order to calculate their physical characteristics by evaluation of their function within the model. The New York City Dynamometer Drive Cycle (NYCC) was used

as the primary input. The NYCC was chosen due to its low-speed, high acceleration, and high stop ratio, which is characteristic of densely populated urban areas. A piecewise evaluation of the MHEV's operation under the NYCC was undertaken, by evaluating each mode of operation separately. The time-domain summation of the piecewise output gave energy storage requirements of 0.462kWh, or 0.154kWh per cycle repetition. Evaluation of the cycle power demands showed an electric motor with a continuous power output of 10kW and peak pulse output of 30kW would also satisfy the demands, based on the model output.

After the determination of key electric powertrain component characteristics, selection of the major physical components of the prototype was undertaken. The components required for procurement include the electric motor, motor controller, traction battery, battery management system, and supervisory controller. A range of ancillary items, such as contactors, fuses, relays, and isolators, are also required. These ancillary items were not selected at this stage.

The selection of the physical prototype components was not just constrained by the outcome of the model analysis, but also external factors such as part availability and cost. Therefore, in some cases a component was identified that would very closely match the desired characteristics, but due to unavailability or cost, a poorer match that could meet most needs was selected. Nevertheless, the components selected are deemed sufficiently capable for the development and assembly of the prototype, as well as validation and proof-of-concept.

Chapter 5: Simulation and Modelling

This chapter presents the simulation of the Electric Propulsion System (EPS) which forms the electric side of the powertrain installed in KERMIT IV. The simulation process follows the well-established model-based design (MBD) principles, which are commonly being utilized to develop complex hybrid powertrains for which an optimized solution is not immediately apparent using traditional methods (Mahapatra et al. 2008) The MBD process follows on from the initial design methodology described in Chapter 4, and also in (Awadallah, Tawadros, Walker & Zhang 2017b). and uses the outputs of the initial analysis as inputs into the software model developed in the MATLAB/Simulink environment. The initial analysis process described in Chapter 4 is an example of what is typically described as backward-facing modelling, where the desired system output is used to calculate the required system inputs. In this case, the system output was a series of vehicle specifications based on the assumption that the vehicle would exactly follow the New York City drive cycle (NYCC). The inputs required to be calculated were engine and motor characteristics, such as power and torque, as well as battery energy storage. The nature of backward-facing modelling is that it is time-independent, in that each model timestep can be solved without any real time constraint. The backward-facing model also assumes that the plant will meet the desired system output exactly. The backward-facing modelling has been described in detail in Chapter 3 and the reader is directed to that chapter for any further details.

Once calculated, the system parameters are fed into a forward-looking model, which is a time-dependent model that is provided with system parameters as an input, and a target output. The forward-facing model then controls the system within its constraints to achieve the desired target output. Typically, forward-facing models are not furnished with “future” target data unless there is some real way to obtain this data during operation of the physical plant. Rather, an instantaneous target output is provided to the model driver which then

adjusts the plant operation to meet that output as closely as possible within the time parameter given. In this sense, a forward-looking model is time-dependent but is not necessarily required to run in real-time. In contrast to a backward-facing model, the output of the forward-looking model does not exactly match the target output, but is a representation of how the plant behaves in reality.

There are many ways to verify the model output. If time and money are not significant limitations the model can often be validated simply by building the physical plant and proceeding directly to testing. However, depending on the fidelity of the plant model and the simulation environment, there can often be significant divergence between model behavior and physical plant behavior. To address this, Hardware-in-the-loop (HIL) simulation has been developed. HIL can be a more cost- and time-effective means of system verification than proceeding directly to prototype. It is a real-time process, which requires specific real-time implementation techniques to process the model, interface with the physical hardware and manage power requirements. The HIL method offers significant advantages, in that subsections of physical plant can be bench-tested, physical or virtual representations of the physical plant can be used in place of valuable final hardware (for instance, an electric motor can be used to simulate an engine, or two opposed motors can be used to simulate a vehicle and road loads). By studying the real time output, verification can be achieved relatively simply, cheaply, quickly, and safely. HIL is therefore an intermediary step between software modelling and physical prototyping.

This chapter will present the software modelling and HIL verification processes that were used in the development of the KERMIT IV prototype hybrid vehicle. The software modelling methodology was also described in (Awadallah et al. 2018).

5.1 Introduction

The increasing complexity of automotive systems has spawned a wide range of increasingly powerful methods of achieving verification and validation (V&V). The need to be assured of system functionality despite often complex non-linear system definitions requires computational acrobatics that draw on a variety of different tools, concepts, and techniques to deliver acceptable fidelity and confidence in the modelling environment. MBD is an umbrella term that groups the variety of methods that can be used to develop a virtual plant model. The basic premise behind MBD is the gradual development of a high-fidelity model, followed by the gradual verification of its function, leading to final validation.

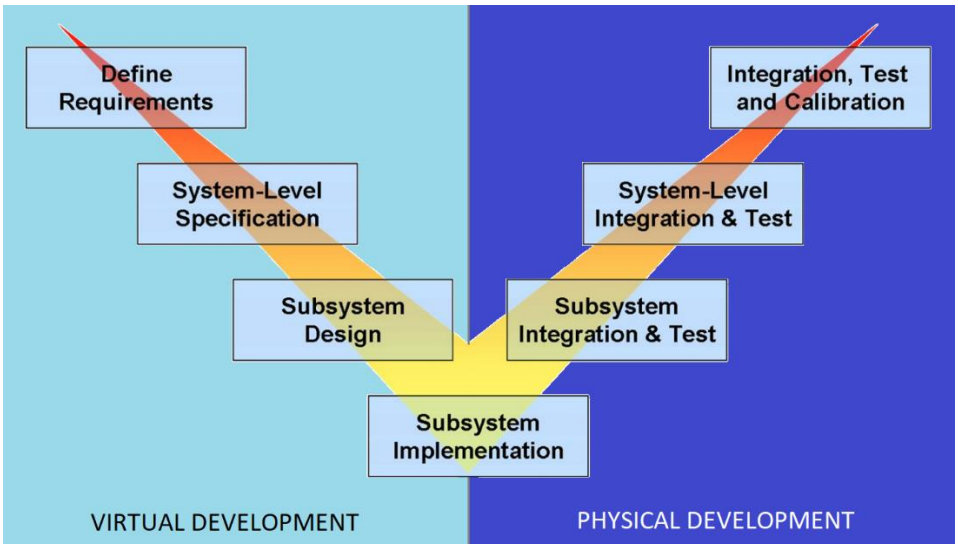

Figure 5.1 The MBD process can be divided into virtual development work (developing the plant model) and physical development work (verification and validation)

Whilst the model is being developed in software only, the MBD environment is typically referred to as software-in-the-loop (SIL). The intermediate steps between development of a model and final validation require increasing levels of hardware to be integrated into the system loop. In the first instance, running the software on a production microcontroller but with virtual I/O allows the engineer to verify the operation of the controller, checking stability and debugging. This is called processor-in-the-loop, or PIL. After the controller

operation has been verified, the virtual I/O from the plant model can be replaced with physical I/O as required, by replacing controller inputs with physical sensors and transducers, and outputs with actuators. The integration of hardware into the system under test is known as HIL (Newberger & Johnson 2014), and is typically the final verification step before the development of the prototype which is used for system validation.

This chapter describes the use of MBD, and specifically, achieving HIL verification of the electrical componentry and supervisory controller design of the low-cost MHEV powertrain. The HIL verification process demonstrates that a relatively simple test bed, paired with appropriate control, may be used to successfully investigate, develop, and validate a complex control solution. The simplicity is derived from appropriate system-level assumptions allowing the representation of forces at their most fundamental level and programming in as much fidelity as required by utilizing appropriate control methods.

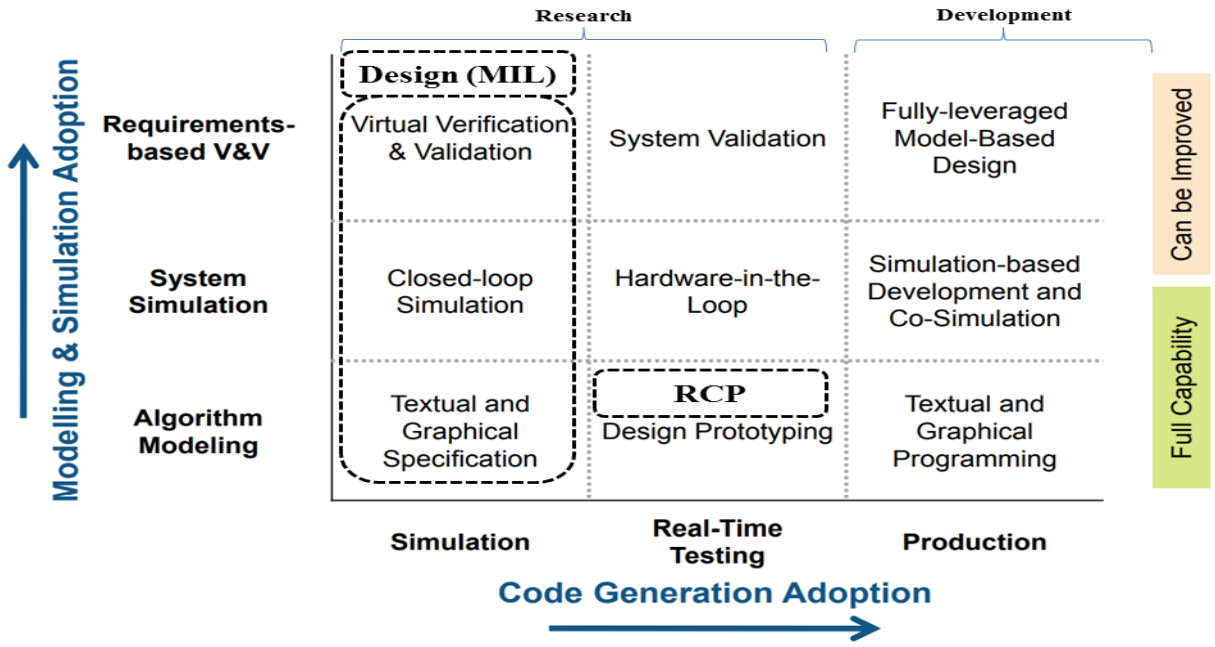

Figure 5.2 Model-Based Design Adoption Grid

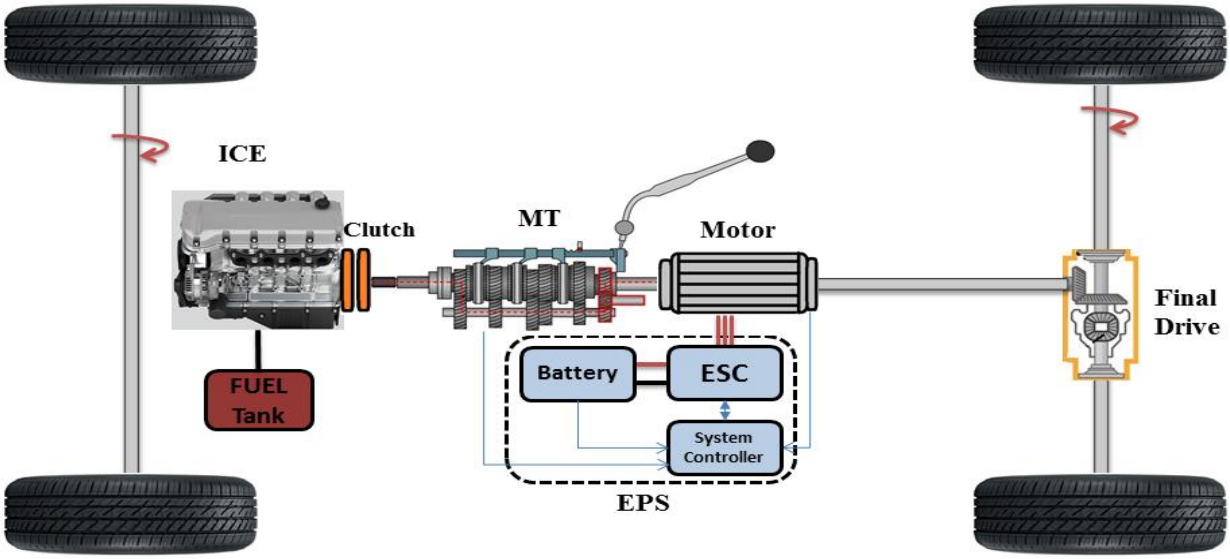

Figure 5.3 The prototype MHEV powertrain architecture used in KERMIT IV

5.2 Design and System Definition

The primary goal of the system verification is to confirm various aspects of the performance of the vehicle and understand their operation under test conditions. These aspects include fuel economy and emissions performance, as well as the performance of the continuous torque delivery functionality during gear changes. The vehicle model is built according to the representation described in Figure 5.3, using standard vehicle component libraries that have been developed in a parametric sense for deployment in the Simulink modelling environment. The individual components are described as “blocks” which are linked together in a graphical programming interface. The blocks are easily modifiable due to their parametric nature, making the process of development relatively straightforward. The output from each block flows to the input of the next to describe the system. This is the basis for essentially all vehicle simulation tools available today (Tammi, Minav & Kortelainen 2018).

The electric propulsion system (EPS) is modelled as a torque modifier which operates according to a heuristically derived rule-based control scheme, shown in Figure 5.6 and described in 5.2.3.

5.2.1 Mathematical Model

The fundamental longitudinal vehicle dynamics describing vehicle loads are well-understood and have been described in numerous previous publications. For this reason, they are omitted from the following model. However, the reader is encouraged to refer to (Schaltz et al. 2011) or (Chen et al. 2019) for a treatment of the longitudinal dynamic model that must be considered when designing a parallel hybrid powertrain. The process that was followed in this work is identical.

The modelling of the vehicle powertrain in in these simulations is satisfied by an eight degree-of-freedom (DOF) vehicle dynamics model. The model was created using Simulink and sits at the core of the vehicle simulation. The model is described using lumped mass techniques commonly implemented in such models, and is shown in Figure 5.4. It has been previously discussed and examined in testing and verification contexts, discussion of which is presented in (Awadallah et al. 2016) and (Awadallah, Tawadros, Walker, Zhang, et al. 2017a).

The equations of the dynamic system are derived from Newton's second law as it applies to rotational systems. To model the system, the major components are represented as a series of "lumped" inertias, interconnected by torsional springs and dampers, representing shaft stiffness and losses, respectively. The generalised representation of the system is shown in Figure 5.4. Necessarily, there are several simplifications and assumptions made when modelling a system using this technique. These simplifications must be made with reference to the desired level of fidelity of the model, the investigation outcomes required, and the available computing power.

The system has eight degrees of freedom, one of which is reduced if the clutch is engaged. The eight degrees of freedom are: the engine; the flywheel; clutch side 1 (pressure plate),

clutch side 2 (friction plate); the gearbox; the electric motor; the differential; and the wheels and driven mass. Engagement of the clutch reduces the two clutch elements to one lumped inertia, thereby reducing the degrees of freedom to seven. The equations of motion for the 8-DOF system are provided in eqs. 5.1 – 5.8. Symbol definitions are provided in Table XVI and Table XVI, and values for all model parameters may be found in Appendix B (page 303).

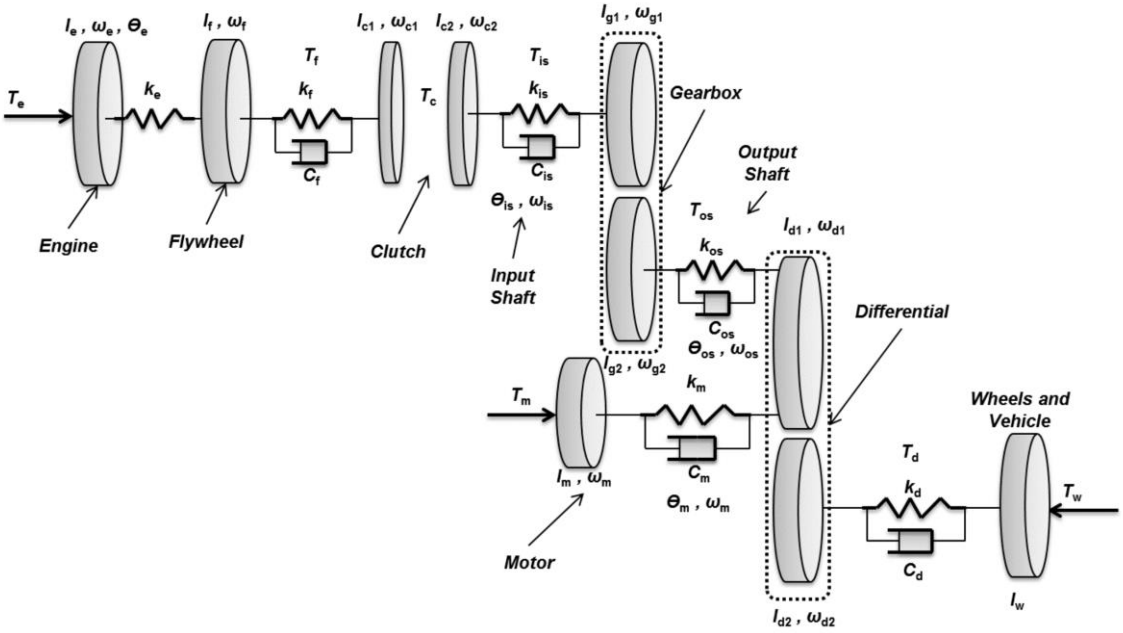

Figure 5.4 Kinematic diagram of the MHEV architecture (Awadallah 2018)

$$I_e\ddot{\theta}_e - K_e(\theta_f - \theta_e) = T_e \tag{5.1}$$

$$I_f\ddot{\theta}_f - K_e(\theta_f - \theta_e) - K_f(\theta_{c1} - \theta_f) - C_f(\dot{\theta}_{c1} - \dot{\theta}_f) = 0 \tag{5.2}$$

$$I_{c1}\ddot{\theta}_{c1} + K_f(\theta_{c1} - \theta_f) + C_f(\dot{\theta}_{c1} - \dot{\theta}_f) = -T_c \tag{5.2}$$

$$I_{c2}\ddot{\theta}_{c2} - K_{is}(\theta_{g1} - \theta_{c2}) - C_{is}(\dot{\theta}_{g1} - \dot{\theta}_{c2}) = T_c \tag{5.3}$$

$$\ddot{\theta}_{g1}(\gamma_1^2 I_{g2} + I_{g1}) + K_{is}(\theta_{g1} - \theta_{c2}) + C_{is}(\dot{\theta}_{g1} - \dot{\theta}_{c2}) - \gamma_1 K_{os}(\theta_{d1} - \gamma_1\theta_{g1}) - \gamma_1 C_{os}(\dot{\theta}_{d1} - \gamma_1\dot{\theta}_{g1}) = 0 \tag{5.4}$$

$$\ddot{\theta}_{d1}(\gamma_2^2 I_{d2} + I_{d1}) + K_{os}(\theta_{d1} - \gamma_1\theta_{g1}) + C_{os}(\dot{\theta}_{d1} - \gamma_1\dot{\theta}_{g1}) - \gamma_2 K_d(\theta_w - \gamma_2\theta_{d1}) - \gamma_2 C_d(\dot{\theta}_w - \gamma_2\dot{\theta}_{d1}) = 0 \tag{5.5}$$

$$\ddot{\theta}_{d1}(\gamma_2^2 I_{d2} + I_{d1}) + K_{os}(\theta_{d1} - \gamma_1\theta_{g1}) + C_{os}(\dot{\theta}_{d1} - \gamma_1\dot{\theta}_{g1}) + K_m(\theta_{d1} - \theta_m) + C_m(\dot{\theta}_{d1} - \dot{\theta}_m) - \gamma_2 K_d(\theta_w - \gamma_2\theta_{d1}) - \gamma_2 C_d(\dot{\theta}_w - \gamma_2\dot{\theta}_{d1}) = 0 \quad (5.6)$$

$$I_w\ddot{\theta}_w + K_d(\theta_w - \gamma_2\theta_{d1}) + C_{\mathrm{d}}(\dot{\theta}_w - \gamma_2\dot{\theta}_{\mathrm{d1}}) = T_w \quad (5.7)$$

$$I_{\mathrm{m}}\ddot{\theta}_m + K_m(\theta_{\mathrm{m}} - \theta_{d1}) - C_{\mathrm{d}}(\dot{\theta}_{\mathrm{d1}} - \dot{\theta}_{\mathrm{m}}) = -T_{\mathrm{m}} \quad (5.8)$$

When the clutch is closed, the two clutch elements are modelled as one single lumped inertia, as it can be assumed that slip is zero. Therefore, the equations describing clutch motion 5.2 – 5.3 may be combined, and the resulting equation of motion is eq. 5.9 below.

$$(I_{\mathrm{c2}} + I_{\mathrm{c1}})\ddot{\theta}_C + K_f(\theta_c - \theta_f) + C_f(\dot{\theta}_c - \dot{\theta}_f) - K_{is}(\theta_{\mathrm{g1}} - \theta_{\mathrm{c}}) - C_{is}(\dot{\theta}_{\mathrm{g1}} - \dot{\theta}_{\mathrm{c}}) = 0 \quad (5.9)$$

For this powertrain investigation, the simplifications and assumptions are as follows. The engine is modelled as a single degree of freedom (DOF), therefore supplying a constant torque as commanded by a controller. This simplification neglects torque fluctuations as a result of the combustion and reciprocating motion, as well as engine harmonics, but is convenient for a powertrain study focused on gear shifting. Within the transmission, gears and synchronizers are represented by lumped inertias. Damping components are also provided, representative of drag torque. The differential is modelled as a lumped mass, and damping is provided to the ground to model its losses. Stiffness elements represent shafts, including the driveshafts, propeller shaft and transmission input/output shafts. The wheel model is lumped to include hub, wheel, and tyre inertia, spring stiffness of the tyre, rolling resistance, and vehicle inertia. This accurately captures the total load on the powertrain, which is a significantly larger inertia than any other powertrain component.

In modelling using the lumped parameter method, the assumptions applied include neglecting lash and backlash in gear meshes; system temperature dependency, which is most marked by

lubricant viscosity changes; simplification of geometrically symmetrical components such as tyres and driveshafts to one branch ("half-car"), and linearizing viscous damping.

The electrical side of the powertrain is described in the following. The relationship between voltage and torque can be used for describing the dynamics of the electric motor. The phase voltage is expressed as follows, as a function of input current and back-emf (Al Ibraheemi 2018):

$$V_a = Ri_a + L\frac{di_a}{dt} + e_a \tag{5.10}$$

$$V_b = Ri_b + L\frac{di_b}{dt} + e_b \tag{5.11}$$

$$V_c = Ri_c + L\frac{di_c}{dt} + e_c \tag{5.12}$$

Alternatively, the compact matrix form is presented below. It is assumed that the stator resistances of all the windings are equal and the mutual and the self-inductances are constant.

$$\begin{bmatrix} V_a \\ V_b \\ V_c \end{bmatrix} = \begin{bmatrix} R & 0 & 0 \\ 0 & R & 0 \\ 0 & 0 & R \end{bmatrix} \begin{bmatrix} i_a \\ i_b \\ i_c \end{bmatrix} + \begin{bmatrix} L & 0 & 0 \\ 0 & L & 0 \\ 0 & 0 & L \end{bmatrix} \frac{d}{dt} \begin{bmatrix} i_a \\ i_b \\ i_c \end{bmatrix} + \begin{bmatrix} e_a \\ e_b \\ e_c \end{bmatrix} \tag{5.13}$$

The back-EMF as a function of rotor position is given in 3-phase rotor reference frame below. Each phase has 120º phase angle difference:

$$e_a = K_w f(\theta_e)\omega \tag{5.14}$$

$$e_b = K_w f(\theta_e - 2\pi/3)\omega \tag{5.15}$$

$$e_c = K_w f(\theta_e + 2\pi/3)\omega \tag{5.16}$$

The electrical rotor angle is equal to the mechanical rotor angle multiplied by the number of pole pairs p:

$$\theta_e = \frac{p}{2}\theta_m \tag{5.17}$$

The function $f(\theta_e)$ is described by the trapezoidal relationship with a value of ±1 according to:

$$f(\theta_e) = \begin{cases} 1, & 0 \le \theta_e < \frac{2\pi}{3} \\ 1 - \frac{6\left(\theta_e - \frac{2\pi}{3}\right)}{\pi}, & \frac{2\pi}{3} \le \theta_e < \pi \\ -1, & \pi \le \theta_e < \frac{5\pi}{3} \\ -1 + \frac{6\left(\theta_e + \frac{5\pi}{3}\right)}{\pi}, & \frac{5\pi}{3} \le \theta_e < 2\pi \end{cases} \tag{5.18}$$

The air gap between the stator and rotor and saturation are neglected. Therefore, the flux linkages become a linear function of the phase currents. The mathematical model describing the motor is therefore given as a torque source and is based on electrical first principles. Total torque output can be represented as a summation of that of each phase:

$$T_m = (e_a i_a + e_b i_b + e_c i_c)/\omega \tag{5.19}$$

Symbol	Definition	Unit	Subscript	Definition
T	Torque	N.m	c1	Clutch side 1
I	Equivalent Inertia	$Kg.m^2$	c2	Clutch side 2
ω	Angular velocity	rad/s	d	Differential
θ	Angular displacement	rad	d1	Diff. reduction 1
K	Torsional stiffness	N.m/rad	d2	Diff. reduction 2
C	Friction Coefficient	N.m.s/rad	e	Engine
γ	Gear ratio	---	f	Flywheel
			g1	Gear reduction side 1
			g2	Gear reduction side 2
			is	Input shaft
			m	motor
			os	Output shaft
			w	Wheel

Table XV Mechanical Notation and Nomenclature

Symbol	Definition	Unit
$V_a\ V_b\ V_c$	Terminal phase voltage	V
$e_a\ e_b\ e_c$	Motor back-EMF	V
R	Armature resistance	Ω
L	Armature self-inductance	H
K_w	Back EMF constant of one phase	V/ rad.s-1
θ_e	Electrical rotor angle	º
θ_m	Mechanical rotor angle	rad
$i_a i_b i_c$	Motor input current	A
T_m	Mechanical Torque	N.m
ω	Angular velocity	rad/s
$f(\theta_e)$	Back-emf reference function	---
p	Number of poles	---

Table XVI Electrical Notation and Nomenclature

5.2.2 Simulation model

Model-in-the-loop (MIL) is the step in the development process that is characterized by the presence of virtual representations of the physical function of the entire vehicle subsystem; i.e., the detailed mathematical, logical, or numerical models of the engine, transmission and chassis components, controllers (ECU), and connecting hardware. The use of modelling for testing and verification of the vehicle powertrain under different driving cycles has been discussed in (Awadallah et al. 2016, 2018; Awadallah, Tawadros, Walker & Zhang 2017b). Many of the model components are based on pre-existing components in MATLAB/Simulink/Stateflow by using Simscape and SimDriveline libraries. A general structure of a plant model is shown in Figure 5.5. Several standard drive cycles have been considered to evaluate the benefits of the low-cost mild hybrid powertrain – these are presented in (Awadallah, Tawadros, Walker & Zhang 2017c, 2017a).

The software model was developed in the Simscape/Simulink environment Figure 5.5. The model includes physical and control components, and uses numerical solvers to optimise the simulation parameters to achieve sufficient simulation accuracy and speed. The model was subjected to several standard drive cycle simulations in order to understand and evaluate the performance characteristics of the powertrain design.

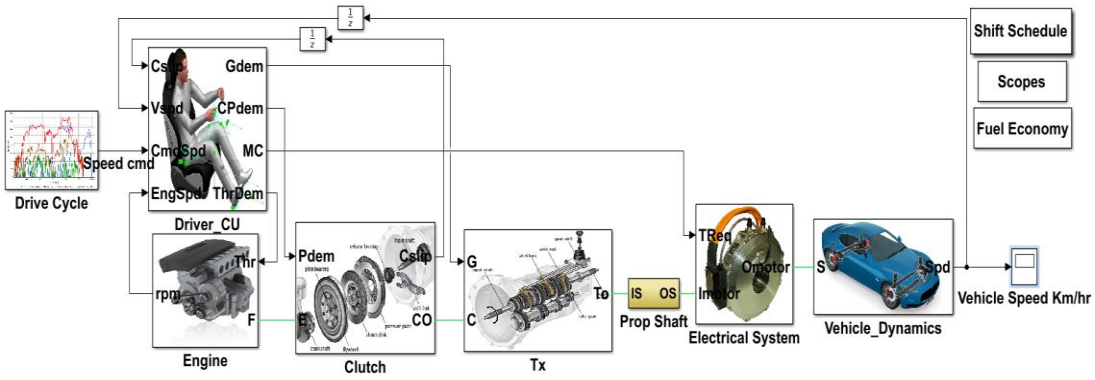

Figure 5.5 A high-level view of the powertrain of the mild HEV model in Simulink

In operation, the simulation requires drive cycle data as an input. The drive cycle data is simply a set of scalar values denoting target speed at a time step of one second. The simulation starts with the plant model at rest. The model is forward-looking, therefore it operates in the time-domain and does not look up "future" values of the drive cycle in order to find an optimal solution. Rather, the drive cycle is read into the simulation one value at a time. The simulation sets the velocity as a target value and generates torque and speed demands, which are distributed throughout the model according to each component's characteristics and the selected mode of operation.

The model components were parametrized in order to allow the testing of various component configurations, such as the insertion of an ultracapacitor into the system, or the scaling of the motor's characteristic curves to investigate the effect of motor sizing on the functionality of the system.

The model includes a "driver" block, which receives the velocity target signal from the drive cycle information. The driver block is based on a PID controller and provides control inputs such as throttle, brake and gear shifting based on a speed feedback loop. This emulates a human driver's behaviour, which, in essence, uses the vehicle controls to make a torque value demand from the vehicle systems, based on the sensory feedback provided by speed indications primarily, but also other sensory feedback based on the environmental surrounds. This method yields more realistic simulation results than would be possible by directly addressing the vehicle controls in simulation, and has been validated in prior literature (Oh 2005).

5.2.3 Energy Management Strategy

The energy management strategy for the MHEV model is a rule-based strategy based on SOC as well as vehicle torque demand and speed, described in (Awadallah, Tawadros, Walker,

Zhang, et al. 2017b). The electric motor is employed either as a motor or generator depending on the vehicle operating condition and driver demand, and has four operating programmes: Regenerative braking; an electric motor (EM) as a generator; Torque-hole filling, and; Idle mode. The torque-hole filling is triggered using a clutch pressure sensor and controlled using predictive models. All other operating modes are as per Figure 5.6, and are managed by the EPS controller, which is also responsible for the control of the engine throttle when operating in a blended mode such as "torque assist" or "EM as generator". It depends on requested power and battery SOC, depending on various conditions the motor may generate power from either the ICE or vehicle kinetic energy. SOC is calculated as:

$$SOC = \frac{(Max\_Capacity \; - \; Ah\_used)}{Max\_Capacity} \tag{5.20}$$

$$SOC = \left(1 - \frac{\int_0^{time(s)} Current(A)}{3600 \times Max.Capacity(Ah)}\right) \times 100\% \tag{5.21}$$

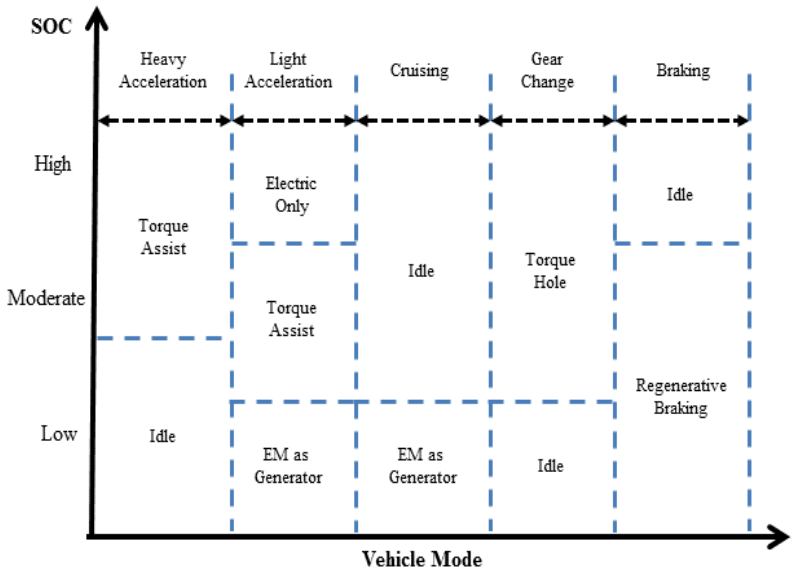

Figure 5.6 The rule-based energy management control strategy

5.3 Model Verification

When the software model was completed, it was necessary to verify its operation. The means to verify the operation is through simulation scenarios. The simulation scenarios allow the investigation of the operation of the plant in a variety of settings. In this case, scenarios were deployed based on the input of drive cycle information. The drive cycle information is tailored to observe various functions and functional outputs. One drive cycle is a constant acceleration curve, which is used to test the functionality of the continuous torque delivery control method. Other cycles are based on standardized drive cycles that are used for emissions benchmarking. These cycles can be tailored to investigate low-congestion performance (by deploying a rural or high-speed cycle such as the highway fuel economy test (HWFET), city performance (by deploying an urban cycle such as the New York City Dynamometer Drive Schedule, NYCDDS or NYCC, or Indian Urban cycle). Another method for model verification is the adjustment of parametric values. For instance, the PID parameters in the driver block can be used to vary the aggressiveness of the driver control, emulating a calm driver or an aggressive driver. The current limits and storage capacity of the battery can also be altered to emulate the insertion of an ultracapacitor into the system.

5.3.1 Continuous Torque Delivery Simulation

A simplified drive test involving a series of upshifts from 2nd to 3rd gear was selected for initial testing. The test scenario was selected as an initial benchmark for its simplicity and its ability to highlight gear shift characteristics consistently. Up-shifting control can be completed in four seconds, with the total period of clutch disengagement about half of that time. For comparison to the mild-hybrid, an otherwise identical conventional ICE-only powertrain was modelled by removing the electric parts of the powertrain from the model. The results are shown in Figure 5.7 and Figure 5.8. As expected, a large hole in the output torque and a corresponding speed decrease are evident during the gear shift process, as compared to the reduced, but not eliminated torque hole shown using the continuous torque delivery control method for the MHEV powertrain. Noting the variation in transient system response also shows a reduction in the torque oscillation amplitude of approximately 40N.m when using the continuous torque delivery method. This is likely because torque is constantly applied in the same direction across the drivetrain during the gear change, therefore the effect of lash is significantly reduced. In contrast, the lash present in drivetrain components results in significant discontinuities when the torque direction is reversed, or is removed and re-applied.

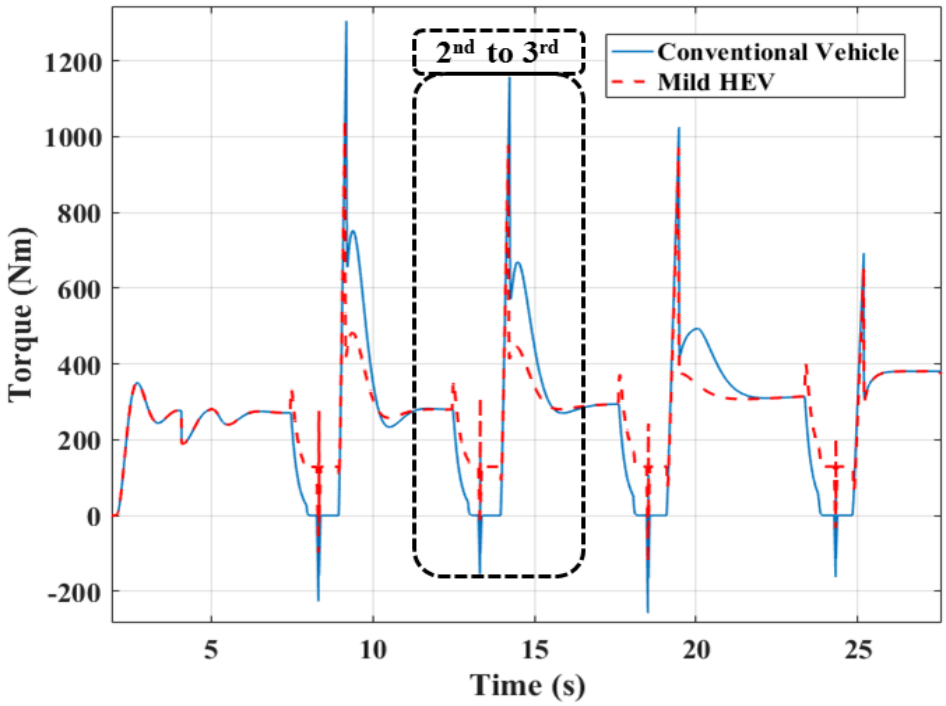

Figure 5.7 Gear shifting torque profile

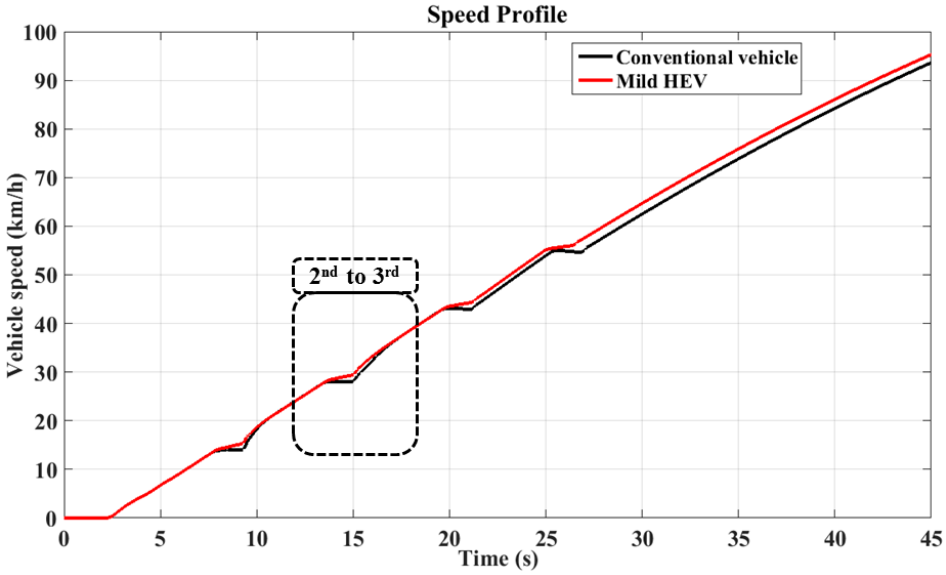

Figure 5.8 Gear shifting speed profile

5.3.2 Fuel Economy and Emissions Simulation

The results presented in this section have previously been described in (Awadallah 2018) and are presented herein for completeness. There is some additional discussion provided but the substantive results are the same.

To investigate the fuel economy and emissions performance of the vehicle, a number of drive cycle studies were undertaken. The drive cycle studies are comparative, giving the opportunity to evaluate not only the performance of the MHEV powertrain in isolation, but also its performance in comparison to the base vehicle. The studies are designed to investigate fuel economy (F.E.) and emissions performance in low- and high-density traffic. To this end, the Indian urban cycle and the HWFET were implemented as the input to the model. The cycles are shown in Figure 5.9 and Figure 5.10. The HWFET covers 765 seconds cycle time with an average speed of 77.7km/h and a total distance of 16.45km. The cycle begins with a 100s acceleration phase to reach approximately 70km/h. The speed stays approximately constant for the next 200s until a braking event to bring vehicle speed to 45km/h, followed by an acceleration to approximately 95km/h. There are no intermediate stops in this cycle.

The Indian urban cycle is not an officially mandated drive cycle, but is included in ADVISOR and has been used extensively in research. Rather than being a formulated drive cycle, it is instead a datalogged journey in an urban setting in India, taken on 12 March 2000 (National Renewable Energy Laboratory 2002) The sample data is for a total of 2689s and 17.4km, and is characterized by frequent starts and stops, with a low top speed of 62km/h and an average speed of 23.3km/h. Due to its inclusion in the analysis tool ADVISOR, its basis in a real journey, and its adoption by multiple researchers (Babu & Ashok 2015; Manish & Banerjee 2006; Sarkar & Banerjee 2005; Williamson et al. 2005), it is a good standard for

evaluating real-world high-congestion performance. The characteristic parameters of both the Indian urban and HWFET cycles are summarized in Table XVII. Based on their characteristic parameters, the cycles can be categorized into low and high congestion traffic patterns (Samuel, Austin & Morrey 2002; Schwarzer & Ghorbani 2013).

	HWFET	INDIAN URBAN
Distance (km)	16.5	17.4
Max Speed (km/h)	96.4	62.2
Duration (Sec)	765	2689
Average Acc (g)	0.19	0.3
Average Speed (km/h)	77.6	23.3
Number of stops	1	52
Idle Time (sec)	6	267

Table XVII Drive cycle parameters

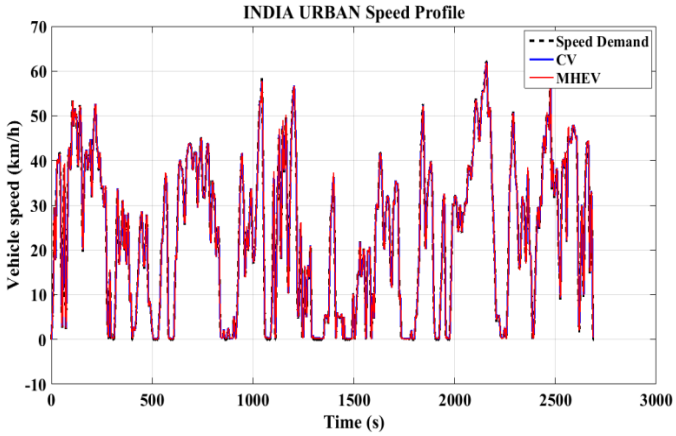

Figure 5.9 The speed profile of Indian Urban Drive Cycle

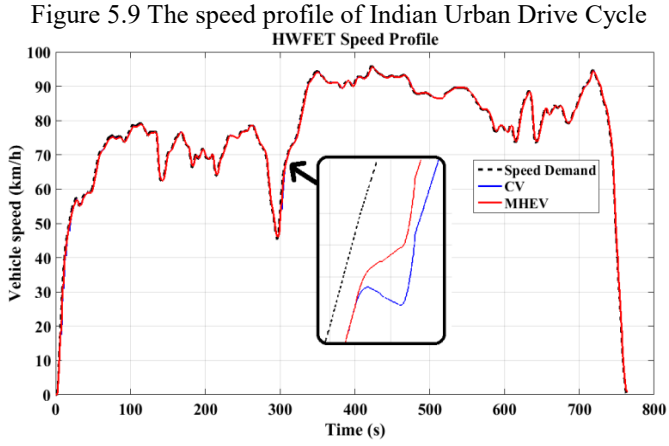

Figure 5.10 The speed profile of HWFET Drive Cycle

The F.E. and emissions results for the two drive cycles are shown in Table XVIII. The results illustrate the interdependency between fuel economy outcomes, powertrain topology, and driving environment. As expected, the MHEV attains higher performance as compared to the conventional powertrain. The improvement is approximately 10% in the Indian Urban cycle, and 2% under the HWFET. The stop-start conditions and high speed fluctuation in the Indian urban cycle data represent the best-case for achieving maximum electric utilisation. This is due to the adaptation of the powertrain to be particularly suited to use in low-power acceleration at low speed, as well as the intensive use during gear changes (torque-filling). The resulting output is that the mild hybrid configuration delivers significant benefits to urban fuel economy, with considerably smaller improvements in the highway cycle.

The combined F.E. is determined by weighting the highway data at 45% and the urban at 55%, as expressed in eq.20 (Ahluwalia, Wang & Rousseau 2005). This equation cannot be used to determine emissions performance because the emissions outcome can be changed dramatically depending on the section of cycle data taken, whereas F.E. is largely insensitive. The weighted average data is 7.9 and 7.4 L/100 km for the CV and MHEV, respectively. This represents a 6% improvement for the MHEV over the CV.

$$FE_{combined} = \frac{1}{\frac{0.55}{FE_{city}} + \frac{0.45}{FE_{highway}}} \qquad (5.22)$$

		Fuel		Emissions (grams/km)		
		Fuel Consumption (L)	Fuel Economy (L/100 km)	HC	CO	NOx
INDIAN URBAN	CV	1.9	11.1	0.45	1.9	0.69
	MHEV	1.7	10	0.42	1.2	0.57
HWFET	CV	0.95	5.8	0.43	1.59	0.62
	MHEV	0.93	5.7	0.41	1.43	0.57

Table XVIII Emissions and fuel economy simulation results

Whilst these results are good indicators, they represent the best- and worst-case scenarios for operation. The Indian urban data is atypical in its congestion and the HWFET data is also atypical in that it does not include any intermediate stop times. Further, there is a general consensus that prescribed drive cycles are no longer adequate indicators of fuel economy and emissions outputs, due to the wide variance between prescribed cycles and typical real-world drivers' experiences. Prescribed cycles do not capture wide regional variance in traffic or geography, nor do they capture temporal changes in traffic patterns unless they are regularly updated. Many regional drive cycles may not be updated for decades, losing relevance over time. Efforts have been made to create uniform worldwide regulation. Early efforts resulted in many countries adopting European or US emissions regulation – for instance, Indian Bharat emissions or Australian ADR79. The cross-compatibility allows manufacturers to ensure compliance over larger worldwide markets but does not optimise emissions outcomes. A recent development, the "world harmonized light vehicle test procedure" (WLTP) has been developed, moving toward "real-world" testing using portable emissions measurement systems (PEMS). In the absence of real-world data repositories and analysis techniques, drive cycles remain the most practical and relevant means of emissions and fuel economy modelling for researchers (André et al. 2006; Chen & Borken-Kleefeld 2014).

In Australia, where this study was conducted, the average daily commute is less than 50km. As shown in Figure 5.11, in Sydney, the country's most populous city, 64% of drivers commute less than this distance (Sharma et al. 2013). In many developing regions the average commute is necessarily much smaller than this. This is typically due to poor road conditions, severe congestion, high urban density and high transportation costs, all of which place a practical limit on the length of a daily commute. To generate an accurate model of typical driving conditions, a second comparative study used 40km driving distance whilst also varying traffic density. The traffic density was altered by appropriating suitable sections of standard drive cycles to capture the varying traffic patterns. They are the result of extensive comparison of existing cycles against expected driving conditions. These developed drive cycles use sections of the urban dynamometer drive schedule (UDDS), the Indian urban dataset included in ADVISOR, and the city-suburban heavy vehicle route (CSHVR) for development of a 40km high congestion cycle dataset, and sections of the new European driving cycle (NEDC), HWFET, and Indian highway dataset (a second dataset also shipped with ADVISOR) for development of the low-congestion cycle dataset. The cycles are shown in Figure 5.12 and Figure 5.13

The use of multiple cycles appended to each other serves multiple purposes. Firstly – it allows the representation of a full typical commute distance where most cycles are significantly shorter. Secondly – it removes any bias a single particular cycle may skew towards in terms of emissions – for instance, high speed cycles typically skew toward increased NOx whereas low speed cycles increase HC emissions (Favre, Bosteels & May 2013). Finally, it results in a more diverse range of operation conditions than a single cycle allows for, which provides a more realistic simulation result. The cycle characteristics are summarized in Table XIX, and simulation results are shown in Table XX.

The results are not unexpected, and follow the trend shown in the previous simulation They show that whilst the MHEV consistently performs better than the base vehicle, the most significant influence on economy and emissions is not the type of powertrain but the operating environment. They also demonstrate the clear advantage the MHEV powertrain topology has in urban environments, where the highest gains in F.E. and economy, as a percentage, are made.

Density traffic patterns	Low	High
Drive cycle	NEDC + HWFET + INDIAN HIGHWAY	UDDS + INDIAN URBAN+ CSHVR
Distance (km)	39.1	40
Time (s)	2832	5840

Table XIX Drive Cycle Characteristics

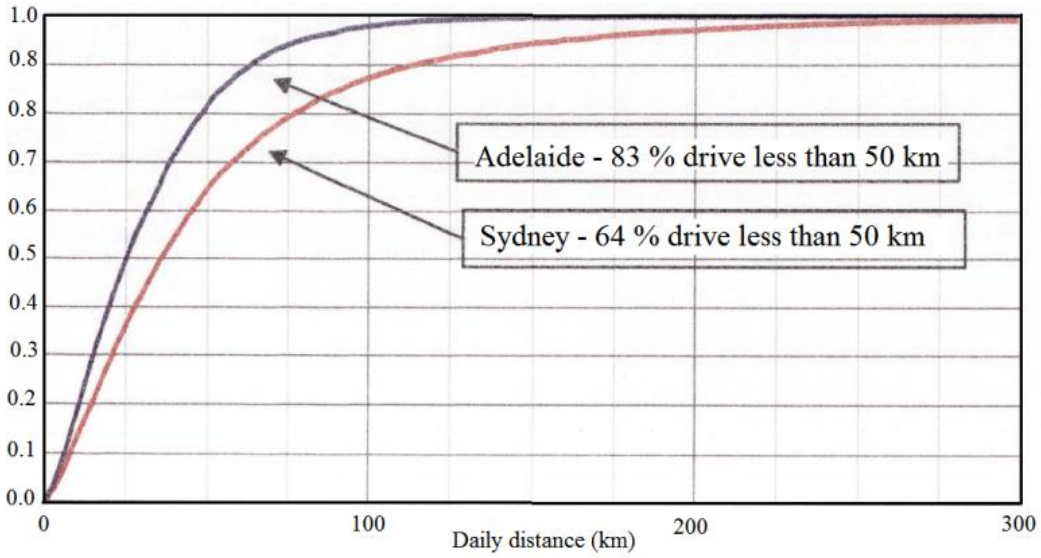

Figure 5.11 Cumulative distribution of daily driving distance in Australia (Sharma et al. 2012)

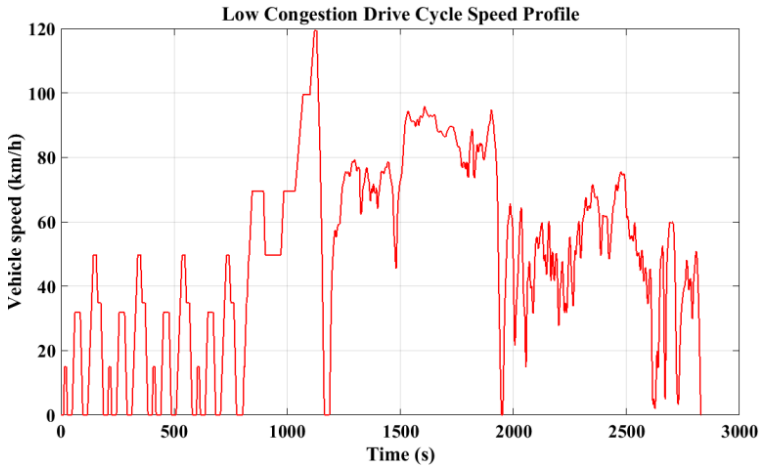

Figure 5.12 The low-density traffic pattern drive cycle

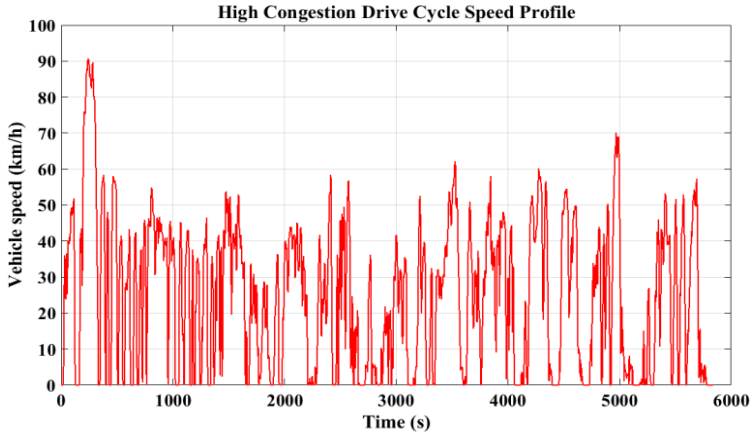

Figure 5.13 The high-density traffic pattern drive cycle

		Fuel		Emissions (grams/km)		
		Fuel Consumption (L)	Fuel Economy (L/100 km)	HC	CO	NO x
INDIAN URBAN	CV	1.9	11.1	0.45	1.9	0.69
	MHEV	1.7	10	0.42	1.2	0.57
HWFET	CV	0.95	5.8	0.43	1.59	0.62
	MHEV	0.93	5.7	0.41	1.43	0.57
Low Density	CV	2.5	6.5	0.22	0.61	0.35
	MHEV	2.2	5.8	0.19	0.56	0.32
High Density	CV	4.5	11.1	0.27	1.2	0.49
	MHEV	3.4	8.5	0.23	0.62	0.36

Table XX Fuel economy and emissions results for all tested cycles

The reasons for this advantage are purely and simply a result of the increased electric utilization factor that is possible in the urban environment. When the vehicle is operating at

low speed or stopped, the engine can be switched off, and the significant proportion of time spent braking is used to recharge the battery using regenerative braking. As a result of the simulation, it can be expected that the lowest observable F.E. improvement limit of only 1.8% may be expected, although this is only in the case that the vehicle is operated purely in a rural setting. A more typical observed improvement of 10.8% is likely to be seen in suburban and rural driving, whereas the upper limit of F.E. improvement is 23.5% may be observed in highly, and atypically congested traffic. The envelope of F.E. improvements is illustrated in Figure 5.14which compares fuel consumption of the CV and MHEV graphically according to individual cycle performance. It shows that there are no situations under which the MHEV performs worse than the CV, but there are situations where improvements are insignificant. In those situations it is unlikely that the MHEV would be financially sound from a total cost of ownership (TCO) perspective. Conversely, many cycles favour the MHEV significantly. For this reason, it is important to consider the nature of the cycle when performing simulation and testing, and the impact that nature has on testing results.

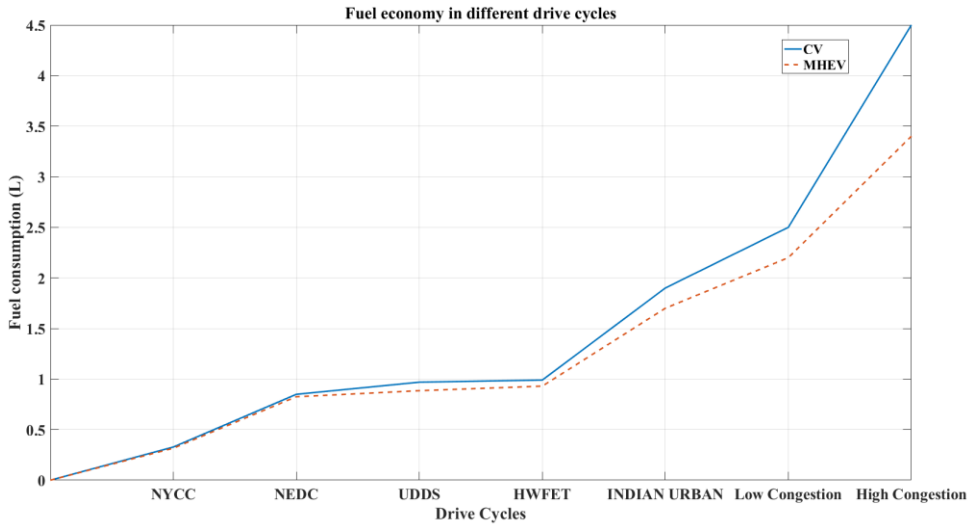

Figure 5.14 Simulated F.E. under all tested drive cycles

5.4 Rapid Control Prototyping

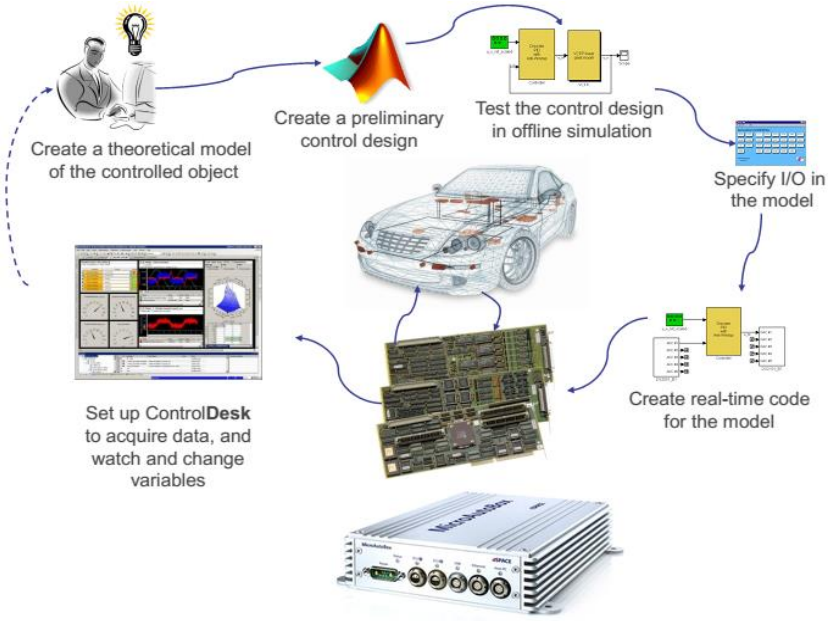

Figure 5.15 Automotive Development Process using dSpace RCP platform

Following the verification of the vehicle model, rapid control prototyping (RCP) was used to develop the EPS. The use of RCP decreases the development and testing time by allowing the testing of the EPS prior to its installation in the prototype vehicle. RCP systems operate in real-time by embedding a system model with a physical microcontroller. Inputs and outputs are routed through a virtual environment to test the function of the controller (Lin et al. 2003). The inputs can be manipulated in the virtual environment and sent to the microcontroller as a physical signal. This allows the examination of the microcontroller outputs to ensure the microcontroller is working as expected without the need to connect it to physical plant.

Because the microcontroller is working in real time and is communicating with a virtual plant model, the simplifications must be made in the plant model to ensure it can operate with real time throughput. To this end, models must be simplified sufficiently to accurately depict the system dynamics, but also to minimize the computing time required. Examples of

simplifications might include the reduction of an engine model to a multidimensional lookup table incorporating at a minimum, torque, speed and manifold pressure, and optionally empirical or experimentally-derived temperature compensations. Simplifications of this nature meet the requirements of RCP.

5.4.1 EPS Architecture

A representation of the EPS is outlined in Figure 5.16, and the system topology is described in Figure 5.17. The dSPACE MicroAutoBox II controller provides supervisory control to the motor controller by reading information through the CAN-bus into a feedback control loop and issuing commands to the motor controller using analog and digital signals through the interface circuitry. The interface circuitry is made up of a custom-designed relay board and wire connections. The interface combines the output ports, e.g. sensor signals, CAN bus signals and motor driver command signals. Relays are responsible for controlling system power; throttle and brake enable, and motor direction. Other functions are effected by analog control signals and CAN-based feedback. The plant model is executed in real-time on the system's processor (Esfandyari et al. 2018).

dSPACE MicroAutoBox II provides supervisory control to determine the distribution of torque across the engine and the electric motor (EM). It coordinates the control of the two power plants using information derived from other controllers and sensors, such as the engine control unit, throttle pedal position sensor, gear position sensors, and motor controller. It then commands each slave controller separately to ensure the output torque from the entire powertrain meets the driver commanded output, in a manner that is imperceptible to the driver. In its physical embodiment, the supervisory controller is responsible for the following tasks:

a. Providing motor torque commands to the motor controller to provide motoring or regenerating torque.

b. Providing throttle position commands to the throttle valve controller.

It makes these commands based on information reported on the communication bus (CAN) including current motor power; driver requested torque, battery voltage, battery state of charge, engine clutch position, current gear selected, vehicle speed, gear shift status, among others.

The host PC serves multiple functions, including the development and design in MATLAB/Simulink, data collection to verify the SIL models, and providing control interfaces for the commands sent to the MicroAutoBox, including simulation start, stop, observation of outputs during simulation, and post-simulation analysis. Considerations must be made toward the selection of step size, solver choice, and a number of solver iterations. Fast and stable control of the full model in this research was determined by the process of trial and error. Based on this, a fixed step size of 0.1 ms was selected. Previous research (Awadallah et al. 2018) has determined the validity of the system.

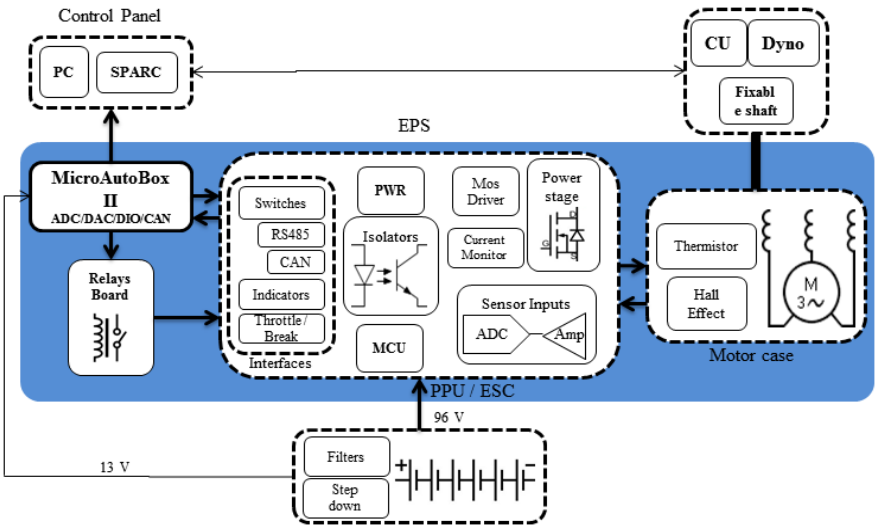

Figure 5.16 The functional block diagram of an electric propulsion system

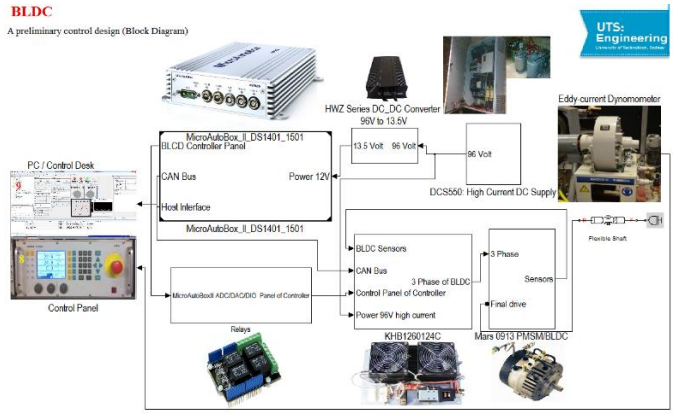

Figure 5.17 The system architecture of the HIL electric propulsion system

5.4.2 Supervisory Controller

Various commercially-available controllers are used for Rapid Control Prototyping. dSPACE MicroAutoBox II is one such controller, suitable for tasks such as development or verification and the plant model is executed in real-time on system's processor. The hardware is based around an IBM PowerPC microprocessor running at 900MHz. It includes a real-time processor unit (RTP), as well as interfaces providing functionality for typical automotive I/O functions for connection and control of sensors and actuators including digital I/O and A/D conversion. This is a prototyping platform typically used for a gateway or bypassing applications when developing or rapid prototyping electronic control units.

The model is downloaded directly to a dSPACE Rapid Prototyping system via auto-code generation using RTI. The validation process also includes design processes for handling real-time simulation using Simulink, dSPACE RTI & ControlDesk environments. The real-time simulation running in dSPACE RTI was hosted on a local computer within the laboratory. This software provides the user with complete control over the dSPACE hardware (MicroAutoBox II) and enables the user to change simulation parameters during runtime. The host computer and MicroAutoBox II together form the supervisory controller of the testing apparatus.

The MicroAutoBoxII connects to a host PC using a host interface cable. The host PC serves multiple functions, including the development and design in MATLAB/Simulink, data collection to verify the software-in-the-loop (SIL) models, and providing control interfaces for the commands sent to the MicroAutoBox, including simulation start, stop, observation of outputs during simulation, and post-simulation analysis.

5.4.3 EPS Control Panel

The use of Auto Code Generation (ACG) technology in MBD is a highly time-efficient method of control unit development. Control algorithms developed in model-based graphical languages such as Simulink can be converted to production code for implementation in hardware (ECU) very effectively. Even more importantly, as revisions to the algorithms due to design changes are developed, the code can be regenerated in minutes versus weeks as is often the case where ACG is not used. The dSPACE software packages provide a graphical programming environment for the development of control strategies and modelling. The control models are designed in Simulink. The real-time interface (RTI) block set provides function blocks to associate Simulink models with real hardware (MicroAutoBoxII). The primary objective of this model was to establish the control system. The signal “Throttle analog input” is provided as one example to indicate how to conduct adaptation of signal between the motor controller and controller model concerning RTI blocks. The throttle is controlled using a 0-5 Volt signal. In order to output these values, one DA conversion RTI block is used as one output port of model as shown in Figure 5.18.

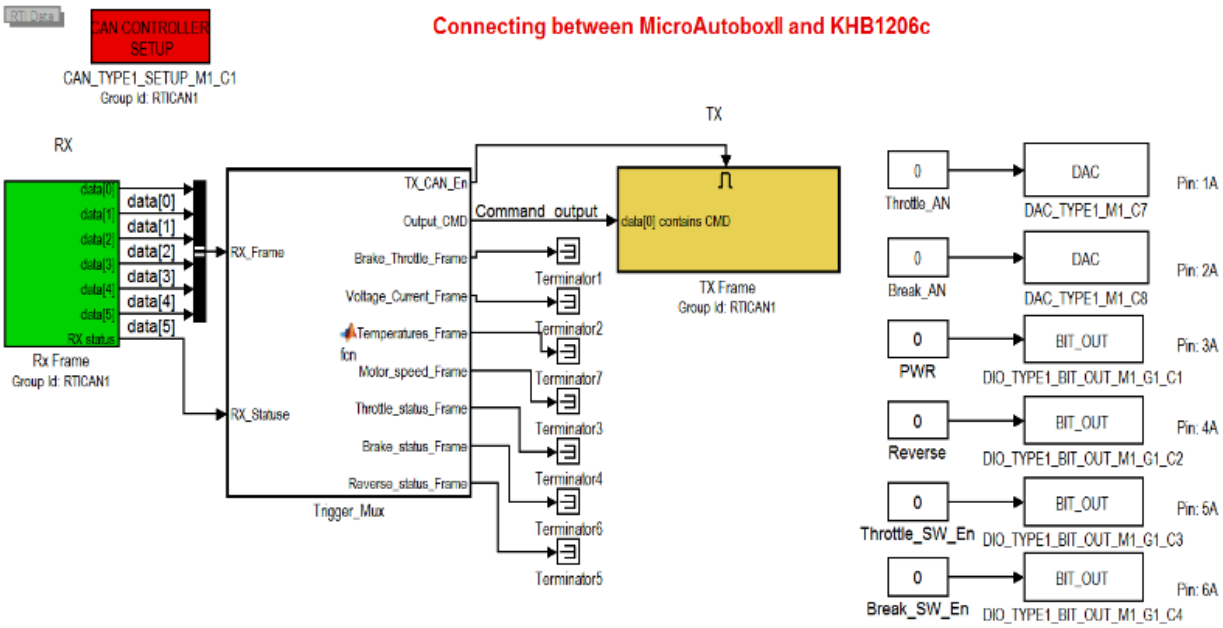

Figure 5.18 Modelling control design of the HIL EPS

The real-time simulation runs in dSPACE ControlDesk, which allows logical configuration of simulation runs. Figure 5.19 shows the dashboard layout of the real-time simulation. The layout is used for setting up relevant parameters during experimentation. The MicroAutoBox II controller receives commands from ControlDesk through a host interface cable. The commands control the output parameters. These commands were interpreted by the controller logic and output to the relevant slave controller. The ControlDesk dashboard was configured to allow control of power, throttle, brake, and direction. Indicators were configured to display controller and motor temperatures, motor speed, direction, motor current, voltage, CAN-Bus activity, power status, and a speed histogram.

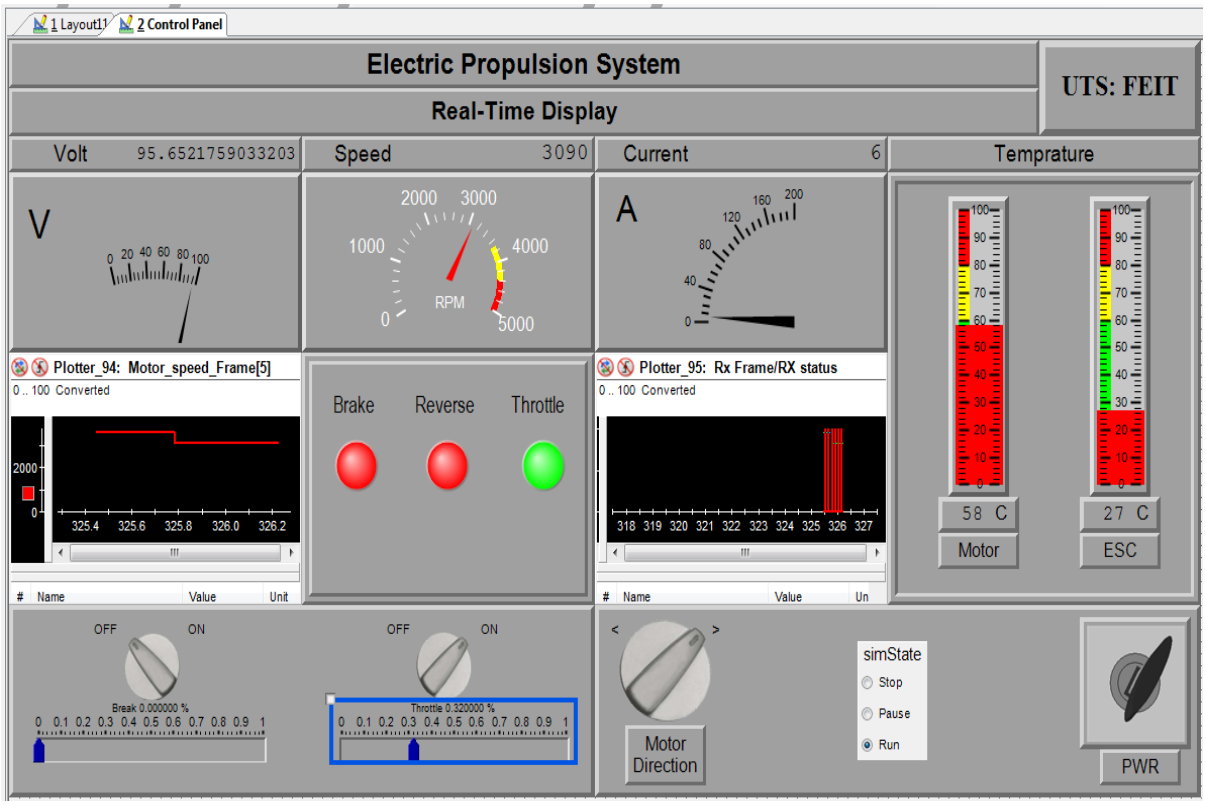

Figure 5.19 The control panel used for the HIL EPS

5.5 Hardware-in-the-loop test bed

Hardware-in-the-loop (HIL) simulation consists of tests performed in the lab on sections or subsystems of the system under development. The technique is beneficial because it means certain points of interest can be investigated without the need to build an entire system, saving time and money. Errors that occur in the laboratory can be reproduced at any time, whereas this is often not the case in traditional prototype testing. The HIL test bed used for the verification of system performance replaces the real environment of the EPS by substituting the engine for an electric motor being controlled to simulate the engine (the engine simulation motor, or ESM), and substituting vehicle loads for an opposed eddy current brake connected axially and being controlled to simulate rolling, inertia, and aerodynamic vehicle loading (the load simulation brake, or LSB). The real EPS equipment (controller, motor and power supply) is connected medially between the simulated engine and simulated load. The test bench setup is described schematically in Figure 5.20, and shown as presented

in the laboratory in Figure 5.21. The numbers in this paragraph refer to the numbers in both figures. The ESM (5), controlled by an ABB motor controller (4), was used to emulate the output from the manual transmission. It was connected to the LSB (8) using a shaft which emulates the propshaft in a roadgoing vehicle. The LSB is used to simulate the resistance loads, such as rolling and aerodynamic losses. The control model uses a MicroAutoBox II supervisory control unit (2), which controls the ABB controller and the EPS controller (3). Supervisory control is implemented in dSPACE ControlDesk (1) and on the MicroAutoBox II control unit (2). The supervisory control references a vehicle model which is used for the generation of torque commands for both the EPS (3) and the IM (9). The reference model is based on acquired data from physical testing, giving an accurate representation of torque, speed, and gear change profiles. The shaft torque is measured using two torque sensors, (6) and (7).

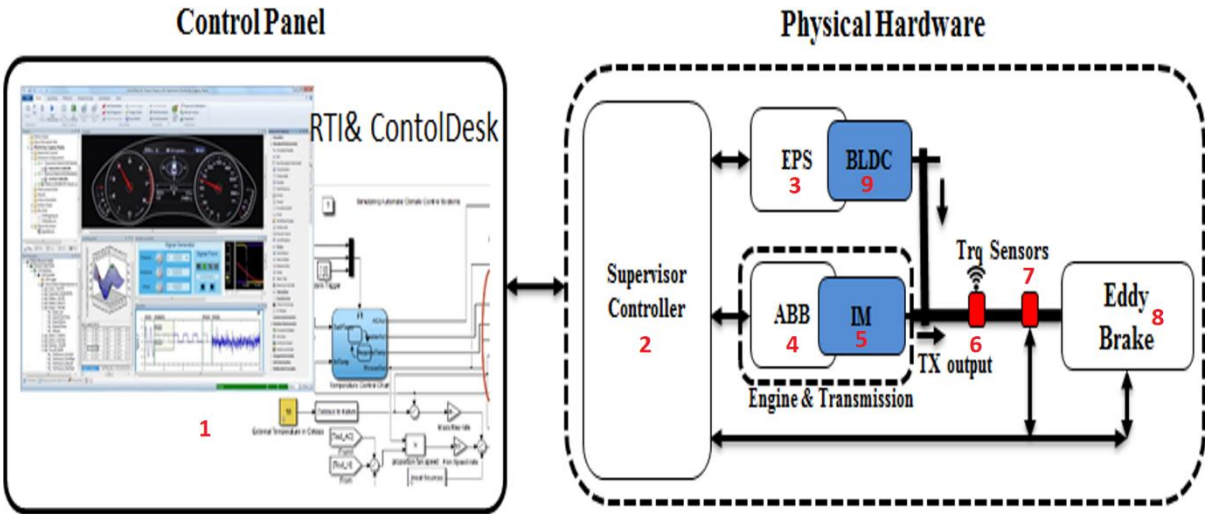

Figure 5.20 Conceptual system structure

The test bench can be used to simulate any driving scenario. HIL has been well-described in the literature, particularly for test and verification of vehicle drivetrains under specific driving cycles (Brown & Kotori 2013; Fotouhi et al. 2018; Oh 2005; Trigui et al. 2007, *inter alia*).

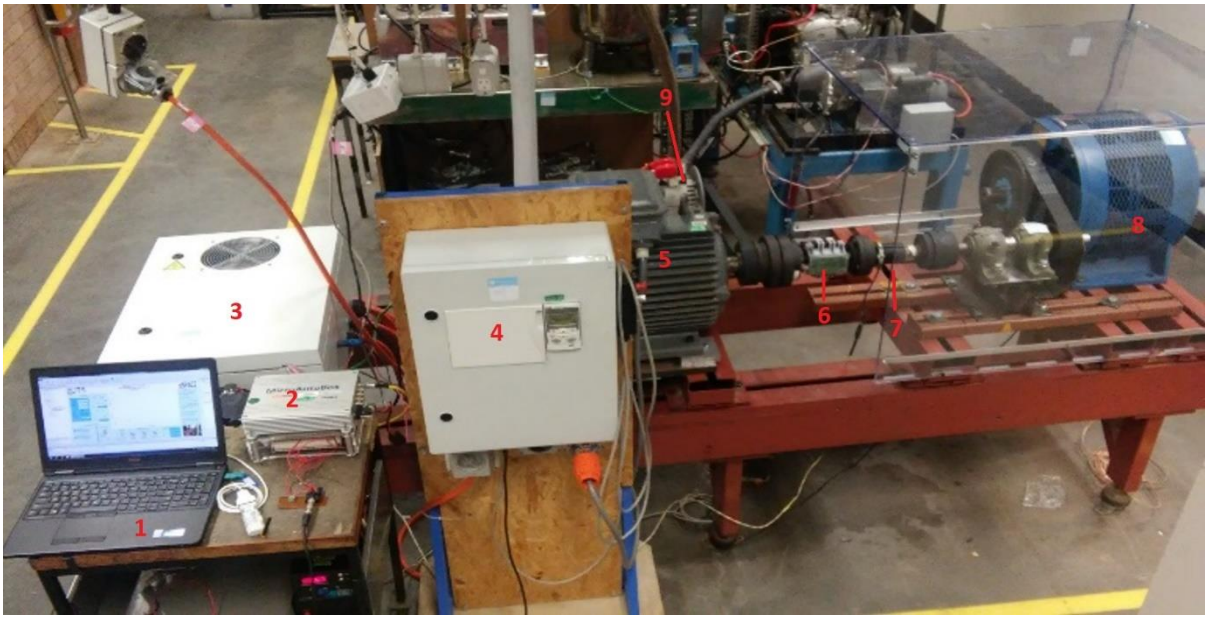

Figure 5.21 The HIL test bench as constructed

The HIL test bench was designed for the purpose of testing the continuous torque delivery function of the EPS, which requires simulating a gear change and managing the modulation of torque demand between the engine and EM. This particular focus was chosen because of the difficulty of obtaining repeatable gear change characteristics in a prototype vehicle equipped with a manual transmission (MT) and using a human driver for gear and clutch actuation. In order to determine effective calibration of the system, the HIL approach is the most effective method, as torque modulation and gear change characteristics are controlled by the host PC and can be simply changed using parametric values in the model.

In operation, the virtual vehicle model is used to generate a gearbox output shaft torque signal, which is then used as a control signal for the engine simulation motor (ESM). The ESM is connected to the motor used in the EPS using a belt-driven power take-off (PTO), which is topologically equivalent to the on-axis post-transmission location of the electric motor in the MHEV powertrain. The simulation captures the bi-directional interactions between its actual and virtual components using a combination of external transducers (shaft encoders and strain-gauging torque transducer) and internal datalogging of commanded

outputs. The setup implements a fixed step-size routine to ensure continuous synchronization between the virtual simulator and real-time. This is implemented within the MATLAB real-time workshop.

The same principle can be used to develop most generalized HIL environments – connected loads on either side of the system under test are simulated using generalized emulation devices which are controlled by a software model. Providing the software model and emulated devices are of sufficiently high fidelity, the system under test can be developed rapidly and with a high degree of confidence. Naturally, insufficient development of the software model or inability of the physical emulation device to accurately reproduce simulated output limits the value of the HIL process as a development tool.

5.5.1 HIL Bench Model

The top level RTI-Simulink blocks used for the control of the test bench is shown in Figure 5.22. The sub-systems are: drive cycles, control units, EPS, ESM controller (ABB), torque transducer, and shaft speed encoder. Each block contains I/O, ADC, DAC, encoder, and CAN blocks from the RTI blockset. Additionally, the controller block uses the feedback from the torque sensor and shaft speed encoder to track the speed and torque and compute the required output, closing the control loop (Figure 5.23).

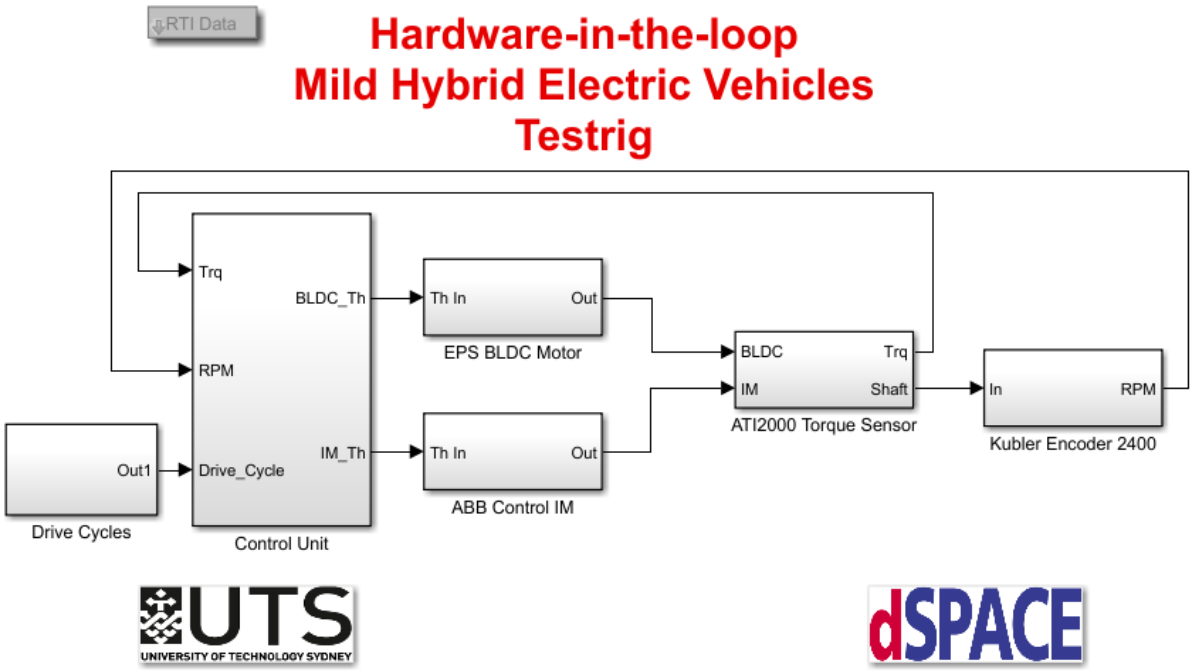

Figure 5.22 The top level of the RTI-Simulink blocks used for the Test Rig

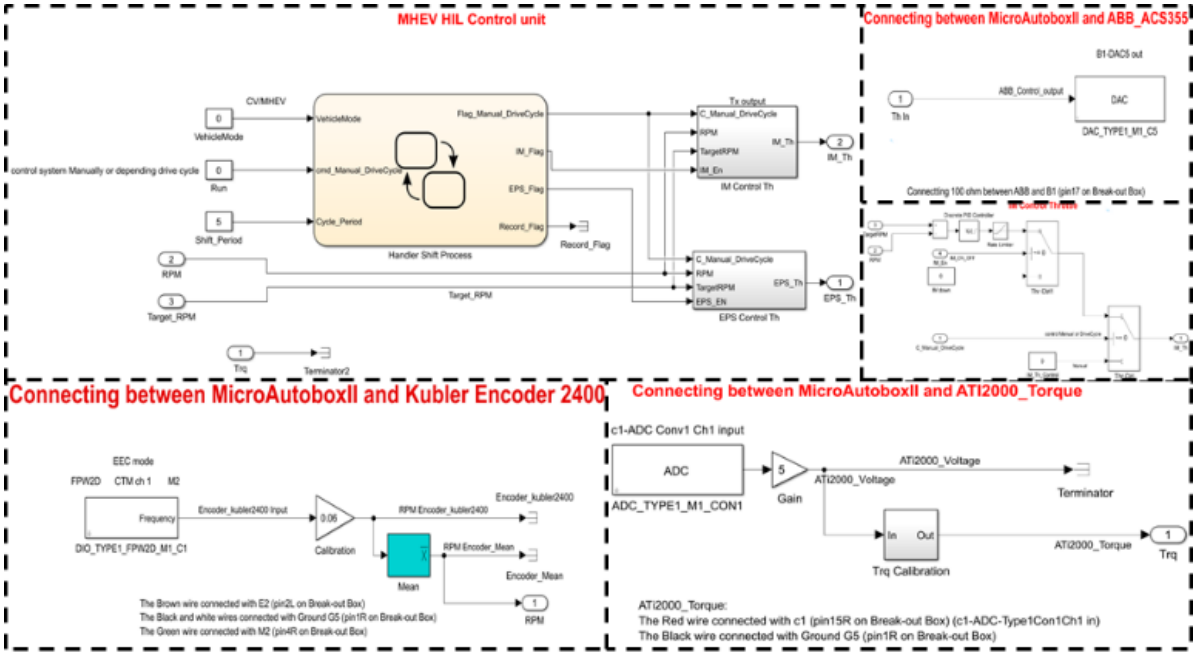

Figure 5.23 Test rig modelling control design

5.5.2 Control Panel

Figure 5.24 shows the virtual control panel (dashboard) for the HIL simulation. The dashboard is the monitoring interface and also provides user controls for driver throttle, brake and key input control signal. The dashboard is used to set up simulation parameters such as cycle selection and speed control, as well as displaying simulation outputs, including shaft torque and speed. The data is updated in real-time based on the input and can be datalogged. The MicroAutoBox II communicates with the host PC at a frequency of 1 MHz, and data can be logged at 1 KHz.

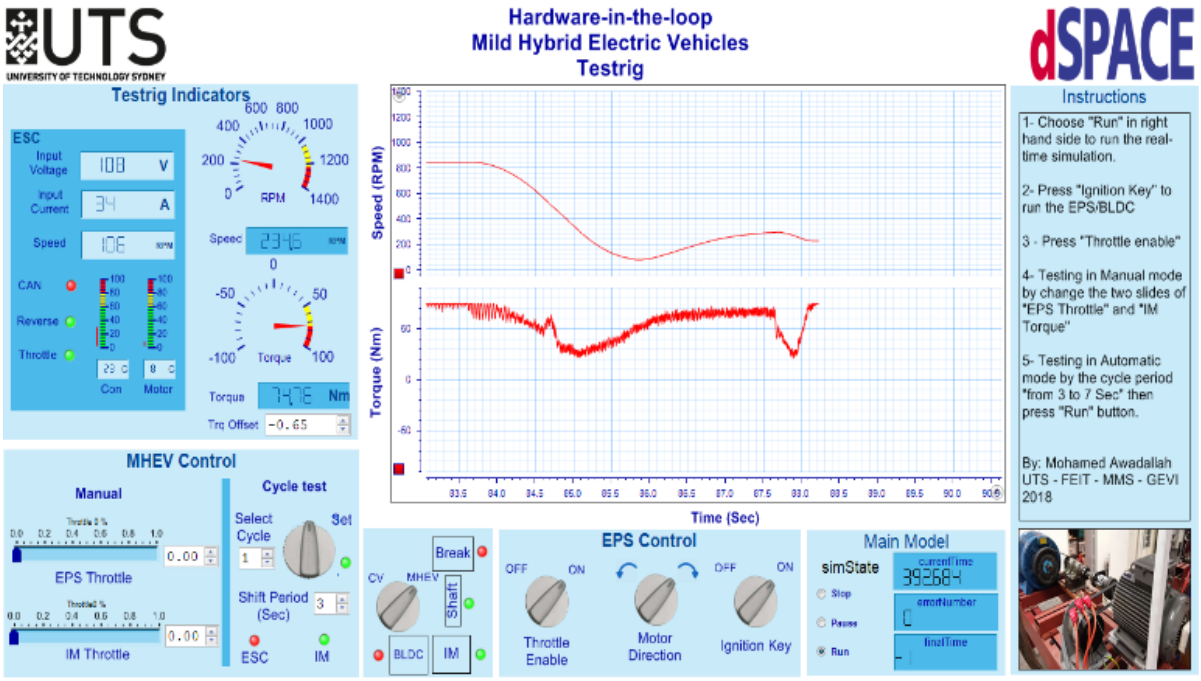

Figure 5.24 PC display panel for data acquiring, variables changing in ControDesk

5.5.3 Test Scenario

The continuous torque delivery scenario essentially mimics a gear change, and then commands the EPS motor to provide infill torque. To mimic the gear change, a cruise condition is achieved using the ESM to drive against a defined load. A gear change command

is initiated which causes the software model to simulate the clutch disengagement. This results in a zero torque command being sent to the ESM.

This torque drop is sensed by a torque sensor and triggers the torque infill subroutine, which controls the EPS motor to fill in torque until the gear change event is finalized, which is flagged by the simulation of the clutch re-engagement. When the gear change event is over, the ESM resumes a non-zero torque value. This is sensed separately and used by the supervisory controller to turn off the torque-filling function. Data acquired over the gear change event can be analysed in post-processing for system calibration and improvement of emulation fidelity. Varying parameters in the torque infill subroutine allows system calibration. Parameters include the clutch position value at which torque infill is initiated and terminated, torque rise rate and fall rate, and PID parameters.

The results of the torque hole simulation are shown in Figure 5.25 (a)-(c). These are compared to experimental results in Chapter 9.

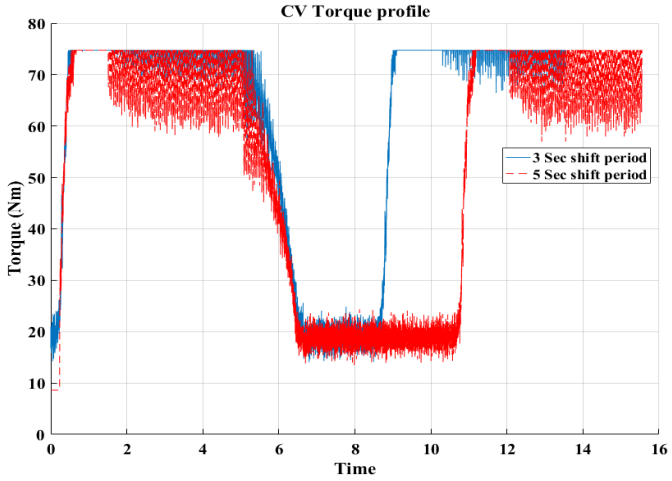

a. CV Torque in different shift period

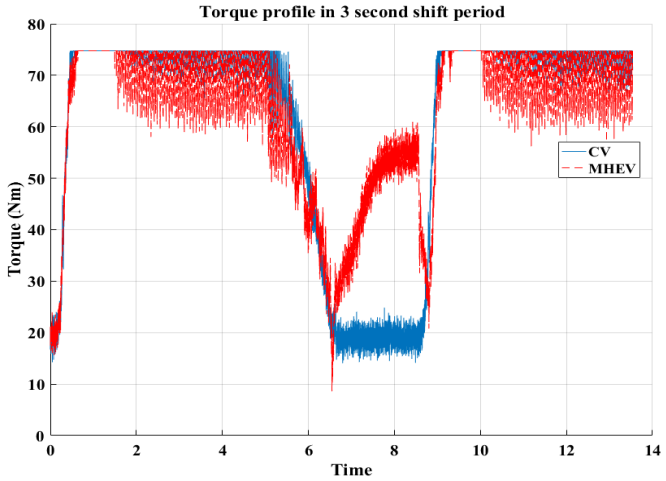

b. MHEV Torque profile in 3 seconds shift period.

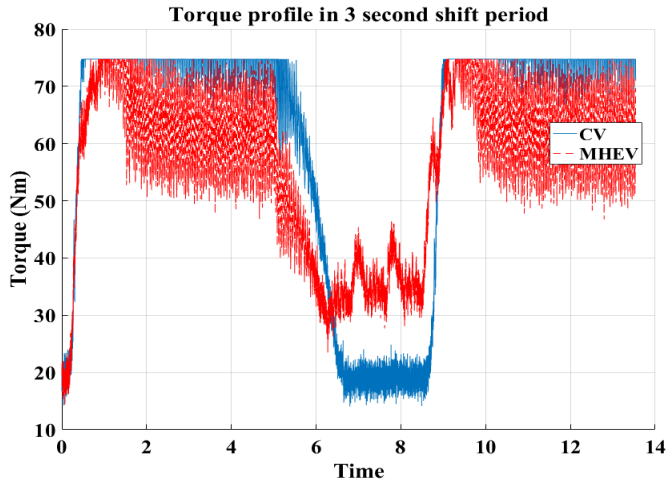

c. MHEV Torque profile in 3 seconds shift period with PID.

Figure 5.25 HIL torque profile

5.6 Summary

The simulation, RCP, and HIL process was used as part of the V-model for product development. It was necessary to follow the process of modelling, simulation, control prototyping, and then HIL testing to gain an understanding of the functionality of the system, as well as develop an initial system calibration that could be used with a high level of confidence on the prototype vehicle. This is important as it reduces the time taken on system development using the prototype and provides some verification of system operation prior to the validation stage. The control architecture and the detailed functionalities of the system in simulation, RCP and HIL stages are discussed in detail. The HIL test bench allows for the integration of the EPS for testing, but also, importantly, allows a wide variety of powertrain configurations to be tested owing to its relatively simple opposed on-axis source and sink configuration. Simulations of longitudinal vehicle dynamics can be accomplished using a range of virtual powertrain configurations and environments.

The real-time modelling completed using HIL principles allowed rapid verification of fundamental system design decisions made for this HEV system, particularly as they relate to the continuous torque delivery functionality. The HIL model could be further refined by replacing the eddy current brake with a DC motor controlled in four quadrants, and adding an emulated engine with ripple control rather than the relatively simple torque source that was used for the ESM. However, there is further work that could also be completed in terms of improving fidelity of the HIL software model that could also improve the current setup without significant expense. More refinement on the HIL hardware components would negate its advantages in development time, and reduce the resources available for the development of the future prototype.

The process followed and described is the model-based design (MBD) development process, which represents a series of development challenges that have been met using a selected

combination of state-of-the-art software and hardware tools. The EPS model was designed using a combination of high-level programming languages and graphical environments. Draft control algorithms were developed and optimized using a rapid control prototyping process, which utilized a development platform capable of controlling the EPS componentry and containing a significant and easily modifiable feature set to allow flexible, efficient, and quick prototype evaluations. Once the acceptable performance has been achieved in the laboratory, the final step in embedded control development is EPS Calibration, which incorporates the fine-tuning of system and control parameters using vehicle prototype testing. This is discussed further in Chapter 8 and 9. Alternatively, further refinement could also be achieved on a more fully developed HIL test bench incorporating greater hardware emulation capability.

Chapter 6: Prototype Assembly

Assembly of the prototype vehicle required significant engineering design to successfully retrofit the hybrid powertrain components to the existing base. The primary powertrain components being installed are the electric motor, battery pack, and controller. Secondary components include sensors and transducers, safety cut-off devices, mounts, and other ancillary hardware. The assembly can be categorized into mechanical fabrication and assembly, which describes the considerations relating to physical driveline mounting, alignment and vibration management, and the electrical assembly, which includes electrical connections between the various sensors, controllers, and actuators, battery pack assembly, and mounting or fabrication of sensors and subsystems.

To provide ease of reference, terminology used throughout this chapter is depicted in Figure 6.1:

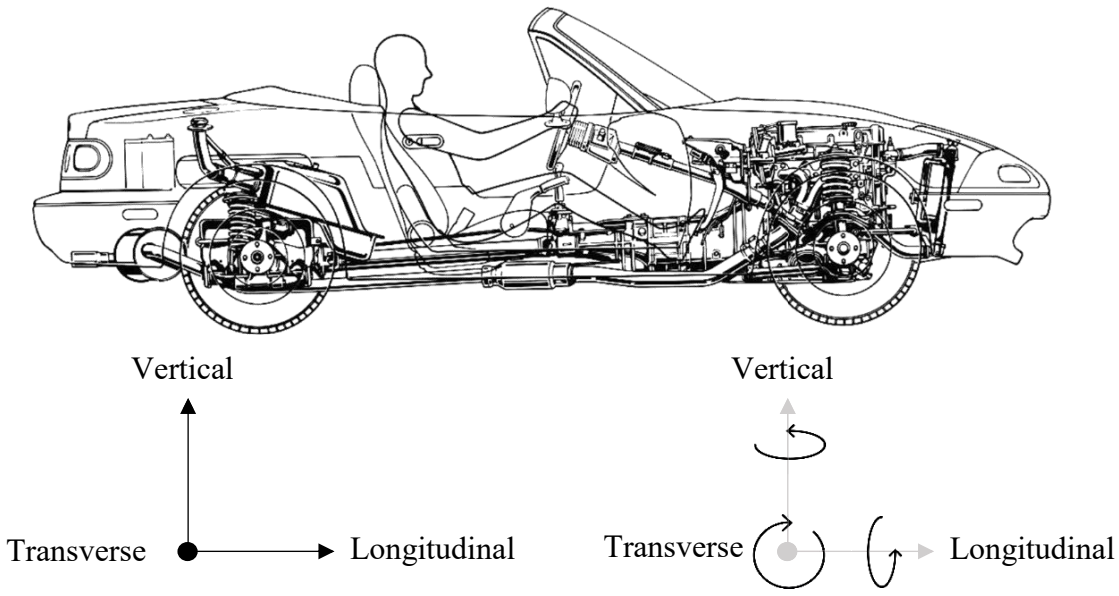

Figure 6.1 Axes of linear and rotational motion (terminology)

6.1 Overview

The physical construction of the prototype vehicle was designed as far as possible to fit without significant modification to the vehicle structure. Minimizing ancillary changes outside of those strictly required for the functionality of the prototype allows a more accurate comparison between the base vehicle functionality and the prototype. For this reason, as well as for the reasons of accessibility and ease of modification, many of the additional parts that constitute the electric side of the powertrain are located sub-optimally from a manufacturing perspective. For instance, the traction motor is placed medially in transmission tunnel, necessitating a split prop shaft design, rather than being directly flanged to the differential or being integrated with the transmission extension housing. However, such locations in the prototype vehicle are generally chosen to aid the testing process – for instance, the split prop shaft allows for the simple and direct measurement of torque before and after the motor, which would not be easily possible if the motor is flanged to downstream or upstream components. Topologically, the differences are also insignificant, relating mainly to the location of the prop shaft spring constant and inertia values.

The donor vehicle was specifically chosen after lengthy investigation into the best platform on which to build the prototype. This investigation is described in Chapter 4. The platform is quite unique due to its convertible, rear-wheel drive, lightweight nature. These characteristics made it ideal for conversion to P3 hybrid topology. The folding roof was removed to make room in the cabin for mounting the system controllers and ancillary electronic components such as optocouplers and relays, which occupy the roof stowage space on the rear parcel shelf. The front-engine, rear-wheel drive powertrain simplified the addition of the AC Induction motor at the transmission output shaft, which would have required extensive, costly, and difficult modification to fit to a transaxle housing in a front wheel drive application. Instead, the modifications were relatively simple welded additions to the unibody

and rear subframe to provide mounting locations for the motor and differential. Due to the low kerb weight of 990kg, keeping the total modified kerb weight under 1200kg as required by the design goals, was relatively straightforward.

The list of assembly tasks described in detail in this chapter are, in summary order of execution:

1. Remove Powerplant frame (PPF)
2. Design, fabricate and install body-transmission mount
3. Design, fabricate and install differential mount
4. Design, fabricate and install electric motor mount
5. Install electric motor
6. Design, fabricate and install motor input and output flanges
7. Shorten propeller shaft for re-use as transmission output shaft
8. Design, fabricate and install motor output shaft
9. Install strain gauge torque sensors on transmission output and motor output shafts
10. Install electronic throttle body
11. Install electronic throttle pedal
12. Install and wire throttle body controller
13. Assemble and 96V install traction battery pack
14. Install and wire battery management system (BMS)
15. Install and wire Curtis 1238e motor controller
16. Install, wire and plumb motor controller cooling system
17. Install and wire system sensors
18. Install and wire dSpace MicroAutoBox supervisory controller

6.2 Mechanical Assembly

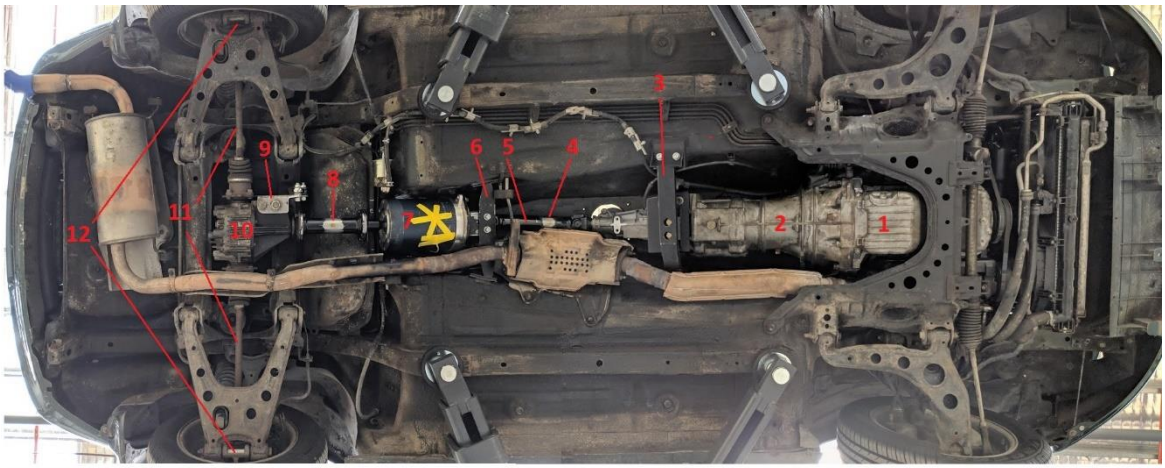

Powertrain Components

1. Engine
2. Transmission
3. Transmission mount
4. Output shaft torque sensor (strain gauge)
5. Transmission output shaft
6. Electric motor mount
7. AC Induction motor
8. Motor output shaft (dogbone shaft) Includes shaft torque sensor (strain gauge)
9. Adjustable differential mount
10. Differential
11. Driveshafts
12. Wheel & hub assemblies

Figure 6.2 Vehicle underside showing the powertrain assembly and layout

Mechanical assembly of the hybrid powertrain required mounting of the electric motor within the driveline, in the footprint of the prop shaft. In summary, this required the removal and shortening of the prop shaft, removal of a longitudinal member connecting the differential and transmission, fabrication of an electric motor output shaft, fabrication of a replacement differential mount, replacement differential mount, and electric motor mount, and minor relocation of exhaust hardware. The resultant powertrain is shown in Figure 6.2. Additionally, in order to allow for electronic engine speed control, the cable-operated throttle body was replaced with an electronic throttle body. The throttle pedal was also replaced with a hall-effect type throttle pedal. The control of the throttle body was accomplished using a Pololu JRK12V12 motor controller.

The front and rear sections of the powertrain are connected for power transfer through a prop shaft measuring 950mm in length. The prop shaft is contained within a 290mm diameter transmission tunnel, in which the motor must also be mounted. A C-section beam known as a

powerplant frame (PPF) runs within the transmission tunnel, statically constraining the relative angular motion of the transmission and differential subframe in the transverse axis (Figure 6.3). The PPF is a rigid member connecting the gearbox and differential, running parallel to the prop shaft. Its role is to limit angular misalignment of the transmission output flange and differential input flange, as well as providing rigid axial mounting and co-location for the transmission and differential.

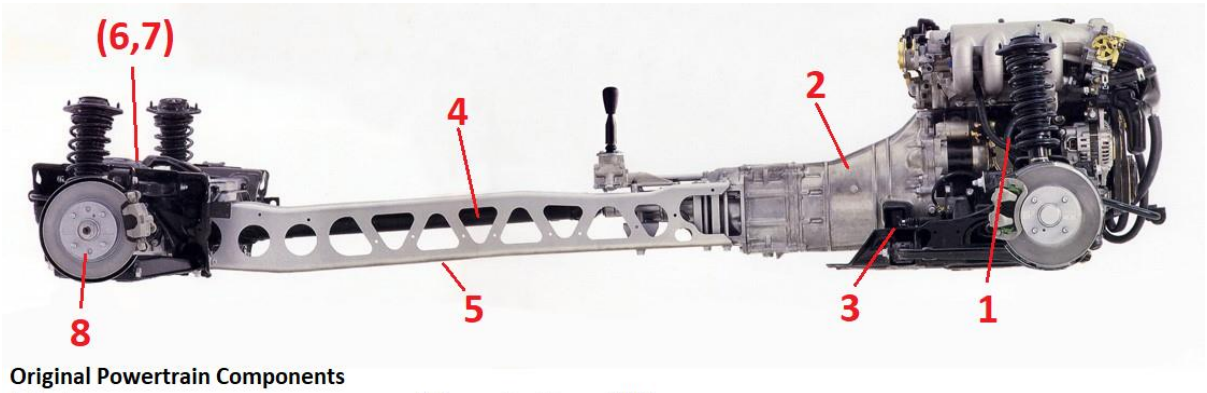

Original Powertrain Components

1. Engine
2. Transmission
3. Transmission mount
4. Output (propeller) shaft
5. Powerplant Frame (PPF)
6. Differential (not shown)
7. Driveshafts (not shown)
8. Wheel & hub assembly (wheel not shown)

Figure 6.3 Standard MX-5 powertrain showing the PPF connecting front and rear assemblies

The PPF and the prop shaft run longitudinally down the vehicle chassis within the transmission tunnel. Due to space restriction within the tunnel, mounting the electric motor inline with the prop shaft requires the removal of the PPF. This necessitates alternative solutions for the angular alignment and axial location of driveline components. Rigid transmission and differential mounts were designed and fabricated, relying on the unibody frame of the vehicle to support the powertrain reaction forces.

6.2.1 Transmission support cross-member

The transmission support was built of the cross-member type, fabricated from mild-steel rectangular hollow section (RHS) and flat plate. It was rigidly secured to the vehicle floor pan using welded reinforced plates with threaded mounting holes, and supports the gearbox atop a rubber pillow mount with a shore hardness of 52. This shore hardness was chosen to be identical to the left and right engine mount shore hardness. The engine and gearbox are interfaced rigidly and bolted together at a planar interface. They are considered to be a rigid assembly. The engine is mounted at its left and right side, providing constraint in the vertical and longitudinal rotational axes. The transmission support cross-member constrains the assembly in the transverse rotational axis, replacing the function of the PPF and mounting using the existing mounting boss cast into the transmission housing. It is not adjustable, therefore using materials of similar properties for all three mounts assists in keeping vibrations from the assembly in phase.

6.2.2 Differential Mount

The differential is mounted in three locations. The existing wing mounts cast into the differential casing are retained. These wing mounts are through hole rubber bushings which retain the differential within the rear subframe. The wing mounts provide constraint in the three linear axes of motion, as well as in the vertical and longitudinal axes of rotation. To

constrain rotation in the transverse axis of rotation, a third mount was fabricated. The third mount is rigid, fabricated from aluminium by re-using the end-section of the PPF. This allowed for the existing differential mounting holes to be re-used. A link with adjustable rod-ends was bolted to the re-used section of the PPF. On the opposing end, the link is secured to the rear assembly subframe using a bolt-through bracket, fabricated of welded mild steel. The adjustable link is used to finely adjust the pinion angle, ensuring that angular misalignment of the front and rear sections of the drivetrain are minimised.

6.2.3 Electric Motor Mount

The electric motor was mounted using a NEMA 143TC face mount plate, which is integrated with a transverse cross-member located medially across the transmission tunnel. The motor is mounted and supported at its forward face only, and relies upon a rigid bolted connection to the differential input flange for support of the rearward end of the motor. The NEMA 143TC face mounting standard allows for cantilever mounting as implemented. Because the 143TC face mount was used, no rubber vibration damping elements are utilised between the chassis and the motor face. The motor may be considered to be a rigid element of the vehicle structure. This arrangement was selected as the motor, which is double-ended, is equipped with sliding spline shaft sockets on each end. If compliance is introduced in the motor mount, an extra degree of freedom is introduced in the system. This can lead to problems with driveline vibration, as the motor mount may be excited by existing system imbalances.

6.2.4 Rotating Assembly

Due to the location of the motor within the transmission tunnel, new rotating hardware was required to replace the single-piece prop shaft connecting the transmission and the differential. The rotating hardware consists of four separate assemblies. These are; the front

prop shaft, the electric motor input flange, the electric motor output flange, and the differential input shaft.

The rotating hardware was fabricated from mild steel, with the exception of the front prop shaft, which was made by shortening the factory-installed single-piece prop shaft to suit the new application.

The front prop shaft is a double-cardan shaft with a female spline interfacing the transmission output shaft, and a four-bolt flange interfacing the motor input flange. The motor input flange splines into the electric motor's rotor, which is equipped with a Dana Spicer 7/8" 19-spline input. The motor output is a 7/8" shaft with a ¼" keyway. For this reason, the motor output flange is keyed to the rotor and then the shoulder of the flange was welded to provide increased joint strength. The output flange is also a four-bolt flange, as is the differential input flange. Between them a rigid "dog bone" shaft completes the driveline.

All fasteners used for the assembly were grade 8.8 M8x65mm bolts.

6.2.5 Electronic Throttle Body

An electronic throttle body was required to replace the existing cable-operated throttle body, which could not be electronically controlled using the EPS. The existing throttle body assembly combines two functions. It includes the primary throttle valve which is actuated by the throttle pedal, and also includes an idle speed control (ISC) valve, which regulates the bypass air allowed around the primary throttle valve to control engine idle speed. The ISC valve is a rotary valve that is driven using a pulse-width modulated signal to regulate idle speed. The function of the valve is primarily engine temperature related, providing higher bypass air when the engine is cold to increase idle speed. Its function and location in the intake system are provided in Figure 6.4. Electronic throttle bodies are not usually equipped with secondary valves because the idle speed control can be accomplished using the primary

valve. Instead, a small relief is usually present in the valve which provides a failsafe should active control be impossible. The relief ensures a minimum amount of air bypasses the throttle valve to prevent engine stall, but does not provide closed-loop speed control.

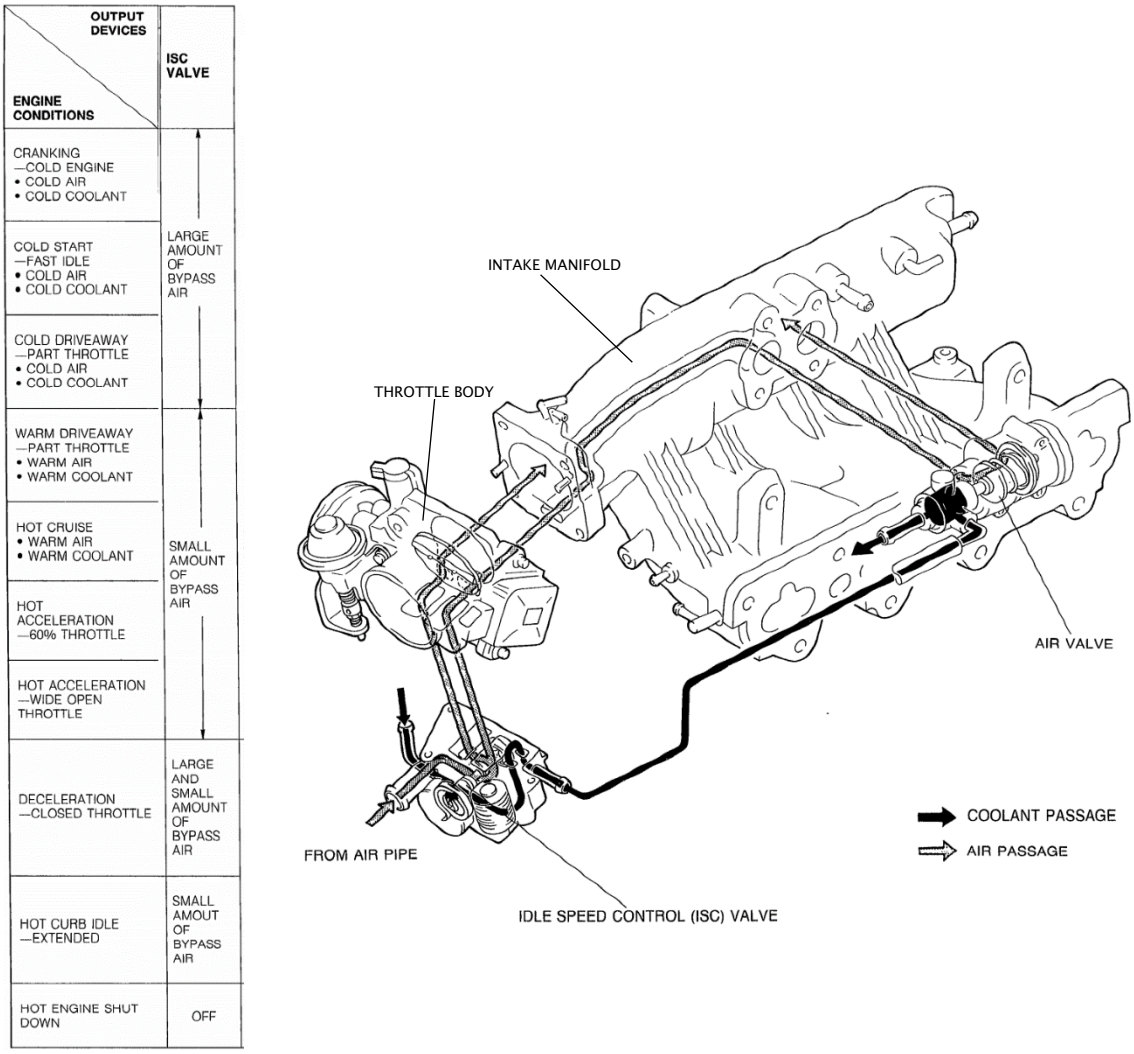

Figure 6.4 Standard intake system arrangement (Mazda Motor Corporation 1989)

The physical constraints for the electronic throttle pedal are that it must match the standard throttle diameter of 55mm and the mounting face must be physically similar to the original throttle so that it can be mounted to the intake manifold. A throttle body from a Toyota Estima ACR50, bearing part number 22030-28070 was found to be suitable. The throttle body matched the original diameter of 55mm, and the mounting stud pattern was near

identical, with the only change being the bottom-left hole in the intake manifold requiring drilling to slot it out by approximately 4mm (Figure 6.5). Once slotted, the throttle body could be mounted to the manifold directly. A custom gasket was used between the mounting faces, which also served to seal the idle bypass passage in the intake manifold.

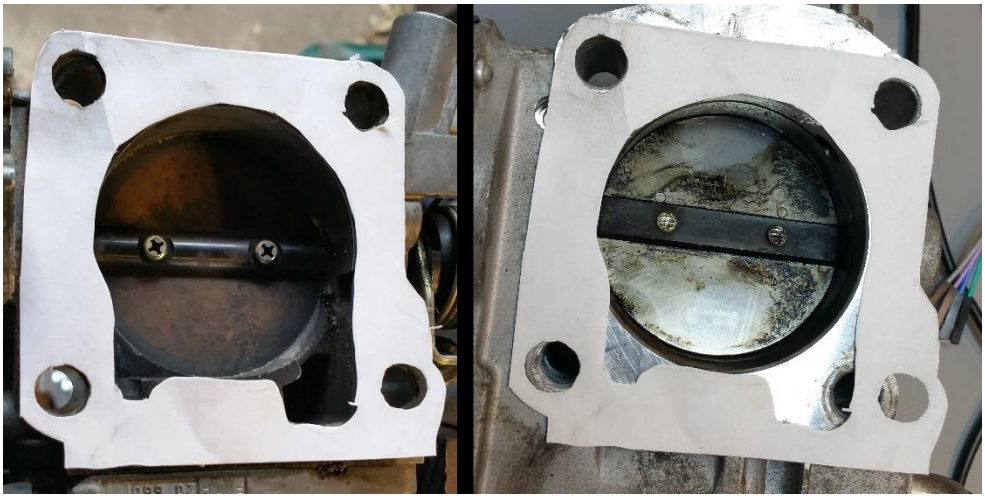

Figure 6.5 Comparison of manual (left) and electronic (right) throttle body flanges

6.2.6 Electronic Throttle Pedal

The base vehicle throttle pedal is a simple lever operating a Bowden cable. The Bowden cable is connected to a sprung 90° bellcrank which operates the throttle valve.

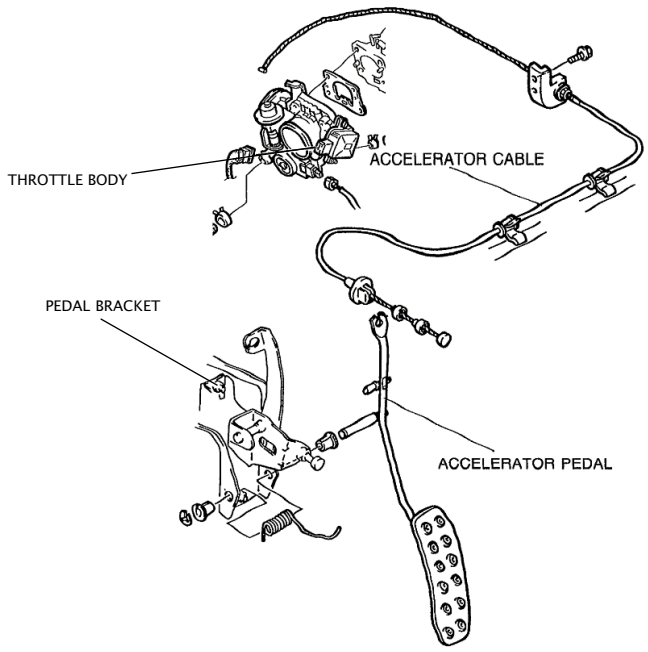

Figure 6.6 Standard throttle pedal arrangement (Mazda Motor Corporation 1989)

To control the electronic throttle body, a suitable electronic throttle pedal was required. Electronic throttle pedals are typically hall-effect sensors mounted on a foot-actuated pedal. A 0-5V output is provided to a servomotor controller which then drives the throttle valve to the corresponding position. The base vehicle throttle pedal assembly was removed from the vehicle and in its place, a Toyota throttle pedal bearing part number 78110-28010 was installed. The base vehicle pedal is mounted from a bracket on the firewall in the pendant style. However, for simplicity, the electronic throttle pedal was mounted in reverse on the floorpan of the vehicle in the organ pedal style.

6.2.7 Traction Battery

The traction battery was built into a laser-cut prismatic housing made of 8mm fire resistant plywood. A false floor made of 16mm plywood was installed into the vehicle boot, to which the battery housing was affixed. The false floor was not affixed to the vehicle, but its tight fit in the boot ensured the battery was immobile.

6.2.8 Motor Controller Cooling

A small convective cooler was required to cool the motor controller, which is supplied with a sandwich-plate type cooling pad fabricated from aluminium. The convective cooler is a Davies Craig transmission oil cooler which is placed in free air on the rear parcel shelf sill (Figure 6.7). A Davies Craig EWP115 electric water pump is used for flow control. The pump has a maximum flow of 115L/min which was significantly higher than is required, but for the purpose of prototype validation this was acceptable. The total capacity of the cooling circuit is less than 3 litres.

Figure 6.7 Davies Craig water pump and transmission cooler used for cooling the Curtis 1238E

6.2.9 Improvements

Whilst the powertrain modifications were fit-for-purpose for the development of the proof-of-concept prototype, several simple improvements were identified upon testing. These improvements pertain to the drivetrain.

The principal improvement that could be made is the mounting of the motor using both faces, rather than just the forward 143TC face plate. The cantilever mounting introduced a radial load on the motor output shaft, and even though the shaft was rigidly connected between the differential and motor, excessive vibration was introduced into the driveline. This was

because of slight misalignment between the motor output and differential input. The through-hole bushings mounting the differential provided sufficient compliance to take up much of this vibration, and the effect was not noticeable in measured data, however, test driving the vehicle on the dynamometer revealed excessive in-cabin vibration. Double-hanging the motor by using the second face for mounting would have minimized much of this vibration.

Additionally, if the motor was not cantilevered, an articulated shaft or joint could be utilized between the differential and motor. Such articulation could include the use of a double-cardan shaft, or the use of a guibo or flex disc between flanges. This would make the drivetrain more robust to minor misalignment, although the introduction of an extra compliant element such as a guibo would be a significant departure from the system as modelled in software, and therefore this was not a preferred solution from the point of view of system validation.

Another drivetrain improvement that could be made is the reduction of the joint angle of the front prop shaft. The motor rotational axis is coincident with the rear differential rotational axis. However, the motor input is shifted approximately 700mm forward from the differential input flange. Because of this significantly decreased distance between the transmission output and the motor input, the front prop shaft operates at a joint angle of approximately 17°. Whilst this did not result in any noticeable vibration, the high angle necessarily results in increased parasitic losses and wears the cardan joints prematurely. Optionally, the motor could be flanged directly to the transmission extension housing, although this would have required significant fabrication work to relocate exhaust hardware and modify the tail housing.

6.3 **Electrical Assembly**

The vehicle is equipped with both a 12V electrical system and a 96V traction system. The 12V network is powered by a 6-cell sealed lead acid battery mounted in the rear of the vehicle. It is used to power engine sensors and the engine control unit, ancillary components

such as lights and driver aids, and the dSpace MicroAutoBox II supervisory controller. The network is referenced to battery negative ground, and the vehicle chassis is tied to this reference.

The 96V traction system is powered by a 30-cell lithium iron phosphate battery pack mounted in the rear of the vehicle. The battery pack is solely used for providing tractive power for the motor. It is connected to the motor controller through a Gigavac GV200-QA1 contactor and fused at 200A, which represents a discharge rate of 5C. The motor controller uses field-oriented control (FOC) to control the 3-phase motor torque. The 96V system is floating with reference to the 12V chassis ground. This reduces the risk of ground isolation faults causing the chassis to energize to the same potential as the battery.

There are a number of devices that require connection to both the 12V system and the 96V system. The Curtis 1238E controller uses 12V for system control power, as well as the Orion BMS2. Both these devices are internally isolated and equipped with both a high-voltage and low-voltage ground, to prevent ground isolation faults through the device. The dSpace MicroAutoBox II is equipped with only a single ground. It interfaces with the motor controller to command a motor throttle value, and to read motor encoder information to determine drivetrain and vehicle speed. Because both these signals are referenced to the traction battery ground, it is necessary to isolate the signals from the dSpace. Optical isolation is used to achieve this.

The electrical subsystems assembled within the vehicle include the Curtis 1238E motor controller, Orion BMS2 48 cell battery management system, Orion Thermistor Expansion Module, the battery pack consisting of 30 individual 40152s LiFePO4 cells, the Pololu JRK12V12 motor controller, and the dSpace MicroAutoBoxII rapid prototyping controller.

Additionally, several sensors, switches, and ancillary components were required as part of the assembly.

A battery pack mount was fabricated in the rear storage compartment of the vehicle. This is particularly convenient as the rear storage also contains the 12-volt battery and its associated wiring. It allows the battery pack to be built as one unit rather than distributed wherever it may fit, and puts the pack in proximity to the motor and controller, limiting the length of cable runs.

Most other electronic systems, including the motor controller, BMS, and supervisory controller, were mounted on the rear parcel shelf. The exception to this is the electronic throttle controller, which was mounted in the engine bay near the intake manifold, using a custom-built housing.

The following sections provide detail on some of the the electrical subsystems with schematic diagrams to aid understanding.

6.3.1 Battery and BMS

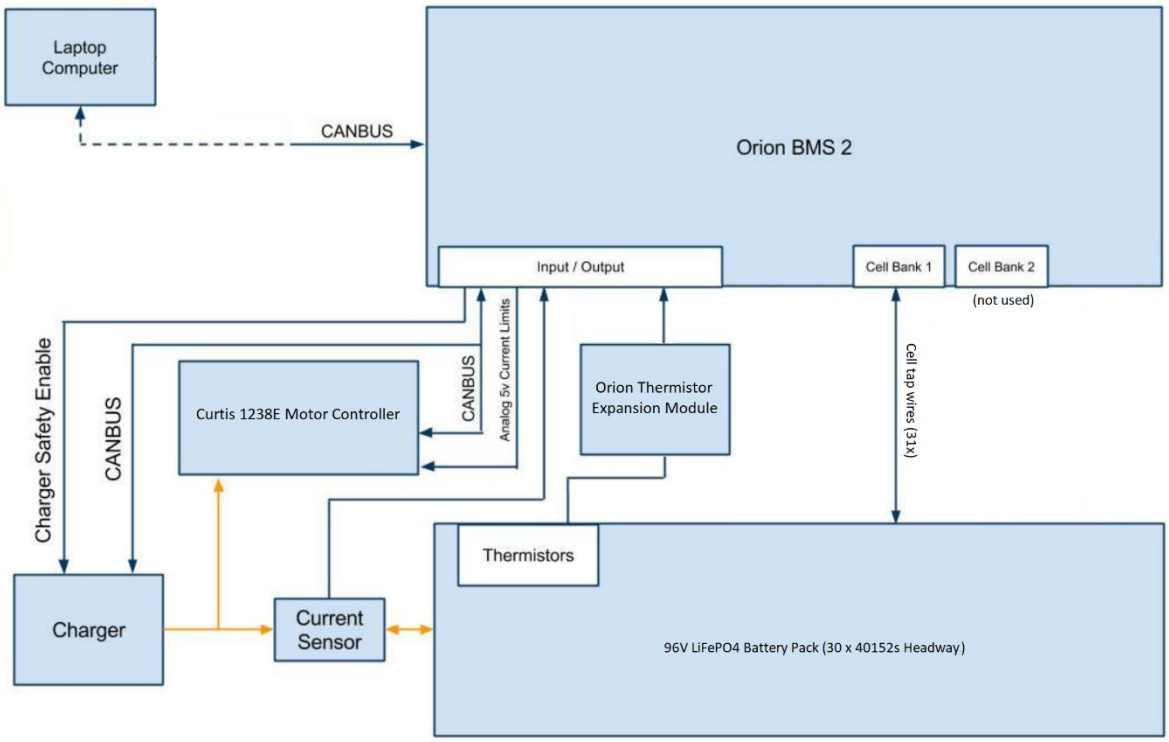

Figure 6.8 BMS Connection diagram

The battery is a 96V pack comprised of 30 Headway 40152s battery cells. Each cell is a 15Ah $LiFePO_4$ cylindrical unit. The pack provides a nominal total of 1.44kWh storage and is electrically connected as a single string in series. It is physically arranged to be two cells deep and 15 cells wide. The Orion BMS2 has two connections to each individual cell in the pack. The connections are cell voltage taps, which are arranged at the junction of each cell and its adjacent cell, as well as the pack positive and negative terminal, and thermistors, which are physically adhered to each cell to monitor cell temperature. The BMS monitors individual cell voltages, resistances and temperatures, as well as the pack voltage, resistance and temperature, calculating SOC and balancing cell voltages to ensure no parasitic draw occurs within the pack, which optimizes cell life.

A current transducer is placed on the positive output on the pack. The current transducer is used to measure pack current draw and control limits. The hard safety limits are controlled directly by the BMS through its discharge enable output, which switches the contactor. Soft limits can also be used to vary the maximum current draw depending on temperature or battery safety characteristics. The soft limits are communicated to the Curtis 1238E motor controller using a CAN bus line, which operates on the CANOpen protocol.

6.3.2 Electric Motor Throttle Control

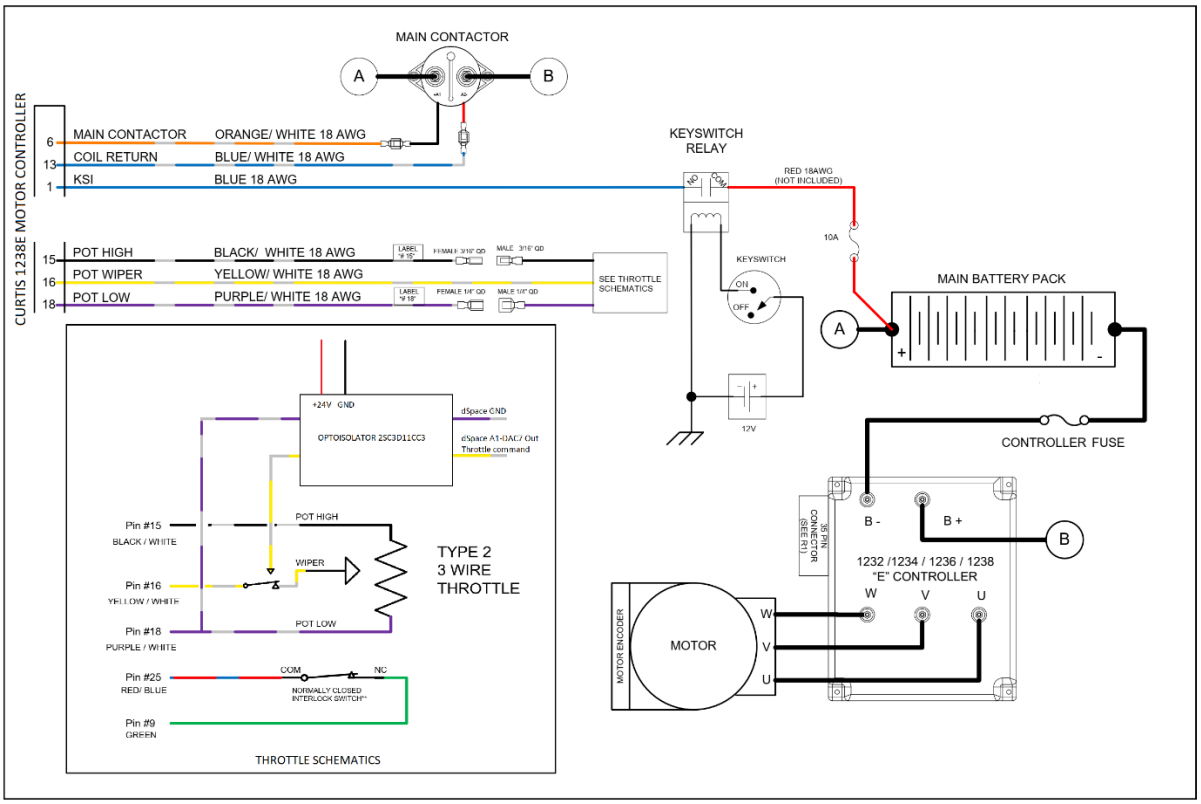

Figure 6.9 Electric motor throttle control system schematic

The electric motor throttle input is on pin 16 of the motor controller. Manual and automatic controls are provided using a single-pole double-throw switch to connect the controller alternately between a 5kΩ potentiometer or the dSpace throttle input. The dSpace throttle input is isolated using a GIC 2SC3D11CC3 analog signal converter. The manufacturer of the

isolator claims the introduces a small delay of no greater than 100ms, however in practice no noticeable delay was present.

6.3.3 Electronic Engine Throttle Control

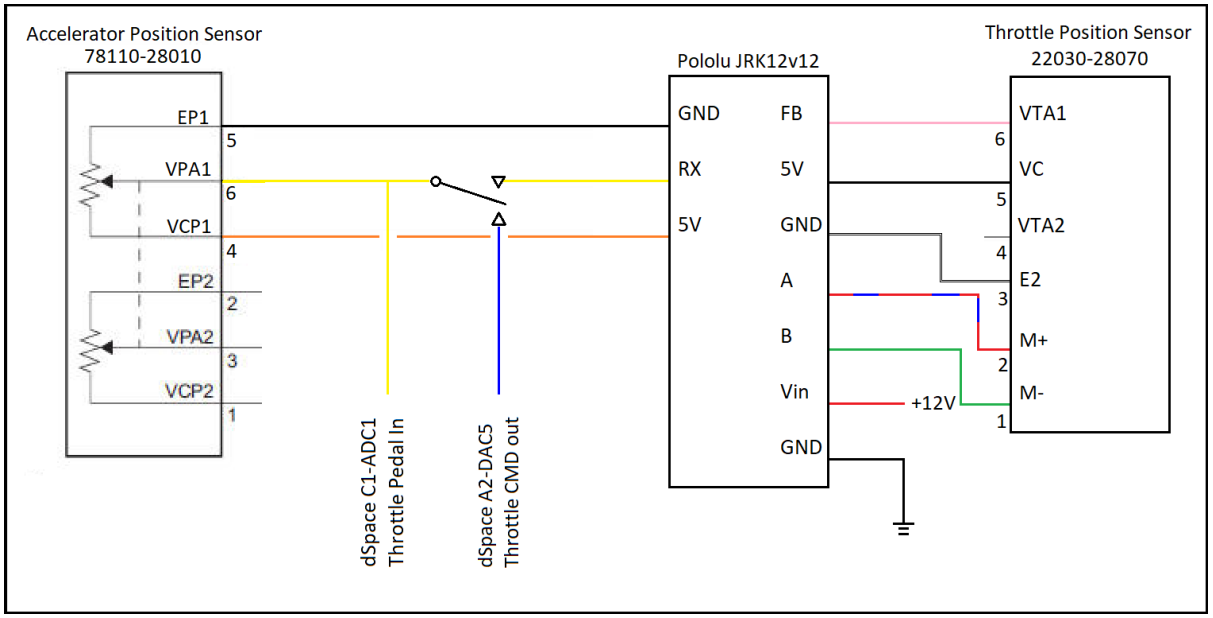

Figure 6.10 Engine throttle control system schematic

The engine throttle control was accomplished using a Pololu JRK12v12 motor controller. The motor controller is a general-purpose closed-loop servomotor controller operating on 12V and supplying up to 30A peak current. Feedback control is accomplished using a PID loop with a 0-5V position signal from VTA1, which is output from the throttle position sensor. Because PID control is accomplished onboard JRK12v12, the feedback signal VTA1 is not monitored by the supervisory controller.

The throttle pedal position input is provided at accelerator position sensor pin VPA1. The output is a 0-5V signal. VPA1 is also connected to the supervisory controller at position C1-ADC1 at all times. In hybrid operation, the supervisory controller reads the VPA1 signal and compares it to the engine efficiency table. If a more suitable operating point can be found, the VPA1 signal is modified by the supervisory controller and sent to JRK12v12. Otherwise, the

signal is simply repeated. For continuous torque mode, the supervisory controller monitors the clutch switch input and gear position inputs, and if a gear change is sensed, VPA1 is modified to control engine speed proportional to target gear engine speed. This minimizes inertia discontinuity on clutch re-engagement and also reduces transient emissions from sudden throttle position changes.

An SPDT switch is placed on the VPA1 signal wire to allow the supervisory controller to be simply switched in and out of the circuit. This allows direct engine control if the supervisory controller is not onboard the prototype, or if a fault has been detected.

6.3.4 Supervisory Controller

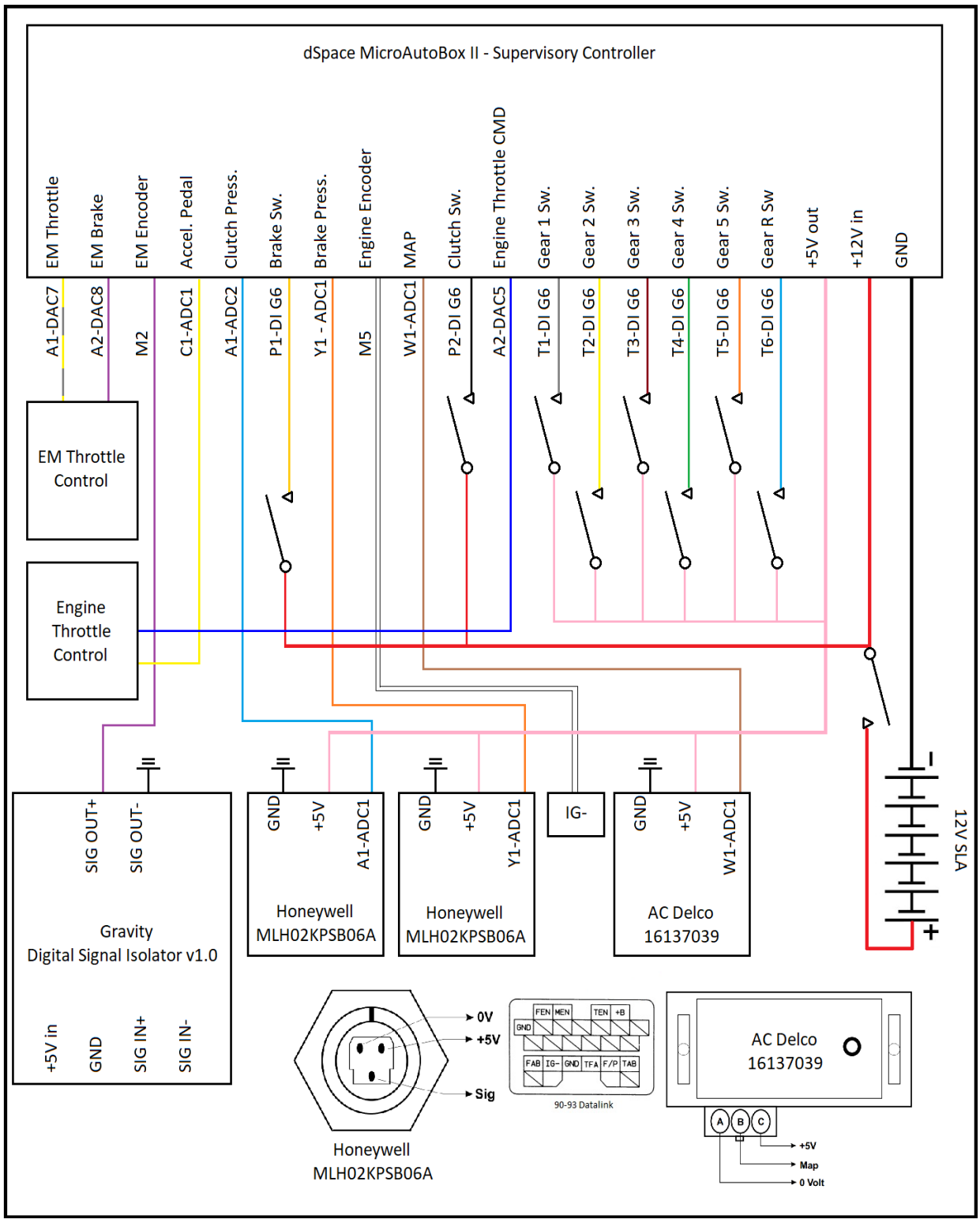

Figure 6.11 Supervisory controller schematic wiring diagram
(EM throttle and Engine throttle are shown in previous sections)

The supervisory controller is responsible for the co-ordination of the hybrid system. It is the main hybrid drive controller and takes data from engine operation, vehicle environment, and EPS sensors to determine the appropriate instantaneous split between engine and electric motor operation.

The supervisory controller determines engine operating condition using a manifold absolute pressure sensor (W1-ADC1) and the existing engine encoder (M5). From these, the controller can determine engine operating conditions using a lookup table, to obtain engine torque, BSFC and other information.

The supervisory controller also determines the transmission state using gear position sensors (T1-DI G6 to T6-DI G6) which are momentary switches shorting inputs to the 5V output to indicate selected gear. It is also provided with a clutch switch input (P2-DI G6) which provides information on clutch pedal actuation and a clutch pressure sensor (A1-ADC2) which is used to estimate clutch engagement. These inputs allow it to determine the selected gear, estimate the target gear and clutch re-engagement.

Speed and torque target information is provided using the EM Encoder (M2) and the Accelerator Pedal Position sensor (C1-ADC1) respectively. The EM Encoder is a 64-tooth wheel that provides a resolved prop shaft speed. The information is used to calculate and target a specific engine RPM during gear change processes to ensure there is no inertia discontinuity when clutch re-engagement occurs. The information is also used to arm and disarm the continuous torque gear change mode, so that no attempt is made to provide continuous drive torque if the speed is below that at which a gear change could be expected. The accelerator pedal position is converted into a driver torque request which is the basis for the operation of the hybrid controller.

The brake switch input (P1-DI G6) is used by the controller to break the continuous torque delivery algorithm. It is also used to engage regenerative braking, which is regulated using proportional control from the brake pressure input (Y1-ADC1).

6.4 Summary

The mechanical and electrical assembly of the prototype vehicle has been described. The mechanical assembly extended to fabrication of mounts and restraints for the rotating assembly, as well as replacement of the rotating assembly between the transmission output and the differential to accommodate the electric motor within the transmission tunnel. In addition, the engine throttle was converted to an electronic system instead of the original Bowden cable type. This necessitated modification of the engine intake manifold by slotting one of the throttle body mounting holes to accommodate an electronic throttle body selected from an ACR50 Toyota Estima. This throttle body was deemed to be the most suitable replacement to the base vehicle throttle body because it was geometrically very similar – sharing the same throttle diameter, centre axis, axial length, and very similar mounting hardware. The idle speed control valve was replaced with open-loop control of idle speed for the purpose of prototyping. This was chosen for ease of implementation as well as suitability, considering the purpose of the prototype was to provide system validation in a controlled environment, therefore idle is unlikely to require significant variation due to environmental stability. An electronic throttle pedal was installed in place of the pendant type pedal. Cooling for the motor controller was satisfied using a small transmission oil cooler and electric water pump. The cooling hardware was over-specified but adequate for the purpose of validation.

Electrically, the main subsystems assembled included the battery and BMS, motor controller, electronic throttle control for the engine, and the supervisory controller. The high voltage systems (battery, BMS, and motor controller) are equipped with a floating ground with reference to the low-voltage vehicle systems which use the chassis tied to the negative

terminal of the 12V battery as the ground reference. Because these systems are designed for EV applications they are equipped with separate grounds for 12V connections and high voltage connections. However, the supervisory controller is only equipped with a single ground reference which must be tied to the 12V battery negative (and chassis). In order to eliminate any potential for ground isolation faults which may cause the chassis to become live at high voltage system potential, optical isolation is used whenever a sensor is required to be connected to both a high-voltage subsystem and the supervisory controller. In this case, the electric motor throttle signal and EM encoder signal are both optically isolated from the supervisory controller.

Chapter 7: Torque Sensing and Control

This chapter describes the sensing and control developed for the MBD testing phase of the project, which followed the conclusion of the HIL verification. The test cell phase involves the integration of the prototype plant, in this case KERMIT IV, with the controller, and the verification of the controller operation on the prototype plant. It is the final stage of the development process which then allows experimental validation testing to take place. The integration of the dSpace MicroAutoBox controller with the prototype and the control methodology are discussed in the following sections, as is the verification of the controller's operation using MIL testing prior to the installation on the prototype. This discussion is with particular reference to the control of the gear change torque in-fill function of the controller which is a key element of novelty in this project.

The torque sensing, which is based on a custom-built Bluetooth torque transducer PCB using strain-based torque sensing, is also discussed in this chapter, with particular reference to its use for the estimation of driveline-induced jerk.

7.1 System Layout

Conceptually, the virtual model of the vehicle, constructed in the dSpace ControlDesk environment mirrors exactly the system layout of the physical prototype. Figure 7.1 shows the virtual system layout. The MicroAutoBox II is directly connected to every system component except the BMS, which operates independently

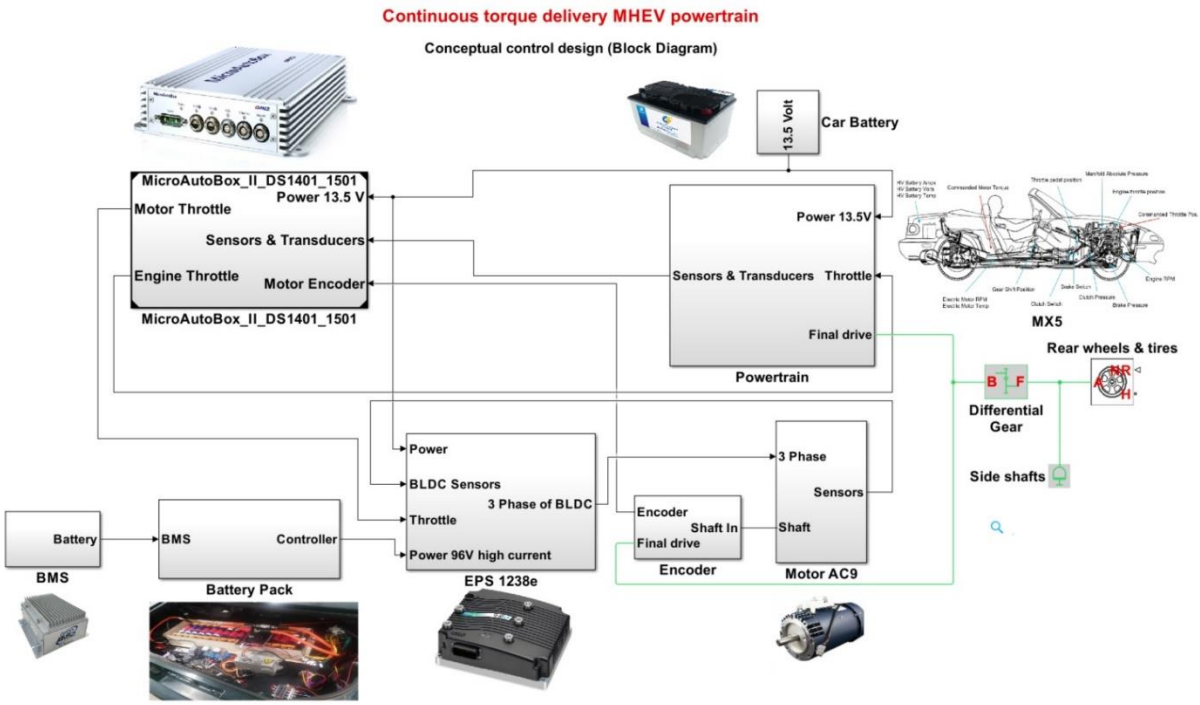

Figure 7.1 The system virtual model mirrors the physical prototype

7.2 Control Model

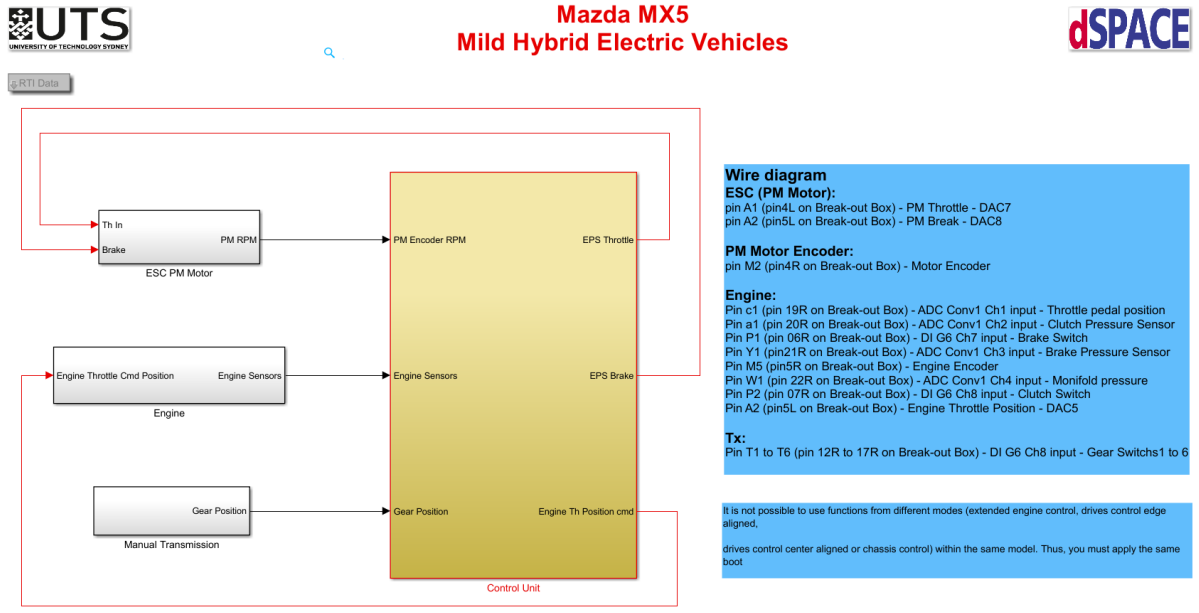

Figure 7.2 Top-level control model representation showing the control unit (right) and ports (left)

The control model for the vehicle consists of a control unit, which is represented at the top level using its input ports and output commands, the ports, which group sensors and actuators and are arranged functionally, and wires, which represent the logical flow of the control algorithm. The top-level system control model is shown in Figure 7.2. The control unit has three closed control loops. These loops are the EPS throttle, EPS brake, and engine throttle position command. The EPS throttle and brake simply work to operate the motor in forward and reverse torque directions, thereby providing electric motoring and regeneration. The loops are kept separate because the inputs on the Curtis motor controller, controlling throttle and brake are on separate pins. The engine throttle position command is used to control the load state of the engine or track engine speed to transmission input shaft speed, depending upon the state of the clutch.

The three ports are functionally grouped into the electric motor port, which provides encoder information only to the control unit, the transmission port, which provides gear position information only to the control unit, and the engine port, to which all engine-related sensors are wired, including; throttle pedal position, throttle valve position, clutch pressure sensor, clutch switch, brake pressure sensor, brake switch, engine encoder, and manifold absolute pressure.

7.2.1 Control Unit Architecture

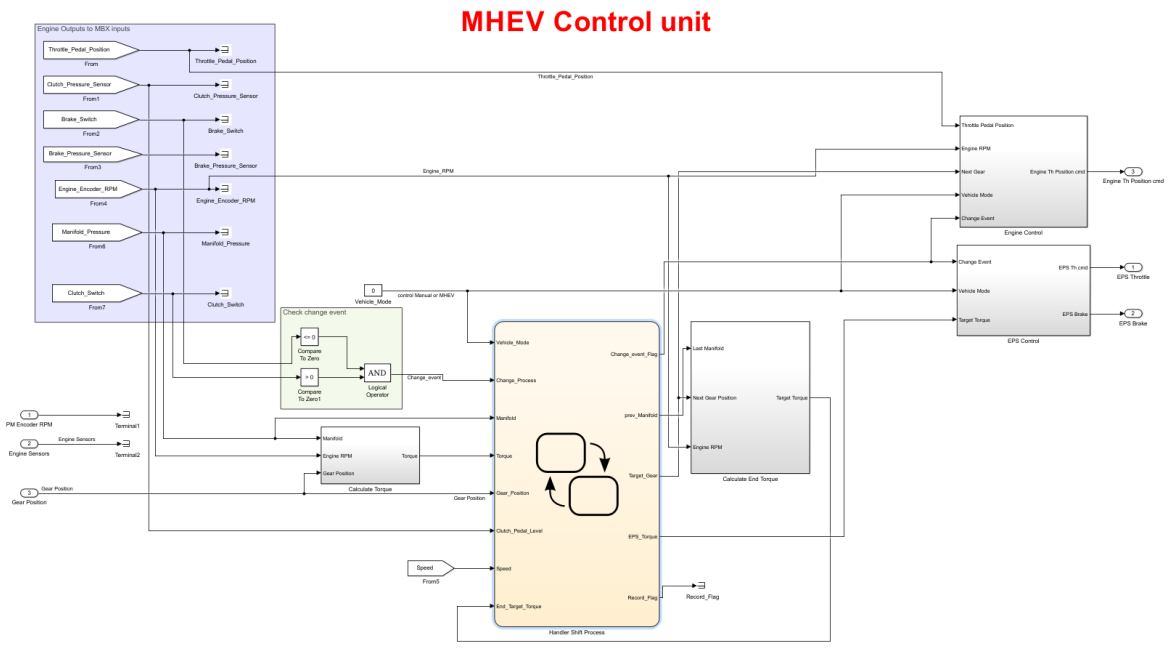

Figure 7.3 Second-level representation of the control unit, showing subsystems and state machine

The second-level representation for the control unit maintains the same programmatic visual structure as the top-level view. Subsystem models are introduced in the controller for determining calculated values and outputting control commands. Subsystem models are designed for control of the electric propulsion system (EPS), engine control (throttle position command), and calculation of start and end torque for the gear shift torque infill. A state-flow machine monitors measured and calculated inputs in real time, issuing control commands to subsystems and actuators. The second-level control unit architecture is internally open, linking to the top-level for its feedback loops.

The control unit for the infill torque is shown in Figure 7.3. In normal operation there are three parallel processes. These processes are “calculate torque”, “calculate end torque”, and “engine control”. The fourth process “EPS control” operates when the state-flow machine detects a gear change event. This sets a flag, “change_event_flag” to true, which then

controls the EPS according to the values calculated by the processes “calculate torque” and “calculate end torque”.

7.2.2 Stateflow State Machine

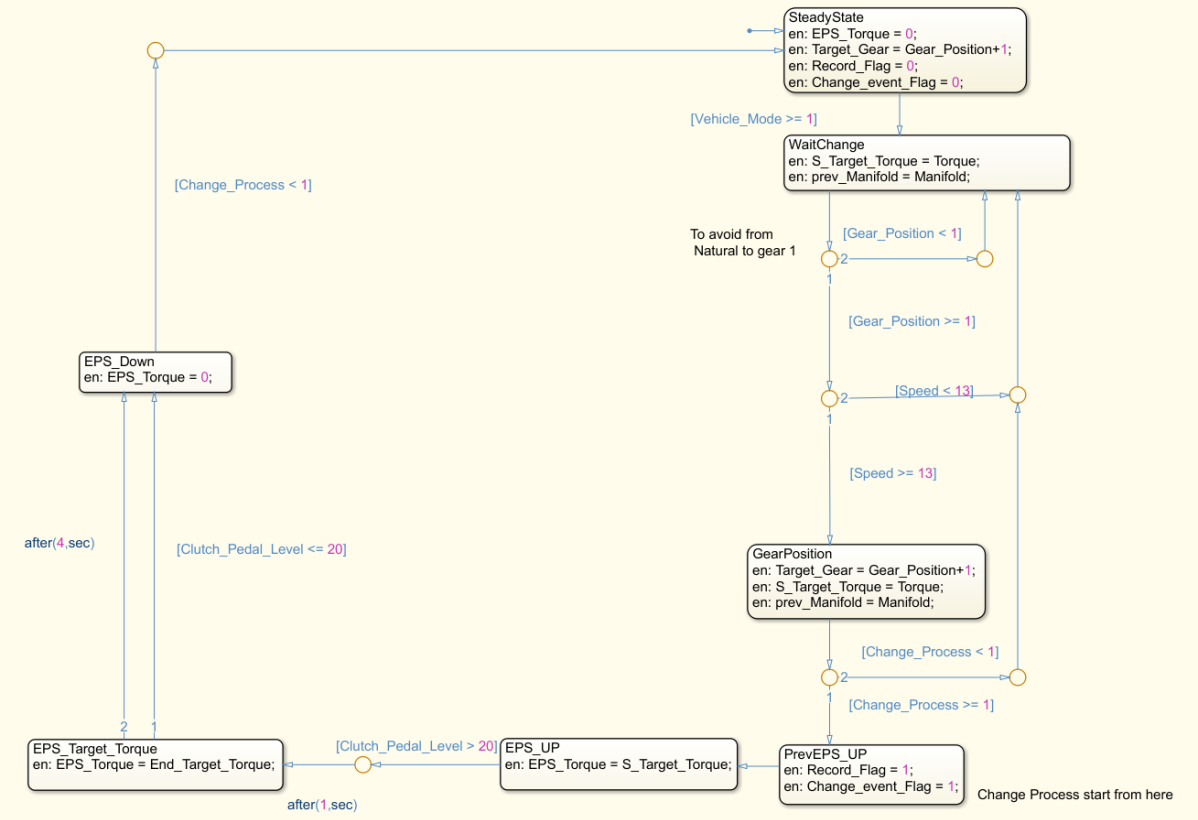

Figure 7.4 Gear change continuous torque delivery state machine

The stateflow machine (Figure 7.4) is essentially a logical control flow diagram which monitors inputs to determine the state the system is in, and defines system outputs based on the actions during that state. For the gear shift infill torque, the stateflow machine begins with a neutral setting wherein target torque is zero and no gear change is assumed. The stateflow machine uses the clutch switch to initiate the torque infill mode. However, if the previous gear position is neutral or the speed is less than 13km/h, the clutch switch is ignored. This logic is used to avoid any infill torque being provided when the clutch is disengaged at rest or low speed, when the driver may be feathering the clutch to crawl the vehicle along. Above

13km/h, if the clutch switch is true, a change event flag is set. This arms the EPS controller, which engages the electric motor to provide torque at the “calculate torque” value. This torque is provided for as long as the clutch pressure value remains above 20% or no greater than one second. The time of one second was chosen because it is equivalent to a relatively aggressive shift, taking into account the entire shift process rather than just the gear change actuation. After one second, the stateflow machine uses the “calculate end torque” value to command the EPS controller. The difference between the “torque” and “end torque” values is equal to the difference between the current gear and target gear ratios. The “calculate end torque” value is held for a maximum of four seconds, meaning that the infill torque is provided for no longer than 5 seconds in total. At any point during the five seconds, if clutch pressure value drops to 20% or less, the infill torque is disengaged.

7.2.3 Torque Model Calculation

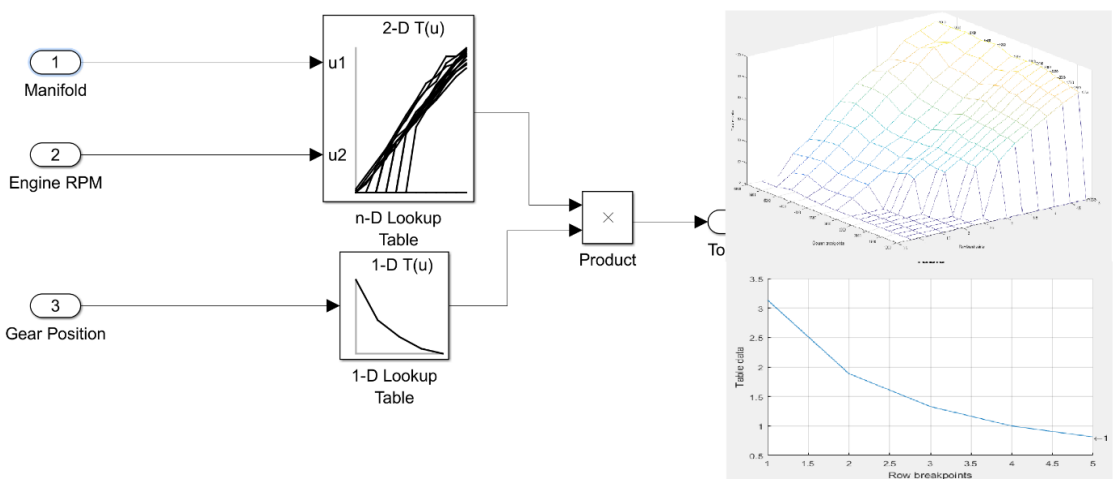

Figure 7.5 The "Calculate Torque" subsystem. The Calculate End Torque subsystem is similar but uses the next gear value instead of current gear value

The torque calculation model (Figure 7.5) uses an engine torque map which is described by engine speed (RPM) and manifold vacuum pressure. The map is input into the n-D lookup table block, and was derived experimentally, and is reproduced in Figure 7.6. The manifold

pressure and RPM are measured in real-time and used to determine the engine's torque load prior to clutch disengagement. The load is multiplied by the gear reduction which is provided using the gear position sensors. A 1-D lookup table contains the gear ratios. The product of the engine load and gear reduction is the calculated torque.

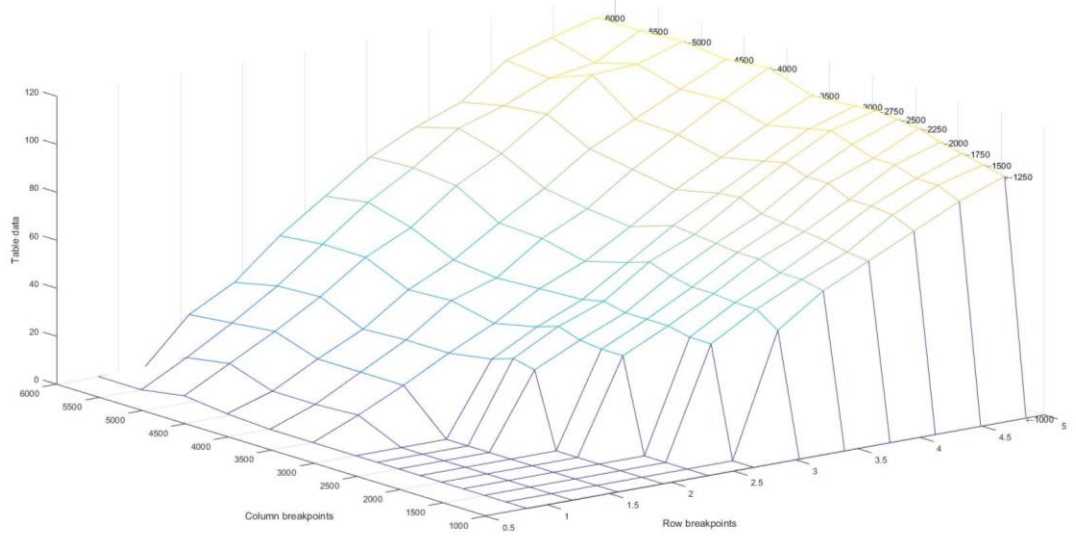

Figure 7.6 An engine torque map was experimentally-derived and was used to determine target torque infill values

The calculated end torque is determined in the same manner as the calculated torque, but the gear ratio multiplier is the next gear ratio, rather than the current ratio. This means that calculated end torque is always lower than calculated torque. As a result, down-shifts are deliberately not optimally infilled. This strategy is chosen for two main reasons. Downshifts are usually executed either due to decreasing vehicle speed requiring the selection of a lower appropriate gear, or due to driver demand for greater tractive torque. In the first instance, tractive torque is undesirable when the vehicle speed is decreasing, and if the brake is activated then regenerative braking mode will be required rather than torque infill mode. In the second instance, the system is not designed to provide the full engine torque capability,

and therefore the partial torque fill-in will also satisfy the driver need without exceeding battery safety limits.

7.2.4 Engine Throttle Control

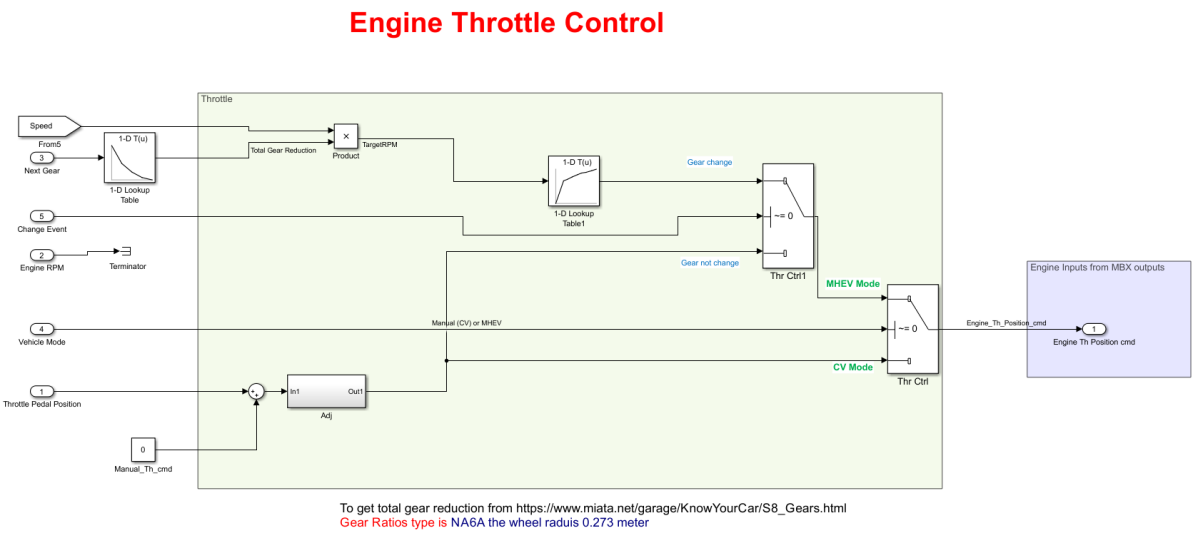

Figure 7.7 Engine throttle control subsystem

The engine throttle control is used to maintain engine speed equal to the transmission input shaft speed at the moment the target gear is engaged. This ensures that the clutch, which is splined to the transmission input shaft, and the pressure plate, which is bolted to the engine flywheel, are rotating at the same velocity when the target gear is engaged, and minimizes inertia discontinuity by eliminating the need to accelerate or decelerate the engine using clutch friction to match the transmission input shaft speed. Because the clutch is actuated by the driver, engine throttle control is the only means available to minimize vibration (lurch) caused during speed synchronization at re-engagement. The engine throttle control within the torque infill control unit has two modes of operation. The first mode of operation is simply a signal pass-thru. This mode is used in most cases of operation – that is when a gear change event is not flagged or when the vehicle is operating in conventional mode (i.e., no electric

propulsion is engaged). In the case of a gear change event, the subsystem reads the propshaft speed from the motor encoder, and matches the engine speed to the transmission input shaft speed using the “target gear” value. It does this by varying the throttle valve position. There were two methods available to control the throttle valve position. The first method is the implementation of a PID controller to vary the throttle opening according to engine speed feedback. This method is robust and fault-tolerant, but may take time to develop and tune PID parameters. The second method is open-loop control based on table data (Newberger & Johnson 2014). Open-loop control offers a significant speed of development advantage but is only highly accurate under constant conditions. Most applications of speed control for gear changes use an open-loop control based on look-up tables (Dolcini, De Wit & Béchart 2008), although there are also closed-loop systems (Gavgani et al. 2015) that are preferable when there is a higher level of gearshift automation. In this case, because the engine throttle control is being used in the laboratory environment which can be maintained essentially constant, and is only used in gear shifting mode when the engine is disengaged from the drivetrain, there is little need for full PID control, particularly as the main aim of the experimental work was the validation of the torque infill. Therefore, the no-load throttle values were plotted against engine speed and used for open-loop control. The throttle values are shown in Figure 7.8. Testing showed this control method to be acceptable for the application.

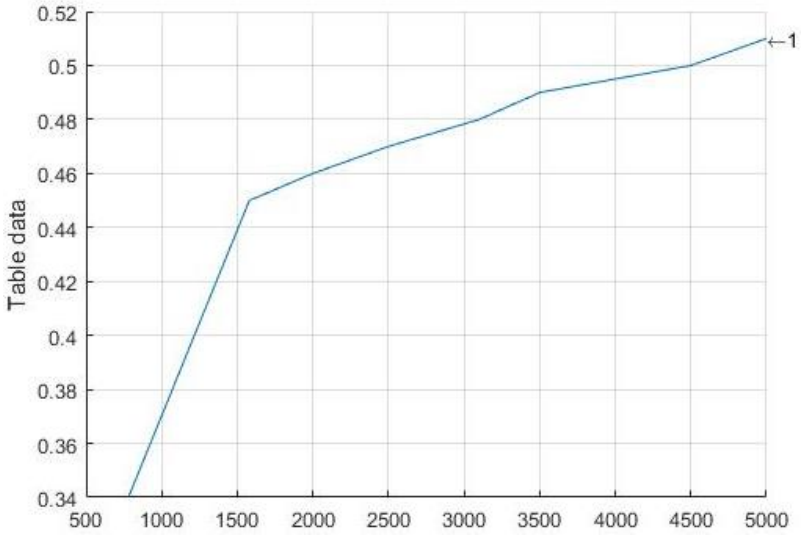

Figure 7.8 Engine throttle control was achieved using a 1D lookup table with throttle valve position plotted against engine RPM

7.2.5 Control Unit Verification

After the control unit was developed, it was verified using only model-in-the-loop principles by deploying dashboard library components. The dashboard library is a series of virtual instruments that can be used to insert input and read values at any point in the control loop. The input values are adjustable and can be either manually controlled or automated, and output values can be read using meters or datalogged. The dashboard setup is shown in Figure 7.9.

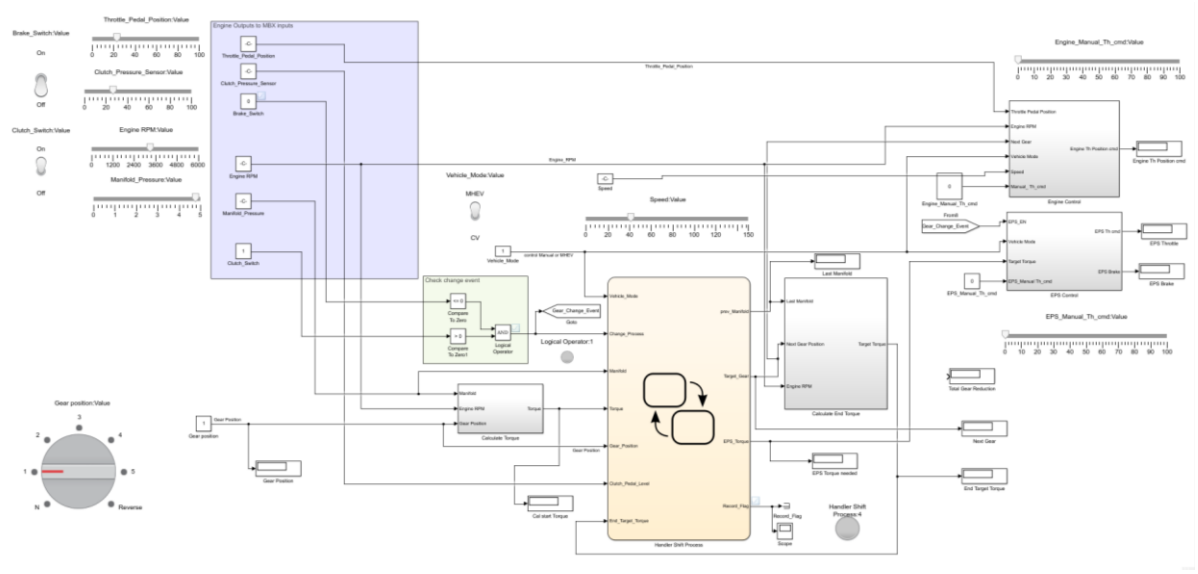

Figure 7.9 Control unit verification using dashboard library components

To verify the operation of the control unit, analog variable inputs were replicated using sliders, and state inputs such as the clutch switch, brake switch, and gear position switches were replicated using virtual switches. The inputs were used to set up a variety of conditions that could be expected during testing, to observe the control unit output. For instance, a gear change could be replicated by adjusting the clutch switch, slider and gear position switch. Once it was determined that no unexpected outputs were observed using MIL verification, the control unit was uploaded to the microcontroller hardware for deployment on the prototype.

7.3 Control Panel

The control panel is the user interface for the physical microcontroller, and is used to control, monitor, and datalog system operation during the prototype testing phase. The control panel (Figure 7.10) is configured to show vital system parameters, switch the EPS on or off to put the vehicle in MHEV mode or CV mode, and can also provide direct software control of the motor and engine throttle values. The indicators in the control panel are simply linked to parameters in the control unit to display live values.

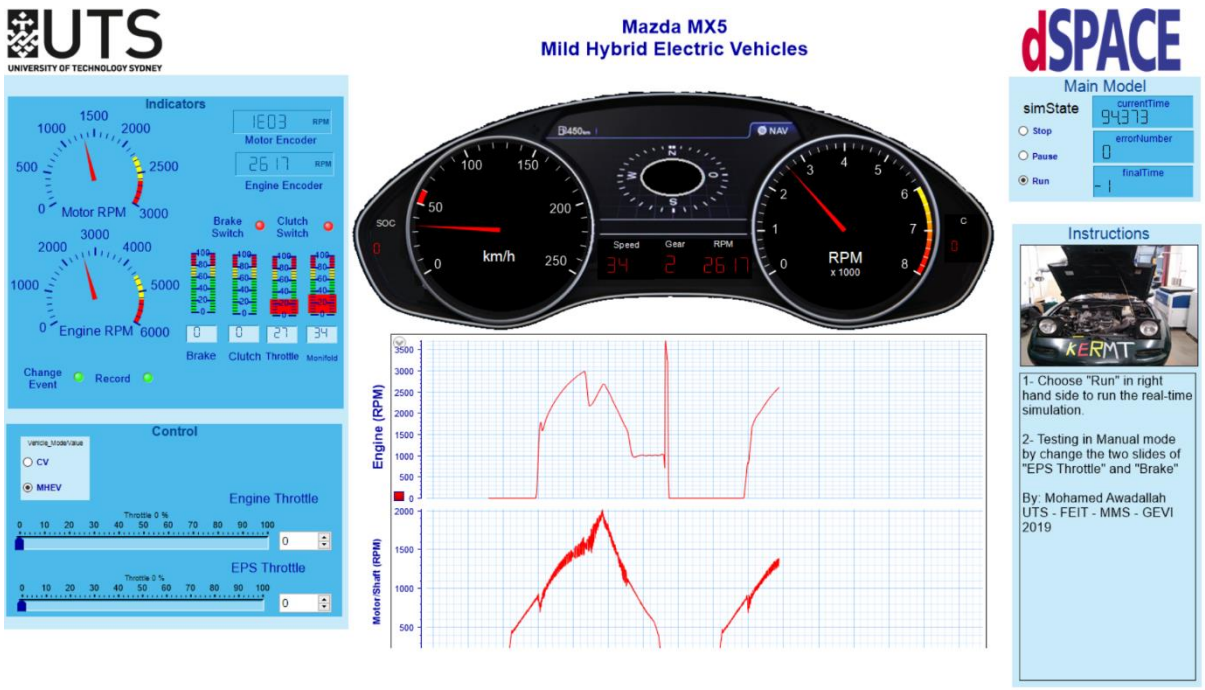

Figure 7.10 The control panel user interface used to monitor and control the prototype during testing

7.4 Torque Sensing

The torque sensors installed at the transmission output shaft and motor output shaft of the vehicle are one of the primary means of system validation. The torque sensors operate independently of the system control and, in conjunction with measurements taken at the wheel using the dynamometer, the torque sensors torque sensor outputs can be compared to simulated output to validate modelling of the system, can be compared to commanded output to validate control operation, and can be analysed separately to determine system efficacy.

7.4.1 Vehicle Jerk

In manual transmissions, the purpose of the clutch is to couple/decouple the gearbox from the power plant and provide a continuous path for torque transmission. In coupling and decoupling, discontinuities and oscillations are introduced which manifest to the vehicle occupants as a jerk. In an automatic transmission, the torque converter is by its nature a hydrodynamic device. It has a continuously variable rotation ratio but serves the same role as a clutch would in a manual transmission system (Hutchinson, Burgess & Herrmann 2014)

Because of its fluidic coupling, torque oscillations and resultant jerk are highly damped, and therefore the shifting quality is noticeably enhanced. However, in non-fluidic transmissions, control of the system, particularly noting and adjusting the transient behaviour of the system during gear changes, is essential to achieving low-jerk, high ride quality results that are valued by the vehicle occupants.

Transient behaviour during the shift period, such as jerk, generally arises from discontinuities present in the system. These discontinuities may be: speed – such as the difference in rotational speed between driving and driven gear pairs; torque - such as the difference between output torque in the current gear and the target gear, or; inertia – such as the difference between engine inertia and vehicle inertia. Minimising these discontinuities improves the transient response of the powertrain (Sun & Hebbale 2005). The P3 hybrid powertrain offers a means of controlling and minimising the transient behaviour and maximising performance and emissions benefits without reclaiming total control of the gear selection process from the driver, which requires complex control hardware or expensive AT or DCT transmissions.

7.4.2 Measuring Shift Quality

Measuring transmission shift quality has aspects that may be defined empirically, analytically, objectively as well as subjectively. An example of this is apparent when the longitudinal acceleration of a vehicle is measured. Quantitative values can be attained for longitudinal acceleration during a gearshift. Also along the quantitative sense, there is a measurable torque interruption to the wheels during a standard upshift in a manual transmission. Figure 7.11 (below) demonstrates this concept. From a subjective viewpoint, a user observation can be made about the performance or behaviour of the vehicle, typically seen as a pitching of the vehicle about its transverse axis, or by a characteristic behaviour

referred to as a ‘bunny-hopping’ Once again, user observation can be a marker of measurement, ranging from slight rider discomfort all the way to uncontrollable handling and poor manoeuvrability. These subjective observations can be correlated to quantitative measurements. By modelling the system, numerical relationships may be defined to allow optimisation of dynamic performance, or noise, vibration, and harshness (NVH).

The *availability* of torque through a powertrain to the road-tyre interface is directly related to dynamic vehicle performance characteristics such as maximum speed, acceleration, and gradability. The *manner* in which torque is delivered is directly related to vehicle drivability and comfort characteristics. Torque oscillations and step changes through a drivetrain are common sources of NVH. Measured torque oscillations can be correlated with parameters such as jerk, snap and higher motion derivatives. Human perception can be analysed using vibration dose value (VDV). These correlations can then be used in the system model as part of a hardware-in-loop development platform, using torque measurement to optimise a wide variety of system characteristics. Achieving this relies on high-quality, reliable torque measurement.

Torque oscillations are caused by sudden changes in inertia combined with angular impulse, such as caused by clutch disengagement, or sudden changes in the equilibrium of the system (such as a rapid throttle actuation) combined with underdamped torsional systems through the powertrain. Damping within the powertrain is typically sourced from vibration absorbers such as rubber or hydraulic mounts (engine mounts, transmission mounts and subframe mounts), parasitic or drag losses in transmission components, and clutch slip. In hydromechanical systems where torque is transmitted through fluid power the fluid itself is also a source of damping, therefore the elimination of fluid couplings, as in a traditional manual transmission, also reduces overall system damping (Walker & Zhang 2014; Zhou et al. 2014), making accurate shift control strategies more critical to achieving acceptable NVH.

Measuring torque oscillations provides a means for validating modelled behaviour and improving system behaviour and shift control strategy through simulation, implementation, and validation.

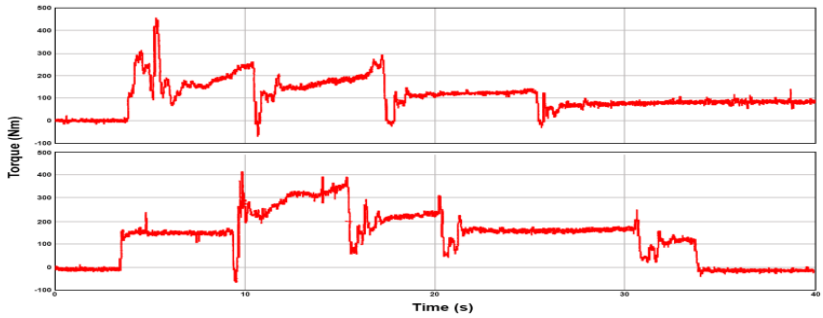

Figure 7.11 Actual measured half shaft torque with fill-in, showing the different phases of the gear change (Baraszu & Cikanek 2002)

By measuring the torque oscillations throughout the powertrain and comparing against modelled behaviour, it is possible to understand the origin of particular torque characteristics, especially those of interest at the gear change events, caused by clutch disengagement and engagement, and the resultant coupling of system inertias which requires careful control to execute smoothly to minimize angular impulse. Because these events can be felt by vehicle occupants in the range up to 10Hz or sometimes higher, it is necessary to measure torque at a much higher sampling rate in order to be able to actively control the oscillation.

7.4.3 Sensor Design

Traditionally, torque monitoring in automotive applications usually has a high cost for the installation of modules, sensors and data logger. Besides the high cost, most commercially available modules offer little flexibility, making the deployment and maintenance a difficult process. In this context, the low-cost Bluetooth module presented provides a number of advantages compared to others. For example, the ease and speed of maintenance, easy modification to fit a wide variety of configurations, ability to be quickly field-deployed without requirements for shaft removal, and insensitivity to axial or radial shaft movement.

Created using 3D printed carbon-filled nylon, the housing features low-density infill to create a light, heat resistant, robust, very low profile structure. The design of the housing speeds the development process by allowing simple parametric modification to suit a variety of shaft sizes and other physical constraints, and adds no more than 25mm to the diameter of the shaft. It fully encloses the PCB and battery pack, mitigating possibility of damage due to environmental exposure. The unenclosed componentry is limited only to the strain gauge and attached conductors, which can be protected using a suitable wrap. In addition to this, module adopts the IEEE 802.15.1 standard for Bluetooth wireless communication. The standard has advantages related to scalability, reduced time for node inclusion, and low cost. The communication protocol adopted is a flexible and inexpensive solution for building portable industrial monitoring and control systems. The module does all the data processing locally, transmitting to the base unit only the targeted parameters previously calculated. Thus, there is a large reduction in the amount of transmitted data, enabling real-time and dynamic monitoring of multiple shafts, even with a high data rate acquisition in the analogue-to-digital converters (ADC).

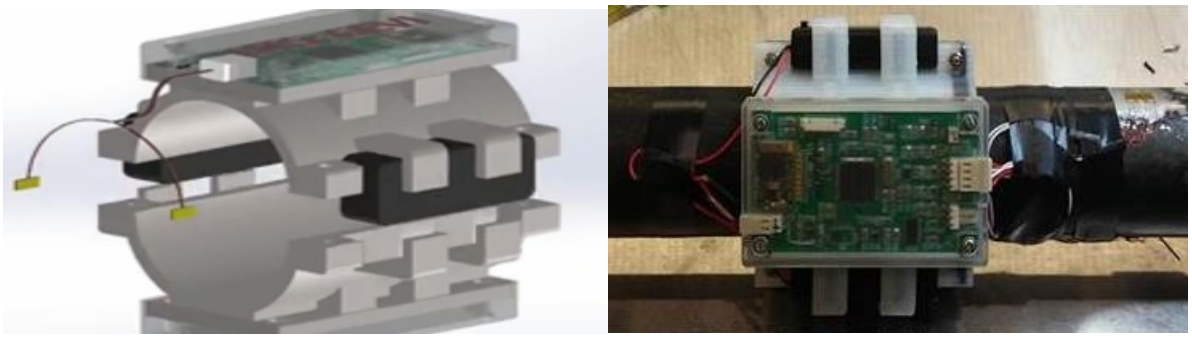

Figure 7.12 The torque sensor assembled in its housing (exploded view and photo)

The torque sensor schematic block diagram is provided in Figure 7.13. The sensor is based around the ATMega2561 microcontroller, which includes an 8-channel 10-bit ADC. Input from the Wheatstone bridge is low-pass filtered with a cut-off frequency of 1 kHz, and

amplified using the TI INA326 instrumentation amplifier, which provides a 0-3V signal to the ADC input.

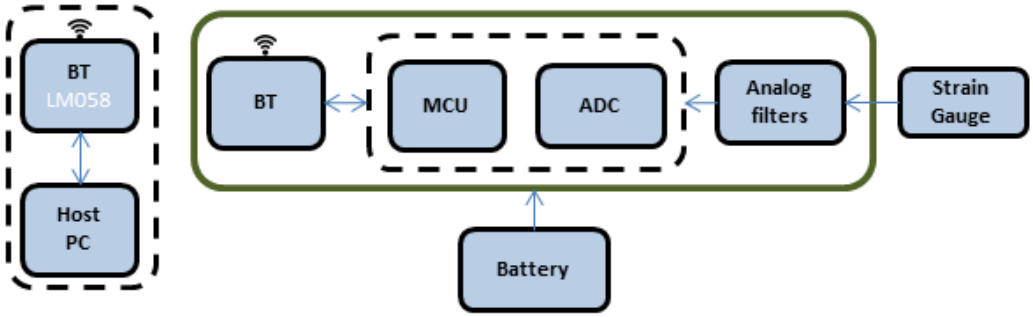

Figure 7.13 Torque sensor module

7.4.4 Sensor Testing

For mechanical testing, the PCB was placed in its 3D printed housing (as shown inFigure 7.12) and spin-tested to 6000 rpm by clamping the housing on the shaft and conducting a maximum speed test. The housing and PCB showed no signs of failure after approximately 30 minutes of testing, although wire retention for the power supply was found to be insufficient. After the wires were shortened and appropriately secured, no further issues were observed.

The module was also tested against a commercially available torque sensor (ATi Telemetry 2024i) which has been extensively used in the past. The commercially available sensor uses a stationary inductive loop to provide power to a rotating assembly. The commercially available torque sensor and the low-cost sensor were installed on a continuous rigid shaft. One end of the shaft is connected to a motor to provide driving torque, and the other end is connected to an eddy brake to provide a sink, inducing a uniform torsion across the shaft which should be read identically by both sensors. The results shown in Figure 7.14 showed good agreement to the ATi (commercial) sensor, with the only noticeable variation being a slight negative offset, particularly noticeable at 3sec and likely due to physical variation in

strain gauge bonding, as well as slight smoothing of the data due to sample-pair averaging. Neither of these variations are significant.

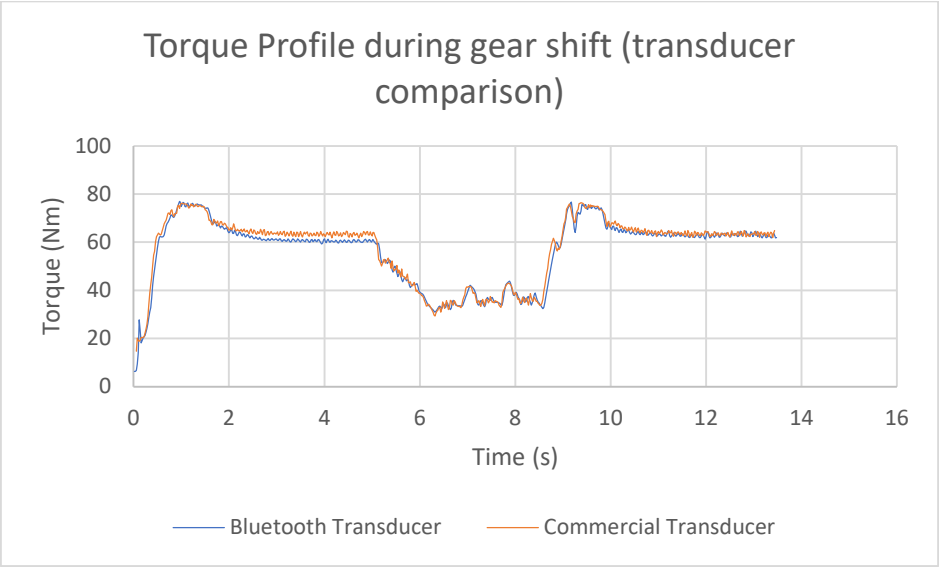

Figure 7.14 Torque profile emulation data (incl. torque fill-in) from the HIL bench, obtained using the commercial transducer and the UTS Bluetooth transducer inline.

7.4.5 Simulation vs Measured Torque

Selected data obtained from the simulation is shown in Figure 7.15, which describes the shift process in the conventional vehicle, when upshifting from 2nd to 5th gear. The various torsional excitations on the output shaft are demonstrated. They are resultant from the clutch re-engagement process and the gear selection process.

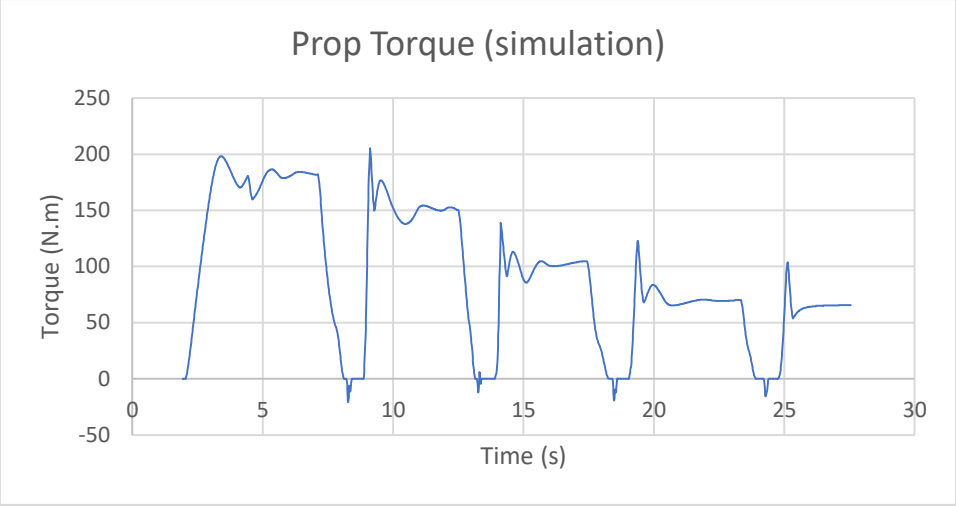

Figure 7.15 Torque profile during constant-throttle acceleration cycle

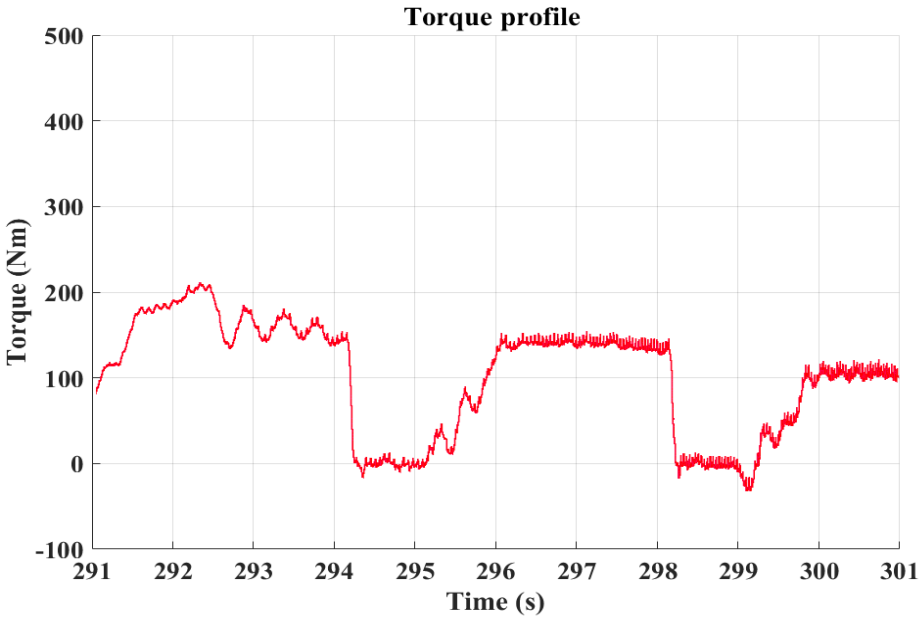

Figure 7.16 Real measured torque on the prop shaft

In comparison, Figure 7.16 shows an extract of the torque results, typical of those obtained from the low-cost torque sensor during a test run. The transient torsional characteristics exhibit many similarities to the simulation. These include the small negative torque artefact during the gear selection event caused by synchronizer friction, and the torque oscillation immediately preceding the full re-engagement of the clutch. In the simulation, the magnitude

of both these events is significantly higher than in the physical validation. In comparison to the simulation, the physical validation shows a higher level of underdamped torsional vibration in the period immediately following the full re-engagement of the clutch. This is likely due to two factors: the first is differences in clutch feed-in technique between the simulation (which feeds the clutch in linearly), and the driver (who feeds the clutch in to maximise smoothness and comfort). The second is variances between spring and damping characteristics of the drivetrain mounting points in the UUT and the simulation. The spring stiffness and damping coefficients of these mounts were estimated in the simulation rather than measured.

To facilitate investigation of the torque profile of the manual transmission equipped vehicle, the low-cost Bluetooth torque sensor was installed on the prop shaft of the vehicle, which is rigidly connected to the output shaft of the transmission using a splined socket. Damping sources for vibration at this point include losses in the differential, play and losses in the constant velocity joints, and tyre deflection, which is by far the largest loss. However, because our work focuses on quantifying powertrain behaviour under gear changes, and particularly, the torque hole and oscillations, the tyre damping and losses could be neglected, as could other sources of damping downstream of the transmission.

7.4.6 Vehicle Jerk Estimation

In practice, vehicle jerk can be estimated using the numerical derivative of vehicle acceleration. This estimation is often achieved with accelerometers on the road, but cannot be easily achieved on rolling chassis dynamometers. Vehicle data obtained using the torque transducer in a dynamometer setting is presented in Figure 7.17. The data consists of calculated acceleration based on dynamometer head speed, and jerk, calculated from the torque data obtained from the sensor. The experimental results are then compared against the

software model of the vehicle, which is run through a similar drive cycle (namely, a gentle acceleration cycle from gear 1 and zero road speed). The aim of this is an exercise is to provide validation of the software model against the developed prototype.

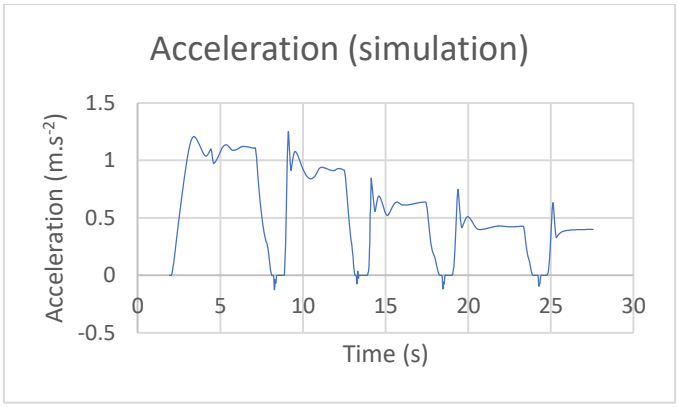

(a) Vehicle acceleration obtained numerically from simulation

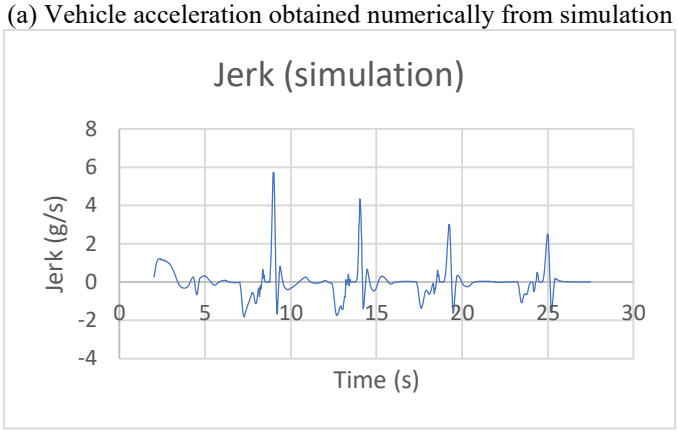

(b) Jerk obtained numerically from simulation

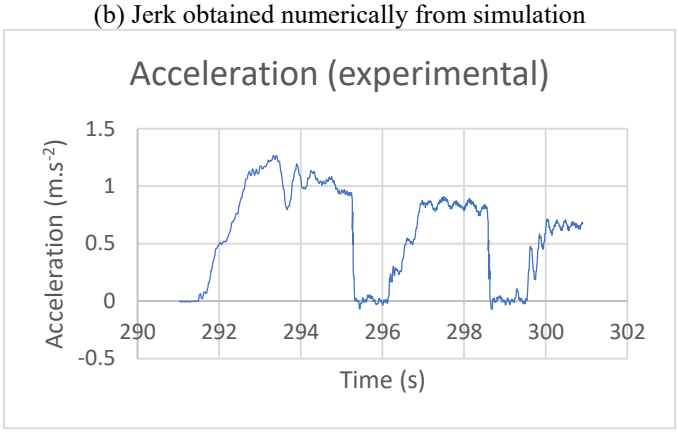

(c) Measured acceleration from comparative experiment

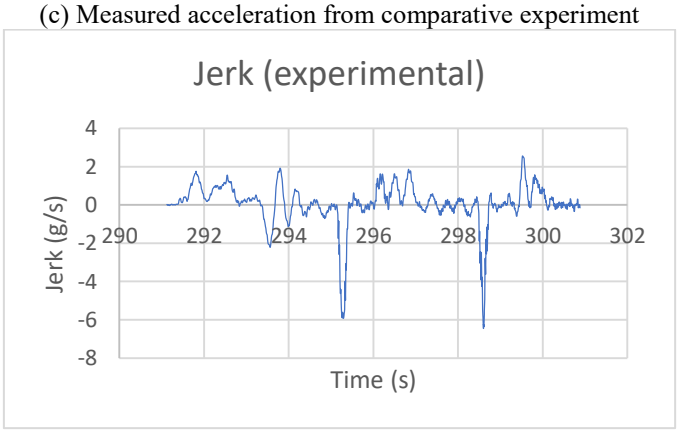

(d) Experimental Jerk results obtained using the numerical derivative method

Figure 7.17. Comparative Jerk and acceleration results

Comparative results between the simulation and experiment show similar characteristics. Notably, the magnitude of peak jerk, as well as oscillation frequencies, are well-matched. Peak jerk falls within the 4-6 g/s range in 1-2 and 2-3 gearshifts, and the primary frequency of 2.5 Hz is measured in both. The major difference between experimental and simulated results is in the direction and timing of the major jerk event during gear change. Where the simulation shows a positive jerk caused by the clutch re-engagement event, the experimental result shows a negative jerk caused by the clutch disengagement. The cause of the difference is presented clearly by examining the rate of change of acceleration on each side of the gear change event. Where in the simulation, the clutch disengagement is characterized by a more gradual loss of drive torque, the opposite is true of the experimental result, which shows the disengagement to be represented by a near vertical rate of change of acceleration. On the re-engagement event, the reverse is true, with a sharp increase in acceleration in the simulated event contrasting against a gradual increase in the experiment.

The results are constructive, in that they provide validation of the vehicle model by confirming natural oscillation frequency and the magnitude of jerk events. The inverted direction of jerk is also constructive as it identifies further work required to refine the clutch disengagement and re-engagement model.

The process shows that the low-cost Bluetooth torque transducer can be successfully used in a rapid prototyping setting to reduce development time and cost by providing directly comparable results across different test platforms.

7.5 Summary

The prototype vehicle controller and sensing as they relate to the development of the torque in-fill functionality have been described in detail. The control platform is responsible for smooth torque control for the powertrain during gear changes, and the sensors are used to validate that control under experimental testing conditions. The control model for the torque

in-fill function was deployed on the MicroAutoBox II controller following the HIL verification of its function. The control system layout is a virtual “twin” of the prototype hardware, and the control model reads sensor data into a state machine to determine torque output and engine speed control in real time.

The torque sensor was tested by physical installation in the HIL development test-bench used for verification of the system control, and easily and quickly transplanted to the prototype for physical validation. Results were also compared against software simulation to provide software validation. This work highlights the advantage of this low-cost torque sensor, and the novelty of particular design characteristics, such as it is low-profile, the robustness of its 3D printed housing, it is onboard ADC and signal conditioning, and the lack of any requirement for wiring of data or power.

The primary advantage of following model-based design principles to reach this stage is that the HIL simulated data can be compared to the system control command data which is recorded from the control model, and the actual sensed system output can be compared to the commanded output. This provides a streamlined method for the verification and validation of system operation.

Chapter 8: Experiment Design

This chapter discusses the conceptualisation of the testing goals and aims, the design of test procedures to achieve those aims, the instrumentation required on board KERMIT IV to deliver This chapter discusses the conceptualisation of the testing goals and aims, the design of test procedures to achieve those aims, the instrumentation required on board KERMIT IV to deliver sufficient data for analysis, the software platforms used for data acquisition, and the supporting infrastructure and environment in which the testing was performed.

8.1 Test Aims and Goals

KERMIT IV was built as a development platform to facilitate the investigation of the P3 parallel hybrid topology. The primary goal of this research was the development of a continuous torque delivery control methodology using the P3 topology.

The aim of testing the vehicle is simply to validate the design, software modelling, and scenario simulation that has been described in previous chapters. To achieve validation, the design goals must be met and the performance benchmarks achieved in simulation must be shown to be achievable in testing. The design goals, as detailed in 3.5 were:

- To eliminate or reduce the torque hole during gear change events
- To provide improved dynamic performance, particularly with respect to acceleration by supplementing engine tractive effort with electric drive
- To provide improved occupant comfort through reduction of powertrain-derived jerk forces
- To provide improved fuel economy such that the increased cost of the MHEV over the base vehicle could be amortized over the average driver's first three years of ownership
- To provide improved emissions performance over the base vehicle

Excluding the financial aspect of the fuel-economy goal, which is calculated based on standardized fleet data, the goals listed above were used as the basis for construction of a test procedure which may be used to show the prototype vehicle's level of achievement in relation to these goals. The test procedure also references simulation results, particularly where such simulations are readily replicated in a laboratory environment.

Simulation and benchmarking results were previously completed in (Tawadros et al. 2019), for acceleration and powertrain-derived jerk, (Awadallah et al. 2016) for fill-in torque during gear changes, (Awadallah, Tawadros, Walker, Zhang, et al. 2017a) for drive cycle fuel economy based on the NEDC, UDDS, and NYCC drive cycles, and (Awadallah, Tawadros, Walker & Zhang 2017c) for emissions performance based on a combined cycle. Results in summary are shown in Figure 8.1, Figure 8.2, Table XXI, and Table XXII.

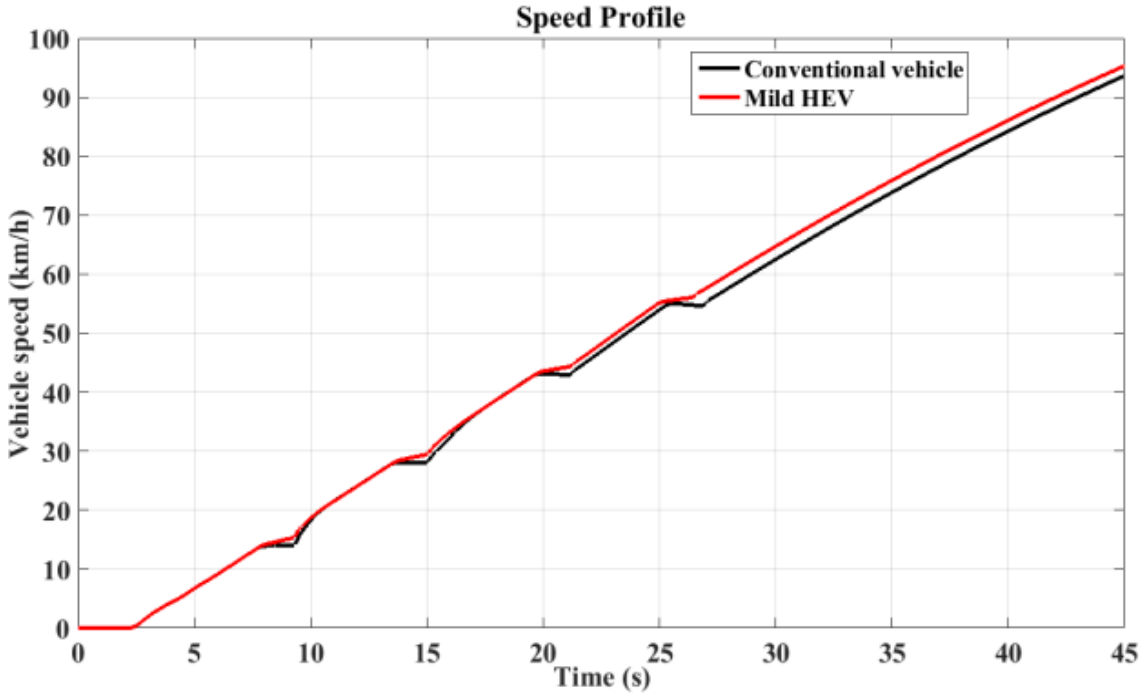

Figure 8.1 Acceleration simulation results

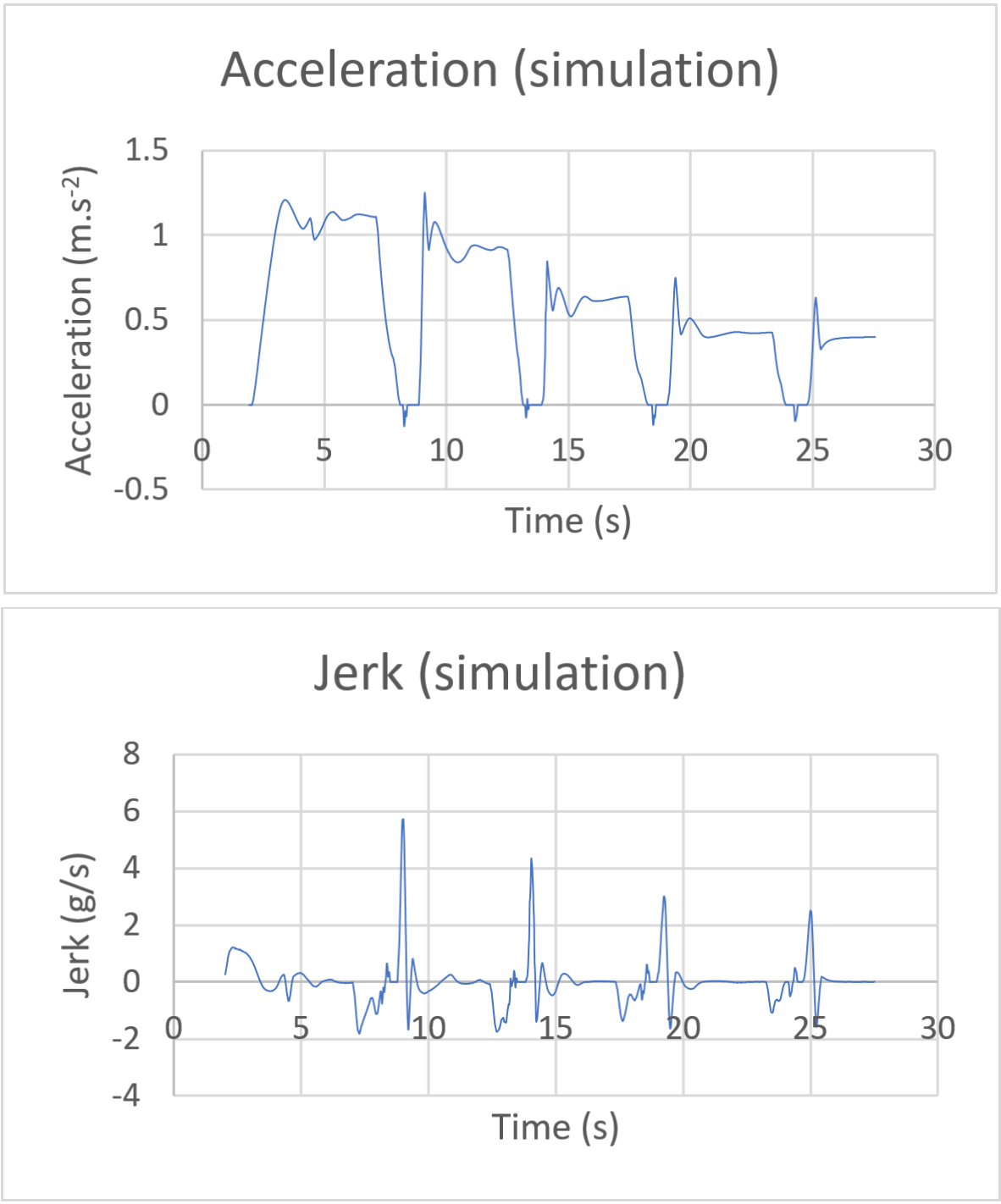

Figure 8.2 Acceleration and powertrain-derived jerk simulation results

Drive cycle	Motor			Fuel Economy (L/100 km)				
	MHEV						CV	Fuel saving (%)
	Ah	kW·h	Equivalent MJ	Motor	ICE	Total		
NEDC	0.9	0.0864	0.31104	0.00909	7.645	7.654	7.841	2.38
UDDS	2	0.192	0.69120	0.02021	7.485	7.505	8.158	8.1
NYCC	0.7	0.0672	0.24192	0.00707	16.98	16.987	17.6	3.48

Table XXI Fuel economy benchmarking simulation results

		MHEV		CV	
		Low	High	Low	High
Fuel economy (L/100km)		5.8	8.5	6.5	11.1
Emissions (grams/km)	HC	0.19	0.23	0.22	0.27
	CO	0.56	0.62	0.61	1.2
	NOx	0.32	0.36	0.35	0.49

Table XXII Lower and higher limit simulation results for tailpipe emissions

8.1.1 Test 1 – Torque Hole

In order to characterize the ability of the MHEV powertrain to provide in-fill torque during gear change events, it is necessary first to characterize the torque hole during a gear change without the electric drive, and then insert the MHEV side into the same test and observe the results. To characterize the torque hole, a steady speed test was derived in which the vehicle is brought up to its test speed, whereupon the dynamometer applies a load to the vehicle to hold the wheel speed steady regardless of the throttle input. When the test speed has stabilized, a gear change event is initiated. Upon completion of the gear change event, the test continues until the speed restabilizes. This test is repeated for gear changes between gears 1-2, 2-3, and 3-4, using both the CV mode and the MHEV mode.

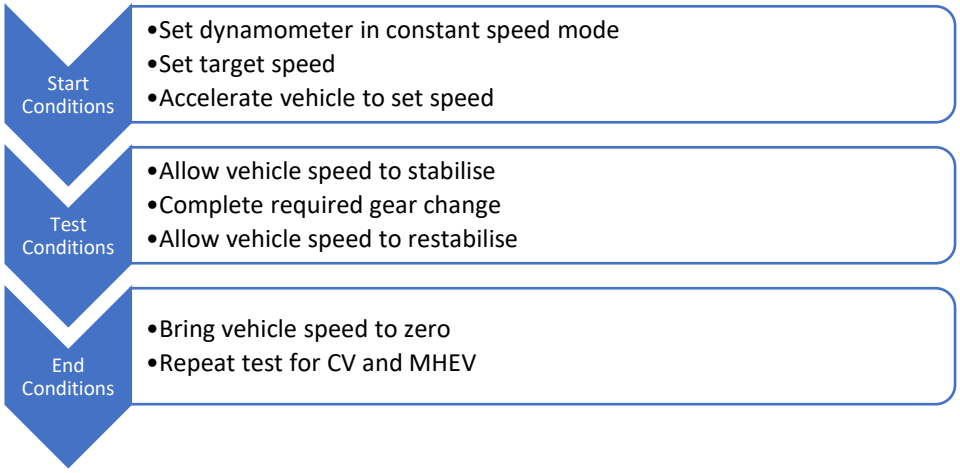

Figure 8.3 Test process for continuous torque delivery validation

This test is structured to minimise change in angular momentum by holding velocities steady, which in turn clearly demarcates the torque hole and aids characterization because accelerations (both positive and negative) are zero until the torque hole begins. Because a higher than normal load is placed on the driven wheels to hold the velocity steady, the torque discontinuity introduced by the gear change induces a larger speed reduction. This translates to a larger discontinuity in inertia which amplifies the characteristics of the torque hole and allows for clear characterization and investigation of the various transient features of the torque hole caused by clutch disengagement, gear selection, powertrain deceleration, and clutch re-engagement. In MHEV mode, the additional features caused by electric motor energization and de-energization can also be investigated.

8.1.2 Test 2 - Dynamic Performance (Acceleration)

The acceleration performance test is conducted in order to ascertain the ability of the vehicle to meet the pre-defined dynamic performance design goal and validate simulation of the torque hole elimination mode. The test is not an outright performance benchmark wherein full-throttle engine acceleration is used. Rather, it is a test using heavy partial throttle such as

would be used by a typical driver accelerating to high speed on a motorway on-ramp. A full-throttle test was not deemed necessary for a number of reasons:

- The design intent for the MHEV system is to improve driveability, economy and emissions. While the MHEV system would have a small effect on the outright performance of the vehicle, it is difficult to characterize driveability improvement and meaningless to characterize economy improvement under a full-throttle test.
- Full-throttle acceleration is generally accompanied by rapid gear shifting and clutch actuation. It is difficult to characterize and control the torque hole under such use conditions
- Such a test would not validate the simulated acceleration scenario, which was conducted under partial throttle
- As engine power fraction increases, it effectively decreases the hybridization ratio

The test is structured as follows. In the first instance, first gear is engaged and the wheels are left free to roll under engine idle power alone, without the use of any throttle input. Once the idle vehicle speed has stabilised, the test begins with the throttle held roughly constant whilst any gear is engaged. The vehicle is accelerated using near-constant throttle input, with gear changes at 20km/h, 40km/h and 60km/h. The vehicle is accelerated to 80km/h before throttle input is returned to idle and the vehicle coasts back down to a stop. The test is repeated using both CV mode and MHEV mode.

The rolling start is preferred as it returns more consistent results than a stationary start, due to omission of stationary clutch re-engagement which induces significant driveline oscillation. The test can be repeated varying the constant value of throttle input or varying the gear change event time, to simulate the inputs of a calmer or more aggressive driver (Awadallah et al. 2018).

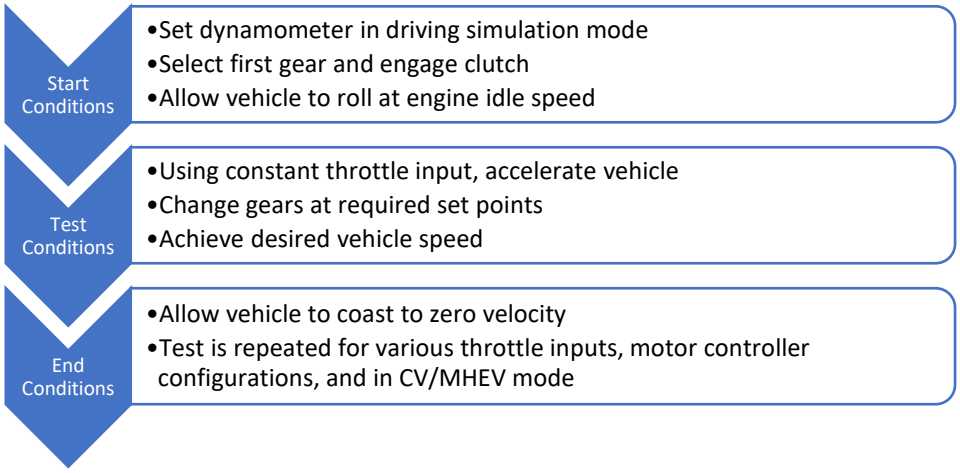

Figure 8.4 Test process for acceleration testing

8.1.3 Test 3 – Driveline induced jerk

Measuring jerk is accomplished by measuring acceleration and then obtaining its rate of change. The best method for making this measurement is the installation of an accelerometer at the seat squab to measure longitudinal acceleration and undertaking on-road drive tests. Due to the prototype nature of KERMIT IV, on-road drive tests are not permissible by law and therefore an approximation must be made using laboratory infrastructure. This is possible by taking the results of the acceleration test described above and obtaining jerk from dynamometer velocity readings. Comparison is also made to jerk figures obtained from motor output shaft data, thereby eliminating the major sources of driveline damping (namely, tyre and suspension compliance) and highlighting driveline-induced jerk. The results of this procedure suffer in comparison to a direct on-road measurement due to the decreased surface slip in the dynamometer roller/tyre interface in comparison to an on-road test, as well as the decreased suspension compliance due to the requirement to tie down the vehicle under test. However, because previous simulation results are also based on measurements of driveline torque, the method provides better validation of the simulation output.

8.1.4 Test 4 - Fuel Economy and Emissions

Vehicle fuel economy and emissions are measured by placing the vehicle under test in a dynamometer drive cycle. There are dozens of such cycles, designed to represent certain driving scenarios. The software model was placed in a number of simulated cycles, including the UDDS, HWFET, NEDC, NYC, and the unofficial Indian Urban and Indian Highway cycles which are provided with the ADVISOR vehicle simulation tool. For validation of fuel economy and emissions, the vehicle under test is instrumented with an emissions measurement device and injector duty is used to calculate injected fuel mass. Whilst there are other, more accurate methods of calculating fuel consumption, most methods are impractical inasmuch as the equipment required to measure fuel consumption directly is not available to the researcher (Coriolis meter), incompatible with a pressurised fuel injection system equipped with return line, or incapable of measuring the wide range of flow rates required for light automotive applications. The tests for both fuel economy and emissions are conducted simultaneously.

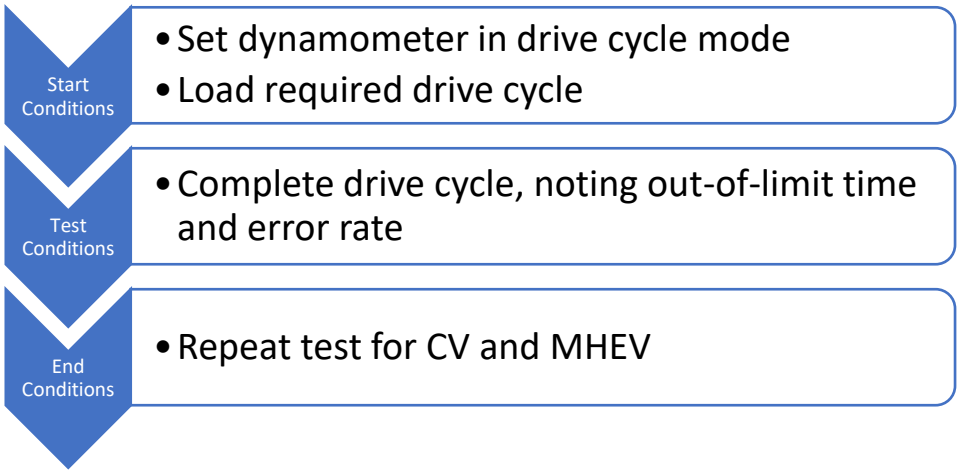

Figure 8.5 Test process for fuel economy and emissions validation

8.1.5 Further Testing

In addition to the testing described above, two further tests were prescribed. The first of these tests aims to characterize the stop-start performance of the vehicle, in respect to its capability to perform low-speed EV crawling. This test measures the battery depletion rate and pack temperature whilst performing a standard EV start. The EV start is characterized by applying a constant motor torque to the driveline until 20km/h is reached, and then firing the engine which takes over as the prime mover.

The second of these tests aims to characterize the ability of the battery pack to pulse charge using regenerative braking, so that safe regenerative braking limits can be set in the motor controller. This is test is required due to the high regenerative braking capability of the motor in comparison to the size of the battery pack and its maximum safe charge rate. In this test, pack SOC is set to a specific start SOC (20%, 40%, 60% or 80%) and the vehicle is accelerated to a constant speed. The motor is then controlled to regenerate at varying powers whilst speed is held constant. The change in pack temperature is monitored while regenerating and after regeneration has ended, to understand the temperature characteristics, which may vary from those of the individual cell due to the pack construction and the lack of provision for forced cooling.

8.2 Test Instrumentation

To collect sufficient data for analysis of system behaviour, an instrumentation package must be developed. The instrumentation package consists of a range of transducers, many of which serve dual roles, being simultaneously required for control of the MHEV powertrain, as well as data acquisition. Data acquisition (DAQ) is also available in two configurations – in the first instance, being included in controller hardware by simply outputting control inputs and outputs to file, or in the second instance, as a standalone DAQ system that is not part of the

control hardware. A brief list of measured quantities is provided in Table XXIII. Sensor data and calibration information can be found in Appendix B.

Measurement Quantity	Function	Transducer Detail
Clutch pedal actuation	Initiate torque fill-in state	SPST N/C momentary switch
Clutch hydraulic line pressure	Modulate fill-in torque	Honeywell MLH02KPSB06A
Brake pedal actuation	Safety shut down Initiate regenerative braking	SPST N/O momentary switch – Mazda Part No. B00166490B
Brake hydraulic line pressure	Modulate regenerative braking level	Honeywell MLH02KPSB06A
Throttle pedal position	Control electronic throttle body	Toyota Part No. 78110-28010
Selected gear	Select appropriate torque multiplier for calculation of target start torque and target end torque	Customized gear selector switch array – 6 off SPDT N/O switches, Electus catalog number SM1038 in custom housing
Engine Manifold Pressure	Input 1 of 2 for engine torque lookup table	AC Delco 1 bar MAP sensor
Engine Speed	Input 2 of 2 for engine torque lookup table	Camshaft position sensor (2 pulses per rev)
Engine Torque	Output of lookup table based on Manifold Pressure and Speed. Calculated quantity based on experimentally-derived lookup table.	(NO SENSOR) The lookup table was derived by discrete load site torque measurement on the dynamometer
Injector duty	Derivation of injected fuel mass	Injector voltage tap
Transmission Output Shaft Torque	No control function – for system verification only	Customized wheatstone bridge strain gauge
Motor Speed	Vehicle speed information System arm and disarm	Hall effect encoder (64 pulses per rev)
Motor Temperature	Safety shut down	Thermistor

Motor Output Shaft Torque	No control function – for system verification only	Customized wheatstone bridge strain gauge
Battery Current	Battery management Safety shut down System energy conversion efficiency calculation	LEM DHAB S/124 hall-effect current transducer Orion BMS2
Battery Voltage	Battery management Safety shut down System efficiency calculation	Orion BMS2
Battery Temperature	Safety shut down	Thermistor Orion BMS2
Wheel Speed	No control function – system verification only	MAHA MSR500 chassis dynamometer
Wheel Torque	No control function – system verification only	MAHA MSR500 chassis dynamometer

Table XXIII Measured quantities for experimental validation

8.3 Test and DAQ Software

There are five major software platforms used for the test apparatus. All software platforms are PC-based, using USB communication for the transfer of data. The software platforms are:

- The Orion BMS2 battery management system utility, which provides configuration and data logging abilities through connection with the BMS
- The Curtis 1314-4402 Programming station, which provides the same functionality for the Curtis 1238e AC motor controller
- National Instruments (NI) LabView, a graphical programming interface that provides a systems engineering approach to test/measure/control applications
- dSPace ControlDesk, a real time experiment environment including control, instrumentation, and data logging which allows the rapid development of electronic control units

- MAHA LPS 3000, which provides control and data logging capability for the MSR 500/2 chassis dynamometer on which testing is conducted

8.3.1 Orion BMS2 Utility

Datalogging for the Orion BMS2 is performed using the included utility. The utility allows direct editing of the battery operating parameters, such as charge and discharge limits, thermal settings, communications, and safety parameters. It also logs multiple channels from BMS function data at a fixed rate of 10Hz. For testing, the data channels relating to battery pack current, voltage, and temperature as well as state of charge and depth of discharge were recorded.

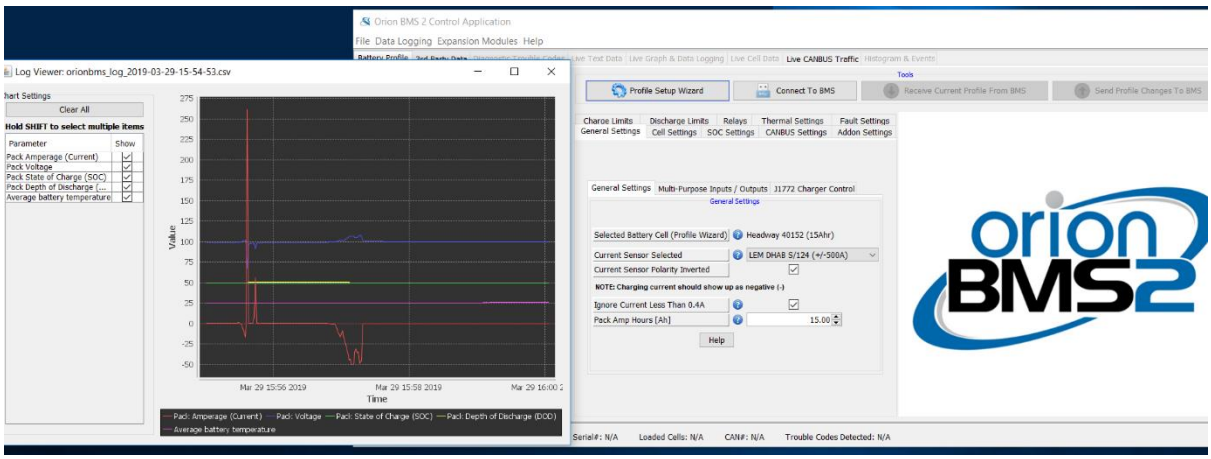

Figure 8.6 The Orion BMS2 software utility

8.3.2 Curtis 1314-4402 Programming Station

The motor controller is also capable of outputting a data stream which can be logged through the Curtis 1314-4402 programming station. The programming station functions similarly to the Orion BMS2 utility. It is able to directly download and edit the motor controller firmware and provides datalogging capability. In this implementation, the datalogging capability is not required as all inputs and outputs are logged using other means. For instance, the throttle

command and motor speed are logged using dSpace ControlDesk, and torque is logged using a customized Virtual Insutrment (VI) written in NI LabView.

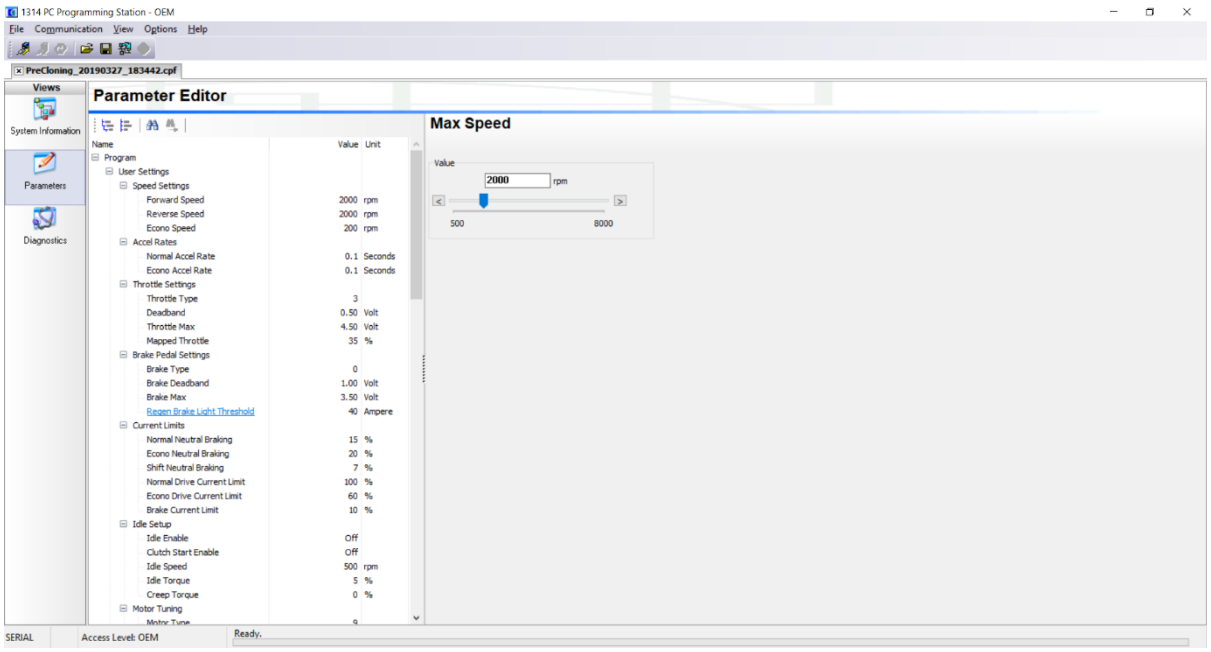

Figure 8.7 Curtis 1314 programming station software

8.3.3 dSPACE ControlDesk

The supervisory controller, dSpace MicroAutoBox II, is provided with an accompanying software package, ControlDesk, and a real time interface (dSpace RTI). ControlDesk is a real time environment allowing complete control over the controller hardware, including modification of the configuration of the controller, logical configuration of hardware-in-the-loop simulations, real time operating parameter changes, system monitoring and data acquisition. The vehicle model is developed in matlab/Simulink and then loaded into dSpace RTI, whereupon the model is downloaded to the MicroAutoBox II controller using automatic code generation (Ashby et al. 2014; Jaikamal 2009). ControlDesk is hosted on a windows-based PC, and connects to the MicroAutoBox II using a USB host-interface cable.

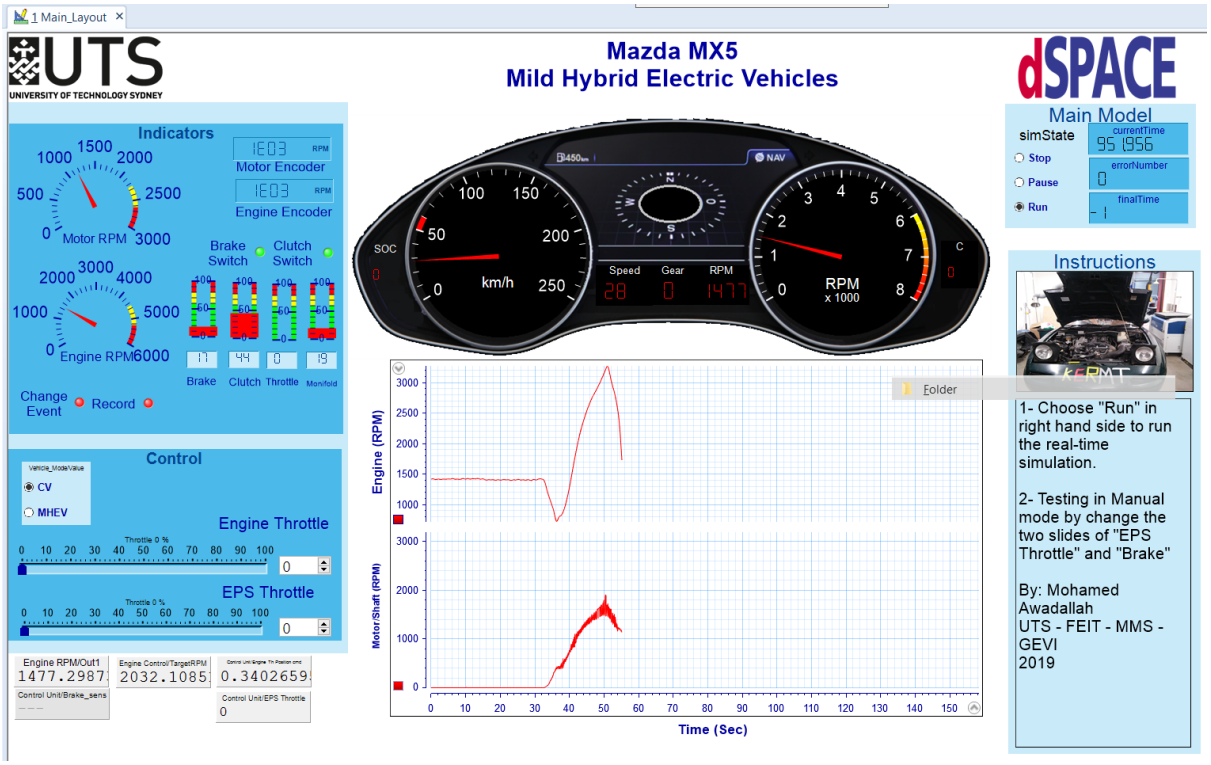

Figure 8.8 The dSpace dashboard used for controlling and monitoring the experiment conditions

8.3.4 NI LabView

NI LabView is used for the collection of transmission output shaft torque and motor output shaft torque data. The shaft torque is sensed using four strain gauges arranged in a wheatstone bridge. Each wheatstone bridge is connected to a Bluetooth data acquisition board, consisting of a DC power supply, signal amplifier, and Bluetooth radio transmitter. An LM Technologies LM058 bluetooth serial adapter receives the signal and a LabView virtual instrument (VI) is used to interface to the serial port, acquire, and save the data. Torque data is collected at a rate of 2.4kHz.

8.3.5 MAHA LPS 3000 Control Station

All testing is conducted on a MAHA MSR500/2 single roller dynamometer installed within an emissions test chamber at UTS. The roller dynamometer is used to provide repeatable test

conditions and, in essence, consists of a roller set mounted on a load cell. One roller set is provided per axle, and each roller set is solidly linked across the axle to ensure transverse differential speed is zero. Each roller set is connected to both a 250kW eddy current brake, and a 30kW electric motor. These provide load and drive simulation for the dynamometer. The dynamometer control interface is through LPS 3000, a Windows-based PC application that can be used to configure, setup, and operate the dynamometer. The interface provides the ability to characterize rolling and aerodynamic losses and simulate them using them eddy current brakes, as well as providing a variety of test modes, including drive simulation, in which roller load varies according to the vehicle's speed and a specified road gradient, constant speed mode, which applies load to hold the vehicle speed at a specified constant, constant torque mode, which ensures a constant force is applied to the drive wheels regardless of the speed. Other modes available are continuous power measurement mode which enables the characterization of engine performance, and drive cycle testing, which is similar to the drive simulation mode but provides the driver with a visual speed prompt to enable the testing of prescribed cycles. This final mode is relevant for emissions testing.

8.4 Laboratory Equipment and Specifications

The emissions laboratory is a temperature and pressure-controlled facility, accommodating the MAHA MSR500/2 single-roller dynamometer, a tailpipe exhaust extraction system, ambient combustion gas monitoring, and a computer room air conditioning (CRAC) unit functioning as the ambient cooler.

8.4.1 MAHA MSR500/2 Dynamometer

Figure 8.9 Prototype MHEV (KERMIT IV) on the MAHA MSR500/2 dynamometer

The MAHA MSR500/2 single roller dynamometer uses a single 504mm diameter roller with a rotating mass of 280kg to support each wheel. Each axle is rigidly connected and coupled to a 250kW continuous/1000kW peak eddy current brake, as well as a 30kW double-ended AC motor for drive power. The single roller type dynamometer is preferred to the double-roller type as it more accurately replicates the tyre-road interface – the increased tyre deformation on a double roller greatly increases rolling losses in comparison to both the single-roller type and typical road losses. Emissions studies are typically conducted on a single roller dynamometer with 48 inch diameter rollers and 110kW of drive power at up to 200km/h surface speed. This equipment specification is prescribed in all emissions standards used for homologation. A 48 inch roller accurately simulates the tyre contact patch due to its large

diameter, but for the purpose of this research, a certification standard dynamometer is not preferred as our emissions study is comparative in nature, rather than absolute.

8.4.2 Tailpipe Exhaust Extraction

A tailpipe exhaust extraction system is provided within the laboratory. The connection is of the hood type and the maximum flow is 400L/s. A remotely mounted centrifugal blower provides suction. This flow is sufficient for low-power emissions studies but does not provide sufficient extraction capacity for high-power testing of internal combustion engines. Dual connection points are provided in the case of vehicle testing where multiple exhaust outlets are present.

8.4.3 Ambient Combustion Gas Monitoring

Ambient gas monitoring is provided for concentrations of carbon monoxide, carbon dioxide, oxides of nitrogen, and hydrocarbons. The monitors are based on the MSR PolyGard 2 sensor system. An alarm sounds if concentrations exceed limits set in the Australian Standard AS1668.2-2012 (Standards Australia 2016).

8.4.4 Ambient Cooling

A Mitsubishi Electric i-NEXT DX Model 068 M2 D E7 computer room air conditioning (CRAC) unit supplies chilled air to the laboratory. The CRAC unit provides a minimum of 24 and maximum of 79kW of cooling to the laboratory, with an airflow rate of 4860L/s. The supply and return temperatures are user-adjustable. Adjustment of the supply temperature changes the flow rate of chilled water through the heat exchanger, whereas adjustment of the return temperature causes the controller to adjust blower duty cycle to ensure returned air is controlled to the return temperature (Logicool AC 2018).

8.5 Laboratory Setup

To prepare the laboratory and achieve standard operating conditions, it is necessary to input the vehicle road load into the dynamometer control software. This is a process that is performed experimentally once, and then the details of the vehicle are stored in the LPS 3000 database for later use. It is also necessary to temperature soak the laboratory and the vehicle to reach the prescribed test temperature. These processes ensure that the testing environment is homogenous and accurately represents real-world driving scenarios.

8.5.1 Hardware and Software Setup

To ensure accurate control and data acquisition during testing it is important to ensure hardware and software is accurately set up. This includes setting the vehicle in the correct control mode, ensuring controllers are initialised, and initialising the various datalogging devices. In total, there are four hardware devices that must be correctly set: KERMIT IV, the MAHA MSR500/2 dynamometer, exhaust extraction, and the CRAC unit. There are also five software devices that must be initialised, being the subject of 0. The basic configuration checks for these nine elements are provided in Table XXIV and Table XXV on the following pages.

Hardware Device	Configuration Element	Configuration Setting
CRAC Unit	Supply Temperature	17
	Return Temperature	20
	Primary system power	On
	Controller status	On
MSR500/2 Dynamometer	Roller Blocks	Disengaged
	Vehicle tie downs	Checked safe
	Wheel centering	Wheels centred on rollers
	Cooling fans	On
	Mode switch	Operation
Exhaust Extraction	Primary duct	Fully open
	Secondary duct	Fully closed
	System primary switch	On
KERMIT IV	Engine Throttle Switch	Auto
	Motor Throttle Switch	Auto
	Motor Controller Power	On
	BMS Power	On
	MicroAutoBox Power	On
	Key Switch Interlock	On
	Traction Battery Pack SOC	95% (unless testing regen)
	Shaft torque sensor batteries	Fully charged and connected

Table XXIV Hardware configuration checks required prior to test commencement

Software Device	Configuration Element	Configuration Setting
Orion BMS2 Utility	Pulse discharge limit duration	6 sec
	Datalogging	Active on Pack Amps, Volts, SOC, DOD, resistance, and temperature
Curtis 1314-4402	Torque mode/Full restraint speed	6000 RPM
	Torque mode/Speed limiter	6000 RPM
	Current Limit/Brake current Limit	15%
dSpace ControlDesk	Measurement	On
	Recording	On
NI LabView	LM058 bluetooth adapter	Torque sensor connection status OK
	Measurement	On
MAHA LPS 3000	Vehicle Data	Road load information loaded

Table XXV Software configuration checks required prior to test commencement

8.5.2 Temperature Soaking

Temperature soaking is a process whereby the entire testing environment is brought to stable testing temperatures. This process is necessary to exclude or minimise temperature-related drift and changes in system function, which may cause unexplained variations in acquired data or performance. Some of the known quantities in the testing environment that are highly temperature dependent include:

- Engine performance, which is markedly different both by design and by constraint, dependent upon temperature. Modern engines utilise a temperature correction factor

for fuel injection, ignition, and/or valve timing to ensure the smooth running, acceptable emissions, and driveability characteristics of an engine, but temperature nonetheless plays a significant role in emissions and efficiency.

- Transmission and driveline efficiency, which is repeatably poorer when the driveline is cold. This is primarily due to elevated low-temperature viscosity of lubricants such as gear oil and grease, increasing pumping and windage losses.
- Thin-film strain gauge readings can also vary with temperature due to a wide range of temperature-related factors, including the expansion and contraction of the substrate material, softening of the adhesive causing creep, and gauge factor temperature co-efficient. Although a full wheatstone bridge can largely compensate for temperature-related drift (as well as, in the application of torque measurement on shafts, bending moments), if the geometric accuracy of the gauge placement is poor, or if the material acts non-homogenously, the strain reading can nonetheless be subject to temperature effects (HBM Australia 2017)
- Tyre performance also varies with temperature (Lang & Klüppel 2017), with the tyre generally becoming more compliant and exhibiting a higher interface friction as it approaches an optimal working temperature (this temperature is usually around 50-70 degrees in road tyres)

Temperature soaking requires the vehicle under test to be placed in the test chamber, running under a similar load to that intended to be applied during the test procedure sufficiently long to bring the powertrain components up to operating temperature, and maintaining the ambient chamber temperature at the desired level. To achieve this, the CRAC unit is switched on and set to its desired setpoints, in this case supply temperature is 17°C and return temperature is 20°C. This ensures the laboratory temperature is set to 20°C whilst also maintaining a relatively constant blower duty cycle and minimising ambient temperature variation caused

by the blower switching on and off. The vehicle is then turned on and allowed to warm up fully, whilst being driven under a constant load. Temperature soaking is complete when the following conditions are met:

- Engine coolant temperature exceeds 82°C
- Idle oil pressure is less than 1.2 kg/cm^2
- The vehicle has been driven under moderate load for at least 15 minutes at a speed greater than 40km/h
- Ambient chamber temperature has remained at the setpoint ±0.5°C for at least 10 minutes whilst the vehicle was being driven

At this point, the vehicle may be brought to a complete stop and testing may begin.

8.5.3 Road Load Determination

The road load is the total energy loss of the vehicle to aerodynamic, rolling, and drivetrain losses. It is described in terms of the forward velocity of the vehicle, and is derived in accordance with the standard SAE-J2264 (SAE Technical Standards Board 2014). There are two standardized methods for the calculation of road loads. The first method, specified in SAE-J1263 (SAE Technical Standards Board 2010) relies on coastdown tests and must be done on a flat, straight road with relatively constant conditions. Twenty tests are required in total according to the standard – ten in each direction to neutralize any environmental error. The second method (SAE-J2264) uses dynamometer simulated coastdown and iterative regression to arrive at a dynamometer approximation. The second method requires measurement of vehicle data such as rotating mass, total mass, and frontal area, for input into the quadratic regression to arrive at simulated forces at the dynamometer. If the measurements are incorrect, a static error is introduced. If the static error is beyond limits set by the standard, the dynamometer will fail the determination process and require new values

to be input for testing. The road load is determined once and assumed constant throughout testing. The general form of the equation of motion is:

$$-m\frac{dv}{dt} = D_{mech} + D_{aero} + D_{grav}, \quad (8.1), \text{ where}$$

$$D_{mech} = D_{tyre} + D_{axle,F} + D_{axle,R} \quad (8.2)$$

$$D_{aero} = \frac{1}{2}\rho C_d A_{frontal}(v + v_0)^2 \quad (8.3)$$

$$D_{grav} = mg\frac{dh}{ds} \quad (8.4)$$

The mechanical drag component can also be modelled as a three-term polynomial. The equation of the model used for mechanical drag is:

$$D_{mech} = A + B.v + Cv^2 \quad (8.5)$$

The aerodynamic co-efficient of drag, C_d, can also be modelled as a fourth-order polynomial with respect to yaw angle. However, this is only in the case of on-road coastdown testing. For dynamometer testing C_d is assumed constant. Additionally, the gravitational drag component D_{grav} can be set to zero for dynamometer testing. Therefore, the equation of motion becomes:

$$-m\frac{dv}{dt} = A + B.v + Cv^2 + \frac{1}{2}\rho C_d A_{frontal}(v + v_0)^2 \quad (8.6)$$

This can be reduced to a compact form by rolling the second order terms together:

$$-m\frac{dv}{dt} = A + B.v + \left(\frac{2C + \rho C_d A_{frontal}}{2}\right)v^2 \quad (8.7)$$

In this way, A, B, and C (or the combined second-order expression) are expressed as constant, first-order, and second-order speed-force relationships, respectively. The constant co-efficient *A* is largely a function of the vehicle mass and rolling resistance. The first-order

co-efficient *B* is correlated to the rolling losses in the drivetrain while the vehicle is in neutral. The second-order co-efficient *C* is mostly the aerodynamic losses term. In most standards, including SAE-J2264, the first-order road load co-efficient is commonly ignored and can be set at zero without introducing significant error, although if measurements determine the co-efficient is greater than 3% of the total drag it must be included.

The road load force is variable according to a wide range of environmental parameters. These parameters include the temperature of vehicle components, ambient temperature, road temperature, tyre temperature and inflation pressure, tested vehicle weight, humidity, air density and fog, prevailing winds, road surface moisture, usage of the vehicle ("breaking-in"), types of lubrication used in driveline components, adjustment of brakes and suspension. Many of these parameters must be checked and adjusted prior to and after testing. These include vehicle weight, tyre inflation pressure, lubrication, and adjustment of brakes, and suspension. Others must be recorded during the test and correction factors applied in post-processing. These include ambient temperature and wind variables. To ensure vehicle components are not affected by temperature gradients, standards typically require the vehicle to be driven for at least 30 minutes and 40km prior to testing.

When performing dynamometer testing, many environmental parameters can be kept constant. For this reason, humidity, air density, wind speed and direction, and road surface moisture can be ignored. The vehicle is run on two cycles of the HWFET procedure for warm-up and test cell conditions are recorded. It is nevertheless important to ensure the test cell reaches the same test conditions as the RLD procedure prior to any test procedure, to ensure the road load is not altered. This also ensures that any road-load error is kept constant throughout any testing, which allows valid conclusions to be computed from testing. It is therefore of utmost importance to follow environmental soaking procedures prior to vehicle testing.

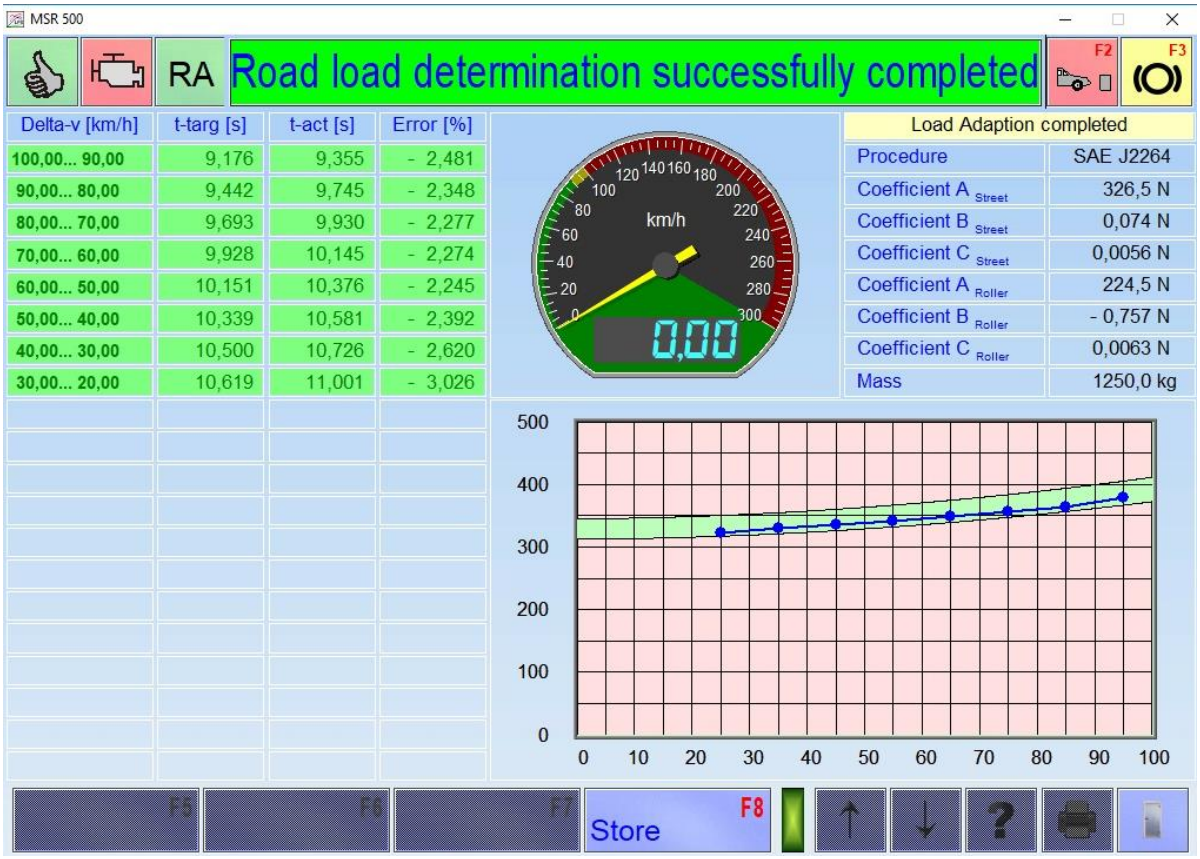

Figure 8.10 Iterative road load determination using SAE-J2264 routine showing the road load co-efficients

One consideration unique to hybrid vehicles is the lack of a neutral gear position. Many hybrid vehicles, including those utilising the P3 topology, do not have a mechanical disconnect between the electric motor and the driven axle. Instead, the motor is actively controlled for zero torque to achieve an equivalent neutral gear. This can affect the RLD due to errors or transients in the control, which may provide slight motoring or braking force on the driven axle (Duoba, Bohn & Lohse-Busch 2010). There are several methods used to ensure this does not occur. One is a mechanical disconnection, such as the removal of a shaft. Another is the installation of a clutch mechanism specifically for testing purposes. The clutch may be a one-way dog clutch or something more complex. For the testing of KERMIT IV, the simplest available method was the complete de-powering of the motor controller. Because the electric motor does not have any permanent magnet material in its construction, the losses

from de-powered rotation are no greater than those experienced when the motor is energized but controlled for zero-torque.

8.5.4 Datalogging Time Alignment

For time alignment of the various data acquisition systems, a short, sharp acceleration event is input to the system prior to the commencement of a vehicle test. The vehicle velocity is then sharply reduced to zero. This allows simple alignment of the disparate data acquisition systems using velocity and torque traces. The data acquisition sampling rates of the systems vary between 2.4kHz and 10Hz. For the systems with high sampling rates, blocks of data were averaged down to a 10Hz rate. The slight (±0.05s) possible misalignment between the various data sets was not considered to be significant for the purpose of evaluating the continuous torque delivery performance of the drivetrain, due to the evaluation being dependent upon the comparison of multiple tests. Further, there was no practical means of reducing the time misalignment due to there being no synchronization input on the dynamometer data acquisition system, which itself is limited to a maximum 10Hz sampling rate. The time alignment method used in this study has previously been validated in (Paulina & McBryde, D. Matthews 2007)

8.6 Summary

This chapter reintroduces the design goals, which relate to the evaluation of continuous torque delivery and jerk reduction, improvement in acceleration performance, and improved fuel economy and emissions. From these, a series of four laboratory test procedures are derived, in addition to two supplementary tests which are used to characterize EV and battery pack charging performance.

The test instrumentation package is introduced and described. The package is the complete list of sensors used to obtain testing results. Many of the sensors used in testing also serve

dual roles, being required as control inputs for the MHEV system installed on KERMIT IV. The software platforms used for system control, testing, and data acquisition are described in brief, with particular reference to the data acquisition role each platform plays in the test procedure.

The laboratory infrastructure is described in detail to orient the user to the laboratory environment. Information is provided on the dynamometer, exhaust extraction system, ambient combustion gas monitoring, and cooling systems used in the test environment.

Finally, the setup procedure developed for ensuring a homogenous test environment is described in detail. The setup procedure requires the configuration of hardware and software parameters, environmental parameters (temperature soaking), and vehicle parameters. In particular, a discussion of road load determination (RLD) is developed. The RLD procedure undertaken for the purpose of this testing differs from that prescribed in SAE J2264 primarily due to the absence of physical coast down (CD) testing. The purpose of CD testing in the intention of SAE J2264 is to ensure parity between manufacturers so that bias in emissions test procedures is minimised. Because the testing undertaken in the research presented herein relies on the comparison of a single prototype vehicle with and without an MHEV system, RLD may be undertaken using estimations based on manufacturer supplied values with small variations due to the increased mechanical losses caused by the insertion of the electric motor in the driveline. The validity of these estimations can to some degree be verified using dynamometer coast down testing. By varying applied drag according to the estimated quadratic losses, linear regression techniques allow the derivation of roller drag losses that are equivalent to RLD. If the estimated RLD is not able to be achieved under dynamometer coast down testing the linear regression fails to meet acceptance limits and roller drag losses cannot be derived.

Chapter 9: Results and Discussion

The results of laboratory testing are described in this chapter. The vehicle was subjected to tests without the MHEV system active, which represents the base vehicle operation. These tests were used as benchmarks for comparison of the performance of the vehicle with the MHEV system active. Three sets of tests were conducted. The first test was a steady-state gear change used to characterize the torque hole. A variety of gear changes were performed at steady conditions and used to characterize the torque hole with and without the MHEV system active. This test was used for a jerk and torque study. The second test was an acceleration test performed under road simulation conditions. This test was also used for jerk, in addition to fuel and emissions study. Finally, an NEDC cycle was run using the base vehicle configuration as well as the MHEV configuration. The NEDC cycle was used purely for fuel and emissions investigation.

9.1 Clutch Characterization

In order to complete controller calibration, particularly with respect to the continuous torque delivery, it was necessary to understand the clutch characteristics. The clutch is a single-plate dry clutch, 200mm in diameter and equipped with four spring elements. The friction material is organic and has a 35mm width. Its construction and installation are shown in Figure 9.1.

The clutch performance is a function of the slip speed (the speed difference between the clutch, which is splined to the transmission input, and the friction surfaces, being the pressure plate and flywheel, both of which are affixed to the engine crankshaft output), and the face pressure, which is controlled by the clutch hydraulic system.

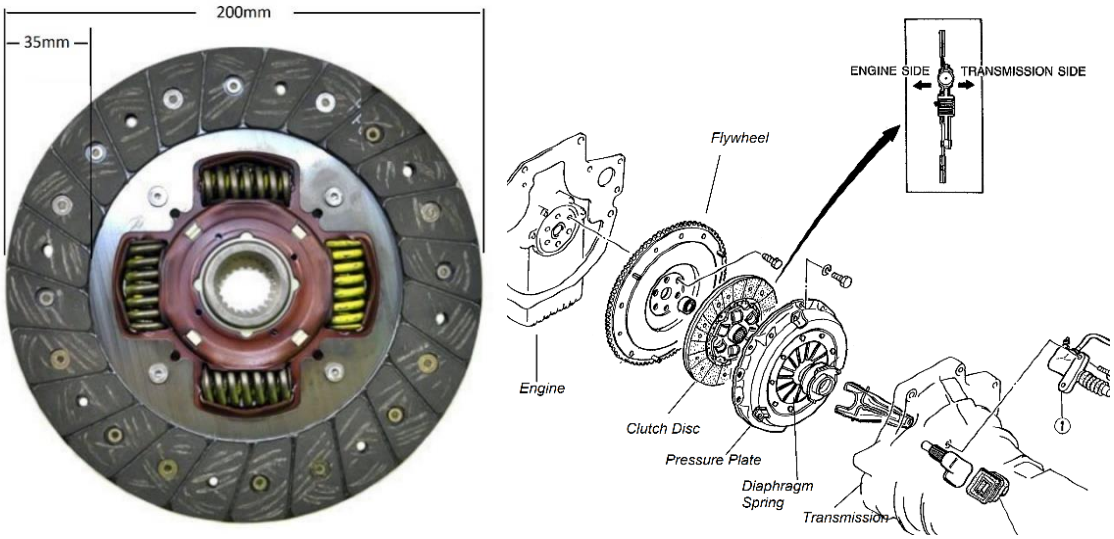

Figure 9.1 Clutch dimensions and assembly diagram (Mazda Motor Corporation 1989)

The characterization of the clutch was performed using a series of stall tests. The driveline was braked using both service brakes and the dynamometer roller brakes to prevent any motion being transferred to the wheels. The clutch was then fully disengaged and the transmission was engaged into second gear. Even though no motion is transmitted the gear selection is an important consideration because torque is measured at the transmission output, therefore the gear must kept constant to ensure tests are comparable. The engine throttle was opened to a constant value corresponding to a particular no-load engine speed. To limit damage to the driveline the no-load speeds selected were 2000 RPM and 3000 RPM. At this point the clutch was slowly re-engaged, holding the driveline stopped and the throttle constant. The clutch line pressure, engine speed, and transmission output torque were all logged to enable clutch characterization. Because the driveline was held stopped, the slip speed in this test is equivalent to engine speed, and a correlation could be derived for clutch line pressure, slip speed, and torque transmissibility. This characterization is essential so that the calibration of motor torque start and stop commands can be completed to a high degree of confidence.

The raw test output is presented in Figure 9.2 below:

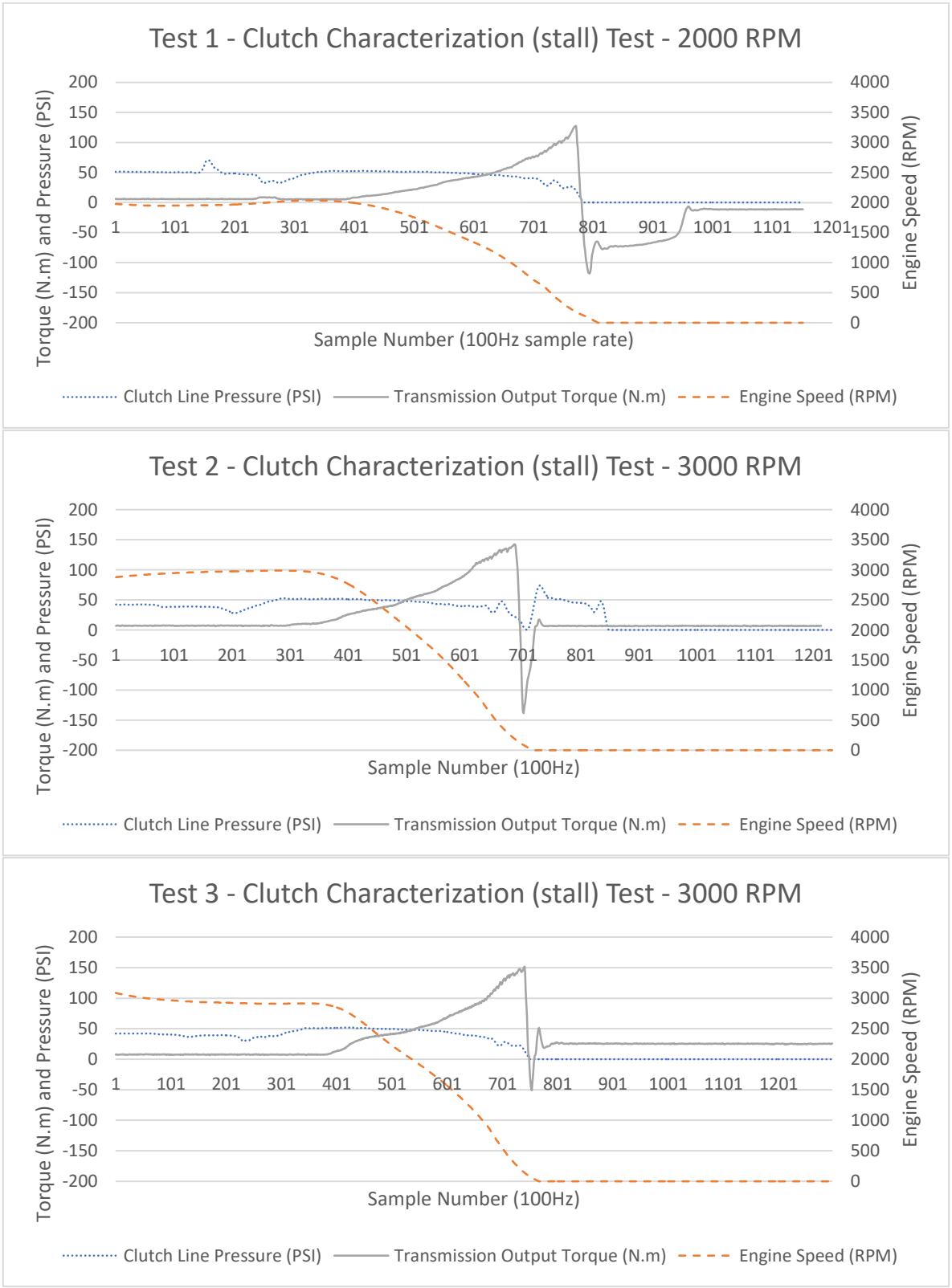

Figure 9.2 Clutch stall test outputs

The stall tests show the engine stall torque of approximately 150N.m at the larger throttle opening used in tests 2 and 3, and a slightly lower stall torque of approximately 126N.m at the smaller throttle opening used in test 1. Test 3 is a repeat of Test 2, which was undertaken due to the release of the clutch in Test 2 immediately after stall. Whilst this did not affect the measurement, it also allows the observation of a torque bias at zero engine speed, due to the engine being forcibly braked during combustion.

The slip speed at which stall begins is relatively constant at 200RPM for all tests, and is clearly seen in Figure 9.3. Torque in Figure 9.3 is expressed as a fraction of the stall torque observed in each test. There is also judder evident at high torque loads just prior to stall, from approximately 1000RPM slip speed. The judder appears to be relatively constant in frequency at about 20Hz, and can also be seen in Figure 9.3. An example of the judder is magnified in Figure 9.4.

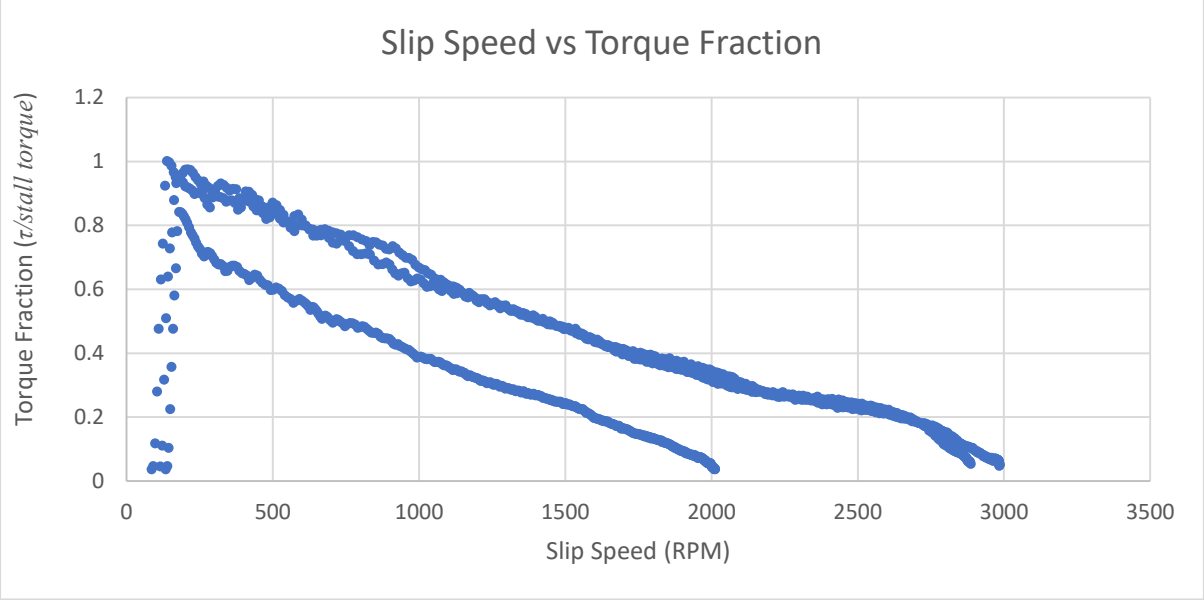

Figure 9.3 Slip speed against torque fraction (transmitted torque expressed as a fraction of maximum observed torque)

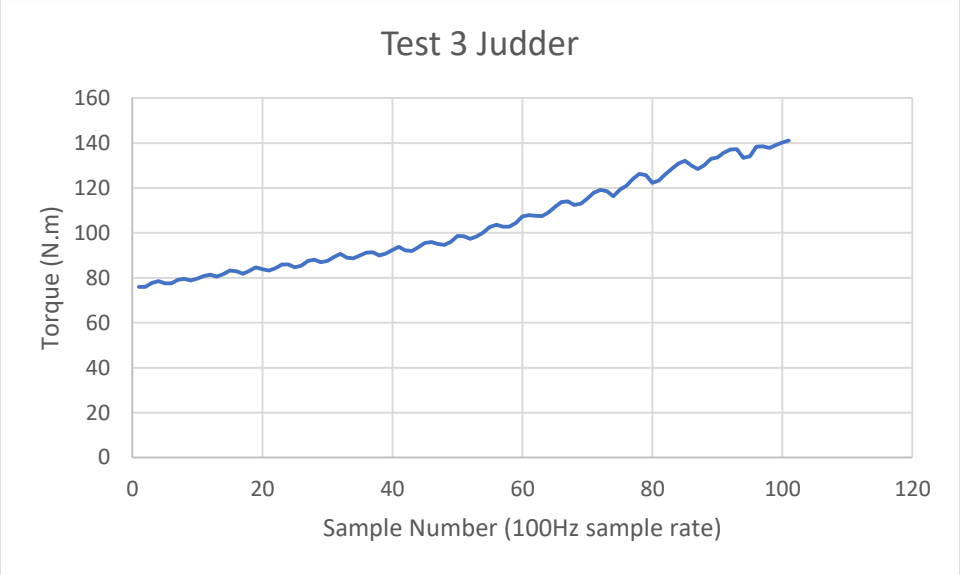

Figure 9.4 An example of clutch judder observed during testing

The test data were collated for analysis to determine a suitable clutch line pressure calibration point for the engagement and disengagement of the torque-hole compensation during gear changes. Figure 9.5 and Figure 9.6 show the correlations between slip speed, torque and clutch line pressure.

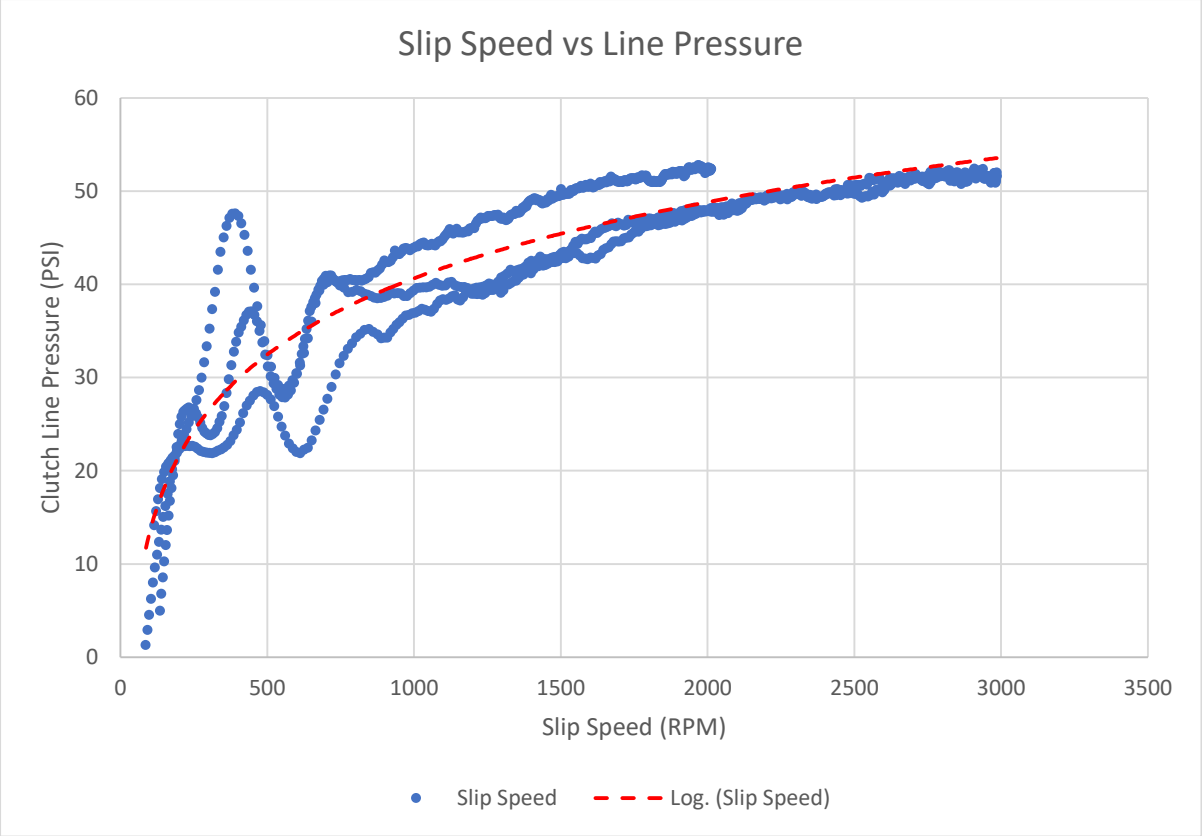

Figure 9.5 Clutch Slip speed against Line Pressure. Self-excitation effects below 900RPM

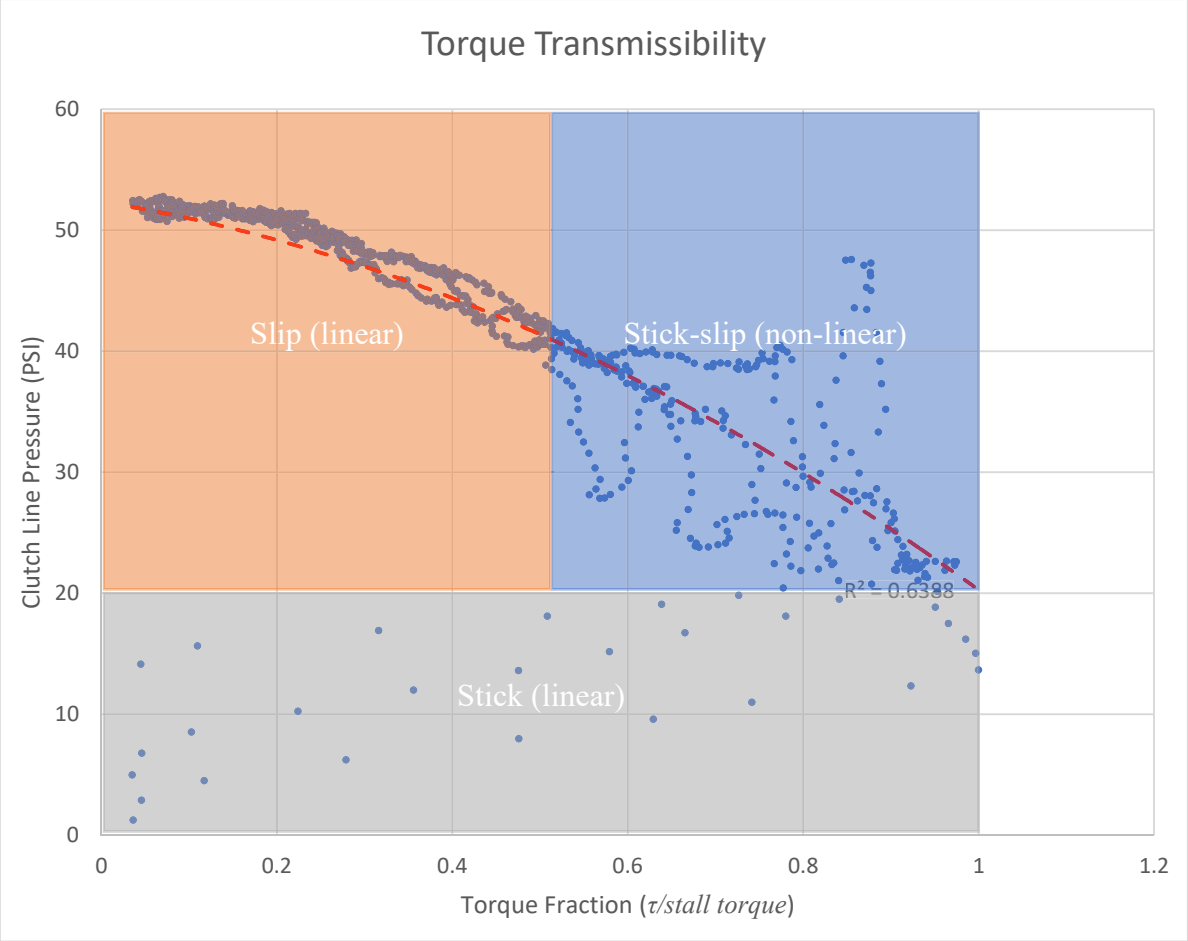

Figure 9.6 Torque transmissibility shows three distinct regions of clutch engagement

Figure 9.6 is useful for understanding the action of the clutch in terms of line pressure. It shows three clear regions. Above 40 PSI line pressure the clutch face is purely in slip. As the clutch pressure decreases the clutch face begins to grip and there is a period of non-linearity in the relationship at around 20-40 PSI. An investigation of this non-linearity could not be carried out because this would require a constant torque source and removal of the clutch assembly from the vehicle, and is beyond the scope of the thesis as presented. However, it is consistent with (Bostwick & Szadkowski 1998). The clutch self-excitation is very clearly delineated at 20 PSI line pressure, where the clutch is fully engaged and causes the engine to stall rapidly.

Based on the characterization of the clutch, in order to ensure continuous torque delivery, the motor is required to be engaged until the period of self-excitation is complete and slip speed is reduced to less than 200 RPM. This provides two functions: firstly, it applies a biasing torque to the driveline to reduce excitation during the torque fluctuation, and secondly, the control of the motor's magnetic field acts as a passive damper for any driveline shocks and vibrations transmitted during this phase. On this basis, the calibration point for the torque fill function of the motor was set such that the function concludes when clutch line pressure reaches 20 PSI. The calibration point for the beginning of the event was set based on the clutch switch signal rather than a pressure signal. This is because the clutch disengagement action by the driver is significantly faster than the clutch engagement action. The clutch switch allows approximately 50mm of pedal travel before switching, which is sufficient to be sure of the driver's intention to change gear providing the car is not creeping at low speed.

9.2 Torque Hole Characterization – Test 1

The characterization of the torque hole was conducted at test road speeds from 20km/h to 60km/h in 10km/h increments. The road speed was held at no more than the target speed by the dynamometer, which is operated in the steady-speed mode. This allows the vehicle to accelerate freely below the target speed but applies load at the target speed to ensure the vehicle does not exceed it. The target gear change is the gear change effected once the target speed is achieved, and the vehicle is under load. The CV mode was tested firstly and then the same test was executed using MHEV mode. An example of the test profile is reproduced in Figure 9.7; the profile is similar in trajectory for 20, 30, 40, and 50km/h.

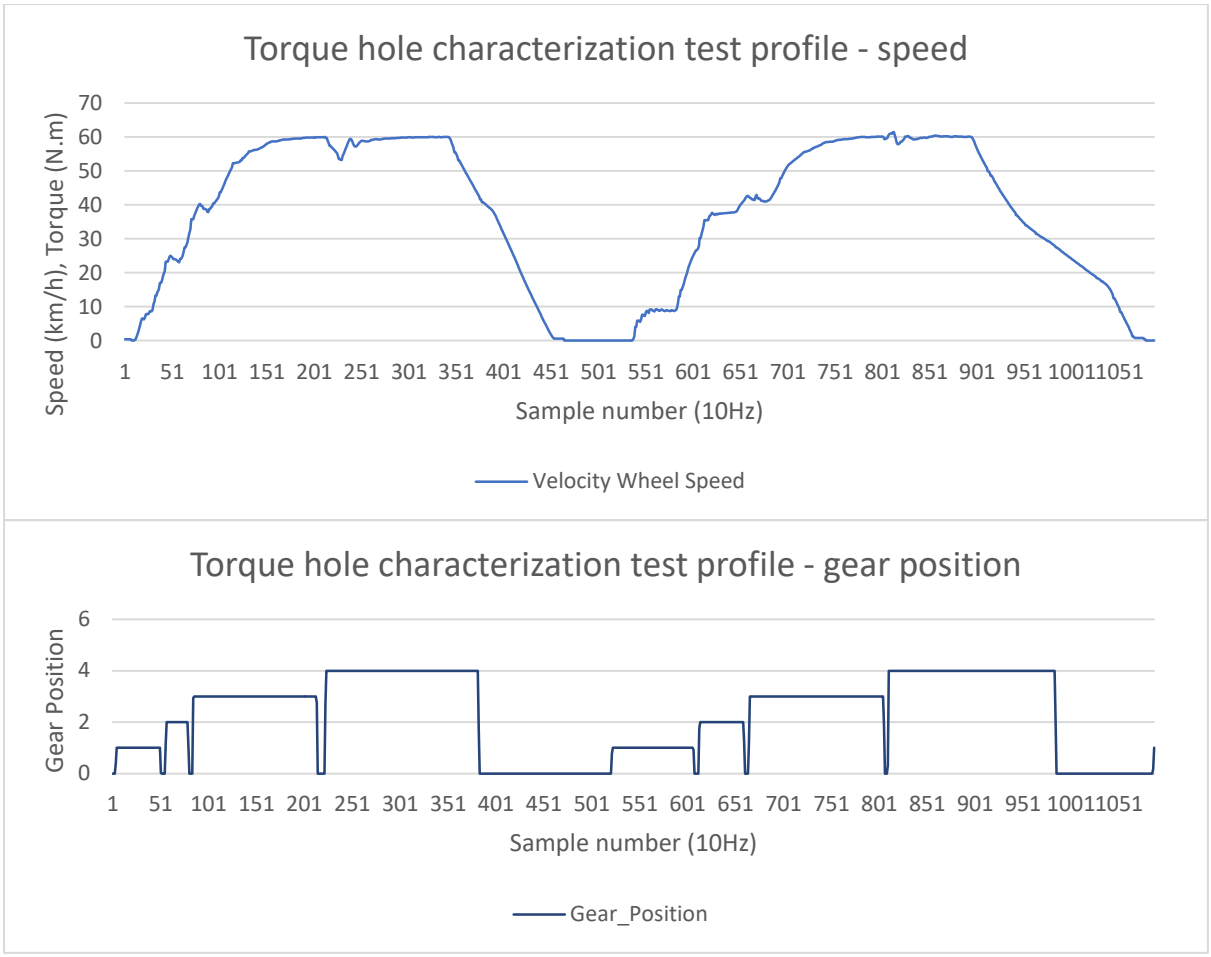

Figure 9.7 Complete test profile for 60km/h 3-4 shift torque hole characterization

9.2.1 Uncontrolled Torque Hole

The uncontrolled torque hole is presented for comparison with the controlled results presented in Figure 9.8. Representative data are provided for each test speed 20km/h-50km/h.

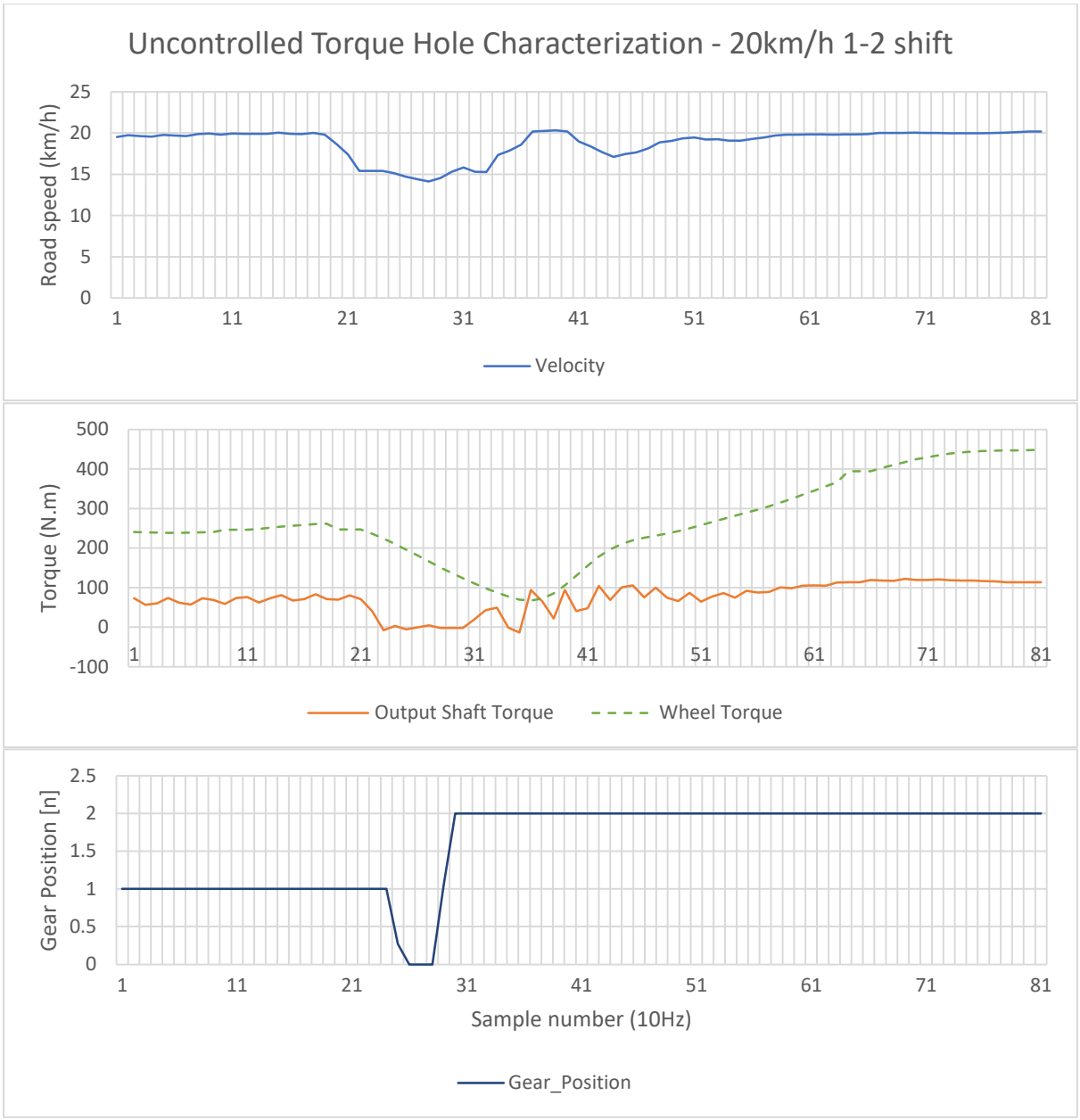

Figure 9.8 Torque hole for a 1-2 shift without continuous torque control

The data shows the gear selection process for a 1-2 shift at 20km/h. The clutch disengagement begins at 1.9s with total disengagement taking approximately 0.4s. the gear selector is actuated at 2.4s, and the 1-2 gear selection takes 0.7s. The clutch re-engagement begins at 3.1s, simultaneously with the successful engagement of gear 2. There is a period of 2s torque oscillation at approximately 4Hz, with the maximum amplitude 106Nm representing the full settled torque value in gear 2. Total shift time is 3.2s.

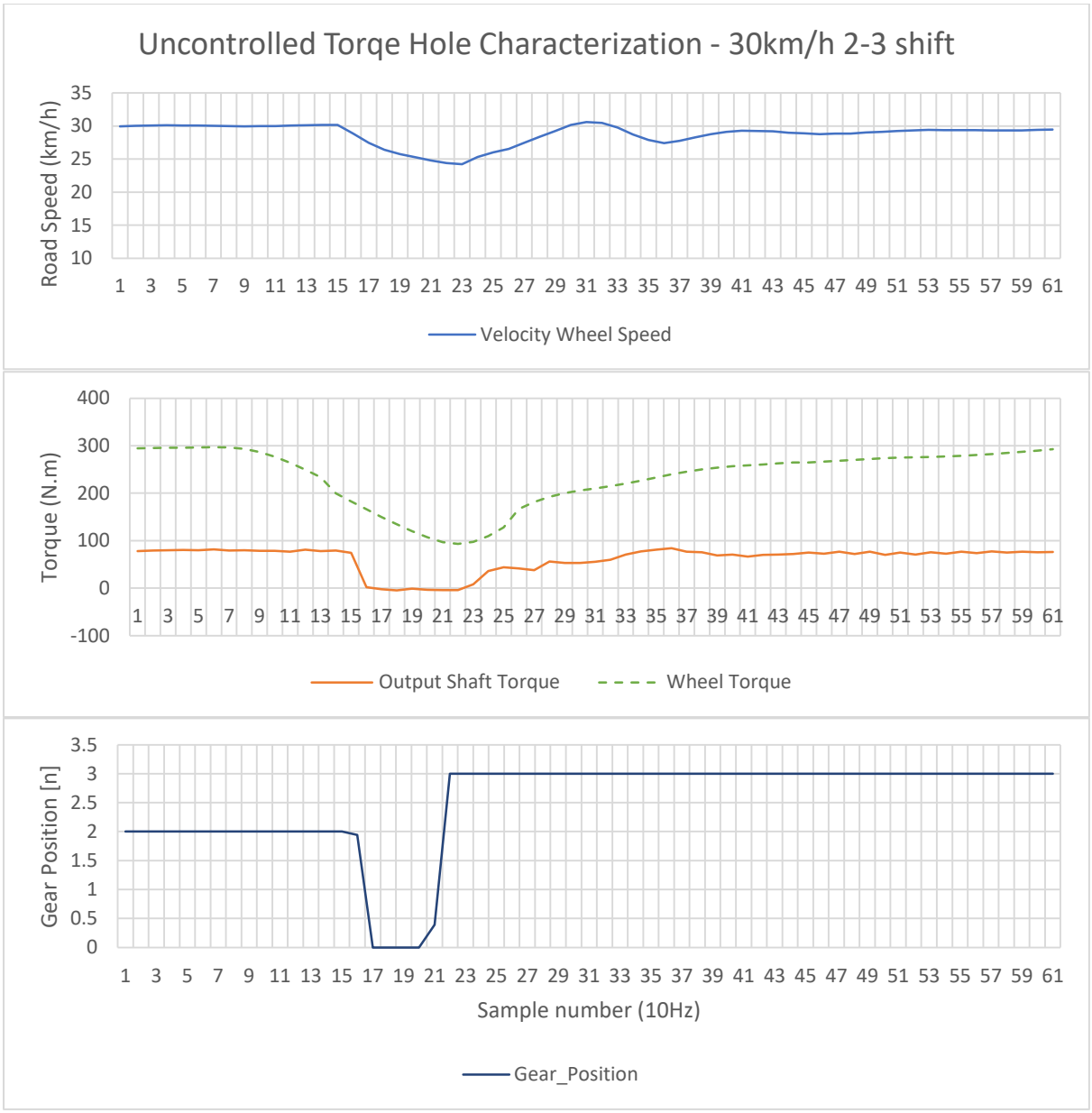

Figure 9.9 Torque hole for a 2-3 shift without continuous torque control

The 2-3 shift at 30km/h (Figure 9.9) is markedly smoother than the 1-2 shift. There is no significant torque oscillation although torque settling time is of roughly the same order as the 1-2 shift, being completed in approximately 1.7s after the beginning of clutch re-engagement. Shift time is 2.5s.

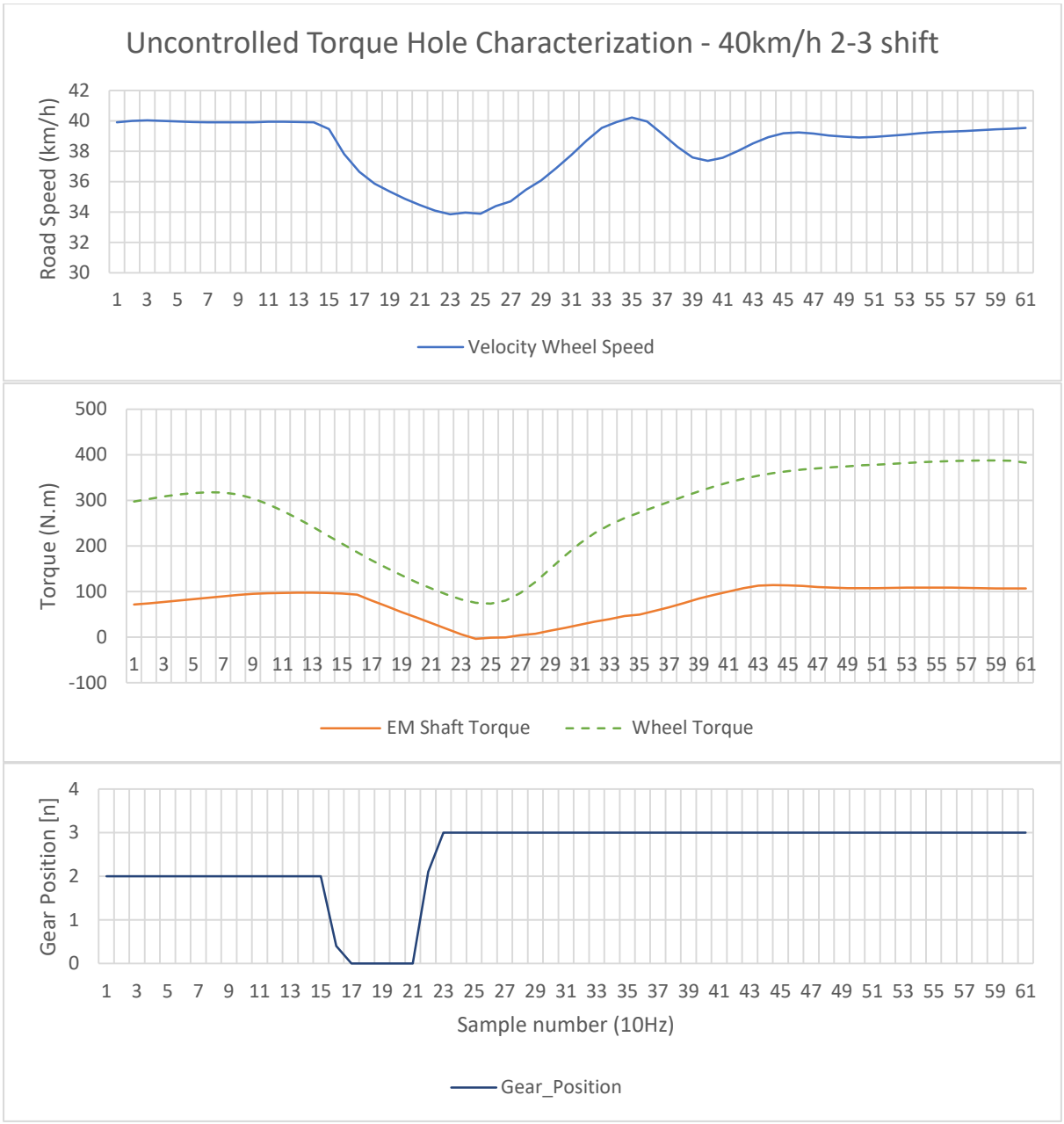

Figure 9.10 Torque hole for a 2-3 shift at 40km/h without continuous torque control

The 2-3 shift at 40km/h (Figure 9.10) is relatively smooth and has no appreciable torque disturbance, with only a very minor overshoot evident at 4.1s-4.6s. As vehicle speed increases the angular momentum of the rotating elements damps torque disturbances.

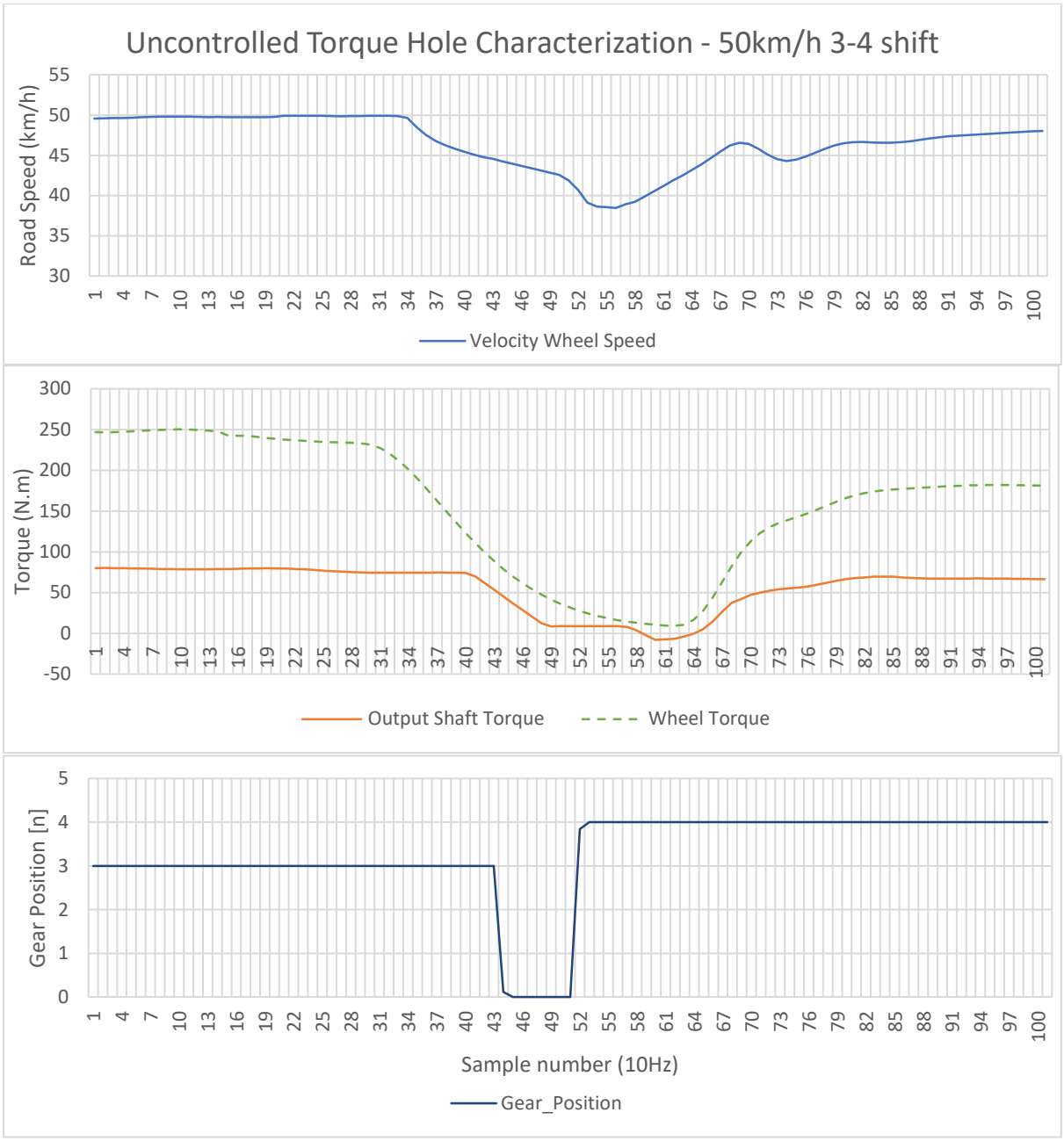

Figure 9.11 Torque hole for a 3-4 shift without continuous torque control

The 3-4 shift (Figure 9.11) is similar in nature to the 2-3 shift but there is no torque overshoot.

There are also some common characteristics to all gear shift data, which are a result of the dynamometer measurement. The road speed in each case shows two dips before settling. The first dip is a result of the gear selection process, but the second dip is a result of the

dynamometer controller acting to re-apply load to the vehicle. The wheel torque in each case also does not reach zero. This is due to the dynamometer inertia. For this reason, shaft torque is used for all analysis but wheel torque is also provided for completeness. It is clear from the characterization of the uncontrolled torque hole, that the jerk reduction functionality of KERMIT's control system is more critical in lower-gear shifts due to the high level of torque oscillation, but the torque in-fill functionality of the control system is more critical in higher-gear shifts.

9.2.2 Torque Fill-In

The gear shift including the torque fill-in can be described in 3 main phases. The first is the slip-open phase, in which the clutch is released. The second is the torque phase, in which the torque control is applied. The last phase is the inertia phase, where the clutch is being engaged and the separate inertias are being matched. The same phases apply to the conventional gear shift except the torque phase, which is replaced with the synchronization phase because there is no torque control. Acceptable torque in-fill requires a number of target characteristics to be met. In the first instance, the clutch disengagement must be detected and the electric motor must be engaged to provide equivalent torque at the instant of disengagement. Therefore, start timing of the torque pulse is important. Secondly, the torque pulse must be halted at the appropriate time to ensure there is no torque spike delivered to the wheels which could result in unintended acceleration. Therefore, the end timing of the torque pulse must also be controlled. Thirdly, the delivered torque value throughout the pulse must be sufficiently scaled to provide reasonable agreement with the engine torque at the start of the gear change event, and must also be predicted with sufficient accuracy to minimize unwanted oscillation at the inertia phase. Finally, the slip speed of the clutch face should be minimized to reduce self-excitation which induces undesirable and uncontrolled non-linearity in the system.

Control Value	Observed effect of non-conformance
Torque Start Timing	Torque peak (early) / trough (late) at gear change start
Torque End Timing	Torque peak (late) / trough (early) at gear change end
Torque Start Value	Torque step at gear change start and during gear change
Torque End Value	Torque step at gear change end
Clutch Slip Speed	Torque oscillation at gear change end

Table XXVI Control values for the continuous torque control system

A selection of gear shift events are presented showing fill-in characteristics, and discussed with reference to the control parameters and methodology. The gear shifts are representative of ideal torque in-fill as well as the various non-conformances. The discussion and analysis in 0 will characterize the effect of ideal control as well as non-conforming control on jerk.

The 20km/h 1-2 gearshift is presented in Figure 9.12. The torque in-fill control was successful for start value but start time was approximately 0.2s late. This is shown in the effective torque hole elimination at 2.5-3.3s. The vehicle speed remains relatively stable, varying only by 1km/h whilst the torque control is active. However, the command ends prematurely as shown in the battery current trace which begins to drop at 3.6s, turning off entirely at 4.0s, resulting in a torque hole of 0.9s duration and a resultant drop in vehicle speed of 6.1km/h. The torque control end conditions are deliberately triggered in the following cases:

- Brake switch trigger
- Clutch pressure below threshold
- Battery pulse time over safe limit
- Gear shift time over limit

By examining the logs of this event, none of these events triggered the premature end command. Instead, the calculated target torque (the torque at the end of the gear shift event) was determined by the controller to be zero. This is due to some load sites in the engine load map having zero value. Effectively, the torque end value was incorrectly calculated and this caused end time error and engine speed being uncontrolled for the clutch re-engagement.

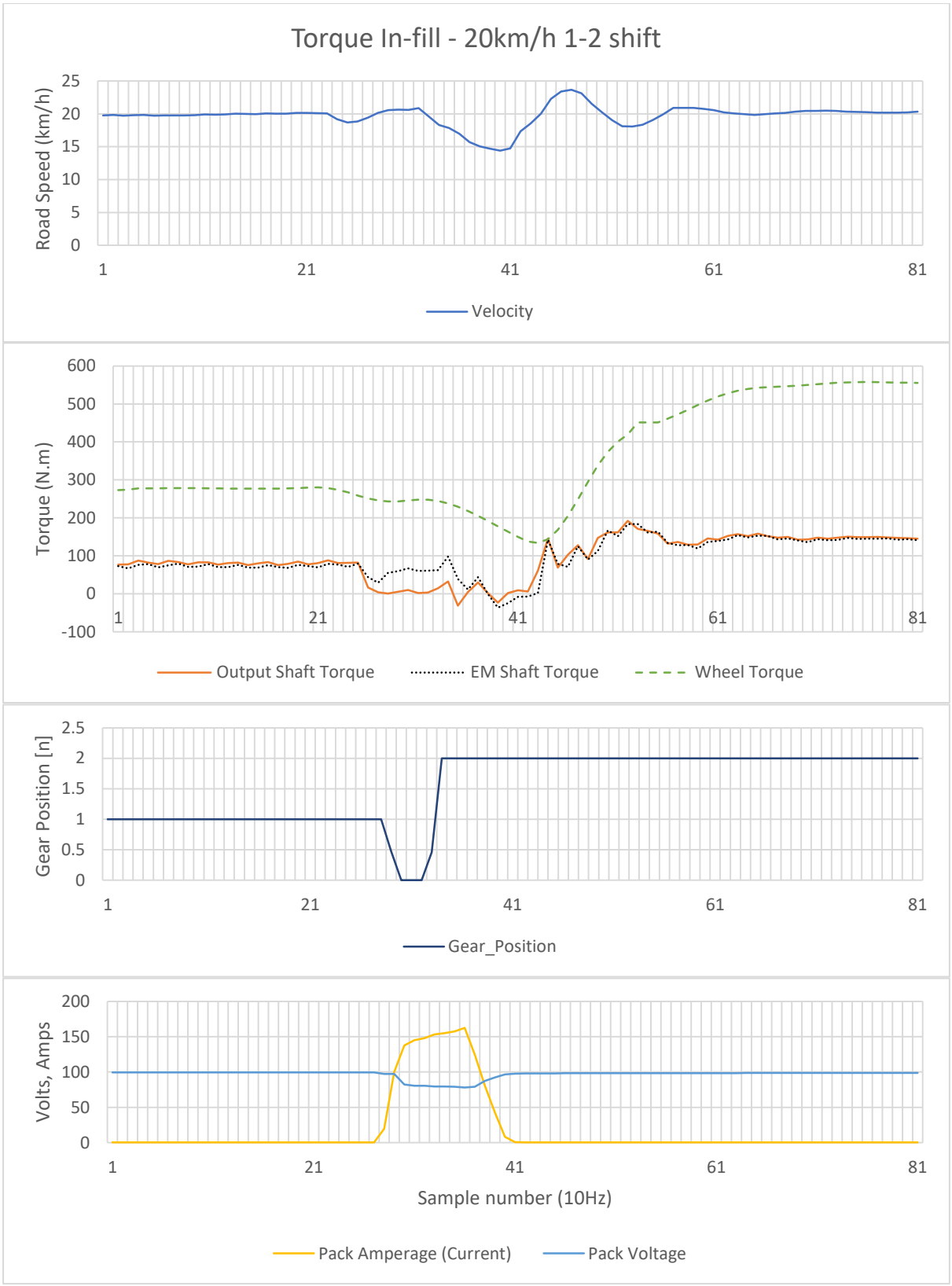

Figure 9.12 Time domain data for a 1-2 shift using continuous torque control

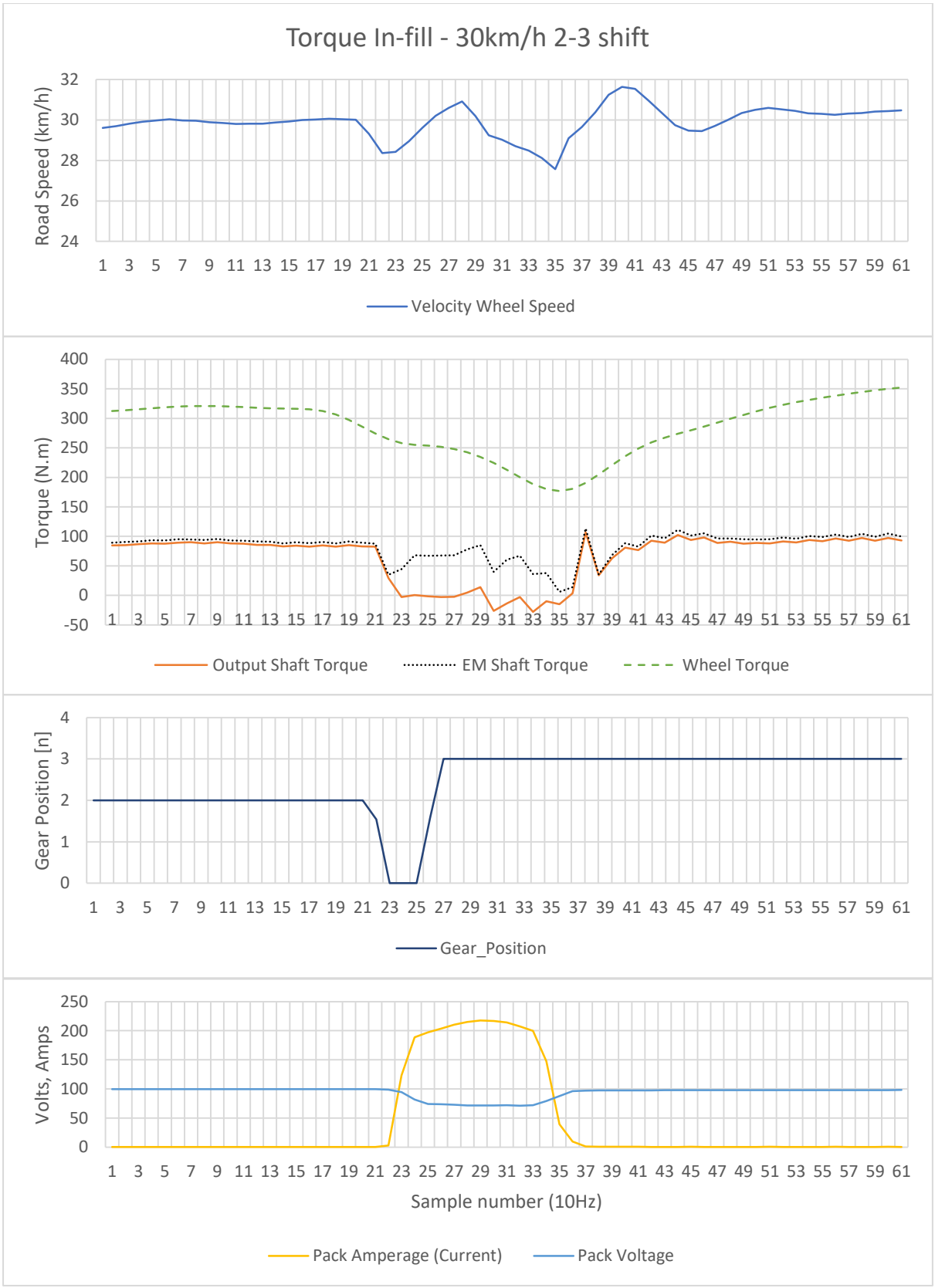

Figure 9.13 Time domain data for a 2-3 shift using continuous torque control

The 2-3 shift shown in Figure 9.13 shows a shift event that is similar in nature to the 1-2 shift shown in Figure 9.12, but achieved better end timing. The torque hole is reduced in duration from 1.5s to 0.4s, resulting in a speed variation of ±2km/h from the 30km/h target speed. The shaft torque shows a full-scale torque spike at 3.7s, immediately following the torque phase. This is induced by rapid clutch engagement without effective clutch slip control. The 4Hz torque oscillation characteristic of the uncontrolled inertia phase is seen again in this example. Examination of the event log shows the smaller torque hole was a result of slow clutch re-engagement by the driver, which induced sufficient self-excitation to cause clutch line pressure to drop below threshold. Because the system relies on manual actuation of gear selector and clutch release, there is no way to differentiate in real time between pressure variation caused by self-excitation and the same caused by driver action. Extra instrumentation could be installed to provide better confidence in the intended driver action, by way of determination of clutch pedal position or clutch plate position. The correlation between pedal position, or pedal velocity and clutch line pressure could then be used to determine the state of the clutch and the driver intention. This could then be used to adjust end timing more accurately in real time.

The 2-3 shift at 40km/h shown in Figure 9.14 demonstrates ideal continuous torque control outcome. The torque hole is almost entirely eliminated. Continuous torque is fully achieved and there is no appreciable torque oscillation during the inertia phase. There is a minor torque drop of 10N.m toward the end of the shift which causes an appreciable jerk at 3.2s, but overall, vehicle road speed is very well controlled in comparison to the same uncontrolled shift. The variation from target speed is +1.8/-2.1km/h. This is reduced by 36% from the uncontrolled shift, which shows variation of +0/-4.1km/h. The variation is, in a large part, due to the test conditions which result in relatively high torque being applied to control the

vehicle speed at the target. When the vehicle is tested under road load conditions only, the output is generally smoother as the tractive load is considerably smaller.

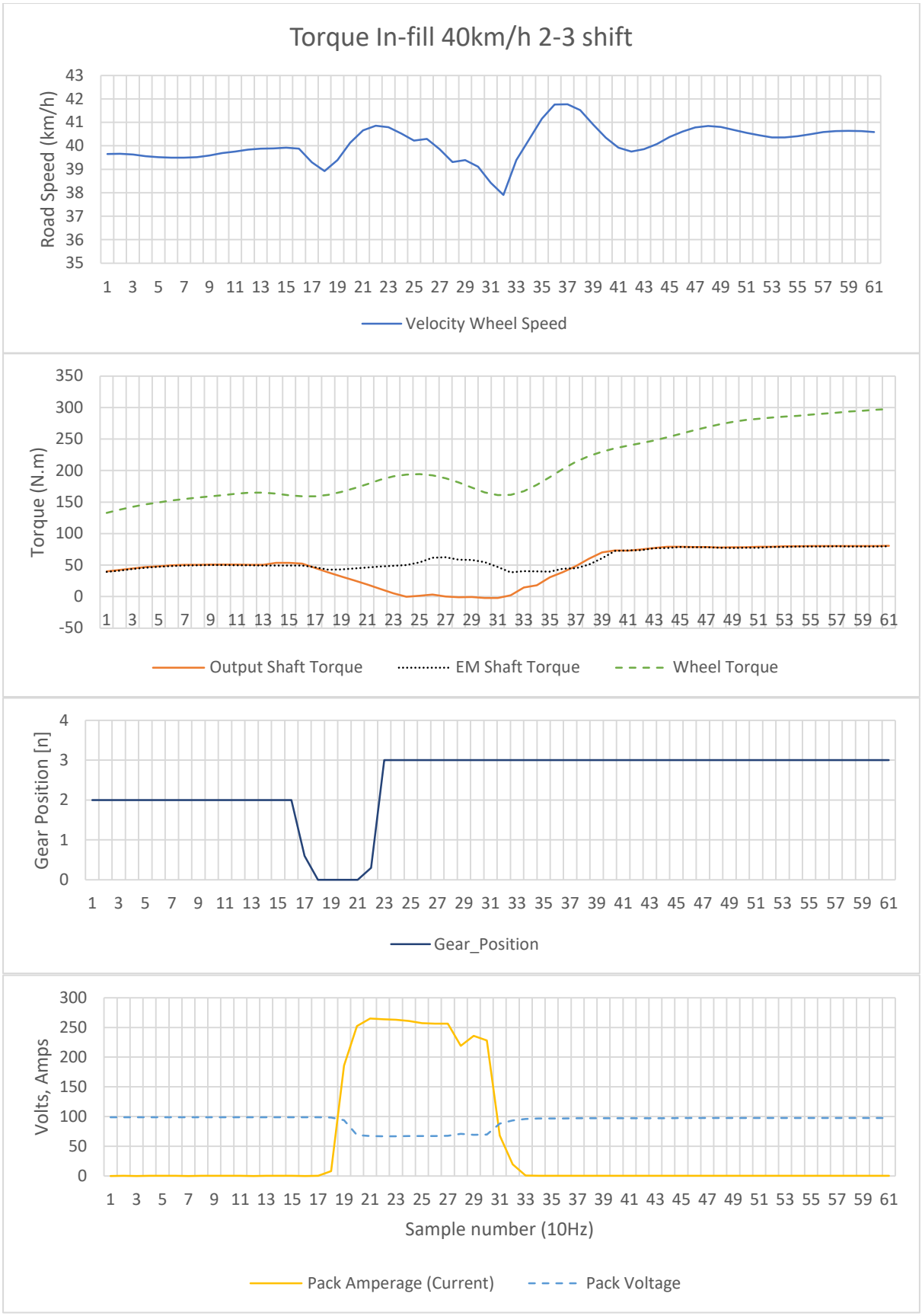

Figure 9.14 Time domain data for a 2-3 shift at 40km/h using continuous torque control

Figure 9.15 Time domain data for a 3-4 shift at 50km/h using continuous torque control

Finally, the 50km/h 3-4 shift is presented in Figure 9.15. The shift achieves continuous torque delivery although the torque hole is not completely filled. None of the start time, start value, and end value parameters were accurately calculated. The output of the incorrect calculations results in an initial torque dip of approximately 25N.m (late start time), then a rise of 15N.m (low start value), followed by a fall of 20N.m (low end value) at the inertia phase. This results in a total torque hole reduction of 51%, with the minimum torque achieved being approximately 30N.m at the end of the torque phase. Nevertheless, despite the inaccurate control, the shift completes 1.6s faster than the equivalent uncontrolled shift and the speed variance is greatly reduced.

The HIL continuous torque control verification run is shown below in Figure 9.16 (top), along with the torque data from the 50km/h 3-4 shift (Figure 9.16 bottom). There is good agreement between the two sets of data. The shift times are similar for both sets of data, with the HIL verification shift taking approximately 4.6s and the validation run taking 4.4s. The primary differences between the data relate to the start and end time. In the HIL data the start time 0.3s later than the experimental data. This causes the torque hole to be momentarily completely unfilled, whereas there is only partial loss of torque in the experimental data. Meanwhile the HIL data shows the continuous torque control ended prematurely resulting in another momentary torque gap, whereas this is less pronounced in the experimental data. The torque overshoot immediately following the shift completion in the experimental data is a result of the dynamometer controller behavior, which magnifies the inertia phase oscillation, and is not evident in the HIL data.

The data show that the target of continuous torque delivery during gear changes was accomplished with acceptable performance, and reasonable agreement with HIL verification.

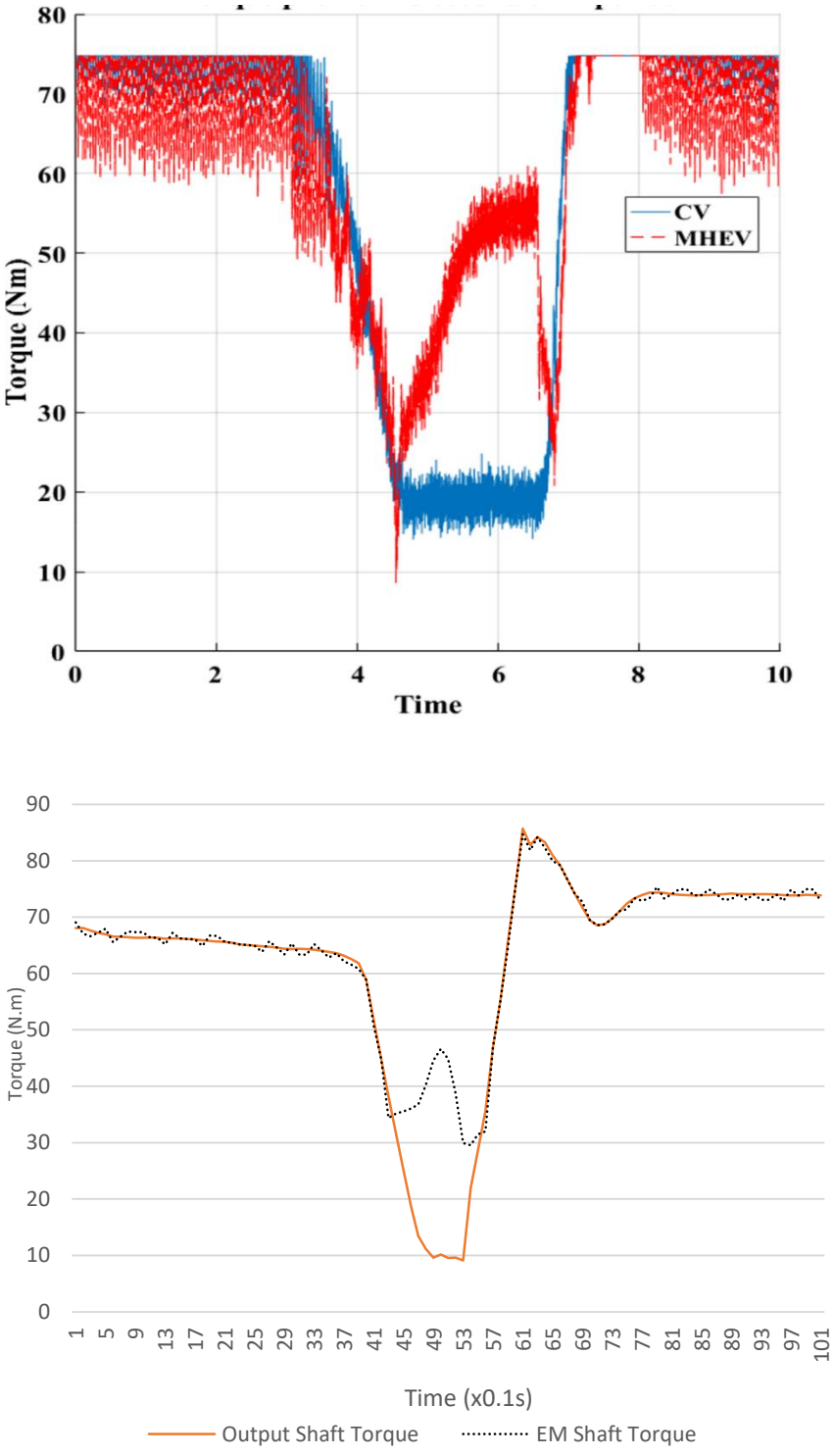

Figure 9.16 Simulated gear shift (top) using HIL compared against experimental data from the prototype vehicle

9.2.3 Jerk

Direct sensing of jerk, although possible, is not commonplace. There does not appear to be any commercially available jerk sensor and there are a few publications in academic literature describing the construction of such a sensor. (Xueshan et al. 2008) describes the construction of a triaxial sensor for earthquake data collection, whilst (Fujiyoshi et al. 2002) describes a 2-DOF micro-electromechanical system for automotive use. In the absence of direct sensing, acceleration data can be differentiated once to obtain jerk, or the second derivative of speed also yields jerk data. For an accelerometer-based study to be accurate, the vehicle being tested must be in motion. On a dynamometer, the vehicle is tied to ground anchors preventing chassis motion, therefore an accelerometer-based dynamometer study of jerk is not possible. In order to investigate jerk on a dynamometer, the analysis of jerk relies on the accurate measurement of wheel velocity. Whilst it is possible to use shaft rotational velocity instead, the jerk experienced in the cabin is a function of the road speed, which is subject to further damping due to the flexible mounting of the differential and rear subframe, as well as suspension mountings and tyre compliance. Because jerk is the second derivative of speed it is also highly susceptible to variation due to measurement noise. Therefore a very smooth data set is required to ensure jerk is representative. For this reason, wheel speed was used for the following jerk study, rather than shaft speed. The gear shift events presented in 9.2.2 have been used for the basis of the jerk study.

The characteristics of the gear shifts are relatively uniform. There is a negative jerk coinciding with slip-open, and a positive jerk coinciding with the beginning of the inertia phase. These two characteristics are qualitatively constant throughout all the gear shifts presented. In the CV mode, during the synchronization phase, jerk is relatively uniform, generally characterized by a small, 1~2g/s jerk which extends for 0.2-0.3s. There is less uniformity in the MHEV mode, due to the variance of the continuous torque control.

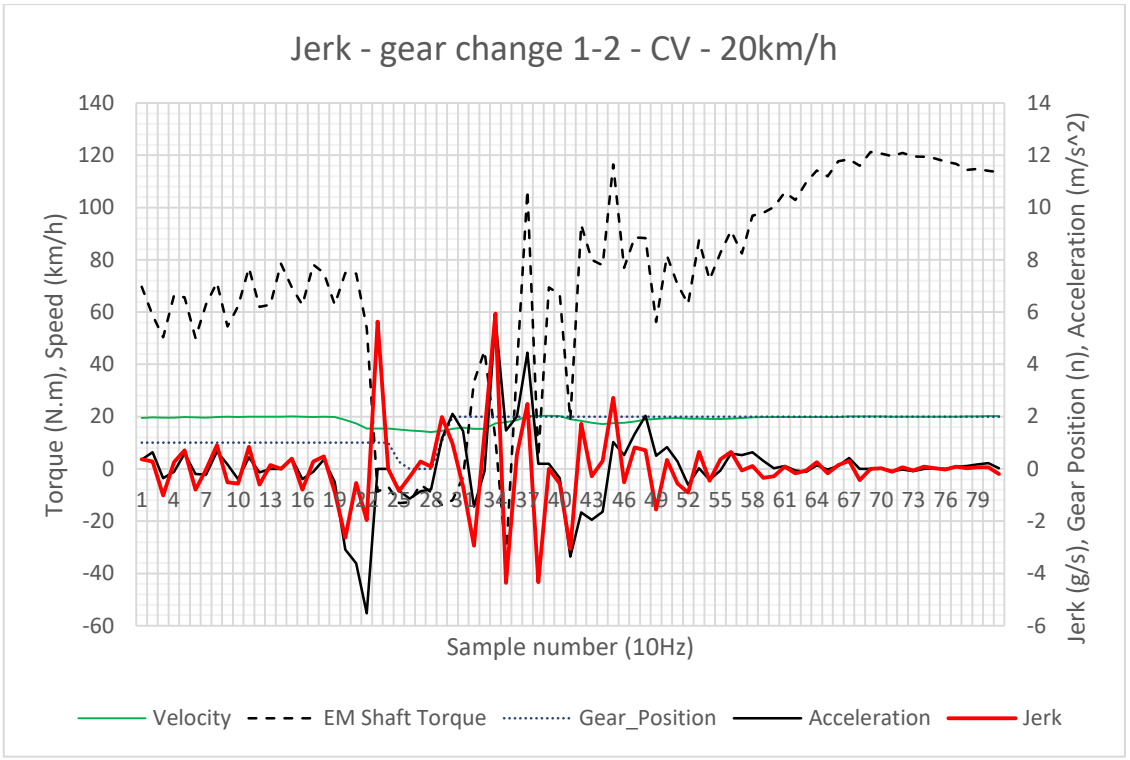

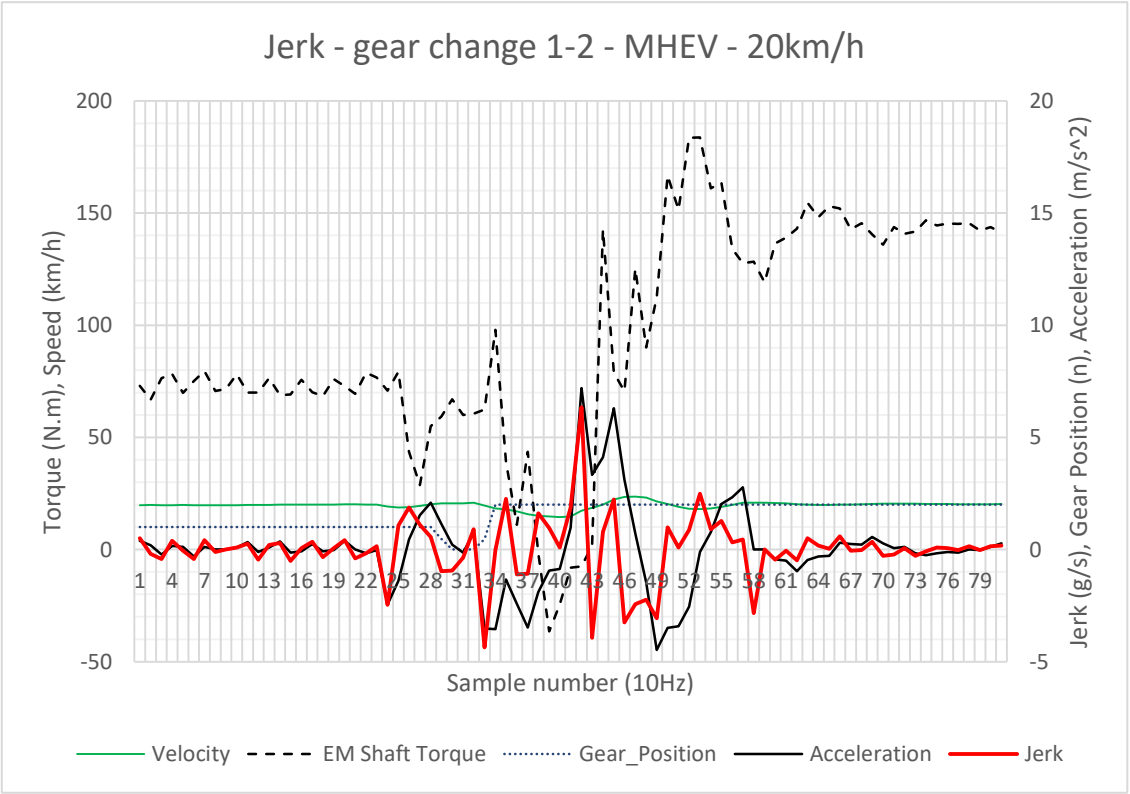

Figure 9.17 Jerk data during the 20km/h 1-2 gear shift

Referring to Figure 9.17, the 1-2 CV gear change exhibits the highest absolute jerk, reaching 5.94g/s. This is a result of the large gap between first and second gear ratios, meaning inertia matching is difficult to achieve smoothly. Notably, there is a positive jerk at the slip-open phase (2.3s) that is generally absent in other gear shifts. This positive jerk can occur when the throttle is released prior to the clutch being fully disengaged. The engine braking causes an initial deceleration and then the deceleration is reduced when the clutch becomes fully disengaged, resulting in a positive jerk. In this case, the MHEV shift shows no positive jerk at the same phase, indicating good throttle co-ordination. The negative jerk at 2.4s is also smaller than that of the CV. Whilst the MHEV has slightly higher jerk at the beginning of the inertia phase, there are fewer oscillations throughout. This suggests the MHEV continuous torque control may deliver better occupant comfort than the uncontrolled shift in this instance, despite the higher initial jerk.

The 2-3 CV gear change in Figure 9.18 (30km/h) is a more typical representation. The negative jerk at slip-open (1.6s) is followed by a relatively smooth synchronization phase indicating the vehicle is generally under its own momentum with no driveline-induced jerk. The inertia phase is characterized by an initial jerk of similar magnitude to that observed at slip-open, The inertia phase settles in approximately three cycles. Compared against the MHEV shift, the slip-open jerk is substantially reduced. However, the torque control induces jerk during the torque phase, which is similar in magnitude to the initial, slip-open jerk. This is due to transitioning from start to end torque values. The inertia phase settles in one cycle with very minor torque overshoot, however the intial jerk is quite high.

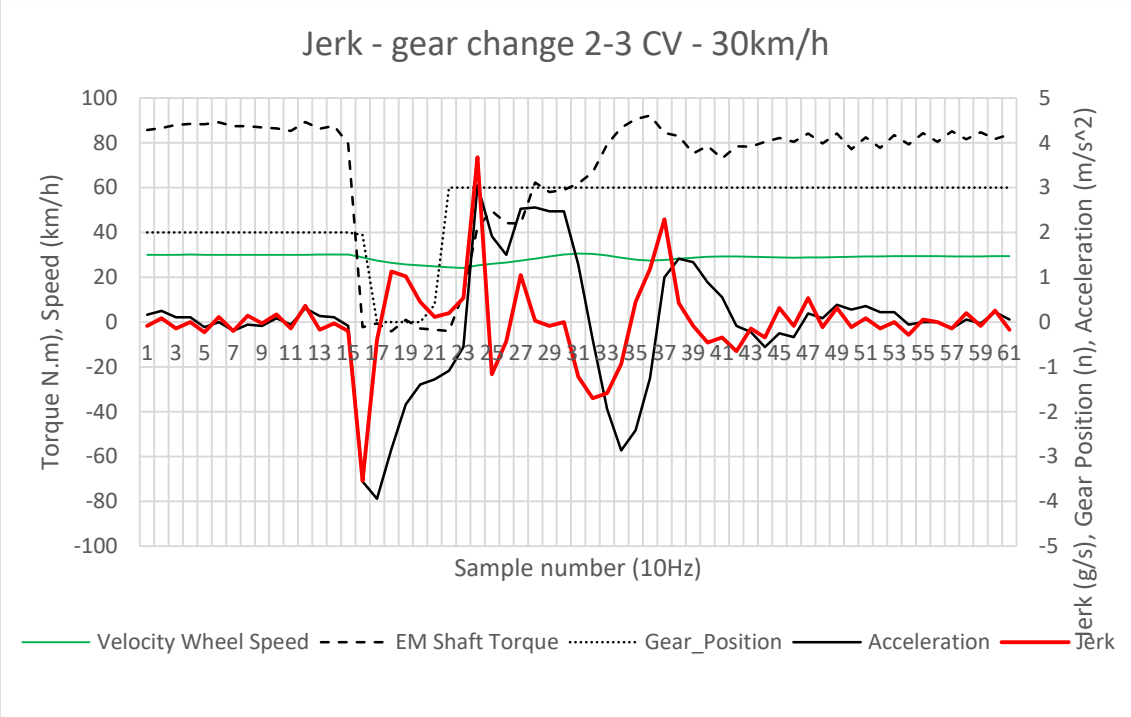

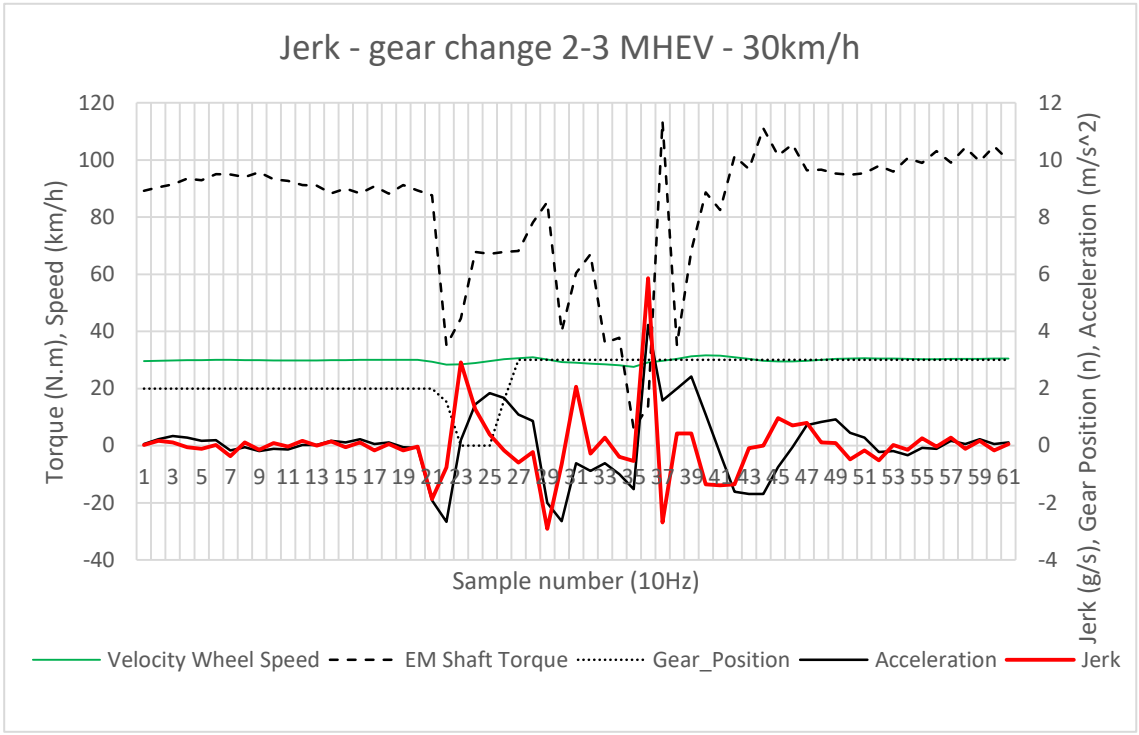

Figure 9.18 Jerk data during the 30km/h 2-3 gear shift

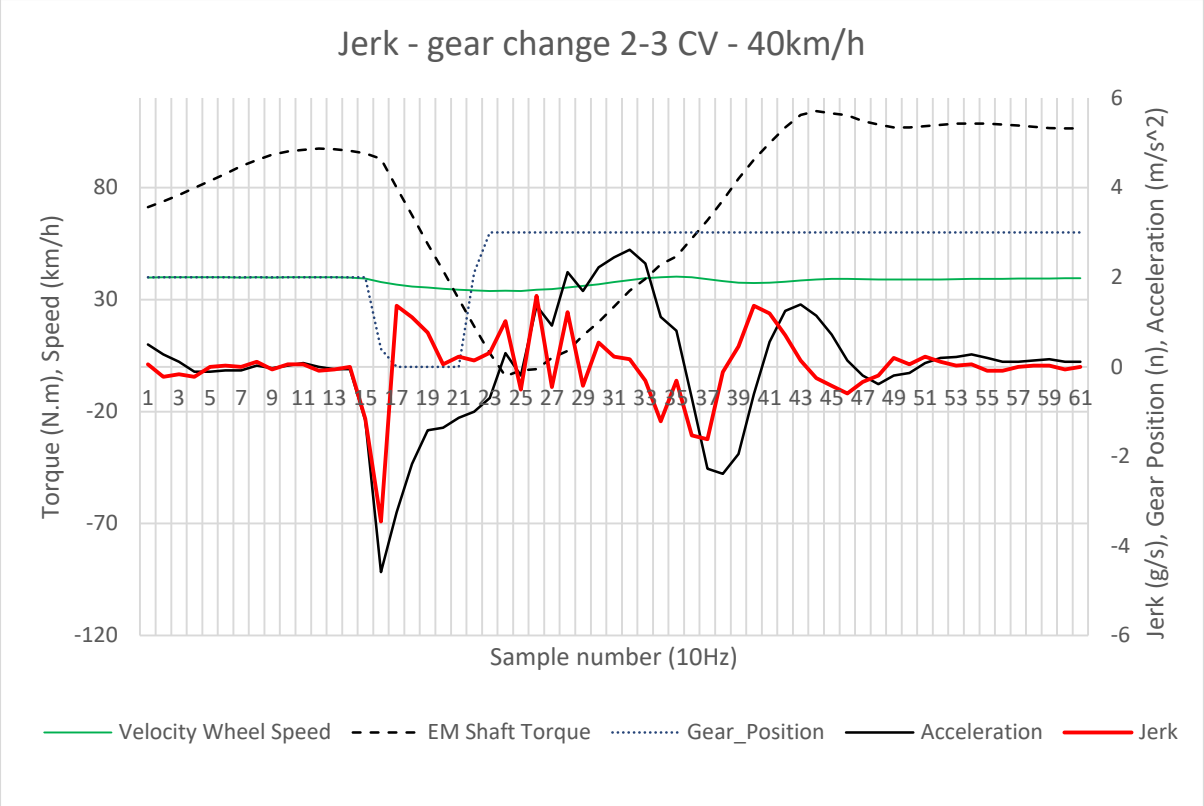

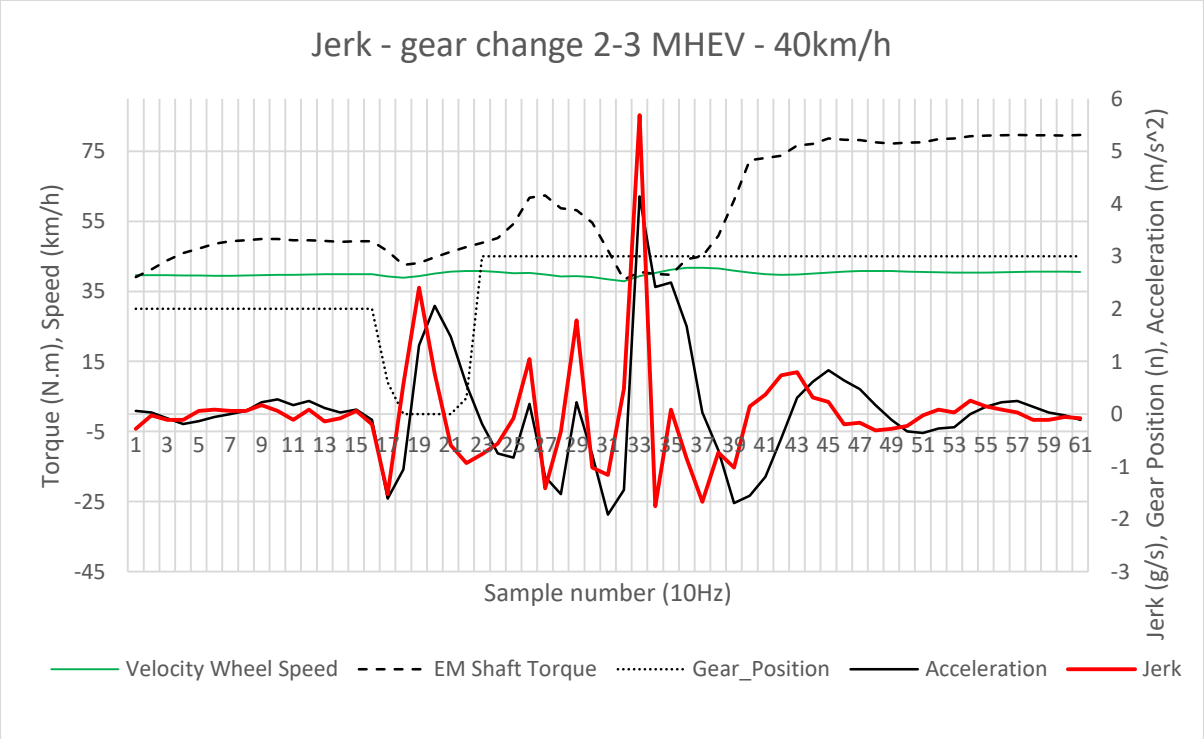

Figure 9.19 Jerk data during the 40km/h 2-3 gear shift

The 2-3 MHEV gear change shown in Figure 9.19 delivered excellent torque hole reduction, resulting in almost full-scale torque being delivered throughout most of the gear shift. However, jerk results during the shift were not ideal. The slip-open jerk was almost eliminated (<1g/s) but a large positive jerk accompanied the beginning of the torque phase, where the CV shift was relatively smooth. Likewise, at the start of the inertia phase, another jerk of 5.69g/s is induced. This is due to a slight overlap between the continuous torque control and the clutch actuation, resulting in torque summation through the driveline causing a small acceleration overshoot.

The 3-4 shift in Figure 9.20 exhibits similar characteristics to that shown in Figure 9.19. The negative jerk associated with the slip-open phase is markedly reduced compared to the CV shift. The positive jerk associated with inertia phase is also reduced in contrast to the CV shift. However, whilst this is ultimately the goal of the jerk reduction, there is also a large negative jerk evident at the inertia phase of this shift that does not appear in others. This negative jerk appears to be a result of engine speed discontinuity forcing the driveline to accelerate the engine during the inertia phase. This is typically caused by the momentary closing of the engine throttle.

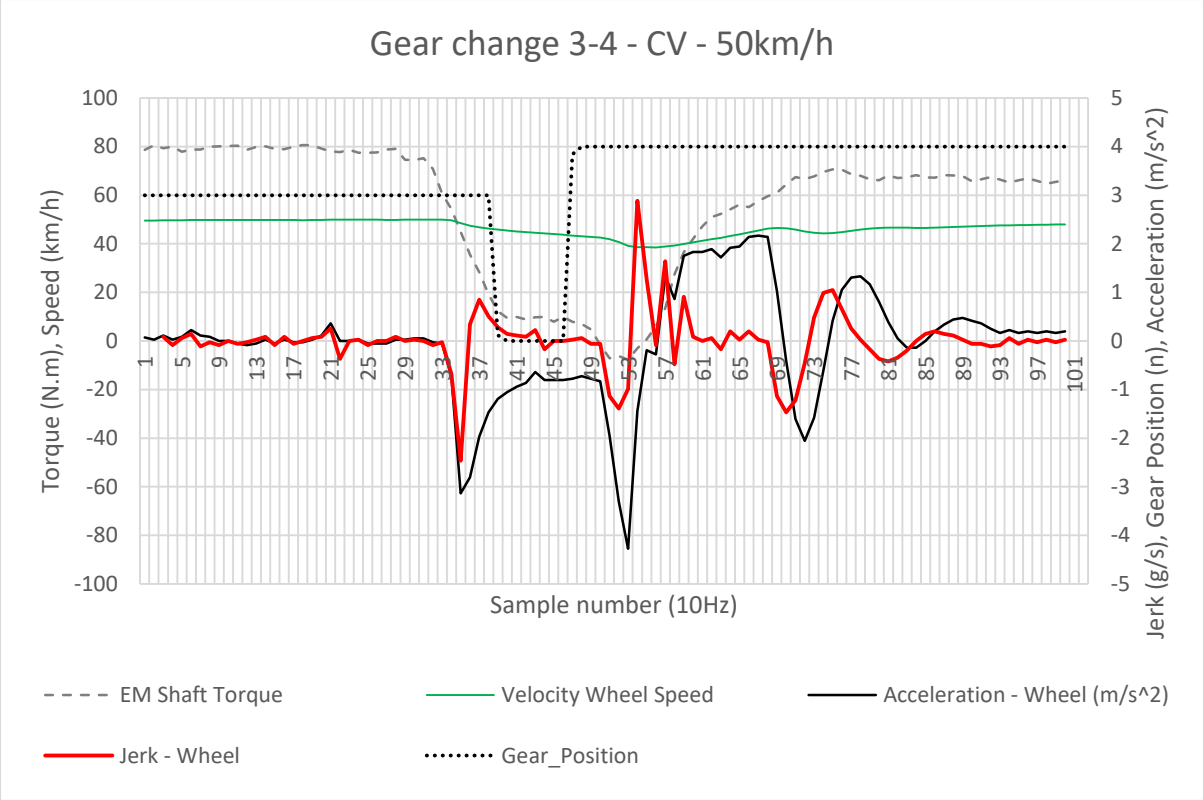

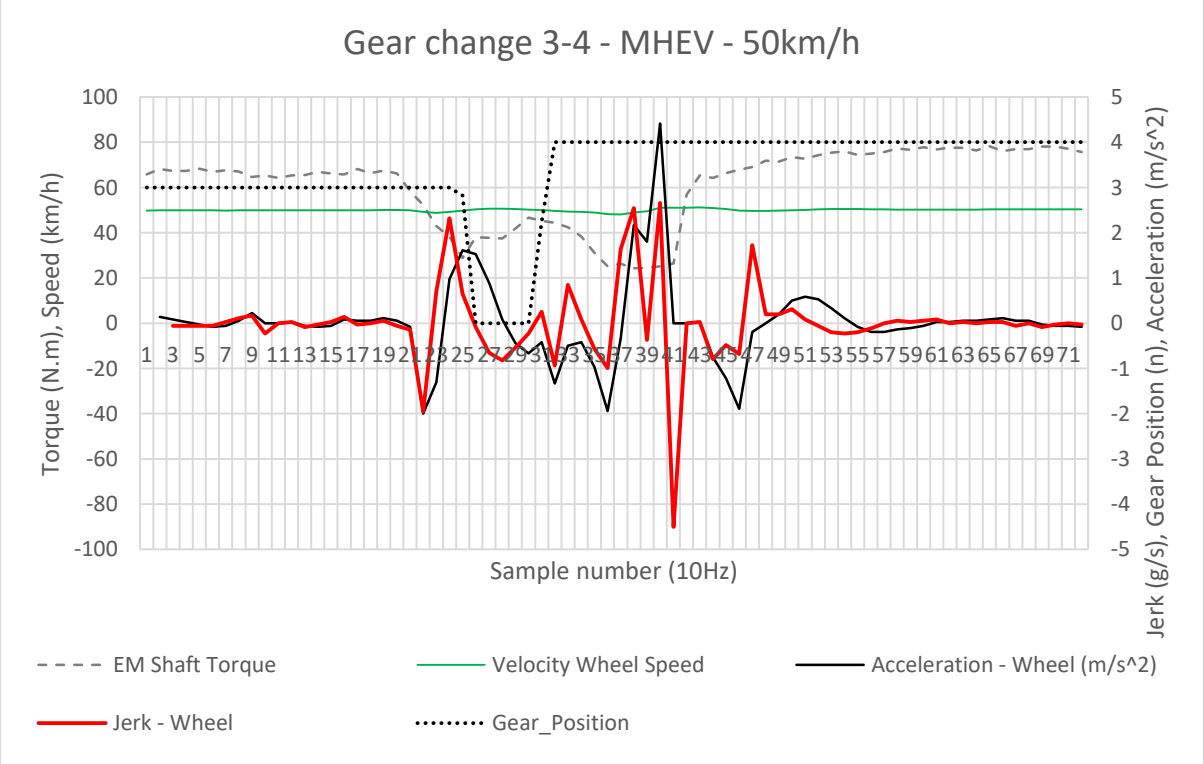

Figure 9.20 Jerk data during the 50km/h 3-4 gear shift

Initial Phase Jerk Results - Summary								
	20km/h 1-2 shift		30km/h 2-3 shift		40km/h 2-3 shift		50km/h 3-4 shift	
	Release	Engage	Release	Engage	Release	Engage	Release	Engage
CV (g/s)	-2.63	5.94	-3.53	3.68	-3.45	1.58	-2.46	2.88
MHEV (g/s)	-2.46	6.34	-1.86	5.86	-1.52	5.69	-1.95	2.66
Difference (%)	-6.5%	+6.7%	-47.3%	+59.2%	-55.9%	+360%	-20.7%	-7.6%

Table XXVII Jerk results in summary

The summary results for steady-state jerk are provided in Table XXVII. In terms of jerk reduction, the control was successful in reducing the jerk resulting from the slip-open phase. However, in almost all cases, the jerk arising out of the inertia phase proved to be higher when using the torque in-fill in MHEV mode than without. Out of the presented shift events in this section, only the 50km/h shift demonstrated a reduced jerk in both control directions, although the positive jerk at the inertia phase was likely not evident due to low engine speed, which instead introduced a negative jerk. Conversely, all shifts demonstrated reduced jerk in the negative direction associated with the slip-open phase.

9.3 Dynamic Performance (Acceleration) – Test 2

The acceleration of the vehicle was tested at part-throttle, using a 30% throttle input. The test methodology was selected primarily to verify simulated performance of the same test, as well as to investigate the effect of the mild hybrid system for jerk reduction under acceleration, in addition to the steady-state testing conducted in 9.2. The test is intended to describe a gentle acceleration onto an arterial road. The acceleration measurement was conducted between 7km/h and 80km/h. The non-zero start condition was selected for better repeatability, as there is a high level of variability arising from a start from rest, particularly on a dynamometer. The selection of 7km/h was corresponding to the vehicle speed in first gear at idle, with the clutch fully engaged. This setup resulted in highly repeatable test conditions. Two tests are shown in Figure 9.21, taken approximately one month apart. They show the test is highly repeatable,

with less than 1% deviation. The acceleration is benchmarked against the base vehicle, and the simulated MHEV and base vehicle.

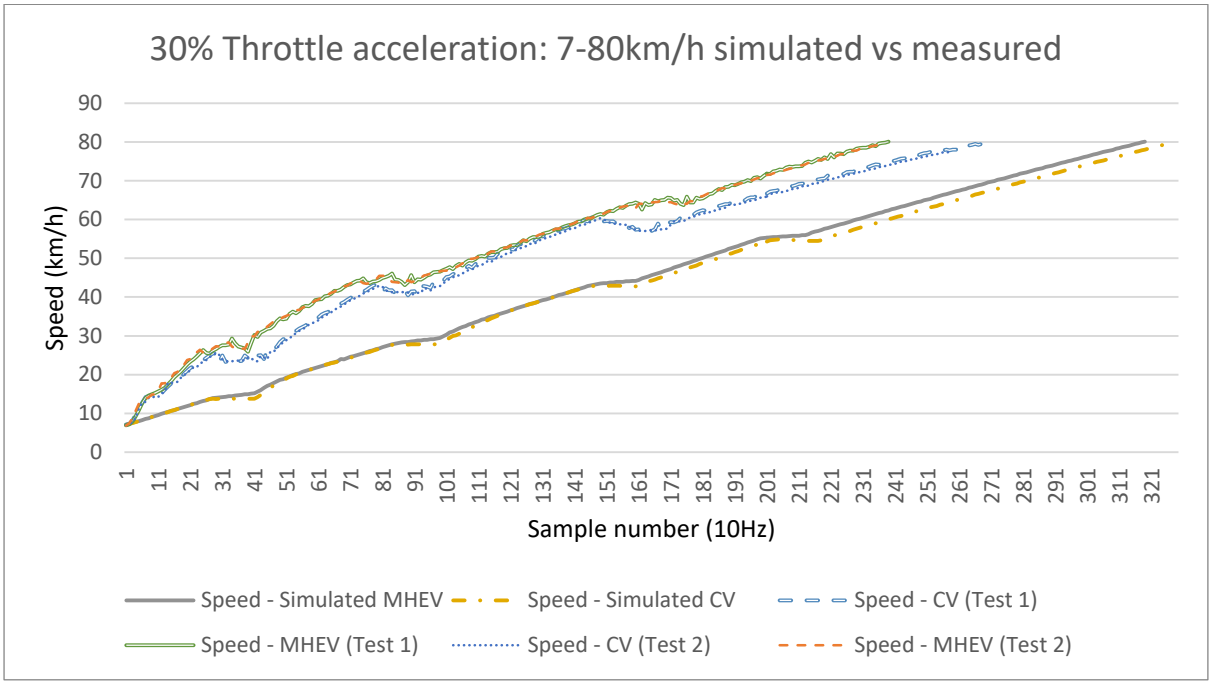

Figure 9.21 Experimental acceleration data compared with simulation data

The simulated base vehicle recorded a time of 32.9s to 80km/h at 30% throttle. The same conditions using the MHEV in simulation recorded 31.9s. In contrast, the prototype recorded 27.0s and 23.9s, with and without the MHEV system respectively. Whilst otherwise similar, the primary reason for the large variation between simulation and experimental data is the 4-5 gear shift in the simulation, which is executed at approximately 55km/h. However, the experimental data is of sufficient quality to investigate jerk under acceleration.

9.3.1 Jerk under acceleration

Predominantly, the data in acceleration reflects the same findings as those found under steady state. That is, the initial jerk caused by the slip-open phase is generally reduced. The second jerk caused by the inertia phase is either marginally higher, in the case of the 1-2 shift, substantially the same. Results are shown in Figure 9.22.

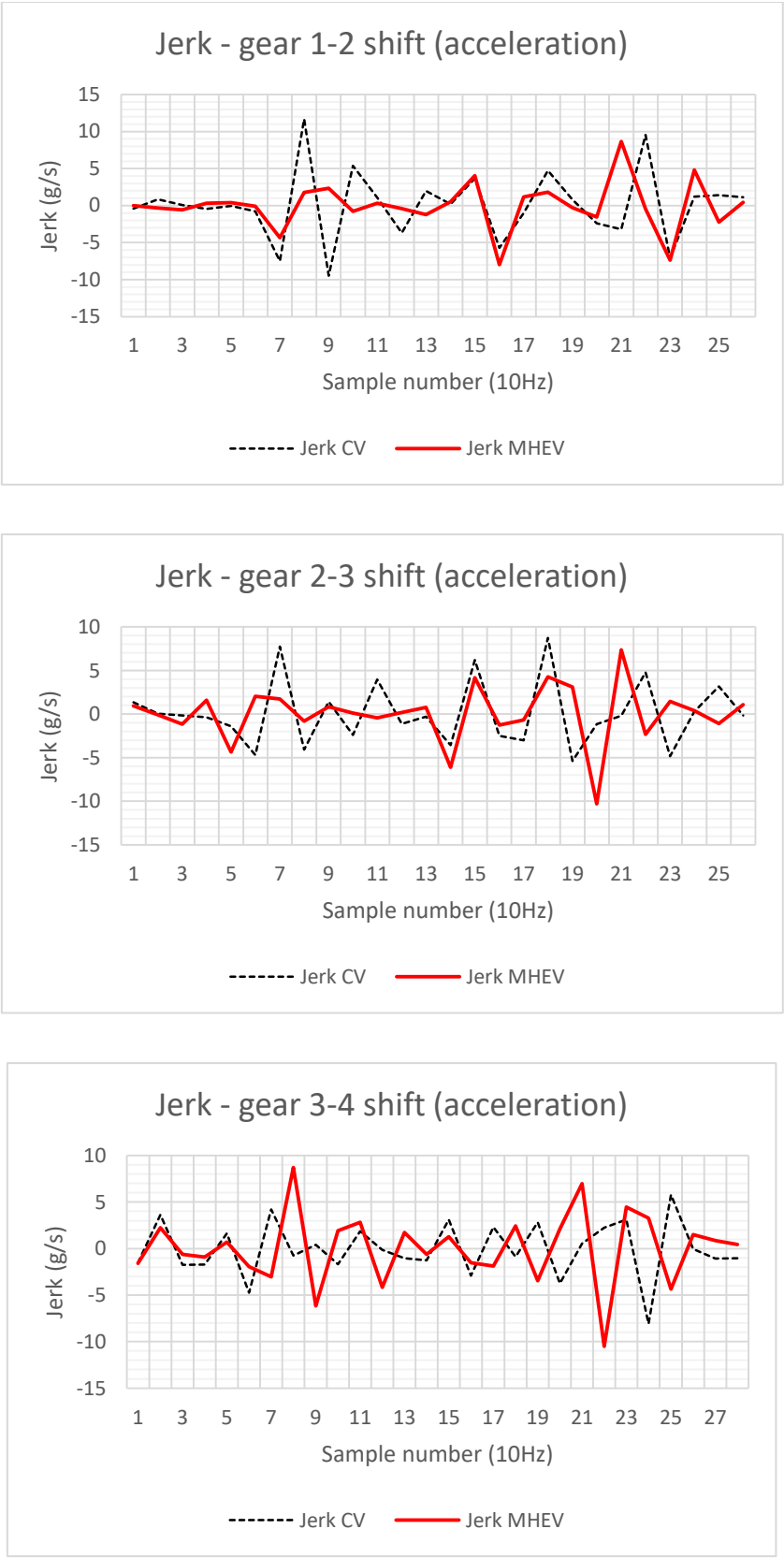

Figure 9.22 Jerk data for shifts 1-2, 2-3, 3-4 for both the MHEV and the CV

9.4 Fuel and Emissions – Test 3

Fuel and emissions testing was conducted using the base vehicle as a benchmark to compare against the MHEV. The testing consisted of a single pass of the New European Driving Cycle (NEDC), which comprised the first test, as well as an acceleration test of the type presented in 9.3. For each test, emissions and fuel consumption information was collected.

The NEDC cycle (Figure 9.23) covers a distance of 10.931km with a total time of 1180 seconds. The cycle is composed of four identical segments representing urban driving conditions, followed by an extra-urban segment with a top speed of 120km/h. The average speed of the NEDC is 43.1km/h, exclusive of idle time, which is 267 seconds out of the 1180 seconds total.

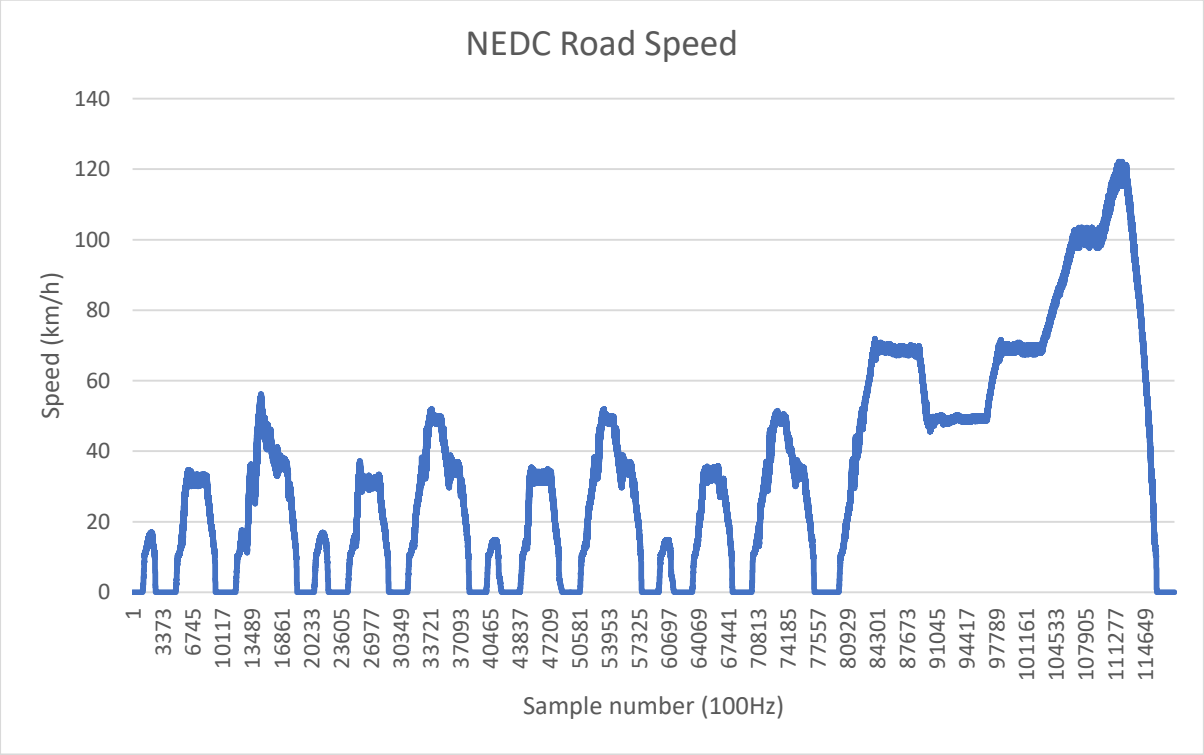

Figure 9.23 Acquired speed data for the NEDC cycle

The testing was conducted with variations from the prescribed standard to account for test facility limitations. The emissions sampling used a Horiba MEXA-584L 5-gas analyser rather

than constant volume sampling which directly measures pollutants in grams. The MEXA-584L provides gas concentrations in parts per million or percentages, and these are then converted to weights using the molar mass of the particular gas component as well as information about engine speed and volumetric efficiency, which is derived from the mass air flow sensor installed on the vehicle.

The fuel consumption was not read directly due to the absence of a mass flow meter. Instead, fuel injection signals were read to determine injector duty cycle. The flow rate of the injectors could then be used to determine fuel volume injected, and a fuel density of 0.75kg/L was assumed to determine fuel weight. This method of fuel calculation assumes that ΔP across the injector remains relatively constant. This assumption is subject to fuel rail pressure fluctuations as well as intake manifold pressure fluctuations. Because the NEDC is a low-load cycle the intake manifold pressure is mostly stable and therefore the assumption can be used without a significant loss of accuracy.

A larger margin of error was allowed in the test rules, as compared to the standard margin. This accounted for the lack of experience of the test driver to allow the test to be completed successfully within a satisfactory time.

Finally, the test was conducted after the vehicle had been thoroughly warmed up on the dynamometer. This removes any variation resulting from cold-start conditions which would be detrimental in this study. Typically, the NEDC is run from cold after soaking a vehicle for several hours.

The results of the testing are presented in summary in Table XXVIII and Table XXIX.

Acceleration 11km/h-80km/h – CV vs MHEV					
	Fuel Consumption (L)	Carbon Monoxide (grams)	Hydrocarbon (grams)	Carbon Dioxide (grams)	Nitric Oxide (grams)
Conventional Vehicle	0.065	9.668	0.58	100	4.05
Mild Hybrid	0.058	7.054	0.46	103	1.99
Difference	-10.8%	-27.1	-21.7	+3%	-50.9%

Table XXVIII Summary fuel and emissions results from the acceleration test

NEDC – CV vs MHEV					
	Fuel Consumption (L)	Carbon Monoxide (grams)	Hydrocarbon (grams)	Carbon Dioxide (grams)	Nitric Oxide (grams)
Conventional Vehicle	1.046	98.81	3.64	2568	33.55
Mild Hybrid	0.850	116.24	6.23	1932	25.60
Difference	-18.8%	+17.6%	+71.1%	-24.8%	-23.7%

Table XXIX Summary fuel and emissions results from the NEDC test

9.4.1 NEDC - Fuel

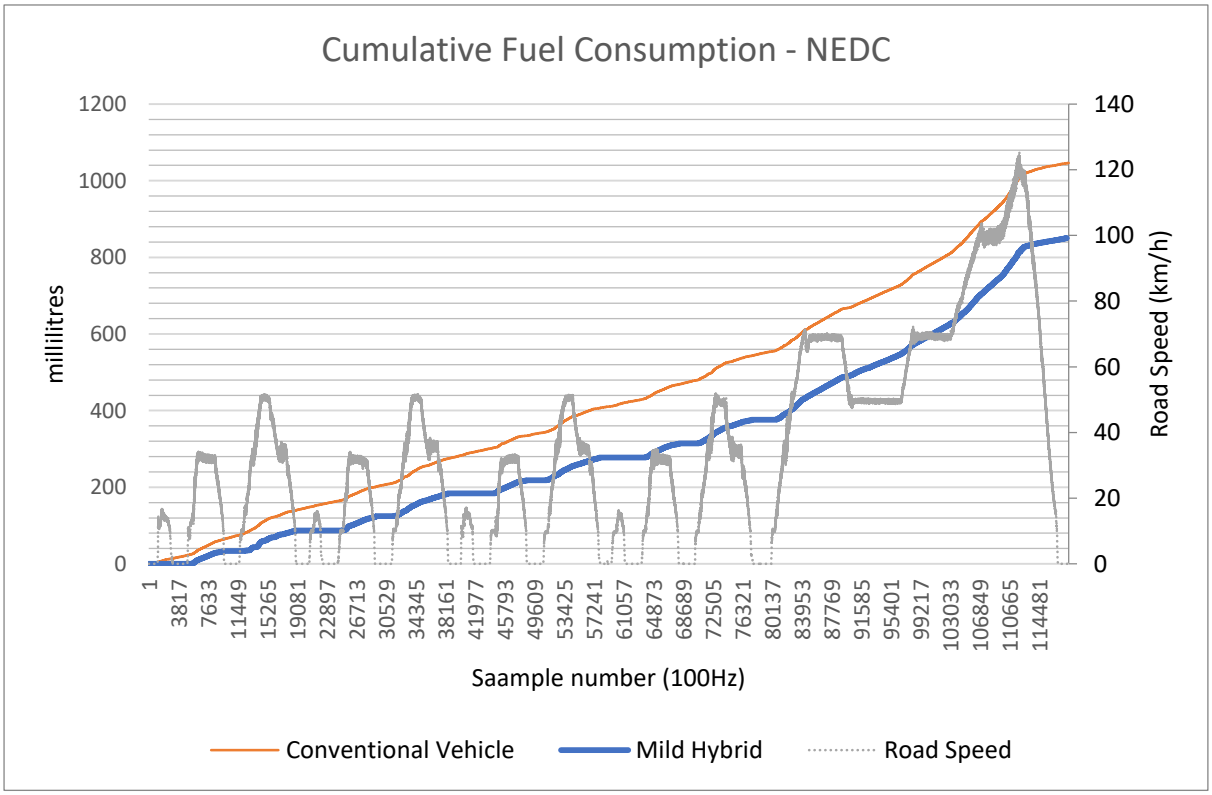

Figure 9.24 Cumulative fuel consumption from the NEDC test shows the effect of engine stop-start on FE

As shown in Figure 9.24, the base vehicle recorded fuel consumption of 1.046 litres under the NEDC, compared to 850 millilitres used by the MHEV prototype. The result was a little better than expected, but this can, in part be attributed to the regenerative function of the controller being inoperable during the testing. Nevertheless, because the NEDC is a relatively short, low-load cycle, there is little opportunity to deplete the battery sufficiently to require engine loading to recharge. The fuel consumption of the MHEV prototype also agrees well with the simulation result, which predicted 0.836 litres of fuel consumption.

The primary source of improved fuel efficiency in comparison to the base vehicle was the stop-start function of the CV, which eliminated fuel use during all 267s of the idle time. Although the low-speed creep was also a contributor to the fuel economy of the MHEV,

because the NEDC cycle is generally low-load, the contribution to fuel saving did not outweigh that of the stop-start.

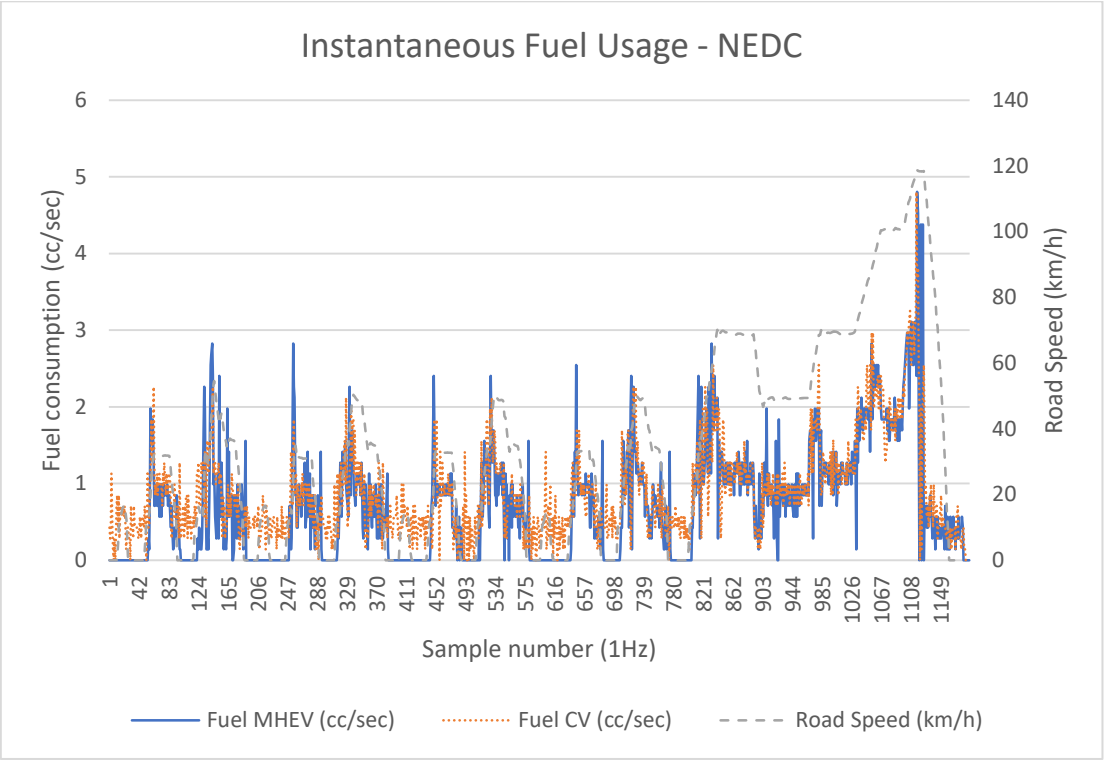

Figure 9.25 Instantaneous fuel consumption data for the NEDC test shows the principal differences at stop-start and initial acceleration

It can also be seen in Figure 9.25 that the torque-fill function did not significantly affect fuel consumption in the NEDC. This indicates that the main benefit of the torque-fill function in terms of fuel consumption is in reducing the time taken by the vehicle to reach cruising speed and reducing deceleration during gear shifts which cause an increase in fuel consumption in the next acceleration event. Because both of these effects are minimised in the NEDC due to its strict speed profile, the benefit of the torque-fill function is also minimized.

9.4.2 NEDC – Emissions

The emissions results were mixed. Whilst CO_2 and NO_x were both reduced (Figure 9.28 and Figure 9.29), CO and HC both increased (Figure 9.26 and Figure 9.27). This is broadly consistent with findings in (Yu, Dong & Li 2008) and (Merkisz et al. 2011), who find that under certain circumstances in vehicles fitted with stop-start systems, levels of HC and CO can increase. The cause of the increase in HC is principally the use of ignition-cut systems to turn off the engine rather than fuel-cut, which reduces HC. The secondary cause of the increase in HC is the catalyser efficiency, which drops when exhaust volume and engine load are lower. This is also the primary reason for the increase in CO.

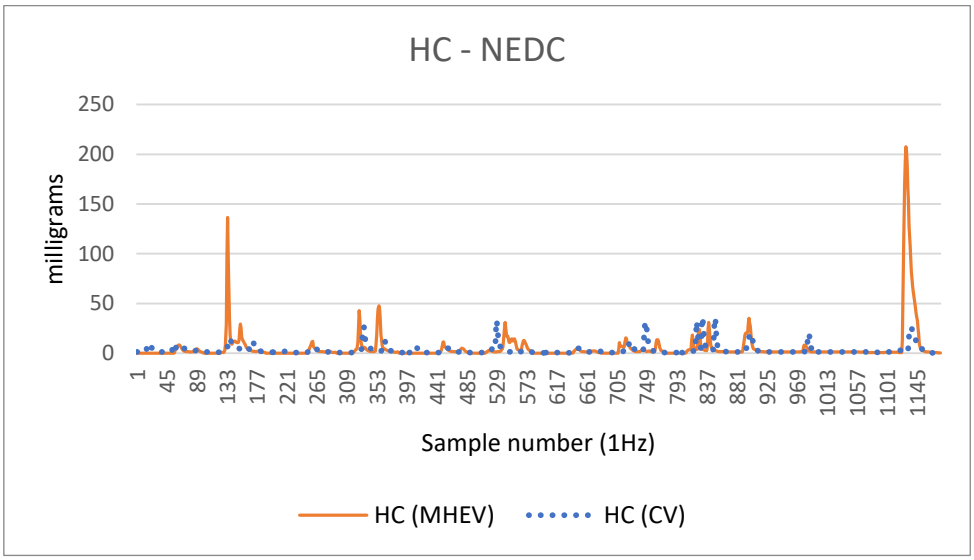

Figure 9.26 Hydrocarbon emissions are highest during engine transient events such as start-up, gear changes, and overrun after the high-speed cycle

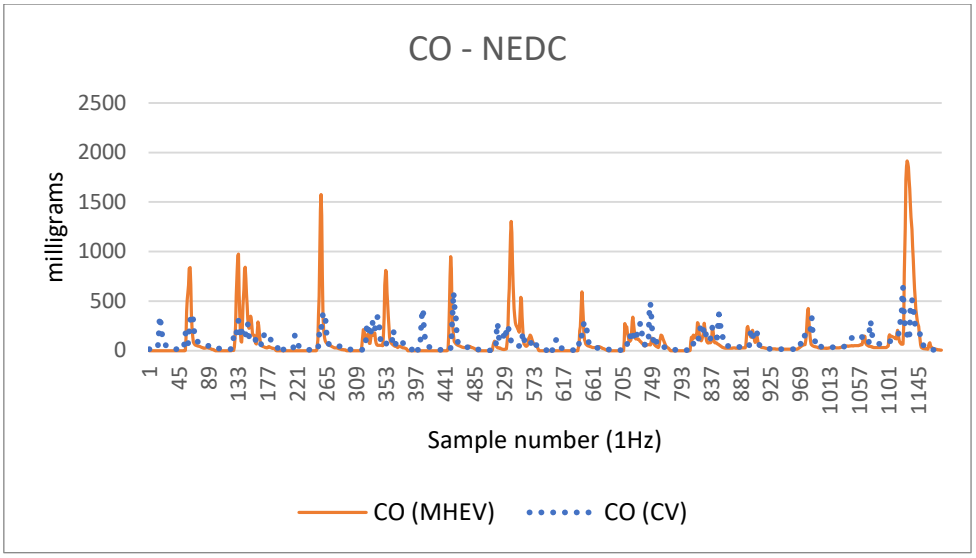

Figure 9.27 CO emissions were higher under MHEV operation

The CO and HC emissions are largely "emissions-event" driven. That is, they are characterized by relatively low levels for much of the driving conditions, but under certain conditions, disproportionately large emissions are released. These conditions are the transient engine start and stop conditions, as well as the long in-gear deceleration from high speed following the extra-urban section of the cycle.

In contrast, CO_2 is very strongly correlated with engine operation speed, and NO_x with engine thermal state. Reducing engine load and operation time through electrification has a direct effect on the emissions quanta, and the results in Figure 9.28 demonstrate the effect. The correlation of CO_2 with engine speed is shown in Figure 9.30.

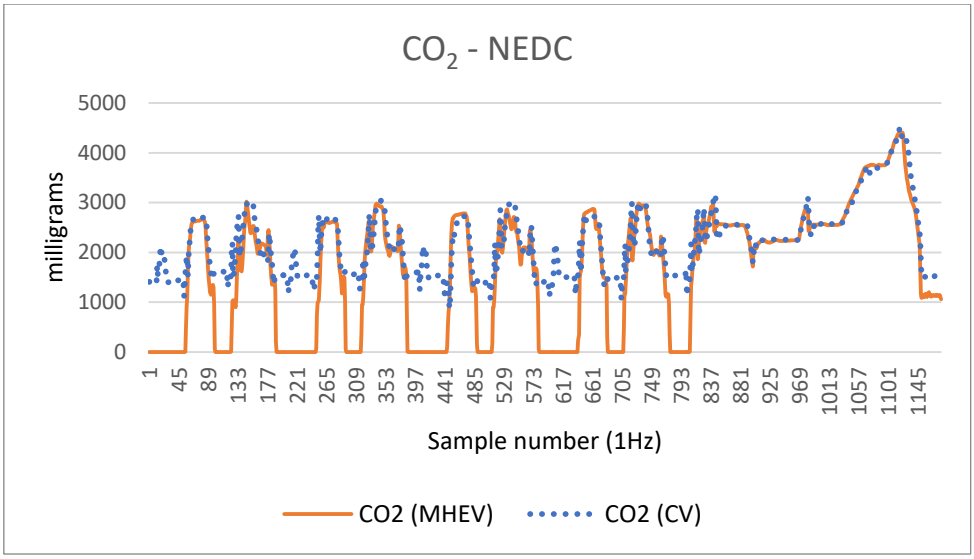

Figure 9.28 Carbon Dioxide emissions followed engine speed, and thus were significantly reduced under MHEV operation

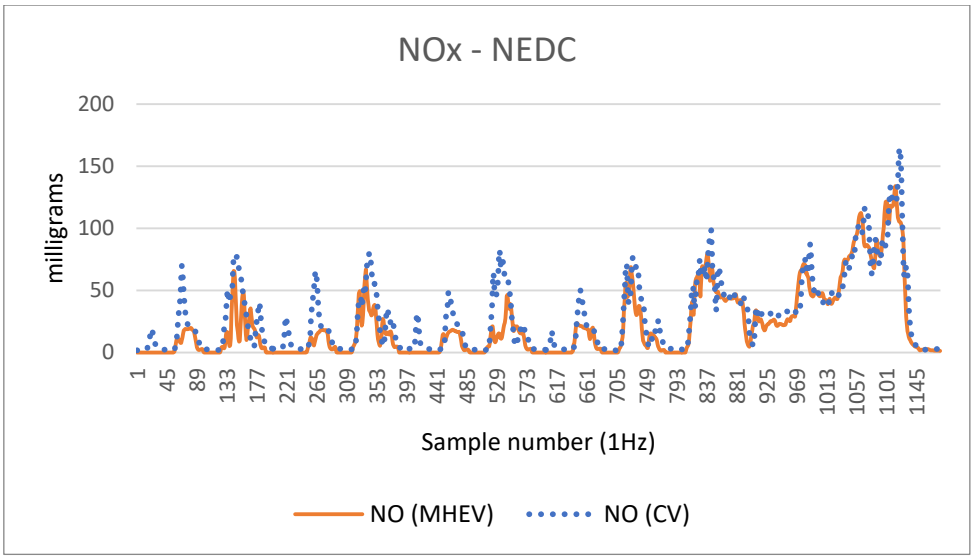

Figure 9.29 Nitric Oxide emissions were somewhat lower under MHEV operation due to reduced engine thermal state

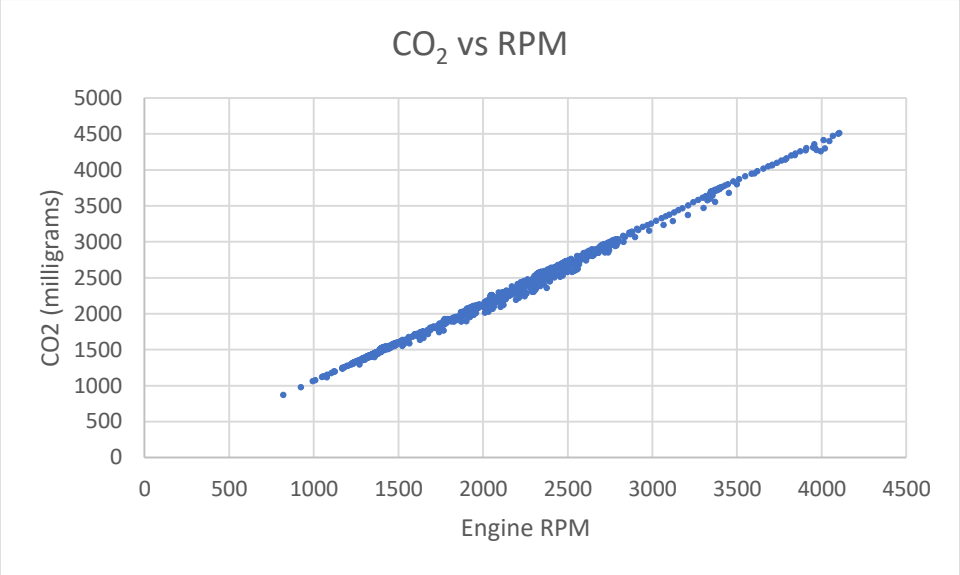

Figure 9.30 Correlation of carbon dioxide output and engine speed

9.4.3 Acceleration – Fuel

The acceleration test was conducted using the base vehicle as a benchmark, and then engaging the MHEV system, which, for the particular run, only provided torque-fill functionality. Therefore, other than difference in driver input, the sole difference is the use of torque in-fill for gear changes. The total fuel consumption was reduced by 7mL using continuous torque control, resulting in consumption of 58mL (Figure 9.31).

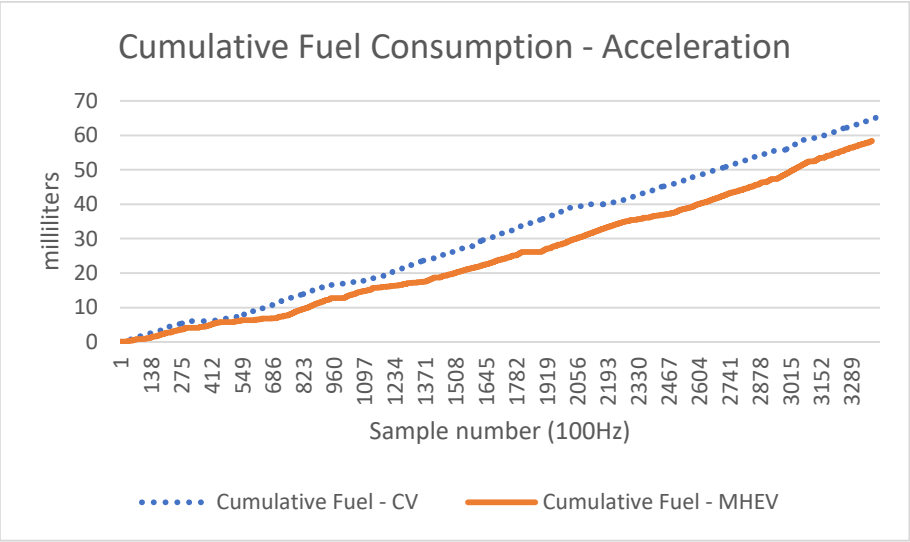

Figure 9.31 Cumulative fuel consumption for the acceleration test

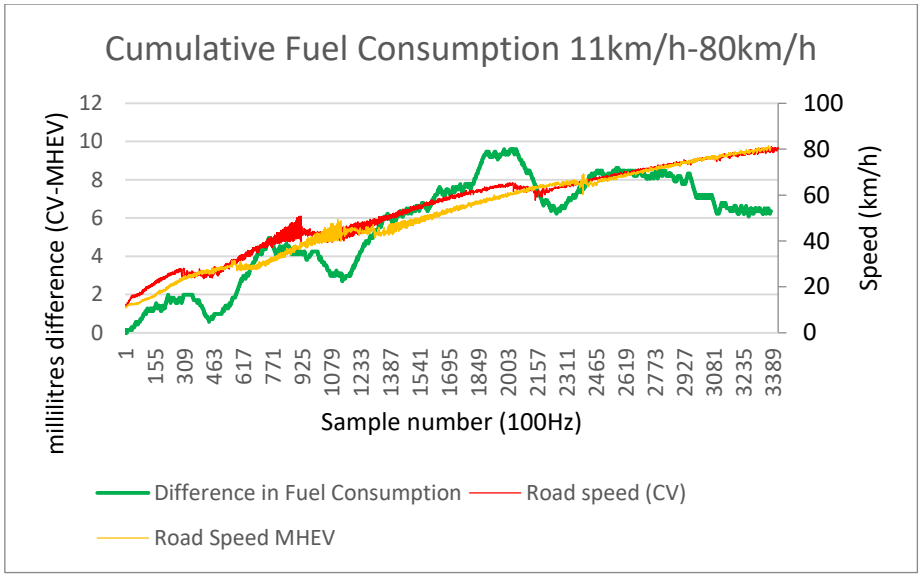

Figure 9.32 Difference in fuel consumption as a function of time shows the effect of gear changes on the overall fuel economy

The majority of the gains are made during the gear changes (Figure 9.32), whereas in-gear gains are also made, but at a lower rate. The total electrical energy consumed during the run was 10.2Wh. This demonstrates the energy efficiency of the continuous torque control system.

9.4.4 Acceleration – Emissions

Emissions results were generally positive. The CO and HC levels are related to the transient throttle states associated with gear changes. The three peaks in the traces (Figure 9.33) coincide with each gear change 1-2, 2-3, 3-4. Because the throttle is controlled open during gear changes in the MHEV, the transients are reduced compared to the CV and therefore results are generally improved.

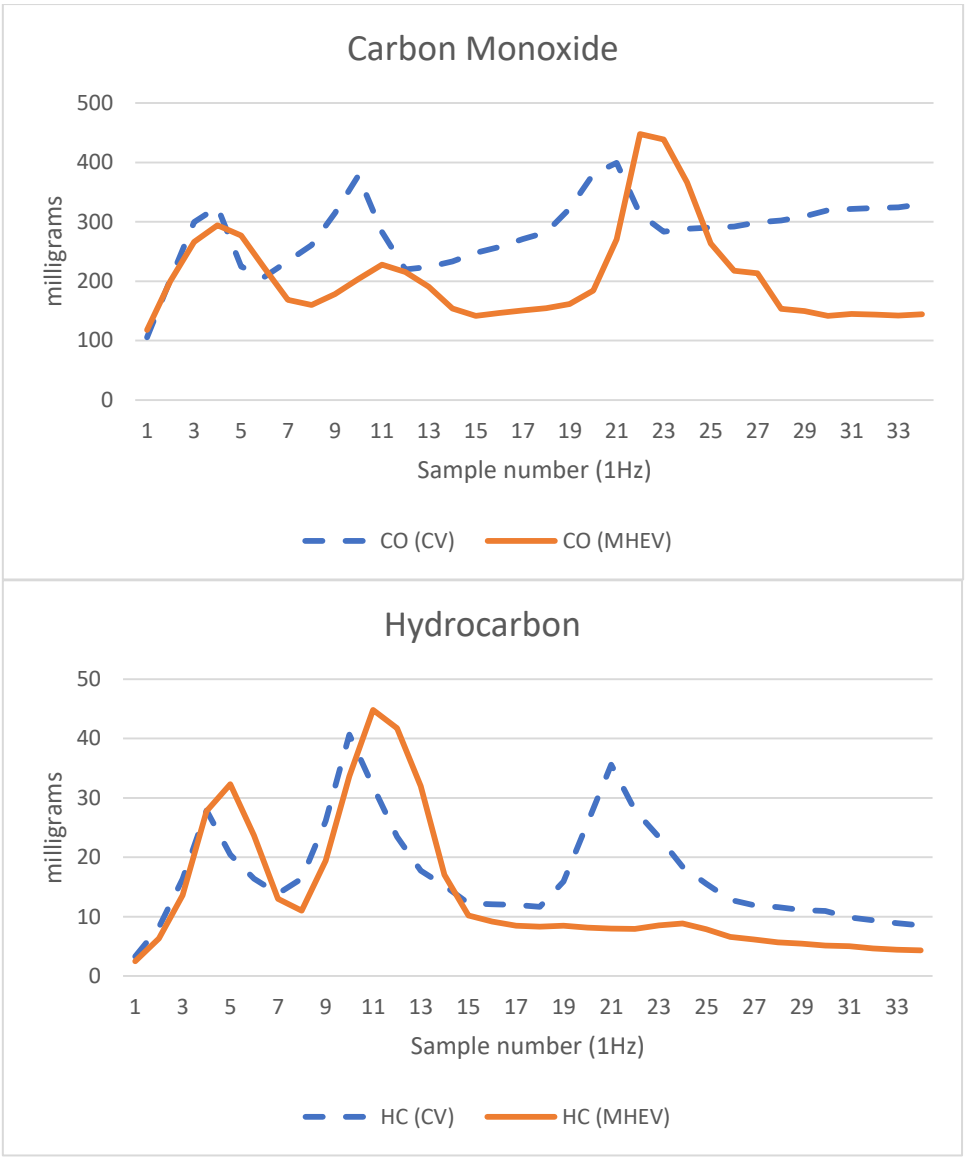

Figure 9.33 Carbon Monoxide (top) and Hydrocarbon (bottom) emissions for the acceleration run

In contrast, CO_2 and NO_x (Figure 9.34) are associated with engine speed and thermal state, respectively. The CO_2 result for the MHEV is 3% worse than the CV, and this reflects the partial-open of the throttle which is required to control engine speed for clutch re-engagement. The NO_x result is likely due to the better control of the road speed, resulting in a lower average engine load over the acceleration test.

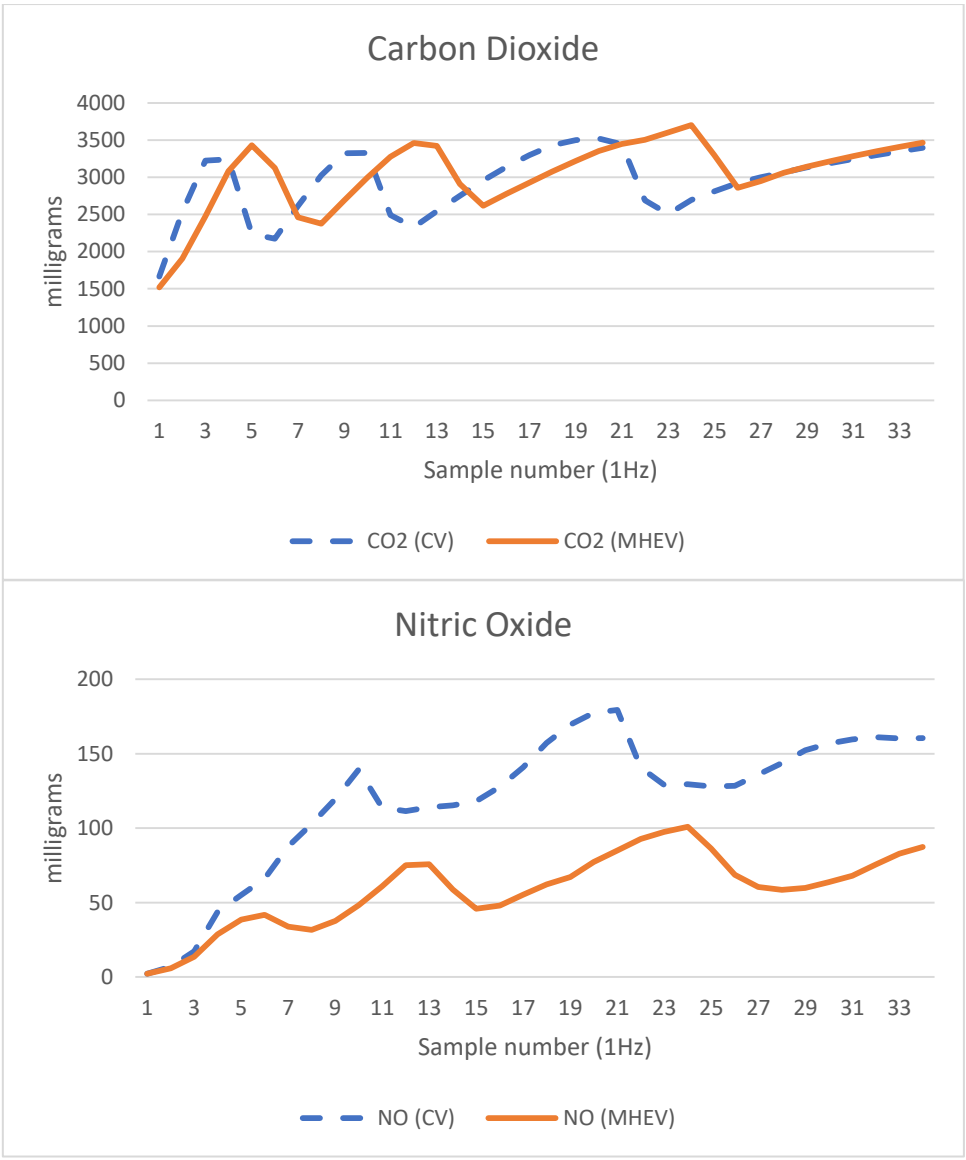

Figure 9.34 Carbon Dioxide (top) and Nitric Oxide (bottom) emissions for the acceleration run

9.5 Summary

The experimental work encompassed investigation of the ability to supply continuous drive torque during gear changes, the ability to minimize jerk during gear changes, a fuel consumption investigation, and an emissions investigation. The ability to supply continuous drive torque was demonstrated comprehensively, although a failure was recorded as a result of engine mapping deficiencies which caused the torque control system to calculate end

torque to zero. Torque hole amplitude was reduced in all cases but could not be completely eliminated. Further work is required in calibration to improve this aspect. The torque and speed output is broadly reflective of similar results obtained in the literature, particularly those shown in (Baraszu & Cikanek 2002; Horn et al. 2002; Zhang et al. 2010)

The performance of the system with respect to jerk was somewhat less successful. The two main jerk events associated with gear changes are the slip-open jerk and the inertia jerk, caused respectively by clutch release and clutch engagement. The first jerk event was, in most cases, reduced due to the continuous torque control, but the second jerk event was increased. Additionally, there was some added vibration introduced during the torque phase of the gear shift due to the torque fill-in, although this was largely insignificant. The reduction of jerk at the inertia phase is difficult to control due to the unpredictable nature of the clutch re-engagement inputs by the driver, and the non-linear correlation between clutch hydraulic line pressure and position. It may be possible to improve the jerk output but is unlikely without additional sensing, such as a clutch pedal position sensor or clutch plate position sensor. Jerk results generally agree with those found in (Zhang et al. 2010), both in the nature of jerk peaks and also in the jerk observed during the torque (or synchronization) phase of the gear shift.

The fuel and emissions performance was demonstrated to be generally positive. There were considerable fuel economy gains in both the NEDC and acceleration tests, and the NEDC emissions were improved in terms of CO2 and NOx, although hydrocarbons and CO were both poorer. This is consistent with other results reported in the literature and with further work the emissions results can be improved across the board. The acceleration emissions were improved in all areas with the exception of CO2, which was 3% higher.

Chapter 10: Conclusions

This thesis presented the development of a novel P3 mild hybrid powertrain topology. The topology has been created using a low-cost base vehicle with the intention of exploring the potential for hybridization to improve driveability and emissions performance. The impetus behind the investigation is the need to improve vehicle fleet electrification on a global level, which requires innovative solutions using low-cost automotive hardware to develop attractive, high-performance, low-emissions solutions for developing markets. The technical objectives of the investigation were, specifically, the development of a prototype vehicle for experimental validation of the P3 topology, use of the prototype vehicle to validate the continuous torque delivery (gear shifting torque-in-fill) function of the EPS, and the validation of emissions and dynamic modelling previously completed.

By creating a mild hybrid based around a low-power powertrain equipped with a manual transmission, we are able to complement the key strengths of the manual transmission, being its simplicity, efficiency, and cost, with the key strengths of the P3 topology – notably, its ability to provide continuous torque delivery during gear shifts, the ability to provide tractive effort independently of the engine, and the ability to regenerate electricity during braking. The use of a manual transmission is particularly well-suited to many developing markets where, in contrast to developed markets, manual vehicles can account for over 90% of vehicle fleets.

Solutions for developing markets must be financially attainable in order to succeed in these environments, as well as being mechanically robust and minimising mechanical differences compared to conventional ICE vehicles to ensure they can be maintained by local technicians who may not have access to training on more complex hybrid topologies.

Careful optimization of the powertrain topology and size has resulted in a robust, familiar, and reasonably-sized system. Sizing study has resulted in a unique, fairly low system voltage of 96V, which is higher than many micro-hybrid topologies that use 48V standards, but significantly lower than the 230-650V systems used in full hybrid vehicles. The 96V traction battery drives 10kW/30kW peak AC induction motor according to a rule-based controller that considers the load case and battery state of charge in determining the mode of operation. The battery size is also optimized, and although the prototype battery is 1.44kWh in size, it has the potential to be reduced to 0.768kWh without any loss in functionality. The P3 topology, whilst not as simple as a P0 or P1, offers good functionality and cost-effectiveness.

The control methodology developed was tested under laboratory conditions. The control was tested for its ability to supply continuous torque delivery during gear changes, quantification of the torque hole elimination, vehicle acceleration testing, jerk control, fuel, and emissions performance.

The system was successful in achieving continuous torque delivery during gear changes and therefore this design objective was met. Continuous torque delivery can be achieved under most conditions, but a single failure was observed due to engine mapping errors which resulted in zero being calculated for end torque value. This failure is not an algorithmic error, but rather a numerical parameter input error. The controller is programmed to abort continuous torque delivery in a number of other, non-failure cases such as brake application or clutch threshold limits.

The complete elimination of the torque hole during gear changes was not consistently demonstrated using the current control methodology. Rather, partial reductions of the full-scale torque hole were achieved for all gear shift events. The full-scale torque fill-in value was shown to be achieved approximately 1 second after the gear shift initiates, which corresponds to a delay of approximately 0.3-0.6s after the minimum drive torque is measured

at the transmission output. The torque holes were typically reduced of the order of 75%-95% of full-scale value. As a result of the continuous torque delivery, vehicle speed was well-controlled in comparison to uncontrolled gear shifts.

The reduction of jerk was partially achieved. There are two main jerks associated with the gear shift. The first jerk is a result of the clutch release, and is in the negative direction. The second jerk is generally in the positive direction, and is associated with clutch engagement. Secondary jerks may follow the clutch engagement if the system inertias are not matched at the time of engagement. The clutch release jerk was consistently reduced whilst the continuous torque control was active. However, generally, the system returned poorer jerk outcomes for the clutch engagement than could be obtained using the IC engine alone. This suggests the system control is not sufficiently developed to determine accurate control values for the end conditions of the shift. One factor that contributes to this is the self-excitation of the clutch plate, which causes pressure variation in the clutch hydraulic line. Because the system relies on line pressure for an estimation of the clutch state, the self-excitation can cause premature or delayed abort conditions. However, the predominant factor that contributes to the engagement jerk is the human actuation of the clutch pedal. Different feed rates of the clutch pedal can cause pressure variations for the same position, and this makes it difficult to accurately predict the end condition. The use of a secondary sensor such as a clutch pedal position sensor or a direct measurement of clutch plate position would simplify the control of engagement jerk, enhancing the system performance. Nevertheless, control issues aside, the hardware incorporated into the system has been shown to be sufficiently capable of controlling jerk.

The hybrid system demonstrated favourable results in terms of vehicle acceleration. The application of continuous torque during gear shifts resulted in significantly improved part-throttle acceleration. Although full-load acceleration testing was not performed, it is expected

that the benefits of the hybrid system would diminish as acceleration load increases due to the decreased electric drive fraction. This is consistent with the design goal of the mild hybrid powertrain, which is intended to improve driveability rather than outright performance. On a 30% part-throttle acceleration, the hybrid vehicle reached 80km/h 3.1 seconds faster than the conventional base vehicle. This was achieved due solely to the continuous torque delivery during the gear changes. Velocity changes during gear shifts were also much better controlled than in the base vehicle.

The fuel consumption and emissions of the mild hybrid vehicle were benchmarked against the conventional base vehicle. The benchmarking considered four gas components – carbon monoxide, hydrocarbon, carbon dioxide, and nitric oxide. Fuel consumption was also recorded and benchmarked. The benchmarking was conducted for two test cases – in the first instance, the NEDC cycle was selected, and in the second instance, the 30% throttle acceleration to 80km/h. The NEDC cycle returned excellent fuel consumption correlation with simulated results. The MHEV obtained fuel consumption of 0.850L over the cycle against a simulated 0.836L. The CV simulation was somewhat less true to experimental results. The CV returned 1.046L in experimental conditions, compared to 0.857L in simulation. The emissions results demonstrated considerable benefits in carbon dioxide and nitric oxide emissions, although hydrocarbon and carbon monoxide emissions suffered as a result of the stop-start function of the controller. In the acceleration emissions benchmark, there were consistent and dramatic improvements in all emissions components with the exception of carbon dioxide, which was 3% poorer. This result was not unexpected as the detrimental effect of engine stop-start on other emissions components was absent during this test.

Tailpipe emissions are a primary source of global air pollution. The treatment, regulation, and reduction of tailpipe emissions has been a focus of national environmental regulation

agencies since at least the 1960's. Typically, reductions in tailpipe emissions have been driven through increasingly stringent regulation adopted at the national and regional level. European and North American standards have become de facto global standards, as most developed nations broadly adopt the same regulations. Meeting these standards is costly, both in terms of R&D investment as well as cost-to-manufacture as emissions hardware becomes increasingly complex. This drives the cost of new vehicles up. In most developed countries, the cost of new vehicles is relatively affordable even factoring in increased costs associated with meeting standards such as emissions and collision safety. Therefore, developed countries with mature automotive markets and relatively steady rates of motorization tend also to be the countries that drive global automotive standards. Due to relative affordability, national vehicle fleets remain relatively modern, averaging approximately 10 years in age as consumers turn over vehicles that no longer meet requirements or in-service standards. These countries are economically capable of sustaining relatively advanced regulation.

In contrast, there are many developing countries reliant on a steady flow of used vehicles from developed economies for motorization. Many of these countries are also serviced by tier 2 regional automotive OEMs that supply developing markets with new vehicles manufactured under license from, often, decades-old designs. By buying manufacturing rights to vehicles that are no longer compliant in developed countries, manufacturers can save on R&D but also, crucially, can only supply to markets that are less regulated. Many of these countries are experiencing increasing demand for motorization as they develop toward affluence, but the cost of a new vehicle compliant with the most modern standards may still be unaffordable to the bulk of the population. Meanwhile, the flow of older vehicles from developed regions has the effect of increasing regional air pollution. For many of these countries, national tailpipe emissions regulations are either non-existent or decades behind the state-of-the-art. Adoption of modern regulations would be an unsustainable option,

dramatically raising the cost of new vehicles and locking much of the population out of vehicle ownership and the national productivity benefits that autonomy brings. A market-based approach to the issue is required in order to increase fleet electrification, reduce emissions, and support increasing motorization. The research project delivered and described in this thesis has addressed this need, by: developing a low-cost, low-emissions prototype vehicle; developing and testing a control scheme for the vehicle, and; developing and testing a novel featureset that aims to improve the functionality of manual transmissions through electrification for improved driveability.

10.1 **Contributions**

The contributions to the automotive research community through this project are as follows:

A prototype P3 mild hybrid vehicle using a manual transmission was constructed for the purpose of experimental validation of modelling and simulation of the same. Whilst there are studies that have been published based on a P3 topology, they invariably utilise AMT or specific variations of electrified transmissions. The development and description of the vehicle prototype appears to be unique in the literature. Chapter 4 described the backward-looking modelling process which yielded initial design. Chapter 5 described the simulation and forward-looking modelling. Chapter 6 contains the description of the prototype as built.

The real time controller for the prototype vehicle was developed, and its development is described in Chapter 7. The real time controller was tested and control values calibrated in line with the simulated controller presented by (Awadallah 2018), and the continuous torque control was described in detail.

The prototype vehicle was used for the experimental validation of simulations of the post-transmission hybrid. The experiments validated the continuous torque delivery functionality of the topology, noting that speed fluctuations were well-controlled, and torque could be continuously delivered throughout gear shift events. The experiments determined that further

control optimization is required for jerk reduction. Whilst jerk was reduced when the clutch was released, in most cases jerk was increased when the clutch was re-engaged, despite the continuous torque delivery. The work serves as a basis for future development of jerk controllers in automotive applications.

The prototype vehicle was used for the experimental validation of fuel consumption and emissions simulations. The experimental validation shows good agreement with simulated fuel consumption. The emissions results, based on a test under the NEDC cycle, differ somewhat from simulated results, particularly in that HC and CO values are increased over the cycle compared to the base, internal combustion-only, vehicle. However, these findings are consistent with other published literature, including (Fontaras, Pistikopoulos & Samaras 2008; Ji et al. 2013). The increase in HC can be attributed to the increased rate of incomplete combustion arising from engine transients during start-stop activity. The increase in CO can be attributed to poorer catalyser efficiency, as a result of the cooler core temperature arising from reduced exhaust gas volume.

The use of mild-hybridization has been discussed as a method for improvement of fleet electrification rates in developing countries. The contextual analysis has provided consideration to the need for market-based solutions to tailpipe emissions problems where there are roadblocks to the implementation of regulatory controls. The vehicle trade flows and their effect on global emissions patterns have been discussed within the framework of the academic literature, and a qualitative analysis of the wider external considerations has been presented.

10.2 Future Research Directions

The MHEV powertrain presented in this thesis has shown the proof of concept is valid. However, there are many opportunities for further improvement and development of the powertrain. These opportunities include: the conversion of the manual transmission to an

automated manual transmission; the deletion of synchronizers and use of closed-loop speed control and dog-clutches for gear selection; the optimization of the traction battery, including the development of an ultracapacitor or ultracapacitor/battery hybrid secondary energy storage device; the redevelopment or simulation of the vehicle using a switched-reluctance motor instead of the AC induction motor used in this iteration, investigation of optimization of the rule-based controller so that the heuristic control methodology can be further refined; development of an active jerk controller that does not rely on the passive damping present in the motor's magnetic flux, and; development of a closed-loop engine speed controller to improve engine/transmission synchronization settling time.

The conversion of the manual transmission to an automated manual transmission has been demonstrated previously by (Gavgani et al. 2015). However, in that context the application was a high-powered performance vehicle and the transmission and hybrid power unit were combined using a unique hybrid coupling. Conversion of the MT to AMT would require an electrohydraulic servo actuator for the clutch and a 2-axis electromechanical actuator for gear selection. Control of the AMT is relatively straightforward and there are many methods described in the literature (Glielmo et al. 2006; Wang et al. 2018). The use of an AMT eliminates the need for predictive control in the continuous torque delivery algorithm. Rather, the target torque is always known because the target gear is selected by the controller rather than the driver. This also provides enhanced driver response because the driver's torque request (throttle pedal position) can be followed at all times during the gear shift event. In the current configuration, this is not possible because the driver must reduce throttle input to zero in order to initiate gear selection. Naturally, the AMT hardware adds cost to the base vehicle and this is not a favourable outcome for the low-cost nature of the MHEV powertrain.

One way to offset the cost of the AMT is the through the removal of synchronizer cones in the transmission. Synchronizer cones are required to bring the speed differential between the

input and output shafts to zero. However, with closed-loop speed control of both the engine and the motor, it is possible to replace their function with an electronic equivalent or an alternative device such as the harpoon-shift synchronizer. (Mo, Walker & Zhang 2019) have presented one potential option. There are many control methods available to perform this function however, it is recommended that a dynamic master/slave model is adopted, wherein for large speed discrepancies the engine speed is commanded as a function of the motor speed, allowing vehicle speed to be maintained in line with the driver input, but as the discrepancy falls to zero, the relationship may be switched, causing the motor to be commanded in line with engine speed. This is due to the much finer speed control possible using the electric motor, and is likely to result in the lowest engagement time and greatest driver feedback.

The optimization of the traction battery is obvious. The battery cells selected in this project were only chosen due to their availability, rather than their suitability. As a result the traction battery is much larger than necessary to ensure safe discharge rates. The inclusion of ultracapacitors or a more optimized pack, such as the A123 nanophosphate cells discussed in 4.4.6 would allow the current limit to be raised significantly. The overall cost would be minor but would result in complete torque hole elimination, rather than the reductions that were achievable under the current setup.

Likewise, the replacement of the AC induction motor with a suitable switched-reluctance drive is recommended for the same reason – the induction motor selected was appropriate, suitable, and available. However, if an SRM with similar specifications were commercially available it would have likely represented a better choice due to higher efficiency and exceedingly low losses in the on-axis application.

The final three future research directions are all related to the control methodology. A heuristic rule-based controller was chosen in this application due to the speed of development

and deployment. Whilst the controller is logical and agrees well with similar disclosures in the literature, there is nevertheless scope to improve its functionality by performing computational optimization. The control values used to move from one state to the next were selected through experience and experimentation, and whilst the state-flow structure itself is likely to be optimal for the current MHEV topology, the trigger values are likely not. The implementation of active jerk control was outside the scope of this thesis and was not considered in the current project. Instead, the passive damping available through the motor and the constant bias torque was utilised to reduce jerk. Finally, the implementation of open-loop engine speed control in the current project delivered sufficiently effective results. Open-loop control is common in the literature and is well-supported as a methodology for speed synchronization. Nevertheless, the conversion of that control to closed-loop would be likely to improve settling time. This is inconsequential in the current research due to the human input required to initiate a gear change event, but particularly if an AMT is developed, closed-loop engine speed control would be likely to deliver shorter gear selection time, and if the synchronizerless transmission is developed, then closed loop control is essential.

APPENDICES

Appendix A : **Vehicle parameters**

KERMIT IV Vehicle global specifications

Component	Parameter	Units
Vehicle	Mass	1100 kg
	Frontal area	3 m^2
	Drag coefficient	0.34
	Distance from CG to front axle	0.9 m
	Distance from CG to rear axle	1.3 m
	CG height	0.5 m
	Air density	1.2 kg/m^3
	Gravitational acceleration	9.81 m/s^2
	Tire rolling radius	0.312 m
	Rolling resistance coefficient	0.015
	Mass as hybrid	1200 kg
Engine	Type	Spark-Ignition
	Maximum power	85 kW
	Speed at maximum power	6250 rpm
	Maximum speed	7200 rpm
	Idling speed	900 rpm
	Cylinders	4
	Swept volume	1.6 L / 1598 cc
Gear ratio	Type	Manual, 5 forward 1 reverse, fully synchronised
	First	3.136
	Second	1.888
	Third	1.330
	Fourth	1.000
	Fifth	0.814
	Final drive ratio	4.300
Clutch	Type	single dry-plate clutch
	Friction coefficient	0.3 (estimated)
Motor (MHEV only)	Model	HPEVS AC-9
	Type	AC Induction
	Voltage	96 V
	Maximum power output	10 kW/30kW pk.
	Torque	20 N.m
	Maximum torque	94N.m
Battery	Type	$LiFePO_4$ 40152s
	Capacity	1.44kW/15A.h
	Discharge/Charge rate	15C / 10C

Appendix B **: Model Parameters**

Parameter	Inertia (kg-m^2)	Parameter	Stiffness (Nm/rad)	Parameter	Damping (Nm/rad)
I_e	0.4	K_e	95000	C_F	2
I_F	0.2	K_F	2000	C_{c}	0.049
I_{c1}	0.0072	K_{is}	5600	C_{is}	0.0044
I_{c2}	0.0125	K_{os}	4700	C_{os}	0.1
I_{g1}	0.0006	K_{m}	9500	C_{d}	0.1
I_{g2}	0.0013	K_{d}	65000	C_{m}	0.0045
I_{d1}	0.16				
I_{d2}	1.6				
I_m	0.0045				
I_w	167.558				

Appendix C : **Sensor and Actuator Datasheets and Calibration Data**

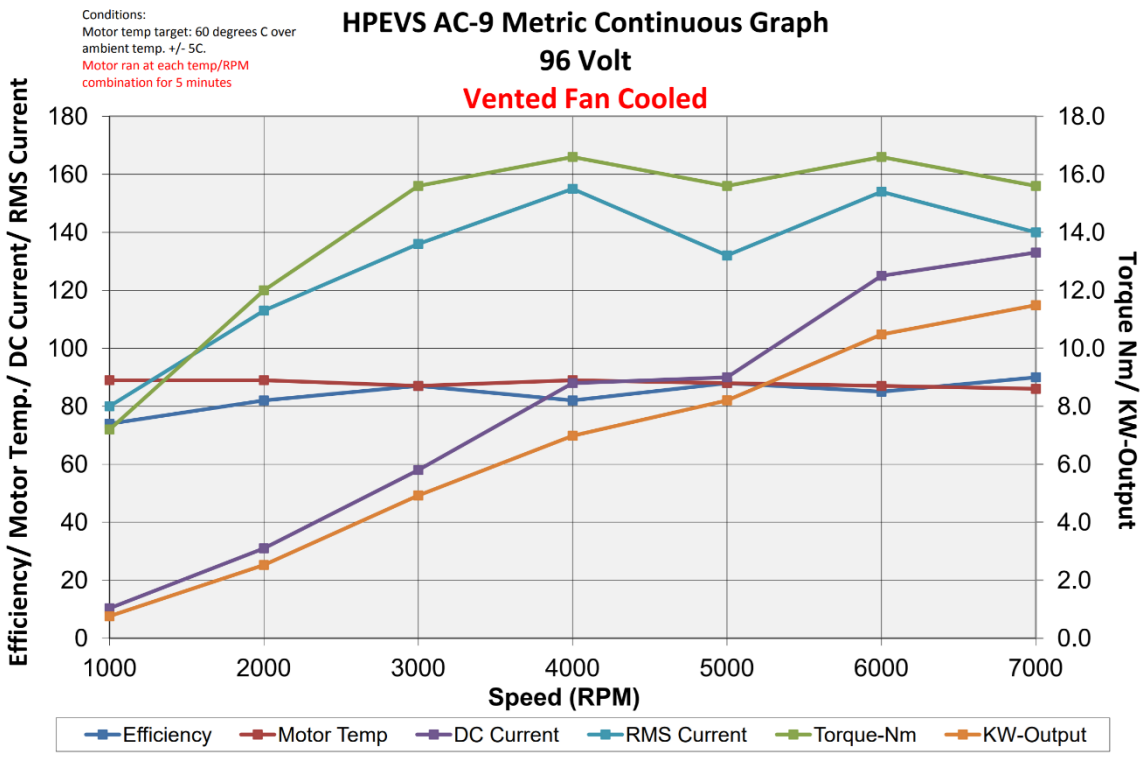

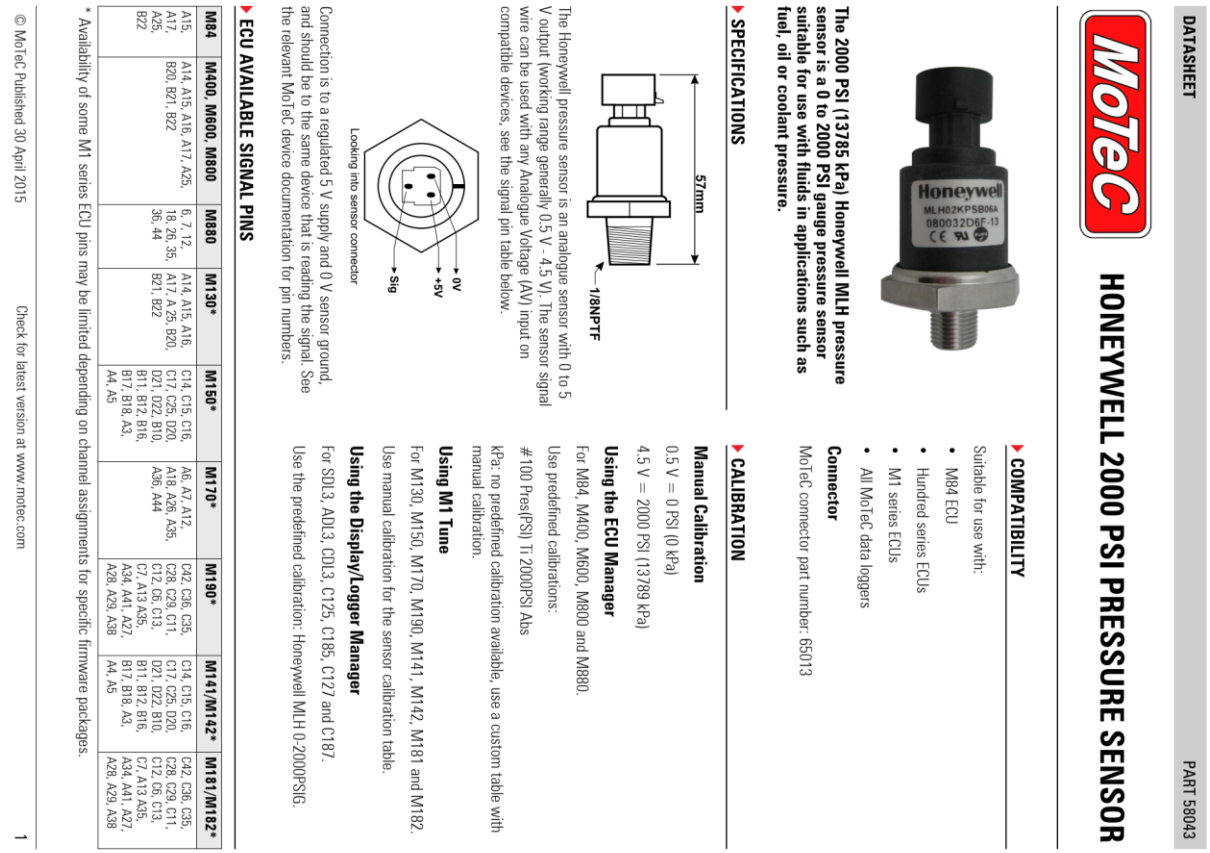

DATASHEET PART 58043

MoTeC

HONEYWELL 2000 PSI PRESSURE SENSOR

The 2000 PSI (13785 kPa) Honeywell MLH pressure sensor is a 0 to 2000 PSI gauge pressure sensor suitable for use with fluids in applications such as fuel, oil or coolant pressure.

COMPATIBILITY

Suitable for use with:

- M84 ECU
- Hundred series ECUs
- M1 series ECUs
- All MoTeC data loggers

Connector

MoTeC connector part number: 65013

CALIBRATION

Manual Calibration

0.5 V = 0 PSI (0 kPa)

4.5 V = 2000 PSI (13789 kPa)

Using the ECU Manager

For M84, M400, M600, M800 and M880.

Use predefined calibrations:

#100 Pres(PSI) Ti 2000PSI Abs

kPa: no predefined calibration available, use a custom table with manual calibration.

Using M1 Tune

For M130, M150, M170, M190, M141, M142, M181 and M182.

Use manual calibration for the sensor calibration table.

Using the Display/Logger Manager

For SDL3, ADL3, CDL3, C125, C185, C127 and C187.

Use the predefined calibration: Honeywell MLH 0-2000PSIG.

SPECIFICATIONS

The Honeywell pressure sensor is an analogue sensor with 0 to 5 V output (working range generally 0.5 V - 4.5 V). The sensor signal wire can be used with any Analogue Voltage (AV) input on compatible devices, see the signal pin table below.

Connection is to a regulated 5 V supply and 0 V sensor ground, and should be to the same device that is reading the signal. See the relevant MoTeC device documentation for pin numbers.

ECU AVAILABLE SIGNAL PINS

M84	M400, M600, M800	M880	M130*	M150*	M170*	M190*	M141/M142*	M181/M182*
A15, A17, A25, B22	A14, A15, A16, A17, A25, B20, B21, B22	6, 7, 12, 18, 26, 35, 36, 44	A14, A15, A16, A17, A25, B20, B21, B22	C14, C15, C16, C17, C25, D20, D21, D22, B10, B11, B12, B16, B17, B18, A3, A4, A5	A6, A7, A12, A18, A26, A35, A36, A44	C42, C36, C35, C28, C29, C11, C12, C6, C13, C7, A13, A35, A34, A41, A27, A28, A29, A38	C14, C15, C16, C17, C25, D20, D21, D22, B10, B11, B12, B16, B17, B18, A3, A4, A5	C42, C36, C35, C28, C29, C11, C12, C6, C13, C7, A13, A35, A34, A41, A27, A28, A29, A38

* Availability of some M1 series ECU pins may be limited depending on channel assignments for specific firmware packages.

© MoTeC Published 30 April 2015

Check for latest version at www.motec.com

1

Injector Volume Flow Rate: 0.212L/min

Encoder to Road Speed Conversion: $\frac{Encoder\ Speed}{38.704} = Road\ Speed$

DATASHEET PART 53001

DELCO 1 BAR MAP SENSOR

This One Bar Manifold Absolute Pressure Sensor is suitable for engine load measurements on naturally aspirated engines.

SPECIFICATIONS

The Delco pressure sensor is an analogue sensor with a 0 V to 5 V output. The sensor signal can be wired to Analogue Voltage (AV) input on compatible devices, see the Pin Table.

COMPATIBILITY

Suitable for use with:

- M1 Series ECUs
- M84 ECU
- Hundred Series ECUs
- All MoTeC Data Loggers

Connector

MoTeC connector part number: 64002

CALIBRATION

Manual Calibration

- 0.247 V = 15 kPa
- 4.853 V = 102 kPa

Using M1 Tune

For M130, M150, M170, M190, M141, M142, M181 and M182.

Use GM Delphi 1 Bar 1.0 from drop down list or use manual calibration.

Using the ECU Manager

For M84, M400, M600, M800 and M880.

Use predefined calibrations:

- kPa: #12 Pres (kPa) Delco 100 kPa
- PSI: #18 Pres (PSI) Delco 100 kPa

Using the Display/Logger Manager

For C125, C185, C127, C187, SDL3, ADL3, CDL3

Use the predefined calibration: Delco 1Bar MAP

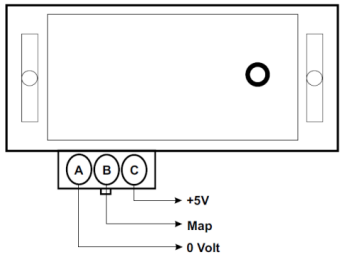

ECU AVAILABLE SIGNAL PINS

M84	M400, M600, M800	M880	M130*	M150*	M170*	M190*	M141/M142*	M181/M182*
A15, A17, A25, B22	A14, A15, A16, A17, A25, B20, B21, B22	6, 7, 12, 18, 26, 35, 36, 44	A14, A15, A16, A17, A25, B20, B21, B22	C14, C15, C16, C17, C25, D20, D21, D22, B10, B11, B12	A6, A7, A12, A18, A26, A35, A36, A44	C42, C36, C35, C28, C29, C11, C12, C6, C13, C7, A13, A35, A34, A41, A27, A28, A29, A38	C14, C15, C16, C17, C25, D20, D21, D22, B10, B11, B12, B16, B17, B18, A3, A4, A5	C42, C36, C35, C28, C29, C11, C12, C6, C13, C7, A13, A35, A34, A41, A27, A28, A29, A38

*Availability of some M1 series ECU pins may be limited depending on channel assignments for specific firmware Packages.

© MoTeC Published 17 July 2018 Check for the latest version at www.motec.com

Throttle Position Control Parameters

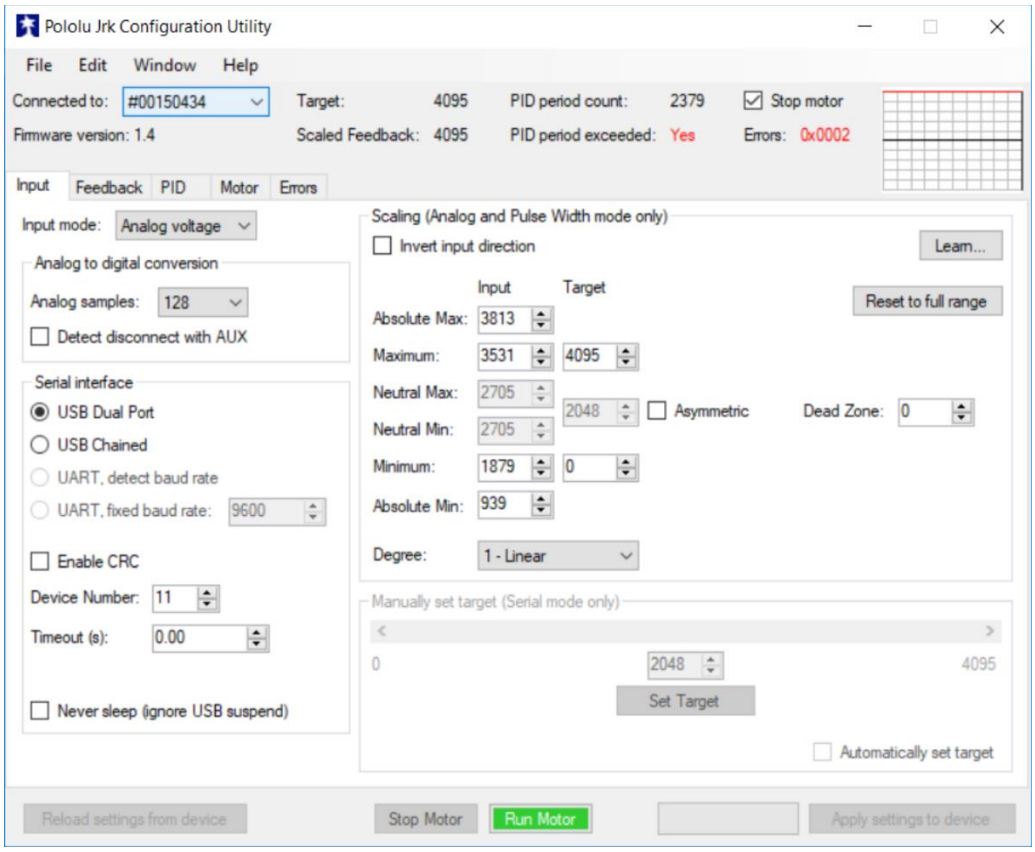

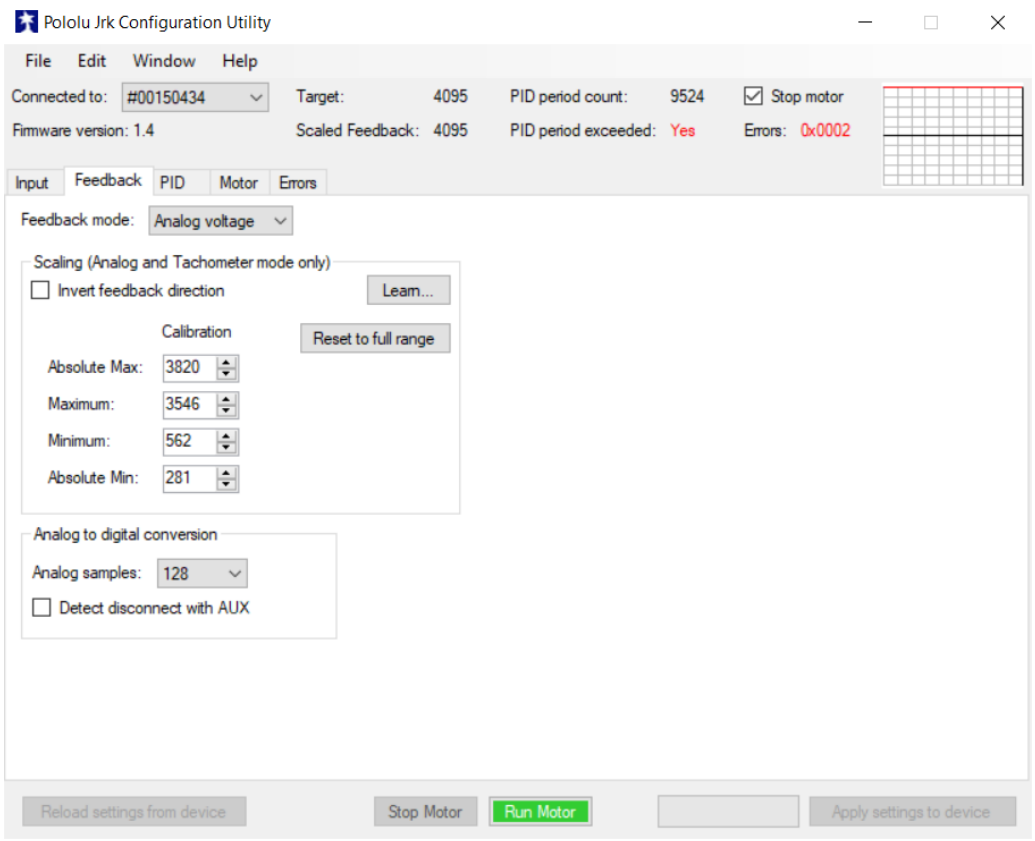

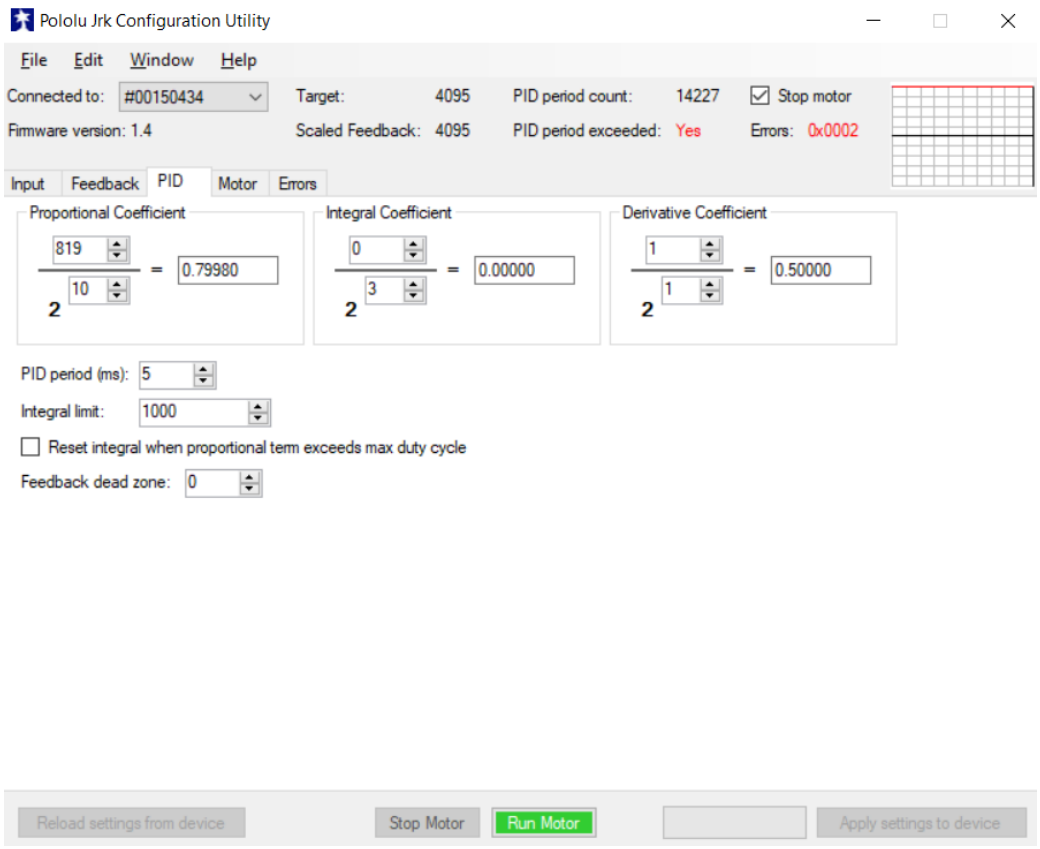
Pololu Jrk Configuration Utility
File Edit Window Help
Connected to: #00150434
Target: 4095
PID period count: 14227
Stop motor
Firmware version: 1.4
Scaled Feedback: 4095
PID period exceeded: Yes
Errors: 0x0002
Input Feedback PID Motor Errors
Proportional Coefficient
819
10
2
= 0.79980
Integral Coefficient
0
3
2
= 0.00000
Derivative Coefficient
1
1
2
= 0.50000
PID period (ms): 5
Integral limit: 1000
Reset integral when proportional term exceeds max duty cycle
Feedback dead zone: 0
Reload settings from device
Stop Motor
Run Motor
Apply settings to device

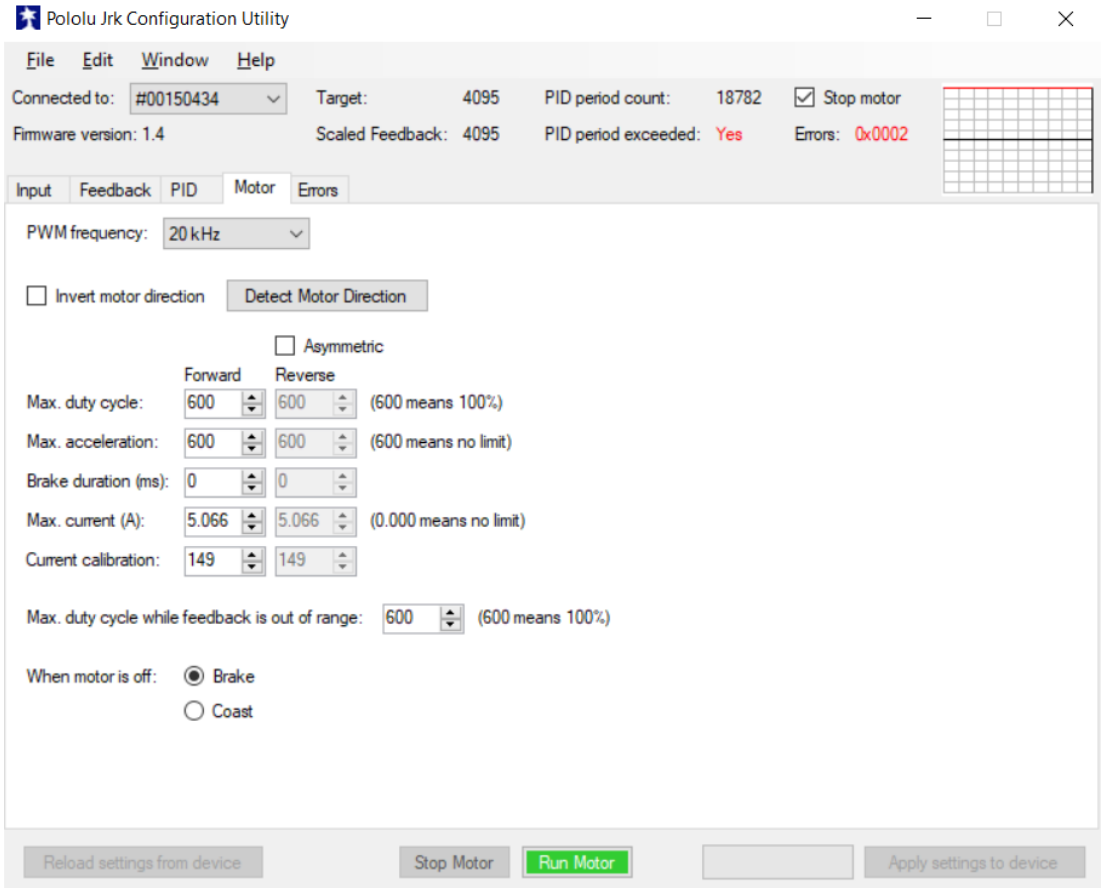
Pololu Jrk Configuration Utility
File Edit Window Help
Connected to: #00150434
Target: 4095
PID period count: 18782
Stop motor
Firmware version: 1.4
Scaled Feedback: 4095
PID period exceeded: Yes
Errors: 0x0002
Input Feedback PID Motor Errors
PWM frequency: 20 kHz
Invert motor direction
Detect Motor Direction
Asymmetric
Forward
Reverse
Max. duty cycle: 600 600 (600 means 100%)
Max. acceleration: 600 600 (600 means no limit)
Brake duration (ms): 0 0
Max. current (A): 5.066 5.066 (0.000 means no limit)
Current calibration: 149 149
Max. duty cycle while feedback is out of range: 600 (600 means 100%)
When motor is off:
Brake
Coast
Reload settings from device
Stop Motor
Run Motor
Apply settings to device

Motor Controller Parameters

Menu 1	Menu 2	Menu 3	Menu 4	Menu 5	Value	Unit
Program						
	User Settings					
		Speed Settings				
			Forward Speed		2000	rpm
			Reverse Speed		2000	rpm
			Econo Speed		200	rpm
		Accel Rates				
			Normal Accel Rate		0.1	Seconds
			Econo Accel Rate		0.1	Seconds
		Throttle Settings				
			Throttle Type		3	
			Deadband		0.5	Volt
			Throttle Max		4.5	Volt
			Mapped Throttle		35	%
		Brake Pedal Settings				
			Brake Type		0	
			Brake Deadband		1	Volt
			Brake Max		3.5	Volt
			Regen Brake Light Threshold		40	Ampere
		Current Limits				
			Normal Neutral Braking		15	%
			Econo Neutral Braking		20	%
			Shift Neutral Braking		7	%
			Normal Drive Current Limit		100	%
			Econo Drive Current Limit		60	%
			Brake Current Limit		10	%
		Idle Setup				
			Idle Enable		Off	
			Clutch Start Enable		Off	
			Idle Speed		500	rpm
			Idle Torque		5	%
			Creep Torque		0	%
		Motor Tuning				
			Motor Type		9	
			Base Speed		2000	rpm
			Field Weakening		100	%
			Econo Field Weakening		50	%
			Weakening Rate		20	%
		Main Contactor				
			Main Contactor Voltage		48	Volt
			Main Holding %		40	%
		Display Menu Items				

	Auto Scroll	Off	
	Scroll Delay Time	7	Seconds
	Display SOC	On	
	Display Motor RPM	On	
	Display Battery Amps	On	
	Display Voltage	On	
	Display Motor Temp	On	
	Display Controller Temp	On	
	Display Minimum Voltage	On	
	Display Maximum Current	On	
BMS			
	BMS Installed	On	
	User Undervoltage	70	%
	Maximum Cell Voltage	3.5	Volt
Dual Drive			
	Dual Drive Mode	Off	
	Response Timeout	500	ms
Misc			
	Max Output Frequency	266	Hz
	Prg Mode Step Timer	5	Seconds
	Generic CAN Message ID Dec	1537	
Control Mode			
Select		2	
0 - Speed Mode Express			
Max Speed		2000	rpm
Kp		40	%
Ki		30	%
Accel Rate		2.5	Seconds
Decel Rate		7	Seconds
Brake Rate		2	Seconds
Pump Enable		Off	
1 - Speed Mode			
Speed Controller			
	Max Speed	1000	rpm
	Kp	30	%
	Ki LS	30	%
	Ki HS	30	%
	Vel Feedforward		
	Kvff	0	Ampere
	Build Rate	1	Seconds
	Release Rate	0.4	Seconds
	Acc Feedforward		
	Kaff	0	Ampere
	Kbff	0	Ampere
	Build Rate	1	Seconds
	Release Rate	0.4	Seconds
Response			
	Full Accel Rate HS	0.1	Seconds

		Full Accel Rate LS	5	Seconds
		Low Accel Rate	0.1	Seconds
		Neutral Decel Rate HS	10	Seconds
		Neutral Decel Rate LS	14	Seconds
		Full Brake Rate HS	1	Seconds
		Full Brake Rate LS	2	Seconds
		Low Brake Rate	5	Seconds
		Fine Tuning		
		Partial Decel Rate	30	Seconds
		HS (High Speed)	70	%
		LS (Low Speed)	30	%
		Reversal Soften	20	%
		Max Speed Accel	1	Seconds
		Max Speed Decel	10	Seconds
	Restraint			
		Restraint Forward	50	%
		Restraint Back	50	%
		Soft Stop Speed	0	rpm
		Position Hold		
		Position Hold Enable	Off	
		Position Hold Timeout Time	0	Seconds
		Kp	10	%
		Kd	15	%
		Set Speed Settling Time	3013	ms
		Set Speed Threshold	30	rpm
		Entry Rate	50	%
		Exit Rollback Reduction	50	%
	Pump Enable		Off	
2 - Torque Mode				
	Speed Limiter			
		Max Speed	2000	rpm
		Kp	40	%
		Ki	30	%
		Kd	20	%
	Response			
		Accel Rate	0.1	Seconds
		Accel Release Rate	0.4	Seconds
		Brake Rate	2.5	Seconds
		Brake Release Rate	0.4	Seconds
		Neutral Braking	15	%
		Neutral Taper Speed	1000	rpm
		Forward Full Restraint Speed	2000	rpm
		Back Full Restraint Speed	2000	rpm
		Fine Tuning		
		Creep Torque	0	%
		Brake Full Creep Cancel	50	%
		Creep Build Rate	0.1	Seconds

		Creep Release Rate	3	Seconds
		Gear Soften	10	%
		Brake Taper Speed	1000	rpm
		Reversal Soften	20	%
		Max Speed Decel	5	Seconds
Current Limits				
	Drive Current Limit		100	%
	Regen Current Limit		100	%
	Brake Current Limit		10	%
	EMR Current Limit		100	%
	Interlock Brake Current Limit		100	%
	Power Limiting Map			
		PL Nominal Speed	1500	rpm
		Delta Speed	500	rpm
		Drive Limiting Map		
		Nominal	100	%
		Plus Delta	100	%
		Plus 2xDelta	100	%
		Plus 4xDelta	100	%
		Plus 8xDelta	100	%
		Regen Limiting Map		
		Nominal	100	%
		Plus Delta	100	%
		Plus 2xDelta	100	%
		Plus 4xDelta	100	%
		Plus 8xDelta	100	%
Throttle				
	Throttle Type		2	
	Forward Deadband		0.5	Volt
	Forward Map		35	%
	Forward Max		4.5	Volt
	Forward Offset		0	%
	Reverse Deadband		0.5	Volt
	Reverse Map		35	%
	Reverse Max		4.5	Volt
	Reverse Offset		0	%
	Throttle Filter		10	Hz
	HPD SRO Type		0	
	Sequencing Delay		0.1	Seconds
	VCL Throttle Enable		Off	
Brake				
	Brake Pedal Enable		Off	
	Brake Type		5	
	Brake Deadband		1	Volt
	Brake Map		50	%
	Brake Max		3.5	Volt
	Brake Offset		0	%
	Brake Filter		2	Hz

VCL Brake Enable	Off		
EM Brake Control			
Brake Type		0	
Pull In Voltage		0	%
Holding Voltage		0	%
Battery Voltage Compensated	On		
Set EM Brake On Fault	On		
Set Speed Threshold		30	rpm
Release Delay		50	ms
Set Speed Settling Time		3013	ms
Torque Preload Delay		200	ms
Torque Preload Enable	On		
Torque Preload Cancel Delay		0	Seconds
EM Brake Fault Motor Revs		4	
Drivers			
Main Contactor			
Main Enable	On		
Main Interlock Type		0	
Pull In Voltage		48	%
Holding Voltage		19	%
Battery Voltage Compensated	On		
Interlock Type		0	
Open Delay		0.1	Seconds
Weld Check Enable	On		
Main DNC Check Enable	On		
Main DNC Runtime Threshold		0	Volt
Precharge Enable	On		
Precharge Time		1	Seconds
Precharge Drop Threshold		3	Volt
Proportional Driver			
PD			
Enable	Off		
Hyd Lower Enable	Off		
PD Max Current		2	Ampere
PD Min Current		0.05	Ampere
PD Dither %		0	%
PD Dither Period		16	ms
PD Kp		10	%
PD Ki		10	%
Driver 3			
Pull In Voltage		0	%
Holding Voltage		0	%
Fault Checking			
Driver 1 Checks Enable	On		
Driver 2 Checks Enable	Off		
Driver 3 Checks Enable	Off		
Driver 4 Checks Enable	Off		

	PD Checks Enable	Off	
	External Supply Max	200	mAmpere
	External Supply Min	0	mAmpere
PWM Frequency		200	Hz
Motor			
Typical Max Speed		4000	rpm
Swap Encoder Direction		Off	
Swap Two Phases		Off	
Encoder Steps		64	
Encoder Fault Setup			
	Fault Detection Enable	On	
	Encoder Pulse Fault Detect Time	0.5	Seconds
	Fault Stall Time	5	Seconds
	LOS Upon Encoder Fault	On	
	LOS Max Speed	800	rpm
	LOS Max Current	400	Ampere
	LOS Max Mod Depth	50	%
	LOS Accel Rate	7	Seconds
	LOS Decel Rate	3	Seconds
Temperature Control			
	Sensor Enable	On	
	Sensor Type	3	
	Sensor Offset	0	deg C
	Braking Thermal Cutback Enable	Off	
	Temperature Hot	120	deg C
	Temperature Max	140	deg C
	MotorTemp LOS Max Speed	800	rpm
Battery			
Nominal Voltage		96	Volt
Kp UV		2.5	%
Ki UV		1	%
User Overvoltage		125	%
User Undervoltage		70	%
Reset Volts Per Cell		2.09	Volt
Full Volts Per Cell		2.04	Volt
Empty Volts Per Cell		1.73	Volt
Discharge Time		34	Minutes
BDI Reset Percent		75	%
Insulation Resistance Fault Threshold		0	kOhm
Dual Drive			
Dual Motor Enable		Off	
i:Dual Motor Slave		Off	
CAN Node ID Other		2	
LOS Max Speed		800	rpm
Master			
	Steer Angle Max (deg)	90	
	Turn Accel Rate	5	Seconds
	Critical Angle (deg)	70	

	Max Turn Speed	30	%
	Inner Wheel Speed	-100	%
	Steer Type	5	
	Steer Pot Min	0.5	Volt
	Steer Pot Zero	2.5	Volt
	Steer Pot Max	4.5	Volt
	VCL Steer Enable	Off	
Slave			
	Turn Accel Rate	5	Seconds
	Critical Angle (deg)	70	
	Steer Fault Min	0.25	Volt
	Steer Fault Max	4.75	Volt
Turn Feedforward			
	Turn Accel Rate	5	Seconds
	Turn Kvff	0	Ampere
	Turn ff Build Rate	1	Seconds
	Turn ff Release Rate	0.4	Seconds
Vehicle			
	Metric Units	Off	
	Speed to RPM	80	
	Capture Speed 1	2895	rpm
	Capture Speed 2	4500	rpm
	Capture Distance 1	22	
	Capture Distance 2	100	
	Capture Distance 3	150	
Emergency Reverse			
	EMR Enable	Off	
	EMR Type	0	
	EMR Dir Interlock	Off	
	EMR Time Limit	3	Seconds
	EMR Speed	1000	rpm
	EMR Accel Rate	0.1	Seconds
	EMR Decel Rate	0.1	Seconds
Interlock Braking			
	Enable	Off	
	Decel Rate HS	1.5	Seconds
	Decel Rate LS	2	Seconds
	Interlock Brake Timeout	5	Seconds
CAN Interface			
	CANopen Interlock	Off	
	CAN Node ID 1	1	
	CAN Node ID 2	1	
	CAN Node ID 3	1	
	CAN Node ID 4	1	
	Supervisor Node ID	70	
	Baud Rate	1	

Heartbeat Rate	100	ms
PDO Timeout Period	200	ms
Emergency Message Rate	16	ms
Suppress CANopen Init	0	
Motor Control Tuning		
IM Motor Characterization Tests		
Test Enable	0	
Test Throttle	0	
Motor Poles	4	
Max Test Speed	1040	rpm
Max Test Current	50	%
SlipGain	3.3	
Field Weakening Control		
FW Base Speed	2000	rpm
Field Weakening Drive	100	%
Field Weakening Regen	100	%
Weakening Rate Drive	20	%
Min Field Current	0	Ampere
Motor Type	0	
Reset Controller	0	

References

A123 Systems 2016, *48V Lithium-ion Battery - 8Ah*.

ACEA 2017, *Average Vehicle Age*, European Automobile Manufacturers Association.

Ahluwalia, R.K., Wang, X. & Rousseau, A. 2005, 'Fuel economy of hybrid fuel-cell vehicles', *Journal of Power Sources*, vol. 152, no. 1–2, pp. 233–44.

Akritidis, K.M. 2015, 'Solar Charged Electric Farming Tractors', University of Strathclyde.

Akumu, J. 2017, *Global Trends in Sulphur Reduction*, United Nations Environment, Malawi, Kenya.

Alamoudi, Y.A., Ferrah, A., Panduranga, R., Althobaiti, A. & Mulolani, F. 2019, 'State-of-the-Art Electrical Machines for Modern Electric Vehicles', *2019 Advances in Science and Engineering Technology International Conferences (ASET)*, pp. 1–8.

Anderson, R.L. & Bierley, R.L. 1965, 'Measuring Automatic Transmission Shift Performance', *SAE Technical Paper Series*, no. 650465.

André, M., Joumard, R., Vidon, R., Tassel, P. & Perret, P. 2006, 'Real-world European driving cycles, for measuring pollutant emissions from high- and low-powered cars', *Atmospheric Environment*, vol. 40, no. 31, pp. 5944–53.

Arlet, J. 2017, 'Electricity Tariffs, Power Outages and Firm Performance: A Comparative Analysis', *World bank working paper*, no. 2015, pp. 1–41.

Arze del Granado, F.J., Coady, D. & Gillingham, R. 2012, 'The Unequal Benefits of Fuel Subsidies: A Review of Evidence for Developing Countries', *World Development*, vol. 40, no. 11, pp. 2234–48.

Ashby, R.M., Jeong, J., Rao, S.Y., Heydinger, G.J. & Guenther, D.A. 2014, 'A Primer on Building a Hardware in the Loop Simulation and Validation for a 6X4 Tractor Trailer

Model', *SAE International Journal of Commercial Vehicles*, vol. 7, no. 2014- 01–0118, pp. 8–18.

Australian Government Department of the Environment and Energy 2015, *Air Pollutants*, viewed <https://www.environment.gov.au/protection/air-quality/air-pollutants>.

Awadallah, M. 2018, 'A Mild Hybrid Vehicle Control Unit Capable of Torque Hole Elimination in Manual Transmissions', University of Technology Sydney.

Awadallah, M., Tawadros, P., Walker, P. & Zhang, N. 2016, 'Eliminating the Torque Hole: Using a Mild Hybrid EV Architecture to Deliver Better Driveability', *IEEE Transportation Electrification Conference and Expo, Asia-Pacific*, pp. 173–9.

Awadallah, M., Tawadros, P., Walker, P. & Zhang, N. 2017a, 'A Low-Cost and Novel Approach in Gearshift Control for a Mild-Hybrid Powertrain', *2017 IEEE Transportation Electrification Conference and Expo (ITEC)*, IEEE, pp. 754–60.

Awadallah, M., Tawadros, P., Walker, P. & Zhang, N. 2017b, 'Dynamic modelling and simulation of a manual transmission based mild hybrid vehicle', *Mechanism and Machine Theory*, vol. 112, pp. 218–39.

Awadallah, M., Tawadros, P., Walker, P. & Zhang, N. 2017c, 'Impact of Low and High Congestion Traffic Patterns on a Mild-HEV Performance', *SAE Technical Paper Series*, no. 2017- 01–2458.

Awadallah, M., Tawadros, P., Walker, P., Zhang, N. & Tawadros, J. 2017a, 'A Comparative Fuel Analysis of a novel HEV with conventional vehicle', *IEEE 85th Vehicular Technology Conference*, pp. 1–6.

Awadallah, M., Tawadros, P., Walker, P., Zhang, N. & Tawadros, J. 2017b, 'A System Analysis and Modeling of a HEV based on Ultracapacitor Battery', *2017 IEEE Transportation Electrification Conference and Expo (ITEC)*, IEEE, pp. 792–8.

Awadallah, M., Tawadros, P., Walker, P. & Zhang, P.N. 2018, 'Comparative Fuel Economy, Cost and Emissions Analysis of A Novel Mild Hybrid and Conventional Vehicles', *Proceedings of the Institution of Mechanical Engineers, Part D: Journal of Automobile Engineering*, vol. 232, no. 13, pp. 1846–62.

Babu, A. & Ashok, S. 2015, 'Improved parallel mild hybrids for urban roads', *Applied Energy*, vol. 144, pp. 276–83.

Bao, R., Avila, V. & Baxter, J. 2017, *Effect of 48 V Mild Hybrid System Layout on Powertrain System Efficiency and Its Potential of Fuel Economy Improvement*, SAE International .

Baraszu, R.C. & Cikanek, S.R. 2002, 'Torque Fill-In for an Automated Shift Manual Transmission in a Parallel Hybrid Electric Vehicle', *Proceedings Of The American Control Conference*, Anchorage, Alaska, pp. 1431–6.

Basavaradder, A.B., Dayananda, P.K. & Chethan, K.N. 2018, 'Review on alternative propulsion in automotives -hybrid vehicles', *International Journal of Engineering & Technology*, vol. 7, no. 3, pp. 1311–9.

Baskin, A. 2018, *Africa Used Vehicles Report*.

Bohnsack, R., Pinkse, J. & Kolk, A. 2014, 'Business models for sustainable technologies: Exploring business model evolution in the case of electric vehicles', *Research Policy*, vol. 43, no. 2, pp. 284–300.

Borhan, H., Vahidi, A., Phillips, A.M., Kuang, M.L., Kolmanovsky, I. V. & Di Cairano, S. 2012, 'MPC-based energy management of a power-split hybrid electric vehicle', *IEEE Transactions on Control Systems Technology*, vol. 20, no. 3, pp. 593–603.

Bostwick, C.C. & Szadkowski, A. 1998, 'Self-Excited Vibrations During Engagements of Dry Friction Clutches', *SAE Technical Paper Series*, no. 982846.

Boughanmi, H. & Khan, M.A. 2019, 'Welfare and distributional effects of the energy subsidy reform in the gulf cooperation council countries: The case of sultanate of Oman', *International Journal of Energy Economics and Policy*, vol. 9, no. 1, pp. 228–36.

Bresnahan, T.F. & Yao, D.A. 1985, 'The Nonpecuniary Costs of Automobile Emissions Standards', *The RAND Journal of Economics*, vol. 16, no. 4, pp. 437–55.

Brown, A. & Kotori, D. 2013, ' Dynamic Vehicle Powertrain Model Development and Hardware-in-the-Loop Simulator for Developing and Measuring Fuel Efficient CO 2 Reducing Technologies ', *SAE Technical Paper Series*, vol. 1.

Burress, T.A., Campbell, S.L., Coomer, C., Ayers, C.W., Wereszczak, A.A., Cunningham, J.P., Marlino, L.D., Seiber, L.E. & Lin, H.-T. 2011, *Evaluation of the 2010 Toyota Prius Hybrid Synergy Drive System*, Oak Ridge, Tennessee.

CARB 2012, *2012 Amendments to the Zero Emission Vehicle Regulations*.

CARB 2018, *History | California Air Resources Board*, viewed <https://ww2.arb.ca.gov/about/history>.

Carslaw, D.C., Beevers, S.D., Tate, J.E., Westmoreland, E.J. & Williams, M.L. 2011, 'Recent evidence concerning higher NOx emissions from passenger cars and light duty vehicles', *Atmospheric Environment*, vol. 45, no. 39, pp. 7053–63.

Chen, P.-T., Pai, P.-H., Yang, C.-J. & Huang, K.D. 2019, 'Development of Transmission Systems for Parallel Hybrid Electric Vehicles', *Applied Sciences*, vol. 9, no. 8, p. 1538.

Chen, Y. & Borken-Kleefeld, J. 2014, 'Real-driving emissions from cars and light commercial vehicles - Results from 13 years remote sensing at Zurich/CH', *Atmospheric Environment*, vol. 88, no. 2014, pp. 157–64.

Coffin, D., Horowitz, J., Nesmith, D., Coffin, D., Horowitz, J. & Semanik, M. 2016,

Examining Barriers to Trade in Used Vehicles.

Collantes, G.O. 2008, 'Electrifying Our Way to Fuel Economy: Regulatory Perspectives on Hybrid Vehicles', *SAE Technical Paper Series*, no. 2008-21–0013.

Coren, M.J. 2018, 'Nine countries say they'll ban internal combustion engines. So far, it's just words.', *Quartz.com*, viewed <https://qz.com/1341155/nine-countries-say-they-will-ban-internal-combustion-engines-none-have-a-law-to-do-so/>.

Crolla, D.A. & Cao, D. 2012, 'The impact of hybrid and electric powertrains on vehicle dynamics, control systems and energy regeneration', *Vehicle System Dynamics*, vol. 50, no. SUPPL. 1, pp. 95–109.

Davis, L. 2014, 'The Economic Cost of Global Fuel Subsidies', *American Economic Review*, vol. 104, no. 5, pp. 581–5.

Ding, W., Liu, G. & Li, P. 2019, 'A Hybrid Control Strategy of Hybrid-Excitation Switched Reluctance Motor for Torque Ripple Reduction and Constant Power Extension', *IEEE Transactions on Industrial Electronics*, vol. PP, no. c, pp. 1–1.

Dockery, D.W., Schwartz, J. & Spengler, J.D. 1992, 'Air pollution and daily mortality: Associations with particulates and acid aerosols', *Environmental Research*, vol. 59, no. 2, pp. 362–73.

Dolcini, P., De Wit, C.C. & Béchart, H. 2008, 'Lurch avoidance strategy and its implementation in AMT vehicles', *Mechatronics*, vol. 18, pp. 289–300.

Dunn, B., Kamath, H. & Tarascon, J. 2011, 'Electrical Energy Storage for the Grid : A Battery of Choices', *Science Magazine*, vol. 334, no. November, pp. 928–36.

Duoba, M., Bohn, T. & Lohse-Busch, H. 2010, 'Investigating Possible Fuel Economy Bias Due To Regenerative Braking in Testing HEVs on 2WD and 4WD Chassis

Dynamometers', *SAE Technical Paper Series*, vol. 1, no. 724.

Ebbesen, S., Elbert, P. & Guzzella, L. 2013, 'Engine Downsizing and Electric Hybridization Under Consideration of Cost and Drivability', *Oil & Gas Science and Technology – Revue d'IFP Energies nouvelles*, vol. 68, no. 1, pp. 109–16.

Edwards, S. 2017, 'Developed countries "exporting pollution" by trading second-hand vehicles to poorer countries, experts say', *Inside Development*, viewed 26 January 2017, <https://www.devex.com/news/developed-countries-exporting-pollution-by-trading-second-hand-vehicles-to-poorer-countries-experts-say-89457>.

Ehsani, M., Gao, Y., Longo, S. & Ebrahimi, K. 2018, *Modern Electric, Hybrid Electric, and Fuel Cell Vehicles*, 3rd edn, CRC Press, Boca Raton, Florida.

Elias, M.G. 2010, *Egypt State of the Environment Report 2009*, Egyptian Environmental Affairs Agency, Cairo.

Emadi, A., Lee, Y.J. & Rajashekara, K. 2008, 'Power electronics and motor drives in electric, hybrid electric, and plug-in hybrid electric vehicles', *IEEE Transactions on Industrial Electronics*, vol. 55, no. 6, pp. 2237–45.

Engeljehringer, K. 2016, *AVL Emission Testing Handbook 2016*, AVL GmbH, Graz, Austria.

Esfandyari, M.J., Yazdi, M.R.H., Esfahanian, V. & Nehzati, H. 2018, 'A Low-Cost Single PC Based HiL Simulation Platform for Verification of the Hybrid Electric Vehicle Control Unit', *26th Iranian Conference on Electrical Engineering, ICEE 2018*, pp. 760–5.

European Environment Agency 2017, *Emissions of Air Pollutants from Transport*, viewed <https://www.eea.europa.eu/data-and-maps/indicators/transport-emissions-of-air-pollutants-8/transport-emissions-of-air-pollutants-5>.

Favre, C., Bosteels, D. & May, J. 2013, 'Exhaust Emissions from European Market-Available Passenger Cars Evaluated on Various Drive Cycles', *SAE Technical Paper Series*, no. 2013-24–0154.

Fontaras, G., Pistikopoulos, P. & Samaras, Z. 2008, 'Experimental evaluation of hybrid vehicle fuel economy and pollutant emissions over real-world simulation driving cycles', *Atmospheric Environment*, vol. 42, no. 18, pp. 4023–35.

Fotouhi, A., Longo, S., Propp, K., Samaranayake, L. & Auger, D. 2018, 'A hardware-in-the-loop test rig for development of electric vehicle battery identification and state estimation algorithms', *International Journal of Powertrains*, vol. 7, no. 1/2/3, p. 227.

Freescale Semiconductor 2014, *Permanent Magnet Synchronous Motor Control*, NXP Semiconductors, p. 3.

Fujiyoshi, M., Nonomura, Y., Arai, F. & Fukuda, T. 2002, 'A new micro jerk sensor with viscous coupling', *MHS 2002 - Proceedings of 2002 International Symposium on Micromechatronics and Human Science*, pp. 219–22.

Gaines, L. 2014, 'The future of automotive lithium-ion battery recycling: Charting a sustainable course', *Sustainable Materials and Technologies*, vol. 1–2, pp. 2–7.

Gavgani, A.M., Bingham, T., Sorniotti, A., Doherty, J., Cavallino, C. & Fracchia, M. 2015, 'A Parallel Hybrid Electric Drivetrain Layout with Torque-Fill Capability', *SAE International Journal of Passenger Cars - Mechanical Systems*, vol. 8, no. 2, pp. 767–78.

Gavgani, A.M., Sorniotti, A., Doherty, J. & Cavallino, C. 2016, 'Optimal gearshift control for a novel hybrid electric drivetrain', *Mechanism and Machine Theory*, vol. 105, pp. 352–68.

Gengaraj, M., Kalaivani, L., Koodammal, K., Krishnashini, M., Aniana, L. & Prithi, S.D.

2018, ‘A Comprehensive Study of Multilevel Inverter fed Switched Reluctance Motor for Torque Ripple Minimization with Multicarrier PWM Strategies’, *Proceedings of the 4th International Conference on Electrical Energy Systems, ICEES 2018*, pp. 1–7.

Glielmo, L., Iannelli, L., Vacca, V. & Vasca, F. 2006, ‘Gearshift Control for Automated Manual Transmissions’, *IEEE/ASME Transactions on Mechatronics*, vol. 11, no. 1, pp. 17–26.

Golchoubian, P. & Azad, N.L. 2017, ‘Real-Time Nonlinear Model Predictive Control of a Battery-Supercapacitor Hybrid Energy Storage System in Electric Vehicles’, *IEEE Transactions on Vehicular Technology*, vol. 66, no. 11, pp. 9678–88.

Guo, N., Shen, J., Xiao, R., Yan, W. & Chen, Z. 2018, ‘Energy management for plug-in hybrid electric vehicles considering optimal engine ON/OFF control and fast state-of-charge trajectory planning’, *Energy*, vol. 163, pp. 457–74.

Harendt, B., Körner, L., Läßle, E. & Oehmen, S. 2016, *International Benchmarking on the Status Quo of Electromobility in Germany 2015*.

HBM Australia 2017, *Temperature Compensation of Strain Gauges*, viewed <https://www.hbm.com/en/6725/article-temperature-compensation-of-strain-gauges/>.

Horn, J., Bamberger, J., Michau, P. & Pindl, S. 2002, ‘Flatness-based Clutch Control for Automated Manual Transmissions’, *IFAC 15th Triennial World Congress*, Barcelona, Spain.

Huang, Q. & Wang, H. 2010, ‘Fundamental Study of Jerk: Evaluation of Shift Quality and Ride Comfort’, *SAE Technical Paper Series*, vol. 1, no. 724.

Huang, Y., Wang, H., Khajepour, A., Li, B., Ji, J., Zhao, K. & Hu, C. 2018, ‘A review of power management strategies and component sizing methods for hybrid vehicles’, *Renewable and Sustainable Energy Reviews*, vol. 96, no. July, pp. 132–44.

Hutchinson, T., Burgess, S. & Herrmann, G. 2014, 'Current hybrid-electric powertrain architectures: Applying empirical design data to life cycle assessment and whole-life cost analysis', *Applied Energy*, vol. 119, pp. 314–29.

Al Ibraheemi, M.M. 2018, 'Modelling and Practical Set-up to Investigate the Performance of Permanent Magnet Synchronous Motor through Rotor Position Estimation at Zero and Low Speeds', Cardiff University.

IHME 2018, *State of Global Air 2019 - Global Burden of Disease Study 2017*, Health Effects Institute.

Isenstadt, A., German, J., Dorobantu, M., Boggs, D. & Watson, T. 2016, *Downsized, boosted gasoline engines*, *The Internaltional Council of Clean Transportation*.

Jaikamal, V. 2009, 'Model-based ECU development–an integrated MIL-SIL-HIL approach', *SAE Technical Paper Series*, no. 2009- 01–0153.

Ji, C., Wang, S., Zhang, B. & Liu, X. 2013, 'Emissions performance of a hybrid hydrogen-gasoline engine-powered passenger car under the New European Driving Cycle', *Fuel*, vol. 106, pp. 873–5.

de Jong, R. 2017, 'Used Vehicles: A Global Overview', *UNECE/ITC-UNEP conference on Ensuring Better Air Quality and Reduced Climate Emissions through Cleaner Used Vehicles*, Geneve.

Kaiser, G., Holzmann, F., Chretien, B., Korte, M. & Werner, H. 2011, 'Torque vectoring with a feedback and feed forward controller - Applied to a through the road hybrid electric vehicle', *IEEE Intelligent Vehicles Symposium, Proceedings*, no. Iv, pp. 448–53.

Kamble, S.H., Mathew, T. V. & Sharma, G.K. 2009, 'Development of real-world driving cycle: Case study of Pune, India', *Transportation Research Part D: Transport and Environment*, vol. 14, no. 2, pp. 132–40.

Karaoğlan, M.U., Kuralay, N.S. & Colpan, C.O. 2019, 'The effect of gear ratıos on the exhaust emıssıons and fuel consumptıon of a parallel hybrid vehicle powertrain', *Journal of Cleaner Production*, vol. 210, pp. 1033–41.

Kelly Controls 2017, *Kelly KAC-8080I High Power AC Induction Motor Controller User's Manual*.

Kim, J., Kim, G. & Park, Y. 2018, 'Component Sizing of Parallel Hybrid electric Vehicle Using Optimal Search Algorithm', *International Journal of Automotive Technology,* vol. 19, no. 4, p. 743−749.

Krambeck, H. 2010, 'The Average Age of a Taxi in Egypt is 32 Years Old', *World Bank Blogs*, viewed <https://blogs.worldbank.org/transport/the-average-age-of-a-taxi-in-egypt-is-32-years-old>.

Lakshminarayanan, S., Doshi, P.A., Kneissler, M., Kapur, D. & Divekar, A. 2017, 'Farewell to the Clutch Pedal', *SAE Technical Paper Series*, no. 2017-26–0062.

Lang, A. & Klüppel, M. 2017, 'Influences of temperature and load on the dry friction behaviour of tire tread compounds in contact with rough granite', *Wear*, vol. 380–381, pp. 15–25.

Lin, C.-C., Peng, H., Grizzle, J.W., Liu, J. & Busdiecker, M. 2003, 'Control System Development for an Advanced-Technology Medium-Duty Hybrid Electric Truck', *SAE Technical Paper Series*, no. 2003- 01–3369.

Liu, J. & Peng, H. 2008, 'Modeling and Control of a Power-Split Hybrid Vehicle', *IEEE Transactions on Control Systems Technology*, vol. 16, no. 6, pp. 1242–51.

Logicool AC 2018, *Mitsubishi Electric IT Cooling i-NEXT DX*, viewed <https://www.logicool-ac.com/products/i-nextdx/>.

López, M., Claudio, A., Loyola, F. & Cano, U. 2018, 'Sizing Methodology of Fuel Cell Electric Vehicle Power Plant', *14th International Conference on Power Electronics (CIEP)*, IEEE, pp. 174–80.

Lord, M. 2017, 'TOYOTA's Electrification Roadmap', *34th International Battery Seminar & Exhibit*, Ft. Lauderdale, pp. 1–24.

Lukic, S.M., Emadi, A., Rajashekara, K. & Williamson, S.S. 2005, 'Topological Overview of Hybrid Electric and Fuel Cell Vehicular Power System Architectures and Configurations', *IEEE Transactions on Vehicular Technology*, vol. 54, no. 3, pp. 763–70.

Lutsey, N. 2015, 'Global Climate Change Mitigation Potential From a Transition To Electric Vehicles', *International Council on Clean Transportation*, no. December, pp. 1–17.

Mahapatra, S., Egel, T., Hassan, R., Shenoy, R. & Carone, M. 2008, 'Model-Based Design for Hybrid Electric Vehicle Systems', *SAE Technical Paper Series*, vol. 2008- 01– 00.

Mamikoglu, S. & Dahlander, P. 2019, 'Modelling of Hybrid Electric Vehicle Powertrains - Factors That Impact Accuracy of CO_2 Emissions', *SAE Technical Paper Series*, vol. 1, pp. 1–9.

Manish, S. & Banerjee, R. 2006, 'Techno-economic assessment of fuel cell vehicles for India', *16th World Hydrogen Energy Conference 2006, WHEC 2006*, vol. 1, no. July.

Mansour, C., Haddad, M. & Zgheib, E. 2018, 'Assessing consumption, emissions and costs of electrified vehicles under real driving conditions in a developing country with an inadequate road transport system', *Transportation Research Part D: Transport and Environment*, vol. 63, no. June, pp. 498–513.

Masrur, M.A. & Mi, C. 2011, 'Advanced HEV Architectures and Dynamics of HEV Powertrain', *Hybrid Electric Vehicles: Principles and Applications with Practical*

Perspectives, 1st edn, John Wiley & Sons, pp. 69–106.

Matthews, J.L. & Roback, L.G. 1998, 'California Cruisin' - New York's Adoption of California's Motor Vehicle Emissions Program', *Albany Law Environmental Outlook*, vol. 4, p. 36.

Mazda Motor Corporation 1989, *1990 Mazda MX-5 Workshop Manual*, Mzda Motor Corporation, Hiroshima, Japan.

Mazur, C., Offer, G.J., Contestabile, M. & Brandon, N.B. 2018, 'Comparing the effects of vehicle automation, policy-making and changed user preferences on the uptake of electric cars and emissions from transport', *Sustainability (Switzerland)*, vol. 10, no. 3.

McDonald, J. 2016, *Electric Vehicles to be 35% of New Car Sales by 2040*, viewed 16 February 2020, <https://about.bnef.com/blog/electric-vehicles-to-be-35-of-global-new-car-sales-by-2040/>.

McKerracher, C., Izadi-Najafabadi, A., Soulopoulos, N. & Doherty, D. 2019, *Electric Vehicle Outlook 2019*.

McLaren, J., Miller, J., O'Shaughnessy, E., Wood, E. & Shapiro, E. 2016, 'CO2 emissions associated with electric vehicle charging: The impact of electricity generation mix, charging infrastructure availability and vehicle type', *Electricity Journal*, vol. 29, no. 5, pp. 72–88.

Merkisz, J., Pielecha, I., Pielecha, J. & Brudnicki, K. 2011, 'On-road exhaust emissions from passenger cars fitted with a start-stop system', *Archives of Transport*, vol. 23, no. 1, pp. 37–46.

Mo, W., Walker, P.D. & Zhang, N. 2019, 'Dynamic analysis and control for an electric vehicle with harpoon-shift synchronizer', *Mechanism and Machine Theory*, vol. 133, pp. 750–66.

Molin Valdés, H. 2018, *African countries move toward cleaner car imports*, Climate & Clean Air Coalition.

Momen, F., Rahman, K. & Son, Y. 2019, 'Electrical propulsion system design of chevrolet bolt battery electric vehicle', *IEEE Transactions on Industry Applications*, vol. 55, no. 1, pp. 376–84.

Montero, J.-P. 1999, 'Voluntary Compliance with Market-Based Environmental Policy: Evidence from the U. S. Acid Rain Program', *Journal of Political Economy*, vol. 107, no. 5, pp. 998–1033.

Murata, S. 2012, 'Innovation by in-wheel-motor drive unit', *Vehicle System Dynamics*, vol. 50, no. 6, pp. 807–30.

Mutenyo, J., Banga, M., Matovu, F., Kimera, D. & Lawrence, K. 2015, *Baseline Survey on Uganda's National Average Automotive Fuel Economy*, Kampala, Kenya.

Narins, T.P. 2017, 'The battery business: Lithium availability and the growth of the global electric car industry', *Extractive Industries and Society*, vol. 4, no. 2, pp. 321–8.

National Renewable Energy Laboratory 2002, *ADVISOR Release Note - Version 3 Change Log*, viewed <http://adv-vehicle-sim.sourceforge.net/version_archive.html>.

Newberger, N. & Johnson, B. 2014, 'Testing Electrified Drivetrains for Vehicles without the Battery or Engine', *Readout - Horiba Technical Reports*, no. 42, pp. 56–60.

Nikowitz, M. 2016, *Advanced Hybrid and Electric Vehicles: System Optimization and Vehicle Integration*.

Nitta, N., Wu, F., Lee, J.T. & Yushin, G. 2015, 'Li-ion Battery Materials: Present and Future', *Materials Today*, vol. 18, no. 5, pp. 252–64.

Oglieve, C.J., Mohammadpour, M. & Rahnejat, H. 2017, 'Optimisation of the vehicle

transmission and the gear-shifting strategy for the minimum fuel consumption and the minimum nitrogen oxide emissions', *Proceedings of the Institution of Mechanical Engineers, Part D: Journal of Automobile Engineering*, vol. 231, no. 7, pp. 883–99.

Oh, S.C. 2005, 'Evaluation of motor characteristics for hybrid electric vehicles using the hardware-in-the-loop concept', *IEEE Transactions on Vehicular Technology*, vol. 54, no. 3, pp. 817–24.

Olszewski, M., Rogers, S.A., Staunton, R.H., Ayers, C.W., Marlino, L.D., Chiasson, J.N. & Burress, T.A. 2005, *Evaluation of 2004 Toyota Prius Hybrid Electric Drive System*, Oak Ridge, Tennessee.

Opila, D.F., Wang, X., McGee, R. & Grizzle, J.W. 2012, 'Real-Time Implementation and Hardware Testing of a Hybrid Vehicle Energy Management Controller Based on Stochastic Dynamic Programming', *Journal of Dynamic Systems, Measurement, and Control*, vol. 135, no. 2, p. 021002.

Park, S.H., Lee, J., Lee, Y. Il & Ahmed, A.A. 2017, 'Development of electric vehicle powertrain: Experimental implementation and performance assessment', *2016 18th International Middle-East Power Systems Conference, MEPCON 2016 - Proceedings*, pp. 932–7.

Passalacqua, M., Lanzarotto, D., Repetto, M., Vaccaro, L., Bonfiglio, A. & Marchesoni, M. 2019, 'Fuel Economy and Energy Management System for a Series Hybrid Vehicle Based on Supercapacitor Storage', *IEEE Transactions on Power Electronics*.

Paulina, C. & McBryde, D. Matthews, M. 2007, 'Steady State Speeds Load Determinations Using Electric Vehicle Power or Dynamometer Measurements on Conventional Vehicles', *SAE International Journal of Engines*, vol. 10, no. 4, pp. 1820–8.

Pesaran, A.A. 2001, 'Battery Thermal Management in EVs and HEVs', *Advanced*

Automotive Battery Conference, no. January 2001.

Rahmani, D. & Loureiro, M.L. 2018, 'Why is the market for hybrid electric vehicles (HEVs) moving slowly?', *PLoS ONE*, vol. 13, no. 3, pp. 1–14.

Requia, W.J., Mohamed, M., Higgins, C.D., Arain, A. & Ferguson, M. 2018, 'How clean are electric vehicles? Evidence-based review of the effects of electric mobility on air pollutants, greenhouse gas emissions and human health', *Atmospheric Environment*, vol. 185, no. October 2017, pp. 64–77.

Roy, R. 2016, *The cost of air pollution in Africa*, African Economic Outlook, Paris, France.

Sadat, A.R., Ahmadian, S. & Vosoughi, N. 2018, 'A novel torque ripple reduction of switched reluctance motor based on DTC-SVM method', *2018 IEEE Texas Power and Energy Conference, TPEC 2018*, vol. 2018- Febru, pp. 1–6.

Sadri, A., Ardehali, M.M. & Amirnekooei, K. 2014, 'General procedure for long-term energy-environmental planning for transportation sector of developing countries with limited data based on LEAP (long-range energy alternative planning) and EnergyPLAN', *Energy*, vol. 77, pp. 831–43.

SAE Technical Standards Board 2010, *SAE-J1263 - Road Load Measurement and Dynamometer Simulation Using Coastdown Techniques*, Society of Automotive Engineers, Warrendale, PA.

SAE Technical Standards Board 2014, *SAE-J2264 - Chassis Dynamometer Simulation of Road Load Using Coastdown Techniques*.

Samuel, S., Austin, L. & Morrey, D. 2002, 'Automotive test drive cycles for emission measurement and real-world emission levels - A review', *Proceedings of the Institution of Mechanical Engineers, Part D: Journal of Automobile Engineering*, vol. 216, no. 7, pp. 555–64.

Sandy Thomas, C.E. 2012, 'How green are electric vehicles?', *International Journal of Hydrogen Energy*, vol. 37, no. 7, pp. 6053–62.

De Santis, M., Agnelli, S., Patanè, F., Giannini, O. & Bella, G. 2018, 'Experimental Study for the Assessment of the Measurement Uncertainty Associated with Electric Powertrain Efficiency Using the Back-to-Back Direct Method', *Energies*, vol. 11, no. 12, p. 3536.

Sarkar, A. & Banerjee, R. 2005, 'Net energy analysis of hydrogen storage options', *International Journal of Hydrogen Energy*, vol. 30, no. 8, pp. 867–77.

Schaltz, E., Jaber, K., Fakhfakh, A. & Neji, R. 2011, *Electrical Vehicle Design and Modeling*, S. Soylu (ed.), InTech, Rijeka, Croatia.

Schwarzer, V. & Ghorbani, R. 2013, 'Drive cycle generation for design optimization of electric vehicles', *IEEE Transactions on Vehicular Technology*, vol. 62, no. 1, pp. 89–97.

Scrosati, B. & Garche, J. 2010, 'Lithium batteries : Status , prospects and future', *Journal of Power Sources*, vol. 195, pp. 2419–30.

Sharer, P., Rousseau, A., Nelson, P. & Pagerit, S. 2006, 'Vehicle Simulation Results for Plug-in HEV Battery Requirements', *Proceedings of the 22nd Electric Vehicle Symposium*, Yokohama, Japan.

Sharma, R., Manzie, C., Bessede, M., Brear, M.J. & Crawford, R.H. 2012, 'Conventional, hybrid and electric vehicles for Australian driving conditions - Part 1: Technical and financial analysis', *Transportation Research Part C: Emerging Technologies*, vol. 25, pp. 238–49.

Sharma, R., Manzie, C., Bessede, M., Crawford, R.H. & Brear, M.J. 2013, 'Conventional, hybrid and electric vehicles for Australian driving conditions. Part 2: Life cycle CO2-e emissions', *Transportation Research Part C: Emerging Technologies*, vol. 28, pp. 63–

73.

Silva, C., Farias, T. & Ross, M. 2010, 'Evaluation of Energy Consumption, Emissions, and Costs of Plug-in Hybrid Vehicles', *Electric and Hybrid Vehicles*, vol. 50, no. 7, pp. 193–210.

Simmons, R.A., Shaver, G.M., Tyner, W.E. & Garimella, S. V. 2015, 'A benefit-cost assessment of new vehicle technologies and fuel economy in the U.S. market', *Applied Energy*, vol. 157, pp. 940–52.

Skeete, J.P. 2017, 'Examining the role of policy design and policy interaction in EU automotive emissions performance gaps', *Energy Policy*, vol. 104, no. November 2016, pp. 373–81.

Skoog, S. 2017, 'Experimental and Model Based Evaluation of Mild Hybrid Fuel Consumption Gains and Electric Machine Utilization for Personal Vehicle Application', *2017 IEEE Transportation Electrification Conference and Expo, Asia-Pacific, ITEC Asia-Pacific 2017*.

Smith, A. & Davies, H. 1996, 'A review of the history of emission legislation, urban and national transport trends and their impact on transport emissions', *Transactions on the Built Environment*, vol. 23, pp. 1–3.

Sovacool, B.K., Noel, L., Axsen, J. & Kempton, W. 2018, 'The neglected social dimensions to a vehicle-to-grid (V2G) transition: A critical and systematic review', *Environmental Research Letters*, vol. 13, no. 1.

Standards Australia 2016, *AS1668.2-2012/AMDT 2-2016*, Standards Australia.

Subramanian, R., Gupta, S. & Talbot, B. 2007, 'Compliance Strategies under Permits for Emissions', *Production and Operations Management*, vol. 16, no. 6, pp. 763–79.

Sugathapala, T. 2015, *Fuel Economy of Light Duty Vehicles in Sri Lanka the Baseline*.

Sun, Z. & Hebbale, K. 2005, 'Challenges and opportunities in automotive transmission control', *Proceedings of the American Control Conference*, pp. 3284–9.

Sung Bang, J., Hwan Choi, S., Kwan Ko, Y., Soo Kim, T. & Kim, S. 2018, 'The Engine Clutch Engagement Control for Hybrid Electric Vehicles', *2018 IEEE Conference on Control Technology and Applications, CCTA 2018*, vol. 21–24, pp. 1448–53.

Tammi, K., Minav, T. & Kortelainen, J. 2018, 'Thirty years of electro-hybrid powertrain simulation', *IEEE Access*, vol. 6, no. c, pp. 35250–9.

Tawadros, P., Awadallah, M., Walker, P. & Zhang, N. 2019, 'Using a Low-Cost Bluetooth Torque Sensor for Vehicle Jerk and Transient Torque Measurement', *Proceedings of the Institution of Mechanical Engineers, Part D: Journal of Automotive Engineering*.

Tawadros, P., Zhang, N. & Boretti, A. 2014, 'Integration and performance of regenerative braking and energy recovery technologies in vehicles', in R. Folkson (ed.),*Alternative Fuels and Advanced Vehicle Technologies for Improved Environmental Performance*, 1st edn, Woodhead Publishing, pp. 541–63.

Toyota 2018, *2.0-liter Dynamic Force Engine, a New 2.0-liter Direct-injection, Inline 4-cylinder Gasoline Engine*, viewed <https://global.toyota/en/mobility/tnga/powertrain2018/engine/>.

Tran, N., Breene, J., Khayesi, M., McInerney, R., Sukhai, A., Toroyan, T. & Ward, D. 2018, *Global Status Report on Road Safety 2018*, World Health Organization.

Tribioli, L. 2017, 'Energy-based design of powertrain for a re-engineered post-transmission hybrid electric vehicle', *Energies*, vol. 10, no. 7.

Trigui, R., Jeanneret, B., Malaquin, B., Badin, F. & Plasse, C. 2007, 'Hardware in the loop

simulation of a diesel parallel mild-hybrid electric vehicle', *VPPC 2007 - Proceedings of the 2007 IEEE Vehicle Power and Propulsion Conference*, pp. 448–55.

Trouve, M., Lesteven, G. & Leurent, F. 2018, 'Private Motorization in Worldwide Developing Countries Metropolitan Areas : Patterns in the early 21st century', *PIARC International Seminar*, Arusha, Tanzania.

United Nations Economic Commission for Europe 2019, 'Air Pollution, Ecosystems and Biodiversity', *Environmental Policy - Conventions and Protocols*, viewed <http://www.unece.org/environmental-policy/conventions/envlrtapwelcome/cross-sectoral-linkages/air-pollution-ecosystems-and-biodiversity.html>.

Vacca, F., De Pinto, S., Karci, A.E.H., Gruber, P., Viotto, F., Cavallino, C., Rossi, J. & Sorniotti, A. 2017, 'On the energy efficiency of dual clutch transmissions and automated manual transmissions', *Energies*, vol. 10, no. 10, pp. 1–22.

Vasconcellos, E.A. 1997, 'The demand for cars in developing countries', *Transportation Research Part A: Policy and Practice*, vol. 31, no. 3, pp. 245–58.

Vinot, E., Reinbold, V. & Trigui, R. 2016, 'Global Optimized Design of an Electric Variable Transmission for HEVs', *IEEE Transactions on Vehicular Technology*, vol. 65, no. 8, pp. 6794–8.

Walker, P.D. & Zhang, N. 2014, 'Active damping of transient vibration in dual clutch transmission equipped powertrains: A comparison of conventional and hybrid electric vehicles', *Mechanism and Machine Theory*, vol. 77, pp. 1–12.

Wang, X., Li, L., He, K. & Liu, C. 2018, 'Dual-loop Self-Learning Fuzzy Control for AMT Gear Engagement: Design and Experiment', *IEEE Transactions on Fuzzy Systems*, vol. 26, no. 4, pp. 1813–22.

Williamson, S.S., Khaligh, A., Oh, S.C. & Emadi, A. 2005, 'Impact of energy storage device

selection on the overall drive Train efficiency and performance of heavy-duty hybrid vehicles', *2005 IEEE Vehicle Power and Propulsion Conference, VPPC*, vol. 2005, pp. 381–90.

World Bank 2017, *Pump price for gasoline (US$ per liter) - World Development Indicators*, viewed <https://data.worldbank.org/indicator/EP.PMP.SGAS.CD>.

World Bank 2018, *Getting Electricity - World Development Indicators*, viewed <http://www.doingbusiness.org/en/data/exploretopics/getting-electricity>.

World Health Organization 2018, *WHO Global Ambient Air Quality Database (update 2018)*, viewed <https://www.who.int/airpollution/data/cities/en/>.

Wu, H. & Zhang, H. 2015, 'Model-Based Design and Evaluation of Electric Vehicle Powertrain with Independent Driving Motors', *Proceedings of the ASME 2015 International Design Engineering Technical Conferences & Computers and Information in Engineering Conference IDETC/CIE*, Boston, Massachusetts, pp. 1–8.

Wu, L., Wang, Y., Yuan, X. & Chen, Z. 2011, 'Multiobjective optimization of HEV fuel economy and emissions using the self-adaptive differential evolution algorithm', *IEEE Transactions on Vehicular Technology*, vol. 60, no. 6, pp. 2458–70.

Wu, W., Partridge, J.S. & Bucknall, R.W.G. 2018, *Stabilised control strategy for PEM fuel cell and supercapacitor propulsion system for a city bus*, vol. 43, pp. 12302–13.

Wu, Y., Zhang, S., Hao, J., Liu, H., Wu, X., Hu, J., Walsh, M.P., Wallington, T.J., Zhang, K.M. & Stevanovic, S. 2017, 'On-road vehicle emissions and their control in China: A review and outlook', *Science of the Total Environment*, vol. 574, pp. 332–49.

x-engineer.org 2019, *Mild Hybrid Electric Vehicle (MHEV) Architectures*, viewed <https://x-engineer.org/automotive-engineering/vehicle/hybrid/mild-hybrid-electric-vehicle-mhev-architectures/>.

Xu, X., Dong, P., Liu, Y. & Zhang, H. 2018, 'Progress in Automotive Transmission Technology', *Automotive Innovation*, vol. 1, no. 3, pp. 187–210.

Xue, X.D., Cheng, K.W.E. & Cheung, N.C. 2008, 'Selection of Electric Motor Drives for Electric Vehicles', *2008 Australasian Universities Power Engineering Conference*, no. January, pp. 1–6.

Xueshan, Y., Xiaozhai, Q., Lee, G.C., Tong, M. & Jinming, C. 2008, 'Jerk and Jerk Sensor', *World Conference on Earthquake Engineering*, Beijing, China.

Yu, S., Dong, G. & Li, L. 2008, 'Transient Characteristics of Emissions During Engine Start/Stop Operation Employing a Conventional Gasoline Engine for HEV Application', *International Journal of Automotive Technology*, vol. 9, no. 5, pp. 543–9.

Zhang, J., LU, X., Wang, L., Chen, S. & LI, S. 2010, 'A Study on the Drivability of Hybrid Electric Vehicle', *SAE Technical Paper Series*, vol. 1, no. 724.

Zhang, J.F., Lu, X.F., Lu, J., Kang, Q. & Dong, X.Z. 2011, 'Study of the new permanent magnet switched reluctance motor', *APAP 2011 - Proceedings: 2011 International Conference on Advanced Power System Automation and Protection*, vol. 3, pp. 1684–7.

Zhao, F., Liu, F., Liu, Z. & Hao, H. 2019, 'The correlated impacts of fuel consumption improvements and vehicle electrification on vehicle greenhouse gas emissions in China', *Journal of Cleaner Production*, vol. 207, no. 2019, pp. 702–16.

Zhou, X., Walker, P., Zhang, N., Zhu, B. & Ruan, J. 2014, 'Numerical and experimental investigation of drag torque in a two-speed dual clutch transmission', *Mechanism and Machine Theory*, vol. 79, pp. 46–63.

Zulkifli, S., Harith Hamdan, M., Saad, N. & Aziz, A. 2017, 'System Integration in a Through-the-Road, In-Wheel Motor Hybrid Electric Vehicle Using FPGA-Based CompactRIO and LabVIEW', *Journal of the Society of Automotive Engineers Malaysia*,

vol. 1, no. 3, pp. 216–27.